

INFLUENCE OF CURRENT DISTRIBUTIONS ON THE INTERPRETATION OF
THE IMPEDANCE SPECTRA COLLECTED FOR A ROTATING DISK ELECTRODE

By

MADHAV DURBHA

A DISSERTATION PRESENTED TO THE GRADUATE SCHOOL
OF THE UNIVERSITY OF FLORIDA IN PARTIAL FULFILLMENT
OF THE REQUIREMENTS FOR THE DEGREE OF
DOCTOR OF PHILOSOPHY

UNIVERSITY OF FLORIDA

1998

Dedicated

To

My Parents

ACKNOWLEDGMENTS

I would like to sincerely thank Prof. Mark Orazem for his constant support, encouragement, and guidance through the course of this research work. Apart from educating me in several aspects of electrochemical engineering, he provided me with the unique opportunity of working for a semester with the electrochemical research group at the CNRS, Paris. I would also like to thank him for equipping the laboratory with state of the art computing facilities without which this gigantic piece of work would not have been finished in this time span.

My heartfelt thanks to Prof. Luis Garcia Rubio of University of South Florida, and to Drs. Claude Deslouis, Bernard Tribollet, and Hisasi Takenouti of CNRS, Paris, for their valuable suggestions during various stages of this research work. I would like to thank Profs. Oscar Crisalle, Chang Park, Raj Rajagopalan of Chemical Engineering, and Prof. C.C.Hsu of the University of Florida for serving on my dissertation committee.

Thanks are due to my colleagues Steven Carson and Michael Membrino, not just for numerous intellectual exchanges I had with them which thoroughly enhanced my understanding of the subject, but for also educating me in various aspects of American culture. Douglas Riemer's help with software and computers is invaluable. I would like to acknowledge the financial support of the Office of Naval Research. I would also like to thank CNRS, Paris, for their supporting my stay in Paris.

On a more personal level there are a number of people who contributed to my success and it would be impossible thank each of them individually. However I would like to make a special mention of my friend and colleague Basker Varadharajan for his wonderful friendship and for being an outstanding roommate through my graduate studies.

I would like to thank my sisters Dr.Padma and Mrs.Sujana for leading the path towards an advanced degree in engineering, and for creating the academic ambience at home. The constant care and encouragement of my sisters and brothers-in-law has been instrumental for my success.

I would like to take this opportunity to thank a very special person, Dr.Aparna, for all the love, care, and encouragement that she provided during the final phase of my research work. I cherish all the sweet moments that we shared and look forward to an exciting future with her.

I would not have been where I am without all the sacrifices made by my mother and father in providing me with every possible opportunity at every phase of my life. Both of them being in academic positions was of tremendous help towards my academic achievements. With their genuine concern for others and with their extremely likable personalities, they serve as my role models in shaping up my overall personality. I owe everything to them for what I was, for what I am, and for what I am going to be. This work is dedicated to them as a small token of my gratitude.

TABLE OF CONTENTS

	page
ACKNOWLEDGMENTS	iii
LIST OF TABLES	ix
LIST OF FIGURES.....	xi
ABSTRACT	xix
CHAPTERS	
1 INTRODUCTION	1
1.1 Rotating Disk Electrode	2
1.2 Frequency Domain Techniques.....	4
1.3 Motivation for this Work.....	5
1.4 Approach to the Problem	6
2 THE SCHMIDT NUMBER FOR FERRICYANIDE IONS: EXPERIMENTAL DESIGN AND DATA ANALYSIS	13
2.1 Measurement Model	14
2.1.1 Importance of identifying the Stochastic Noise Level.....	14
2.1.2 Classification of Errors.....	16
2.1.3 Kramers-Kronig Relations	17
2.1.4 Identification of Noise Level in the Measurement and Consistency Check	18
2.2 Process Model	19
2.2.1 Process Model for EIS	20
2.2.2 Process Model for EHD	24
2.3 Experimental Design	26
2.3.1 Choice of Surface Treatment	26
2.3.2 Experimental Setup	28
2.4 Data Analysis: Measurement Model	30
2.4.1 Initial Regressions of the Data	30
2.4.2 Obtaining the Error Structure	32
2.4.3 Identification of the Self-Consistent Part of the Impedance Spectra.....	34
2.5 Data Analysis: Process Model	36
2.6 Results from the Steady State Measurements.....	38

2.7 Discussion.....	40
2.8 Conclusions	42
3 INFLUENCE OF SURFACE PHENOMENA ON THE IMPEDANCE RESPONSE OF A ROTATING DISK ELECTRODE	82
3.1 Experimental Protocol.....	83
3.2 Results and Discussion.....	84
3.3 Conclusions	87
4 STEADY STATE MODEL FOR A ROTATING DISK ELECTRODE BELOW THE MASS-TRANSFER LIMITED CURRENT	97
4.1 Theoretical Development	99
4.1.1 Diffusion Layer	99
4.1.2 Outer Region: Laplace's Equation	103
4.1.3 Diffuse Part of the Double Layer	104
4.1.3a Solution of Poisson's equation	105
4.1.3b Calculation of double-layer capacitance.....	108
4.2 Numerical Procedure.....	109
4.2.1 Solution to the Convective Diffusion Equation	109
4.2.2 Algorithm for Implementation of the Model.....	111
4.3 Application to Experimental Systems	112
4.3.1 Electrodeposition of Copper.....	112
4.3.2 Reduction of Ferricyanide on Pt.....	113
4.3.2a Current, Potential, and Charge Distributions	113
4.3.2b Zero Frequency Asymptotes of Local Impedance	115
4.4 Conclusions	116
5 A MATHEMATICAL MODEL FOR THE RADIALLY DEPENDENT IMPEDANCE OF A ROTATING DISK ELECTRODE	132
5.1 Theoretical Development	134
5.1.1 Convective Diffusion	134
5.1.2 Conditions on Current	141
5.1.2a Mass transport	141
5.1.2b Kinetics	142
5.1.3 Potential	143
5.2 Numerical Procedure.....	145
5.3 Results and Discussion	148
5.3.1 Uniform Current Distribution.....	148
5.3.2 Non-Uniform Current Distribution.....	149
5.4 Conclusions	152
6 CHEBYSHEV POLYNOMIAL SOLUTION FOR THE STEADY STATE CONVECTIVE DIFFUSION FOR A ROTATING DISC ELECTRODE	170
6.1 Transformation of the Convective Diffusion Equation	173
6.1.1 Series Approximations.....	175

6.1.2 Recursion Relation for x^2y'	177
6.1.3 Substitution into the Convective Diffusion Equation	179
6.1.4 Non Homogeneous Equations	180
6.2 Results and Discussion	181
6.3 Conclusions	182
7 SPECTROSCOPY APPLICATIONS OF THE KRAMERS-KRONIG TRANSFORMS: IMPLICATIONS FOR ERROR STRUCTURE IDENTIFICATION	186
7.1 Experimental Motivation	187
7.2 Application of the Kramers-Kronig Relations	189
7.3 Absence of Stochastic Errors	190
7.4 Propagation of Stochastic Errors	192
7.4.1 Transformation from Real to Imaginary	193
7.4.2 Transformation from Imaginary to Real	197
7.5 Experimental Verification	199
7.6 Implications for the Error Structure	200
7.7 Conclusions	202
8 COMMON FEATURES FOR FREQUENCY DOMAIN MEASUREMENTS	208
8.1 Similarity in Terms of Line Shapes	210
8.2 Similarity in Terms of Transfer Function	211
8.2.1 Electrochemical Impedance Spectroscopy	211
8.2.2 Rheology of Viscoelastic Fluids	211
8.2.3 Optical Spectroscopy	212
8.2.4 Acoustophoretic Spectroscopy	214
8.3 Similarity in Terms of the Kramers-Kronig Relations	215
8.4 Similarity in Terms of Error Structure	215
8.5 Experimental Results and Discussion	217
8.5.1 Electrochemical Impedance Spectroscopy	217
8.5.2 Test Circuit	220
8.5.3 Electrohydrodynamic Impedance Spectroscopy	222
8.5.4 Rheology of Viscoelastic Fluids	224
8.5.5 Acoustophoretic spectroscopy	225
8.6 Conclusions	225
9 CONCLUSIONS	244
10 SUGGESTIONS FOR FUTURE WORK	246
APPENDICES	
A STEADY STATE MODEL FOR THE ROTATING DISK ELECTRODE	247
B FREQUENCY DOMAIN MODEL FOR THE ROTATING DISK ELECTRODE	269

LIST OF REFERENCES.....	300
BIOGRAPHICAL SKETCH	310

LIST OF TABLES

Table	page
2.1. The conditions and the number of repeated measurements chosen for establishing the error structure for treatment 1	43
2.2. The conditions and the number of repeated measurements chosen for establishing the error structure for treatment 2	43
2.3. Results from the process model regression for EIS data collected using treatment 1, without CPE correction.....	44
2.4. Selected results from the process model regression for EIS data collected using treatment 1, without CPE correction.....	46
2.5. Results from the process model regression for EIS data collected using treatment 1, with CPE correction	47
2.6. Selected results from the process model regression for EIS data collected using treatment 1, with CPE correction	48
2.7. Results from the process model regression for EIS data collected using treatment 2, without CPE correction.....	49
2.8. Selected results from the process model regression for EIS data collected using treatment 2, without CPE correction	51
2.9. Results from the process model regression for EIS data collected using treatment 2, with CPE correction	52
2.10. Results from the process model regression for EIS data collected using treatment 2, with CPE correction	53
2.11. Results from the process model regression for EHD data collected at the mass-transfer-limited current using treatment 1	54
2.12. Selected results from the process model regression for EHD data collected at the mass-transfer-limited current using treatment 1	54
2.13. Limiting current values obtained for treatment 2 at different rotation speeds.....	55

2.14. Schmidt numbers obtained from the i_{lim} values presented in Table 2.14	55
4.1. Polynomial coefficients in the expansion for $\theta'_m(0)$ resulting from the solution of the convective diffusion equation. The number of significant digits reported are based on the respective confidence intervals from the regression.	118
4.2. Input parameters used for the ferri/ferro cyanide in 1M KCl system reacting on the Pt disc electrode	119
5.1. One-dimensional frequency domain process model regressions for the two-dimensional model calculations for a Sc value of 1100 and for an exchange current density of 50mA/cm ² . Dimensionless parameter $J = 3.7445$	154
6.1. Comparison between the Chebyshev approximation and the FDM scheme for m = 0 in the convective diffusion equation. Value of $\theta'_m(0)$ obtained by extrapolation to a step size of zero value is -1.119846522021	183
6.2. Comparison between the Chebyshev approximation and the FDM scheme for m = 5 in the convective diffusion equation. Value of $\theta'_m(0)$ obtained by extrapolation to a step size of zero value is -2.340450747254.....	183
6.3. Comparison between the Chebyshev approximation and the FDM scheme for m = 10 in the convective diffusion equation. Value of $\theta'_m(0)$ obtained by extrapolation to a step size of zero value is -2.901505452807	184

LIST OF FIGURES

Figure	page
1.1. Flow near a rotating disk electrode.....	10
1.2. Small-signal analysis of an electrochemical non-linear system.	11
1.3. Flow diagram of the research work performed. Major contributions from this work are italicized.....	12
2.1. The DC polarization curves for various surface treatments. The results are presented for the cathodic region, as this is the region of interest for this work. Measurements were made at 600 rpm.....	56
2.2. Experimental setup for the impedance measurements.	57
2.3. Regression of a measurement model with 8 Voigt elements to the EIS data obtained for rotating disk electrode at 120 rpm, 1/4th of the limiting current. Solid line in the figures is the measurement model fit and circles represent the data.....	58
2.4. Regression of a measurement model with 8 Voigt elements to the EIS data obtained for rotating disk electrode at 120 rpm, 1/4th of the limiting current, corresponding to the condition in Figure 2.3. (a) real part as a function of frequency and (b) imaginary part as a function of frequency.....	59
2.5. Normalized residual errors in the (a)real and (b)imaginary parts as functions of frequency for the regression of a measurement model with 8 Voigt elements to the EIS data obtained for rotating disk electrode at 120 rpm, 1/4th of the limiting current.....	60
2.6. Standard deviations in the real (O) and imaginary (Δ) parts calculated using measurement models with modulus weighting for the 3 replicates of EIS data collected at 120rpm, 1/4 th of limiting current case for the rotating disk electrode system.	61
2.7. Regression of a measurement model with 2 Voigt elements to the EHD data obtained for rotating disk electrode at 120 rpm, mass-transfer-limited current using treatment 1. Solid line in the figures is the measurement model fit and circles represent the data.....	62

2.8. Regression of a measurement model with 2 Voigt elements to the EHD data obtained for rotating disk electrode at 120 rpm, mass-transfer-limited current. The corresponds to that in Figure 2.7. Solid line in the figures is the measurement model fit. (a) real and (b) imaginary parts as functions of frequency.....	63
2.9. Normalized residual errors in the (a) real and (b) imaginary parts as functions of frequency from the regression of a measurement model with 2 Voigt elements to the EHD data obtained (corresponding to Figure 2.7) for rotating disk electrode at 120 rpm, mass-transfer-limited current.....	64
2.10. The solid line represents the error structure model obtained by accounting for various conditions for the rotating disk electrode, using treatment 1. The (O)s and the (Δ)s represent the standard deviations of the stochastic noise obtained by using the measurement model approach applied to 120rpm, 1/4 th of limiting current.....	65
2.11. The solid line represents the error structure model obtained by accounting for various conditions for the rotating disk electrode, using treatment 1. The (O)s and the (Δ)s represent the standard deviations of the stochastic noise obtained by using the measurement model approach applied to 1200 rpm, 1/2 of limiting current.....	66
2.12. The solid line represents the error structure model obtained by accounting for various conditions for the rotating disk electrode, using treatment 1. The (O)s and the (Δ)s represent the standard deviations of the stochastic noise obtained by using the measurement model approach applied to 3000 rpm, 1/2 of limiting current.....	67
2.13. Checking for consistency with the Kramers-Kronig relations. EIS data collected for 120 rpm, 1/4 th of the limiting current case for the rotating disk electrode system. Measurement model was regressed to the (a)real part and (b)imaginary part was predicted based on the 10 lineshape parameters obtained. The outer lines represent the 95.4% confidence limits and the line through the data is the measurement model fit.....	68
2.14. Normalized residual errors in (a) real and (b) imaginary parts corresponding to the regression results presented in Figure 2.13. The outer lines represent the 95.4% confidence limits and the line through the data is the measurement model fit	69
2.15. Checking for consistency with the Kramers-Kronig relations. 120 rpm, 1/4 th of the limiting current case for the rotating disk electrode system. Measurement model was (a)regressed to the imaginary part and (b)real part is predicted based on the 11 lineshape parameters obtained. The outer lines represent the 95.4% confidence limits and the line through the data is the	

measurement model fit	70
2.16. Normalized residual errors in (a) real and (b) imaginary parts corresponding to the regression results presented in Figure 2.15. The outer lines represent the 95.4% confidence limits and the line through the data is the measurement model fit	71
2.17. Process model regression (with error structure weighting) for 120 rpm, 1/4 th of the limiting current case for the rotating disk electrode system. Error structure was used to fit the data to the model. The solid line represents fit of the model to the data.....	72
2.18. Process model regression (with error structure weighting) for EIS data collected at 120 rpm, 1/4 th of the limiting current case for the rotating disk electrode system, corresponds to Figure 2.17. Error structure was used to fit the data to the model. The solid line represents fit of the model to the data. Outer lines represent the 95.4% confidence limits.....	73
2.19. Normalized residual errors in (a) real and (b) imaginary parts corresponding to the regression results presented in Figure 2.17. The outer lines represent the 95.4% confidence limits.....	74
2.20. Process model regression (with error structure weighting) accounting for CPE correction for the EIS data collected for 120 rpm, 1/4 th of the mass-transfer-limited current case for the rotating disk electrode system using treatment 1. The solid line represents fit of the model to the data.	75
2.21. Process model regression (with error structure weighting) accounting for CPE correction for the EIS data collected for 120 rpm, 1/4 th of the mass-transfer-limited current case for the rotating disk electrode system using treatment 1, corresponding to Figure 2.20. The solid line represents fit of the model to the data. (a) real and (b) imaginary parts as functions of frequency.....	76
2.22. Normalized residual errors in (a) real and (b) imaginary parts corresponding to the regression results presented in Figure 2.20. The dashed lines represent the normalized noise level.	77
2.23. Process model regression (with error structure weighting) for the EHD data collected for 120 rpm, at the mass-transfer-limited current case for the rotating disk electrode system using treatment 1. The solid line represents fit of the model to the data.	78
2.24. Process model regression (with error structure weighting) for the EHD data collected for 120 rpm, at the mass-transfer-limited current case for the rotating disk electrode system using treatment 1, corresponds to Figure 2.23. The solid line represents fit of the model to the data.	

(a) Real part and (b) Imaginary part as functions of frequency.....	79
2.25. Residual errors in (a) real and (b) imaginary parts corresponding to the regression results presented in Figure 2.23. The dashed lines represent the noise level.	80
2.26. The square root of the rotation speed plotted against the mass-transfer-limiting current value. The line passing through is regressed ignoring the 3000rpm case.....	81
3.1. Imaginary part of the impedance for reduction of ferricyanide on a Pt disk rotating at 120 rpm and at 1/4 th of the limiting current. The time trending between the spectra can be seen very clearly.....	88
3.2. Real part of the impedance for the repeated measurements with time as a parameter.....	89
3.3. Error structure for the data presented in Figure 3.1 and Figure 3.2: filled symbols represent the statistically calculated standard deviations of repeated measurements; open symbols are the standard deviations of the stochastic noise calculated using the measurement model approach.....	90
3.4. Normalized residual sum of squares for regression of a process model to the data presented in Figure 3.1 and Figure 3.2. The inner and outer dashed lines correspond to the 0.05 and 0.01 levels of significance for the F-test.....	91
3.5. Schmidt number obtained by regression of process model to the data.....	92
3.6. Charge transfer resistance obtained by regression of process model to the data.....	93
3.7. Mass transfer resistance obtained by regression of a process model to the data.....	94
3.8. Double layer capacitance obtained by regression of process model to the data.....	95
3.9. Exponent in the CPE element obtained by regression of process model to the data.....	96
4.1. Determination of the accurate value for $\theta_m'(0)$ for infinite Schmidt number, making use of the values obtained from the FDM scheme using varying step-sizes.	120
4.2. A sixth degree polynomial fit for $\theta_m'(0)$ vs. $Sc^{-1/3}$	121
4.3. Errors in $\theta_m'(0)$ values between polynomial fits and the values calculated from the FDM scheme.....	122
4.4. Calculated (a) concentration and (b) current distribution on the surface of	

the disk electrode for deposition of copper under the condition corresponding to figures (6) and (7) of reference (41) with N=50. Adjacent infinite Sc (dashed lines) and finite Sc (solid lines) are for same applied potential. In the order of decreasing concentration, the applied potentials (V- Φ_{ref}) used were -0.08V, -0.28 V, -0.68V, -0.98V, -1.28V, and -1.58V.....	123
4.5. Calculated current distributions for the reduction of ferricyanide on a Pt disk electrode rotating at (a)120rpm and (b)3000 rpm. System properties are given in Table 4.2.....	124
4.6. Calculated overpotentials for the case of Figure 4.5a (120rpm) at (a)1/4th of i_{lim} , (b)1/4 of i_{lim} on an enlarged scale to show the distributions of η_s^* and ζ	125
4.7. Calculated overpotentials for the case of Figure 4.5a (120rpm) at 3/4th of i_{lim}	126
4.8. Calculated overpotentials for the case of Figure 4.5b (3000rpm) at (a)1/4th of i_{lim} , (b)1/4 of i_{lim} on an enlarged scale to show the distributions of η_s^* and ζ	127
4.9. Calculated overpotentials for the case of Figure 4.5b (3000rpm) at 3/4th of i_{lim}	128
4.10. Calculated charge distributions for the cases of (a) Figure 4.5a (120rpm) and (b) Figure 4.5b (3000rpm).....	129
4.11. Calculated local impedance distributions corresponding to Figure 4.5a (120 rpm) for (a)1/4th of i_{lim} , and (b)3/4th of i_{lim}	130
4.12. Calculated local impedance distributions corresponding to Figure 4.5b (3000 rpm) for (a)1/4th of i_{lim} , and (b)3/4th of i_{lim}	131
5.1. (a) Comparison between one-dimensional and two-dimensional models for the slow kinetics case at 1/4 th of i_{lim} and $\Omega=120$ rpm with $i_0 = 3 \text{ mA/cm}^2$, $D = 0.3095 \times 10^{-5} \text{ cm}^2/\text{sec}$, $J = 0.225$, $N = 0.0695$, and $Sc = 2730$. In this case steady-state distributions tend to be highly uniform. (b) Differences between the calculations from two-dimensional and one-dimensional model normalized with respect to the two-dimensional model as a function of frequency.....	155
5.2. Comparison between the impedance spectra generated by 1D and 2D models for 120rpm, 1/4 th of i_{lim} , $i_0 = 30 \text{ mA/cm}^2$, $D = 0.3095 \times 10^{-5} \text{ cm}^2/\text{sec}$, $J = 2.247$, $N = 0.0695$, and $Sc = 2730$. Results presented for impedance plane plot.	156
5.3. Comparison between the impedance spectra generated by 1D and 2D models for 120rpm, 1/4 th of i_{lim} , $i_0 = 30 \text{ mA/cm}^2$, $D = 0.3095 \times 10^{-5} \text{ cm}^2/\text{sec}$, $J = 2.247$, $N = 0.0695$, and $Sc = 2730$ (corresponds to Figure 5.2). Results presented for (a) real part as a function of frequency (b) imaginary part as a function of frequency.....	157

5.4. Comparison between the impedance spectra generated by 1D and 2D model for 3000rpm, 1/4 th of i_{lim} , $i_0 = 100 \text{ mA/cm}^2$, $D = 0.3195 \times 10^{-5} \text{ cm}^2/\text{sec}$, $J = 7.489$, $N = 0.3552$, and $Sc = 2650$	158
5.5. Comparison between the impedance spectra generated by 1D and 2D model for 3000rpm, 1/4 th of i_{lim} , $i_0 = 100 \text{ mA/cm}^2$, $D = 0.3195 \times 10^{-5} \text{ cm}^2/\text{sec}$, $J = 7.489$, $N = 0.3552$, and $Sc = 2650$ (corresponds to Figure 5.4). Results presented for (a) real part as a function of frequency (b) imaginary part as a function of frequency	159
5.6. Comparison between the impedance spectra generated by 1D and 2D model for 120rpm, 3/4 th of i_{lim} , $i_0 = 100 \text{ mA/cm}^2$, $D = 0.5095 \times 10^{-5} \text{ cm}^2/\text{sec}$, $J = 7.489$, $N = 0.0970$, and $Sc = 1660$. Results presented for impedance plane plot.....	160
5.7. Comparison between the impedance spectra generated by 1D and 2D model for 120rpm, 3/4 th of i_{lim} , $i_0 = 100 \text{ mA/cm}^2$, $D = 0.5095 \times 10^{-5} \text{ cm}^2/\text{sec}$, $J = 7.489$, $N = 0.0970$, and $Sc = 1660$ (corresponds to Figure 5.6). Results presented for (a) real part as a function of frequency (b) imaginary part as a function of frequency	161
5.8. Comparison between the impedance spectra generated by 1D and 2D model for 3000rpm, 3/4 th of i_{lim} , $i_0 = 75 \text{ mA/cm}^2$, $D = 0.6795 \times 10^{-5} \text{ cm}^2/\text{sec}$, $J = 5.617$, $N = 0.5874$, and $Sc = 1250$. Results presented for impedance plane plot.....	162
5.9. Comparison between the impedance spectra generated by 1D and 2D model for 3000rpm, 3/4 th of i_{lim} , $i_0 = 75 \text{ mA/cm}^2$, $D = 0.6795 \times 10^{-5} \text{ cm}^2/\text{sec}$, $J = 5.617$, $N = 0.5874$, and $Sc = 1250$ (corresponds to the condition of Figure 5.8). Results presented for (a) real part as a function of frequency (b) imaginary part as a function of frequency	163
5.10. Distributions for local impedance values for a dimensionless frequencies of K=1 and K=2.8. The parameter values are those given in Figure 5.6 and Figure 5.8.....	164
5.11. Results for regression of the 1D model to a 2D model simulation for 120rpm, 3/4 th of i_{lim} . An input value of $Sc = 1660$ for 2D model resulted in a regressed Sc of 1780 for the 1D model case. (a) complex plane plot (b) real impedance as a function of frequency (c) imaginary impedance as a function of frequency	166
5.12. Results for regression of the 1D model to a 2D model simulation for 3000rpm, 3/4 th of i_{lim} . An input value of $Sc = 1250$ for 2D model resulted in a regressed Sc of 1530 for the 1D model case. (a) complex plane plot (b) real impedance as a function of frequency (c) imaginary impedance as a function of frequency	168

6.1. Chebyshev polynomials as functions of x	185
7.1. Hierarchical representation of spectroscopic measurements. The shaded boxes represent measurement strategies for which the real and imaginary parts of Kramers-Kronig-transformable impedance were found to have the same standard deviation. Following completion of the analysis reported here, an experimental investigation was begun which showed that the real and imaginary parts of complex viscosity also have the same standard deviation if the spectra are consistent with the Kramers-Kronig relations.	204
7.2. Path of integration for the contour integral in the complex-frequency plane.	205
7.3. Weighting factor for Eq. (7.17) as a function of m normalized to show relative contributions to the integral.....	206
7.4. Real (a) and imaginary (b) parts of a typical electrochemical impedance spectrum as a function of frequency. The normal probability distribution function, shown at a frequency of 0.03 Hz, shows that one consequence of the equality of the standard deviations for real and imaginary components is that the level of stochastic noise as a percentage of the signal can be much larger for one component than the other.	207
8.1. Line-shape models yielding the same mathematical structure for spectroscopic response: a) Voigt model for electrochemical systems; b) Kelvin-Voigt model for rheology of viscoelastic fluids.....	227
8.2. (a)The impedance response obtained under potentiostatic modulation for reduction of ferricyanide on a Pt disk electrode rotating at 120 rpm, at 1/4 th of mass-transfer limited current in a 1M KCl aqueous solution. Closed symbols represent the impedance values and open symbols represent the corresponding standard deviation. O) Real part and Δ) Imaginary part. (b) F-test parameters. The inner dashed lines represent the 95% confidence limits for the F-test parameter and the outer lines represent the 99% confidence limits. Circles represent the F-test parameters for the raw standard deviations. (c) F-test parameters after deleting the point close to 50Hz and 100Hz. (d) Histogram with <i>t</i> -test results.....	228
8.3. (a)The impedance response obtained under galvanostatic modulation for a parallel R_1C_1 circuit in series with a resistor R_0 ($R_0/R_1=10$). Closed symbols represent the impedance values and open symbols represent the corresponding standard deviation. The line represents the model for the error structure given as equation (8.18). O) Real part and Δ) Imaginary part. (b) F-test corresponding to the variances of stochastic noise (c) Histogram with <i>t</i> -test results corresponding to the variance of stochastic noise.....	232

8.4. (a)The EHD impedance response obtained for reduction of ferricyanide on a Pt disk electrode rotating at 200 rpm in a 1M KCl aqueous solution. Closed symbols represent the electro-hydrodynamic impedance values and open symbols represent the corresponding standard deviation. The line represents the model for the error structure given as equation (8.18). O) Real part and Δ) Imaginary part. (b) Statistical F-test to verify the equality of standard deviations in the stochastic noise (c) Histogram with <i>t</i> -test results corresponding to the variance of stochastic noise.....	235
8.5. (a)The complex viscosity for high density polyethylene melt. Closed symbols represent the viscosity values and open symbols represent the corresponding standard deviation. O) Real part and Δ) Imaginary part. (b) F-test corresponding to the variances of stochastic noise (c) Histogram with <i>t</i> -test results corresponding to the variance of stochastic noise	238
8.6. (a)The complex mobility for a suspension of polyacrylic acid (PAA) with a density of 0.062 g/L, a pH of 10, and a molecular weight of 5000. Closed symbols represent the mobility values and open symbols represent the corresponding standard deviation. O) Real part and Δ) Imaginary part. (b) F-test corresponding to the variances of stochastic noise (c) Histogram with <i>t</i> -test results corresponding to the variance of stochastic noise	241

Abstract of Dissertation Presented to the Graduate School
of the University of Florida in Partial Fulfillment of the
Requirements for the Degree of Doctor of Philosophy

**INFLUENCE OF CURRENT DISTRIBUTIONS ON THE INTERPRETATION OF
THE IMPEDANCE SPECTRA COLLECTED FOR A ROTATING DISK ELECTRODE**

By

Madhav Durbha

August, 1998

Chairman: Prof. Mark E. Orazem

Major Department: Chemical Engineering

The influence of current distributions on the interpretation of the frequency domain data collected for a rotating disk electrode is presented in this work. Numerous steady state and frequency domain measurements were conducted for ferricyanide reduction on a platinum disk electrode. The error characteristics of the data were established using the measurement model software developed in-house, and this information was used in further regressions of the process model to the experimental data. The frequency domain process model currently used to describe the physics of the system was found to be inadequate. A very sophisticated steady-state model, accounting for a finite Schmidt number and for charge distribution within the diffuse part of the double layer, was developed here to create the base line values needed to study the frequency perturbations. This model was then used to develop a two dimensional frequency-domain process model for the system

of interest. It is shown here that this frequency domain model provides a significant improvement over the one-dimensional model used for the preliminary analysis.

One surprising result from this work is the equality of standard deviations in the real and imaginary parts of the stochastic noise in the frequency domain data analyzed. An analytical proof for this result, based on Kramers-Kronig relations, is presented here. This result was very general and was found to be true even in the case of frequency domain data collected for non-electrochemical systems. Supportive evidence based on a number of diverse spectroscopic techniques is presented in this work.

CHAPTER 1

INTRODUCTION

Proper understanding of the current and potential distributions in electrochemical systems is of great practical importance. The predominant industrial applications are in cathodic protection, electrodeposition, and transdermal delivery of drugs. Underlying principles being the same, the main focus of these applications is in understanding and controlling the distribution of current on the surface of interest. One of the classic examples is the cathodic protection of underground or underwater pipelines by the placement of sacrificial anodes. These anodes are made of metals that are less noble or more vulnerable to corrosion compared to the metal used in making the pipeline. As an example, zinc is used in protecting stainless steel pipes. As the local current density on the pipeline is an indication of the protection to the surface in that location, it is important to know the distribution of current on the pipeline in order to identify the regions that are overprotected or under protected. Knowledge of current distribution is of paramount importance to the corrosion engineer as this facilitates a judicious choice of one cathodic protection system over the other or a choice of one electrode configuration over the other.

One of the recent breakthroughs in semiconductor device fabrication is in the use of copper as an interconnect in integrated circuits. Due to the superior properties of copper over Aluminium which is traditionally used in device fabrication, a large number of integrated circuit manufacturers are expressing increased amount of interest in using copper. Various techniques were attempted for the deposition of copper, such as vapor

deposition, electroless deposition and so on, and electrodeposition of copper is found to be the most viable technique. The use of copper for interconnects is expected to enhance the performance of various appliances such as microprocessors and memory circuits. Uniformity of deposition is a very important issue here and excess of copper should be avoided at all costs, as the semi-conductor process engineers are interested in sub-micron feature sizes. In the context of electrodeposition, the amount of metal being deposited is directly related to the local current density. Hence it is very important to identify and control the local current density distribution in order to achieve layers of desirable quality in specified locations. This is a complicated task, as understanding the current distributions in an electrochemical system requires an in-depth knowledge of the effects of ohmic drop, kinetic contribution, and mass transfer related issues. Recent past has seen a growing amount of literature pertaining to the theoretical and experimental aspects of the current and potential distributions for a number of electrochemical systems. Two electrode setups which are very commonly used are rotating disk electrode and impinging jet disk electrode. These two setups share similarities with respect to the associated fluid mechanics. Models developed for one system can very easily be extended to the other by properly accounting for various velocity components in modeling the convection.

1.1 Rotating Disk Electrode

The metal electrode is made in the form of a cylinder and surrounding it is an insulating material so that the circular face of the disk is exposed to the electrolyte, as shown in Figure 1.1. The metal-insulator assembly is arranged concentrically and is rotated about the center with the help of a rotor. Due to this design, the wall and edge

effects for the electrode can be ignored. This system is very effective for the identification of mechanisms and associated rate constants for electrode reactions, for studying homogeneous reactions accompanied by electrode processes, and for the measurement of diffusion coefficients of dissolved species. Here are some of the very important features of this system:

- The fluid flow for this system is very well defined and the uniform axial velocity yields a uniform mass-transfer-limited current density.
- Due to the imposed rotation rate, the effects associated with the free convection can be ignored.
- By increasing the rotation speed, the mass-transfer-limited current can be increased and this results in an improved signal to noise ratio in measuring the current.
- The fluid mechanics associated with this system are very well understood.

Because of these features, the rotating disk electrode system attracted the attention of a number of researchers interested in the current and potential distribution studies. The introductory parts of chapters 4 and 5 summarize the major contributions in steady state and in frequency domains for the rotating disk electrode system. Steady-state techniques include simple current-voltage measurements with no time dependence, that is, for an imposed value of potential a value of current is obtained and vice versa, after allowing the system to attain a steady-state. Frequency domain data are more complicated to analyze compared to the steady-state data, as the information content is more. Before proceeding further, it is important to gain some basic understanding of the frequency domain techniques.

1.2 Frequency Domain Techniques

The fundamental approach of all frequency domain techniques is to apply a small amplitude sinusoidal excitation signal (such as voltage or current) to the system under investigation and to measure the response (such as current or voltage). The excitation signal can be applied in several ways. The two most commonly employed methods are multi-sine and single-sine techniques. Fast measurement time and mild perturbation of the system under investigation are stated to be the strengths of the multi-sine technique, though it has been shown that by using a fast frequency response analyzer, the difference in the measurement time for a single-sine and a multi-sine technique is small [1]. One of the disadvantages of this technique is that it has a small frequency range. The multi-sine technique is also sensitive to harmonic distortion. In this work impedance data was collected using the single-sine technique.

The use of single-sine technique used for electrochemical impedance spectroscopy is illustrated in Figure 1.2. As shown in this figure, a low amplitude sine wave $\Delta E \sin \omega t$ is superimposed on the dc polarization voltage E_0 . Hence, a low amplitude sine wave $\Delta I \sin (\omega t - \phi)$ is observed to be superimposed on the dc current. The Taylor series expansion for the current is given by

$$\Delta I = \left(\frac{dI}{dE} \right)_{E_0, I_0} \Delta E + \frac{1}{2} \left(\frac{d^2 I}{dE^2} \right)_{E_0, I_0} (\Delta E)^2 + \dots \quad (1.1)$$

As the system under consideration is non-linear in nature, higher order derivatives do exist. However, for a very small perturbation in potential, terms of order $\frac{1}{2} \left(\frac{d^2 I}{dE^2} \right)_{E_0, I_0} (\Delta E)^2$ and higher can be neglected and only the linear terms need to be

retained. This process is known as quasi-linearization and is widely used in non-linear system analysis.

In the rotating disk electrode system, a number of variables can influence the output. In recent years generalized impedance techniques have been introduced in which a nonelectrical quantity such as pressure, temperature, magnetic field, or light intensity is modulated to give a current or potential response [2,3]. Electrohydrodynamic impedance (EHD) is one such generalized impedance technique in which sinusoidal modulation of the disk rotation rate drives a sinusoidal current or potential. One attractive feature of EHD is that this technique can be used under mass-transfer limitation. More details about this technique will be presented in a later chapter.

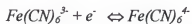
1.3 Motivation for this Work

The importance of the current and potential distributions in case of various engineering problems is highlighted in the beginning of this chapter. The motivating factor for this study is to understand the issue of current distributions in the flow-induced corrosion of copper in seawater. The importance of understanding the current distributions in this case was illustrated earlier through experiments conducted in the steady state as well as in the frequency domain [4]. Images captured through video microscopy during the corrosion process revealed that a number of films were being formed on the surface of the copper disk electrode. However the large number of salts that are present in the synthetic seawater makes the characterization of this system very difficult. Especially, impedance data interpretation is very complicated as the information content obtained from frequency domain techniques is more than what is typically

obtained from the steady state calculations. In order to gain a proper understanding of this system, one needs to possess great expertise in the interpretation of the experimental data based on the current distributions obtained. The interpretation of the data collected in the impedance domain based on the current and potential distributions can be said to be the central theme of this work. A simple model system, which is explained in the next section, is chosen for the purpose of this study. The interpretations can later be extended to the phenomena occurring in more complex systems such as the corrosion of copper in seawater.

1.4 Approach to the Problem

For the purpose of studying the influence of the current distributions on the interpretation of the impedance data, a model system is chosen that is simpler in nature in comparison with the copper in seawater system. This is a platinum rotating disk electrode immersed in an electrolyte containing 0.01M potassium ferricyanide, 0.01M potassium ferrocyanide, and 1M potassium chloride as the indifferent or supporting electrolyte. The reaction that is occurring is the reduction of ferricyanide (the operation is in the cathodic regime), that is,



This system was thought of as an easier system to understand because

1. The surface of the electrode is relatively inactive in highly cathodic regions,
2. Presence of excess supporting electrolyte undermines the influence of the ohmic contributions, and

3. The reaction is very fast and hence the effects of mass transport phenomena are predominant.

However, during the course of this work, the system at hand which was supposed to be easier to understand was observed to be more difficult than what was thought. The impedance data for this system collected at CNRS, Paris, France, was analyzed using the one-dimensional frequency domain model proposed by Tribollet and Newman [5] in order to obtain the Schmidt number values for the ferricyanide ions. This analysis resulted in some anomalous observations. The regressed values for Schmidt number increased with an increase in rotation speed. These values are observed to be quite close to the actual Schmidt number (around 1100 in case of the system of interest) at low rotation speeds (120rpm) and progressively increased to quite high values (as high as 1500) at high rotation speeds (3000rpm). For high rotation speed cases where the Schmidt number values are closer to 1100, the quality of regressions is poor. These observations are in agreement with the results obtained by Deslouis and Tribollet [6]. There are two major issues that could cause the disparity in the determined value of the Schmidt number. The first one is the non-uniform distribution of current and potential on the surface of the disk electrode, which points to the inadequacy of Tribollet and Newman's one-dimensional model. The other issue is the partial blocking of the electrode surface, which could be a result of reactant, product, or intermediate ionic species adhering to the surface of the disk electrode, thus reducing the mass-transfer/reaction rate. The primary focus for this work is in explaining the influence of non-uniform current distributions on the interpretation of impedance spectra.

During the experimental stages of this work, repeated impedance measurements were made for this system, in order to facilitate the use of the measurement model approach of Agarwal *et al.* [7-11] in determining the contribution of the stochastic noise in the measurement. From this analysis, and from a number of other frequency domain techniques studied, it was observed that the standard deviations of the real and imaginary parts of the stochastic noise were equal for the system of interest, when the real and imaginary parts were obtained in a single measurement. This led to investigating a theoretical basis for such an observation. One of the premises the measurement model is based on is that the Kramers-Kronig relations [12] are applicable for the particular system of interest. These are integral transforms, which relate the real and imaginary parts of the complex quantity measured. It was found that the equality of the standard deviations of the real and imaginary stochastic components is a direct consequence of the applicability of Kramers-Kronig relations [13]. An analytical proof is presented in chapter 7.

The research work that was proposed and accomplished for this work is presented in the form of a flow diagram in Figure 1.3. The research work performed in order to analyze the problem is organized and presented in the subsequent chapters in a logical manner. In chapter 2, the experimental procedure and the data analysis of the impedance experiments is presented and the need for studying the non-uniformity and surface blocking issues is established. The evidence for the presence of surface blocking from the electrochemical impedance spectroscopy measurements is established in chapter 3. In chapter 4, a steady state model for the current distributions on the rotating disk electrode surface is proposed. This model explicitly accounts for a finite Schmidt number correction and the charge distribution on the electrode surface. This is used as a building block for

the development of a two-dimensional frequency-domain model that is presented in chapter 5. In this chapter, a comparison is made between the experimental data and the simulated results from Tribollet and Newman's one-dimensional model and the two-dimensional model developed here. In this chapter it is shown that the non-uniformities do play an important role in the data interpretation. However there still is a significant disparity between the experimental and the simulated values from the two-dimensional model, which suggests that surface blocking phenomena play a significant role. Chapter 6 provides an alternative method for solving the steady state convective diffusion equation presented in chapter 4. One could proceed to chapter 7 from chapter 5, without sacrificing the continuity in the flow of text.

An equality of standard deviations in the real and imaginary parts of the stochastic noise in the measured impedance was observed during the course of this work. An analytical proof for this observation is provided in chapter 7. The results presented in Chapter 8 illustrate that the equality of standard deviations in the stochastic noise is valid for a large variety of frequency domain techniques for which Kramer-Kronig relations are applicable. Conclusions from this work and suggestions for future work are provided in chapters 9 and 10 respectively.

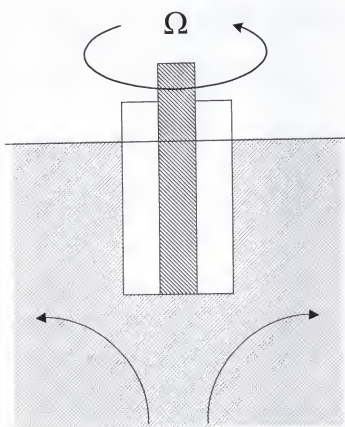


Figure 1.1. Flow near a rotating disk electrode.

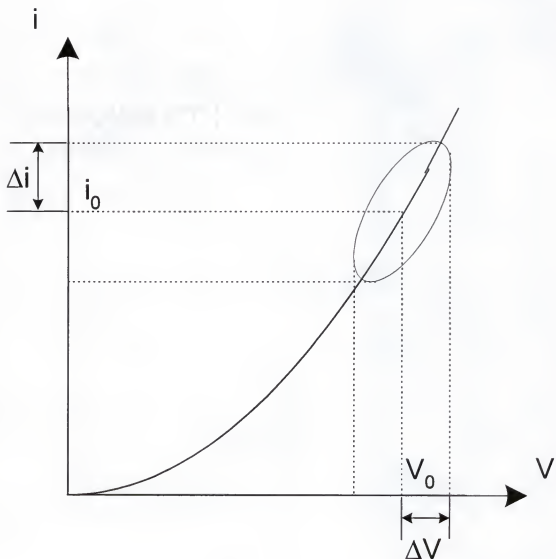


Figure 1.2. Small-signal analysis of an electrochemical non-linear system.

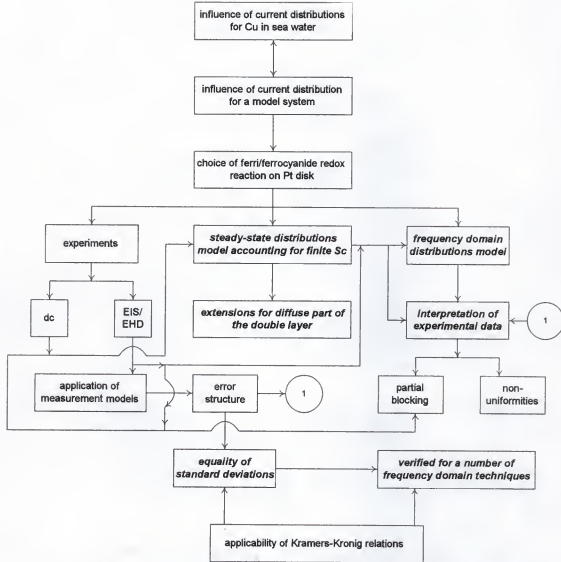


Figure 1.3. Flow diagram of the research work performed. Major contributions from this work are italicized.

CHAPTER 2

THE SCHMIDT NUMBER FOR FERRICYANIDE IONS: EXPERIMENTAL DESIGN AND DATA ANALYSIS

The importance of current distributions in electrochemical systems is emphasized in chapter 1. In the present chapter the need for studying the current distributions in interpreting the impedance data is established. Interpretation of electrochemical/electrohydrodynamic impedance spectroscopy data requires an appropriate model that describes the underlying processes occurring in the system under study. Electric circuit analogue models consisting of resistors, capacitors, inductors, and specialized distributed elements are commonly used to represent the impedance response of an electrochemical system. These models can be classified into process models and measurement models. Process models are used to predict the response of the system accounting for physical phenomena that are hypothesized to be important. Regression of process models to data allows identification of physical parameters based on the original hypothesis. In contrast, measurement models are used to identify the characteristics of the data set that could facilitate selection of an appropriate process model. It should be noted that the measurement models are used mostly for the statistical validation of data rather than to identify the physics of the process. However it is more appropriate to use a process model to gain a deeper insight into the physics of the system. The steady state and frequency domain process models developed for a typical electrochemical system are presented in chapters 4 and 5. In the present chapter, the focus is on the use of

measurement models for impedance data analysis, on the determination of Schmidt number of ferricyanide ions through the application of an available one-dimensional process model, and on identification of the need to understand the current distributions for the system under consideration.

2.1 Measurement Model

The measurement model selected for this work was the Voigt model given by

$$Z(\omega) = Z_0 + \sum_k \frac{\Delta_k}{1 + j\tau_k \omega} \quad (2.1)$$

where $Z(\omega)$ is the quantity being measured, Z_0 is the high frequency asymptotic limit of the impedance, k denotes the number of frequency dependent processes associated with the system under consideration, Δ_k is the gain factor, τ_k is the time constant associated with each of the relaxation processes, and ω is the applied frequency. The above approach can also be viewed as a series of resistance and capacitance elements connected in series as illustrated later in Figure 8.1(a). In this case the time constant τ_k for element k is equivalent to $R_k C_k$ and Δ_k is equivalent to R_k , where R_k and C_k are resistance and capacitance respectively. A detailed discussion on measurement models can be found in reference 14. The major contribution of measurement models has been in identifying the stochastic and bias errors in impedance measurements. Such information has been used to enhance the information content that can be obtained from experimental data.

2.1.1 Importance of identifying the Stochastic Noise Level

The choice of a proper weighting strategy for regression of models to data is facilitated by identification of the stochastic noise in the experimental data. The data with

more noise should be assigned less weight towards the regression parameter and vice versa. The regression parameter is given by

$$J = \sum_k \frac{(Z_{r,k} - \hat{Z}_{r,k})^2}{\hat{\sigma}_{r,k}^2} + \sum_k \frac{(Z_{j,k} - \hat{Z}_{j,k})^2}{\hat{\sigma}_{j,k}^2} \quad (2.2)$$

where $Z_{r,k}$ and $Z_{j,k}$ are the real and imaginary parts of the measured impedance at a given frequency ω_k , $\hat{Z}_{r,k}$ and $\hat{Z}_{j,k}$ are the model values corresponding to either a measurement or a process model, and $\hat{\sigma}_{r,k}$ and $\hat{\sigma}_{j,k}$ are the standard deviations in the real and imaginary parts of the stochastic noise in the measurement, also referred to as the noise level in the real and imaginary parts. Different techniques are in existence for weighting the regressions. One commonly used weighting strategy found in the literature is proportional weighting, where it is assumed that $\hat{\sigma}_{r,k}$ and $\hat{\sigma}_{j,k}$ are proportional to the magnitudes of the respective components [15-17]. However in chapter 7 it would be illustrated that such an assumption is incorrect for the systems that are consistent with the Kramers-Kronig relations. Another form of weighting strategy is the one where it is assumed that the noise level in the real and imaginary parts is proportional to the modulus of the complex quantity being measured [18]. Assumptions are commonly made that the noise level in the measurement is about 3% or 5% of the modulus of the quantity being measured. Overestimation of the noise level may lead to significant loss of information content [19]. For this work, the measurement model approach developed by Agarwal *et al.* is used to assess the noise level. At this stage it is necessary to classify errors in the measurement.

2.1.2 Classification of Errors

The residual errors (ε_{res}) that arise due to the regression of a model (\hat{Z}) to experimental data (Z_{exp}) can be of two types, systematic errors (ε_{sys}) and random or stochastic errors (ε_{stoc}).

$$Z_{exp} = \hat{Z} + \varepsilon_{res} \quad (2.3)$$

$$\varepsilon_{res} = \varepsilon_{sys} + \varepsilon_{stoc} \quad (2.4)$$

The systematic errors can arise due to the lack of fit of the model to the data (ε_{lof}) or due to an experimental bias (ε_{bias}), that is,

$$\varepsilon_{sys} = \varepsilon_{lof} + \varepsilon_{bias} \quad (2.5)$$

Experimental bias errors can arise from non-stationary behavior corresponding to a changing baseline during the course of the impedance scan or from instrumental artifacts. Thus,

$$\varepsilon_{bias} = \varepsilon_{ns} + \varepsilon_{ins} \quad (2.6)$$

Most electrochemical systems are inherently non-stationary and can change during the time required to conduct an impedance measurement. This is one of the limitations in choosing the frequency limits for conducting the impedance measurements. The experimental time should be limited in order to not introduce a significant amount of bias into the system. Identification of the part of the spectrum which is not corrupted by the bias errors is very important. In order to address this issue, Kramers-Kronig relations are used.

For spectroscopic techniques such as optical spectroscopy the noise in the measurement can easily be assessed by calculating the raw standard deviations of the

measurements, as a number of repeated measurements can be made in a very short span of time without changing the system baseline. In other words optical spectra can be “truly replicated”. However this is not the case for impedance measurements. The surface properties of the electrode may change significantly during the course of the measurement. The inability to replicate impedance scans motivates the use of measurement models for filtering lack of replicacy.

2.1.3 Kramers-Kronig Relations

Kramers-Kronig relations are self-consistent integral relations which apply to systems that are linear, causal, stable, and stationary. By using the quasi-linear approach, the condition of linearity is satisfied. Causality requires that the response of input cannot precede the input. Stability refers to the boundedness of the output perturbation, and stationarity refers to the time-invariance of the system. Kramers-Kronig relations can be expressed in a number of different ways as presented in [12]. Through the form of Kramers-Kronig relations chosen for this work, the real and imaginary parts of the complex variable being measured (impedance, in the context of present work) are related as

$$Z_j(\omega) = \frac{2\omega}{\pi} \int_0^\infty \frac{Z_r(x) - Z_r(\omega)}{x^2 - \omega^2} dx \quad (2.7a)$$

and

$$Z_r(\omega) = Z_r(\infty) + \frac{2\omega}{\pi} \int_0^\infty \frac{-xZ_j(x) + \omega Z_j(\omega)}{x^2 - \omega^2} dx \quad (2.7b)$$

These relations have a number of implications. Given the imaginary part of the spectrum, the real part can be obtained and vice versa. For the impedance spectroscopy where both the real and imaginary parts are available, these relations can be used as a consistency check to obtain the part of the spectrum which is not corrupted by bias errors, that is, the part of the spectrum where the time dependent variations and instrumental artifacts are not significant. However using these relations in the form of the above equations is not feasible because:

1. The limits of integration vary from 0 to ∞ . However, there is a lower limit for the frequency range in order to minimize the time dependent variation for a given impedance scan (At lower frequencies measurements take longer times). Also, there is an upper limit on the frequency due to the limitations imposed by the instrumentation. Hence only a finite frequency range is available for the integration.
2. Choice of numerical integration scheme is of high importance in using the relations as they appear. There is a point of singularity in the domain of integration at $x = \omega$ and it should be handled with extreme care. An improper choice of an integration scheme may result in significant errors in the calculations performed.

These issues are the limiting factors for direct application of the Kramers-Kronig relations. However by applying measurement models, these relations can be used to identify the self-consistent part of the spectrum without actually performing the integration.

2.1.4 Identification of Noise Level in the Measurement and Consistency Check

One of the inherent benefits of using the measurement models is that the R-C circuit elements or the Voigt elements used in these models satisfy the conditions

associated with the Kramers-Kronig relations. This eliminates the need for the numerical integration of these relations.

Frequency scans are repeated in order to facilitate the assessment of the noise level in the measurement. An error structure model is obtained for the standard deviations in the noise levels and this model is used in weighting the subsequent regressions. At this stage the measurement models were used to regress the real part of the data to the model and predict the imaginary part and vice versa, in order to eliminate the portion of the experimental data that are inconsistent with the Kramers-Kronig relations. The procedure for using measurement models to identify the noise level in the measurement and to check for consistency with the Kramers-Kronig relations is illustrated in a subsequent section. Once the self-consistent part of the spectrum is identified, this can be used for the process model regressions in order to determine the parameters of interest.

2.2 Process Model

The process model used for data analysis in this chapter is a one-dimensional model for impedance spectroscopy developed by Tribollet and Newman [5]. Their model assumes uniform distributions on the surface of the electrode, and this assumption is valid only at the mass-transfer-limited current or under kinetic control. As EIS (Electrochemical Impedance Spectroscopy) measurements cannot be conducted at the mass-transfer-limited current, the existing process model is used both for the EIS data collected below the mass-transfer limited condition and for the EHD (Electrohydrodynamic Impedance Spectroscopy) data collected at the mass-transfer limited condition. A brief overview of the process model for EIS and EHD is presented in this section.

2.2.1 Process Model for EIS

When a one-dimensional analysis is employed for the impedance response of the rotating disk electrode, the unsteady state convective diffusion can be written as

$$\frac{\partial c_i}{\partial t} + v_z \frac{\partial c_i}{\partial z} = D_i \left\{ \frac{\partial^2 c_i}{\partial z^2} \right\} \quad (2.8)$$

where t is the time, z is the axial coordinate, c_i and D_i are the concentration and diffusion coefficient of species i , and v_z is the axial component of the fluid velocity. The boundary conditions for the steady state form of equation (2.8) are that the concentration approaches a bulk value far from the disk and that the flux at the disk surface is related to the current density. The heterogeneous reaction can be expressed symbolically as

$$\sum_i s_i M_i z_i = n e^- \quad (2.9)$$

where the stoichiometric coefficient s_i has a positive value for a reactant, has a negative value for a product, and is equal to zero for a species that does not participate in the reaction. Thus; the boundary conditions are

$$c_i \rightarrow c_{i,\infty} \quad \text{as} \quad z \rightarrow \infty \quad (2.10)$$

and

$$D_i \frac{\partial c_i}{\partial z} = \frac{s_i i_f}{nF} \quad (2.11)$$

where $c_{i,\infty}$ is the bulk concentration of species i , i_f is the Faradic current density, n is the number of electrons transferred, and F is the Faraday's constant (96,487C/eq). The Faradic current density is expressed as a function of surface overpotential η and concentration as

$$i_f = f(\eta, c_i) \quad (2.12)$$

Thus, the concentration at the surface is dependent on applied potential through a reaction mechanism leading to equation (2.12). The concentration perturbation is given by

$$c_i = \bar{c}_i + \text{Re}\{\tilde{c}_i e^{j\omega t}\} \quad (2.13)$$

where the overbar represents the steady value, j is the imaginary number $\sqrt{-1}$, ω is the frequency, and the tilde denotes a complex variable which is a function only of position. Similar definitions are used for all dependent variables.

The dimensionless form of the equation governing the contribution of mass transfer to the impedance response of the disk electrode is developed here in terms of dimensionless frequency

$$K_i = \frac{\omega}{\Omega} \left(\frac{9\nu}{a^2 D_i} \right)^{\frac{1}{3}} = \frac{\omega}{\Omega} \left(\frac{9}{a^2} \right)^{\frac{1}{3}} Sc_i^{\frac{1}{3}} \quad (2.14)$$

and dimensionless position

$$\xi = \frac{z}{\delta_i} \quad (2.15)$$

where Ω is the rotation rate of the disk in cycles per second, ν is the kinematic viscosity in cm^2/s , and

$$\delta_i = \left(\frac{3D_i}{\alpha\nu} \right)^{\frac{1}{3}} \sqrt{\frac{\nu}{\Omega}} = \left(\frac{3}{\alpha} \right)^{\frac{1}{3}} \frac{1}{Sc_i^{\frac{1}{3}}} \sqrt{\frac{\nu}{\Omega}} \quad (2.16)$$

is a characteristic distance for mass transport of species i . Substitution of the definition for concentration (equation (2.13)) into the one-dimensional expression for conservation of species i (equation (2.8)) yields

$$\frac{d^2\tilde{c}_i}{d\xi^2} + v_z \frac{d\tilde{c}_i}{d\xi} - jK_i \tilde{c}_i = 0 \quad (2.17)$$

A solution to equation (2.17), $\tilde{\theta}_i(\xi) = \tilde{c}_i/\tilde{c}_{i,0}$ can be found which satisfies the boundary conditions

$$\begin{aligned}\tilde{\theta}_i &\rightarrow 0 \quad \text{as } \xi \rightarrow \infty \\ \tilde{\theta}_i &= 1 \quad \text{at } \xi = 0\end{aligned} \quad (2.18)$$

The concentration at the surface of the disk is given in terms of $\tilde{\theta}_i(\xi)$ as

$$c_{i,0} = \bar{c}_i + \operatorname{Re} \left\{ \tilde{c}_{i,0} \tilde{\theta}'_i(0) \right\} \quad (2.19)$$

Thus;

$$\left. \frac{d\tilde{c}_i}{dz} \right|_{z=0} = \frac{\tilde{c}_{i,0}}{\delta_i} \tilde{\theta}'_i(0) = \frac{s_i \tilde{i}_f}{nFD_i} \quad (2.20)$$

where the Faradic current density is expressed as the sum of a steady and oscillating term. The current density consists of contributions from Faradic reactions and charging of the double layer as

$$i = i_f + C \frac{d\eta}{dt} \quad (2.21)$$

where C is the double layer capacitance. Under the assumption that the magnitude of the oscillating terms is sufficiently small as to allow linearization of the governing equations

$$\tilde{i}_f = \left(\frac{\partial f}{\partial \eta} \right)_{c_{i,0}} \tilde{\eta} + \sum_i \left(\frac{\partial f}{\partial c_{i,0}} \right)_{\eta, c_{j,j \neq i}} \tilde{c}_{i,0} \quad (2.22)$$

The charge transfer resistance R_t is defined to be

$$R_t = \frac{1}{\left(\frac{\partial f}{\partial \eta} \right)_{\eta_0}} \quad (2.23)$$

Thus;

$$\tilde{i}_f = \frac{1}{R_t} \tilde{\eta} + \sum_i \left(\frac{\partial f}{\partial c_{i,0}} \right)_{\eta=c_{j,j \neq i}} \tilde{c}_{i,0} \quad (2.24)$$

Equation (2.24) can be expressed in terms of overpotential as

$$\tilde{\eta} = R_t \tilde{i}_f - R_t \sum_i \left(\frac{\partial f}{\partial c_{i,0}} \right)_{\eta=c_{j,j \neq i}} \tilde{c}_{i,0} \quad (2.25)$$

From equation (2.20)

$$\tilde{c}_{i,0} = \frac{s_i \tilde{i}_f}{nFD_i} \frac{\delta_i}{\tilde{\theta}'_i(0)} \quad (2.26)$$

Equation (2.25) becomes

$$\tilde{\eta} = R_t \tilde{i}_f - R_t \sum_i \left(\frac{\partial f}{\partial c_{i,0}} \right)_{\eta=c_{j,j \neq i}} \frac{s_i \tilde{i}_f}{nFD_i} \frac{\delta_i}{\tilde{\theta}'_i(0)} \quad (2.27)$$

or

$$\tilde{\eta} = \tilde{i}_f (R_t + Z_D) \quad (2.28)$$

where

$$Z_D = -R_t \sum_i \left(\frac{\partial f}{\partial c_{i,0}} \right)_{\eta=c_{j,j \neq i}} \frac{s_i}{nFD_i} \frac{\delta_i}{\tilde{\theta}'_i(0)} \quad (2.29)$$

Equation (2.29) provides the Warburg impedance. The cell potential (measured with respect to the potential of a reference electrode), given by

$$V = R_s i + \eta \quad (2.30)$$

can be written in terms of oscillating variables as

$$\tilde{V} = R_e \tilde{i} + \tilde{\eta} \quad (2.31)$$

Equation (2.21) can be written in terms of oscillating variables as

$$\tilde{i} = \tilde{i}_f + j\omega C \tilde{\eta} \quad (2.32)$$

where C is the double layer capacitance. Equations (2.28), (2.31), and (2.32) result in

$$\frac{\tilde{V}}{\tilde{i}} = Z = R_e + \frac{R_t + Z_D}{1 + j\omega C(R_t + Z_D)} \quad (2.33)$$

Equation (2.33) represents a generalized form of the impedance response of a disk electrode.

For the data analysis presented in this chapter, the impedance Z given by equation (2.33) is regressed to the experimental impedance in order to determine various parameters such as R_e , R_t , Z_D , C , and Sc (Schmidt number).

2.2.2 Process Model for EHD

In the usual application of EIS, a complex impedance is calculated as the ratio of potential to current under a small perturbation of current (galvanic regulation) or potential (potential regulation). EHD is a generalized impedance technique in which sinusoidal modulation of disk rotation rate drives a sinusoidal current or potential. EHD has an advantage over EIS for measurement of the transport properties of ionic species because measurements can be made at the mass-transfer-limited current plateau, whereas an EIS measurement must be made on the slope below this plateau.

The angular velocity of the rotating disk electrode in case of EHD is given by

$$\Omega = \Omega_0 + \Delta\Omega \cos(\omega t) \quad (2.34)$$

where $\Delta\Omega$ is a fixed amplitude of perturbation in angular velocity around a mean value of Ω_0 . The frequency of perturbation ω is varied to obtain the widest possible range. The resulting current I , at fixed potential, can be expressed as

$$I = I_0 + \Delta I \cos(\omega t + \phi) \quad (2.35)$$

where I_0 is the average current, ΔI is the amplitude of the sinusoidal current response, and ϕ is the phase shift. These equations can be introduced into the differential equations that describe the physics and chemistry of the system to calculate explicitly the transfer function for the system, as illustrated in case of EIS in the previous section. Details of the development of this model are presented in [5]. From this development a theoretical transfer function for this system can be written as

$$\frac{\tilde{I}}{\tilde{\Omega}} = \frac{2A_0 z_p(u)}{\left\{ \frac{R_e}{Z_d(0)z_d(u)} + j\omega R_e C \left(\frac{R_i}{Z_d(0)z_d(u)} + 1 \right) + \frac{R_i}{Z_d(0)z_d(u)} + 1 \right\}} \quad (2.36)$$

where

$$u = Sc^{1/3} \frac{\omega}{\Omega_0} \quad (2.37)$$

$z_p(u)$ and $z_d(u)$ are tabulated functions for the electrohydrodynamic impedance and the convective diffusion impedance, respectively, which include corrections for a finite Schmidt number, $2A_0$ and $Z_d(0)$ are the respective moduli for the impedance at zero frequency, and Sc is the Schmidt number. The terms $R_i/Z_d(0)$ and $R_e/Z_d(0)$ correspond to corrections for kinetic and ohmic resistance, respectively, normalized by the zero frequency limit for the convective Wauburg impedance. The surface capacitance appears in the lumped parameter $R_e C$. The correction terms $R_i/Z_d(0)$, $R_e/Z_d(0)$, and $j\omega R_e C$ are

generally considered to be negligible as compared to unity if the electrode kinetics are fast. In this work, only one correction term of $R_e/Z_d(0)$, $R_e/Z_d(0)$, or R_eC , could be resolved for any given regression. Order of magnitude of analysis by Tribollet and Newman [5] suggested that R_eC should be the most important correction term to account for high frequency processes on the limiting current plateau. Thus, the process model for this system was given by

$$\frac{\tilde{I}}{\tilde{\Omega}} = \frac{2A_0 z_p(u)}{j\omega R_e C + 1} \quad (2.38)$$

Equation (2.38) was regressed to the experimental data to obtain the values for A_0 , R_eC , and Sc .

2.3 Experimental Design

The system used for this work, potassium ferri/ferrocyanide redox couple reacting on the Platinum rotating disk, is a classic system to study mass-transfer related issues, as the redox reaction is very fast. Also, the effect of migration on this system is very small (Figure 19.3 of reference 20), because the product ion is always present at the electrode surface. In this chapter the experimental procedure and the data analysis for EIS and EHD measurements are presented along with an interpretation of the results obtained. In this section the experimental procedure for conducting these measurements is explained.

2.3.1 Choice of Surface Treatment

Roughness of the surface can influence the charge transfer process and could be strongly associated with the frequency dispersion behavior [21,22]. Hence proper preparation of electrode surface before each measurement is very important. It is also

believed that "partial blocking" of the electrode surface could be related to the surface treatment used. Hence the treatment that results in the least amount of surface blocking among the available surface treatments is needed to obtain reliable information from the system under consideration. The best surface treatment, or the treatment that provides least amount of surface blocking, was considered to be the one that provided the highest value for the limiting current. DC data were collected using four surface treatments:

1. The electrode was polished using a 1200 grit emery cloth and washed with deionized water.
2. The electrode was prepolished with 1200 grit emery cloth, washed in deionized water, polished with alumina paste and then was subjected to ultrasound cleaning in a 1:1 solution of water and ethyl alcohol.
3. The electrode was polished using 1200 grit emery cloth, washed with deionized water, and then prepolarized by sweeping from -0.5V to +0.5V measured against saturated calomel reference electrode, and back to -0.5V at 10mV/sec.
4. The treatment procedure described in treatment 2 was used, followed by a prepolarization sweep from -0.5V to +0.5V and back to -0.5V at 10mV/sec.

The polarization curves in the cathodic region are shown in Figure 2.1. The cathodic region of operation was used for this work because platinum is relatively inactive when compared to the anodic region. The measurements were made at a disk rotation rate of 600 rpm. Treatment 1 yielded the smallest limiting current value, and treatment 2 yielded the largest value. Under microscopic observation, the surface of the electrode appeared to be significantly different from one surface treatment to the other. With treatment 2, a more "mirrorlike" surface was obtained. EIS and EHD measurements were conducted for both

these treatments in order to facilitate a comparative study of the influence of surface treatment employed on the interpretation of impedance data. The data from treatment 2 can be used to validate the existing one-dimensional frequency domain model proposed by Tribollet and Newman with greater confidence as this treatment results in a smaller amount of blocking.

2.3.2 Experimental Setup

A schematic of a typical impedance experimental setup is presented in Figure 2.2. The electrode was rotated using a high-speed low-inertia rotating disk apparatus developed at the CNRS [23]. The rotator was rated at a power of 115W. This high power is necessary to obtain modulation at high frequencies (up to 100Hz). The rise time of the rotator between 0 and 1000rpm when a stepwise potential is applied is less than 2ms (indicating a low inertia). Such low inertia is of extreme importance in case of the electrohydrodynamic impedance (EHD) measurements. The long term stability and accuracy of the rotation speed is 0.2% from 100 to 1000rpm. The tachometer has 24 poles, and the electromechanical constant was 3mV/rpm.

The potentials and currents were measured and controlled by a Solartron 1286 potentiostat. A Solartron 1250 frequency response analyzer (FRA) was used to apply the sinusoidal perturbation and to calculate the resulting transfer function. A matched two-channel Kemo type VBF8 48 low pass Butterworth analog filter was used to reduce the noise level of the input signals to the FRA. However from the experimental observations made during the course of this work as well as from the observations made by Agarwal *et al.* [10] use of the filter resulted in a slightly longer experimental time in case of EHD measurements. Hence EHD measurements were conducted without employing a filter.

Use of filter is necessary for EHD experimentas conducted below the mass transfer limited plateau.

The electrolyte consisted of equimolar (0.01M) concentrations of potassium ferricyanide and potassium ferrocyanide and a 1M potassium chloride solution. The electrode diameter is 5 mm, yielding a surface area of 0.1963cm^2 . The temperature was controlled at $25.0 \pm 0.1^\circ\text{C}$. Temperature control is very important as the transport properties of various species exhibit a very strong functional dependence on the temperature of the electrolyte.

A series of EIS measurements were conducted on a platinum rotating disk electrode for rotation rates of 120, 600, 1200, 2400, and 3000rpm, at $1/4^{\text{th}}$, $1/2$, and $3/4^{\text{th}}$ of the mass-transfer-limited current for all the rotation speeds, using treatments 1 and 2. The EHD measurements were conducted at the mass-transfer-limited condition at rotation rates of 120, 200, 600, and 1200rpm in case of treatment 1. For each of these conditions, repeated measurements were made in order to establish a structure for the stochastic noise in the measurements. The EHD data collected using treatment 2 were found to be corrupted due to the overpolishing of electrode which resulted in the depletion of platinum working electrode.

The EIS data were collected from the high frequency to the low frequency with 12 logarithmically spaced frequencies per decade. The first measurement in each spectrum obtained was discarded in the analysis because the start-up transient often influenced the value of impedance reported by the instrumentation. Also the data points within ± 5 Hz of the line frequency of 50Hz (60Hz if the experiments were to be conducted in U.S.A.) and its first harmonic of 100Hz (120Hz in U.S.A.) were discarded. The influence of these

points on the error structure is illustrated in chapter 8. The EHD data were collected from low frequency to high frequency with 20 logarithmically spaced frequencies per decade. As the signal to noise ratio is quite low at high frequencies in case of EHD, measurements take longer time at higher frequencies. The long (1% closure error) autointegration option of the frequency response analyzer was used, and the channel used for integration was that corresponding to current. The electrolyte was not deaerated but experiments were conducted at a polarization potential of 0V (SCE) in order to minimize the influence of oxygen on the reduction of ferricyanide. FraCom software developed in-house at CNRS by H.Takenouti [24] was used for data acquisition.

2.4 Data Analysis: Measurement Model

In this section the use of measurement models for the assessment of stochastic noise in frequency domain measurements and in identifying the self-consistent part of the impedance spectra is illustrated with the example of EIS data sets collected for 120rpm at 1/4th of mass-transfer-limited current for the system of interest. The data were analyzed employing the user-friendly MATLAB-based visual interface created in-house by Mark Orazem.

2.4.1 Initial Regressions of the Data

The initial regressions to the measurement model were performed using modulus weighting for the EIS data and using no weighting approach for the EHD data, as the error structure was yet to be determined. In accordance with equation (2.1), a measurement model was constructed by sequentially adding k Voigt elements with parameters Δ_k and τ_k until the fit was no longer improved by addition of yet another

element. The best fit was obtained for a model containing the maximum number of lineshapes that satisfied the requirement that the 95.4% confidence intervals of all the regression parameter estimates, calculated under the assumption that the model could be linearized about the trial solution, do not include zero. The results of regression are presented in Figure 2.3 with real part of the impedance plotted against the imaginary part for one of the three replicates for the 120rpm at 1/4th of the mass-transfer-limited current using treatment 1. In this case, 8 line shapes were obtained. In Figure 2.4 (a) and (b) these results are presented with the real and imaginary parts of the impedance plotted as functions of frequency. The normalized residual errors obtained from the real and the imaginary parts are shown in Figure 2.5 (a) and (b). Similar regressions were performed for the rest of the data sets collected for this condition. For the sake of consistency, 8 line shapes were used for the other two replicates also, though more line shapes could be obtained for these cases. Such an approach results in obtaining lack of fit (ϵ_{lof}) errors that are representative of same quality fit for all the replicates and hence do not contribute to the standard deviations. The measurement model parameters for each of the replicates are different because the system changed from one experiment to the other. Hence, by regressing a new measurement model to each individual data set, the changes of the experimental conditions are incorporated into the measurement model parameters. As a consequence non-stationary (ϵ_{ns}) errors are equal to zero for each separate regression. Standard deviations of the residual errors obtained by using measurement model approach for the repeated measurements were calculated and are presented in Figure 2.6. These provide estimates for the standard deviation of the stochastic part of the impedance

response. The standard deviations were also calculated for all other experimental conditions.

The impedance plane plot from the preliminary regression for EHD data, collected for a rotation speed of 120 rpm at mass-transfer-limited current, and using 2 Voigt elements, is presented in Figure 2.7. A no-weighting strategy was used for the preliminary regression of EHD data. The same regression results are represented as real and imaginary parts as functions of frequency in Figure 2.8 (a) and (b). The normalized residual errors from this initial regression are presented in Figure 2.9 (a) and (b).

2.4.2 Obtaining the Error Structure

The standard deviations obtained from the EIS measurements conducted for various rotation rates and various fractions of limiting current were grouped together, and a common model for these standard deviations was obtained. The standard deviations σ_r and σ_i were regressed to the model

$$\sigma_r = \sigma_i = \alpha |Z_j| + \beta |Z_r - R_{sol}| + \gamma \frac{|Z|^2}{R_m} + \delta \quad (2.39)$$

where α , β , γ , and δ are constants determined by regression analysis, R_{sol} is the solution resistance or the high frequency asymptote and R_m is the current measuring resistor. This model is also referred to as the “error structure model” in this work. The equality of standard deviations of the real and imaginary parts of the stochastic noise is found to be true when the real and imaginary parts of the complex quantity are measured using the same instrument for a system that is consistent with the Kramers-Kronig relations. An analytical proof for this observation can be found in Chapter 7, and Chapter 8 illustrates this result for a number of spectroscopic techniques such as electrohydrodynamic

impedance, viscoelastic measurements, and acoustophoretic measurements. This result is found to be true even for systems where the real and imaginary parts differ by several orders of magnitude. The impedance spectroscopy applied to polyaniline (PANI) membranes is an example for such cases [19].

The standard deviations obtained under different operating conditions for the rotating disk electrode were obtained using the measurement model approach. A generalized error structure model was obtained for all the conditions. The conditions and the number of replicates used for treatment 1 are listed in Table 2.1. Only β and γ values could be extracted for the error structure as the confidence intervals for α and δ included zero, and these values are given by $\beta = 1.00249 \times 10^{-3}$ and $\gamma = 2.77789 \times 10^{-4}$. It could be seen from Figure 2.10, Figure 2.11, and Figure 2.12 that the error structure model describes the noise level in the measurement in a satisfactory manner. Similar analysis was performed for the data sets collected using treatment 2 to obtain the error structure. The conditions and the number of replicates used for this treatment are listed in Table 2.2. The error structure parameters that could be obtained for this case are $\beta = 1.00587 \times 10^{-3}$ and $\gamma = 2.53830 \times 10^{-4}$. The error structure of the impedance measurements was not affected by polishing technique. A common model could be found that described the error structure for both sets of experiments.

The model for the stochastic contribution of the error structure for EHD data is given by

$$\sigma_r = \sigma_j = \alpha|Z_j| + \beta|Z_r| + \delta \quad (2.40)$$

where Z_r and Z_f are the real and imaginary parts of the EHD transfer function, respectively, and α , β , and δ are parameters which were found by regression to the set of standard deviations obtained using the measurement model approach. For the set of EHD measurements conducted for treatment 1 it was found that $\beta = 9.87004 \times 10^{-4}$ and $\delta = 3.07652 \times 10^{-5} \mu\text{A}/\text{rpm}$.

2.4.3 Identification of the Self-Consistent Part of the Impedance Spectra

The use of measurement models to identify the self-consistent portion of the impedance spectra takes advantage of the fact that the Kramers-Kronig transforms relate the real part to the imaginary and vice versa. Once the error structure is obtained, it can be used to weigh the subsequent regressions. This strategy assigns less weight to more noisy data and vice versa. The measurement model is regressed to the real (or imaginary) part of the spectrum, and the regression parameters are used to predict the imaginary (or real) part. Experimental data inevitably contain stochastic errors associated with the measurement. The presence of these errors gives rise to an uncertainty in the prediction of parameters in regression. The uncertainty in the parameter estimation is quantified by the standard deviation (σ) of the parameters, that is, one can say with 95.4% certainty that the parameter estimates lie within 2σ of the value calculated by the regression. Due to this uncertainty in parameter estimation, there is uncertainty in any prediction that is made using these parameters. The Monte-Carlo simulation technique is used in determining the 95.4% confidence interval for the prediction. Calculation of this interval takes the stochastic component of measurement error into account. Hence it could be said with 95.4% confidence that the data points which lie outside this predicted confidence interval

are corrupted by systematic error, that is, they represent the inconsistent portion of the spectrum.

The measurement model regression performed for real part of the impedance spectrum obtained for a rotating disk electrode at 120rpm and 1/4th of mass-transfer limited current is shown in Figure 2.13(a). In this case 10 lineshapes were obtained. The imaginary part of the spectrum obtained using these 10 lineshape parameters is shown along with the 95.4% confidence intervals in Figure 2.13(b). The scale of this plot obscures the inconsistent portion of the imaginary part. Normalized residual errors are presented in Figure 2.14(a) and (b). In this case it could clearly be seen that 4 points at the high frequency end are inconsistent with the Kramers-Kronig relations. These data were assumed to be corrupted by instrumental artifacts. In Figure 2.15 (a) and (b), prediction of the real part based on imaginary part is shown, and the corresponding normalized residual errors are presented in Figure 2.16 (a) and (b). It could be seen that at higher frequencies (above 30 Hz) the real part of the spectrum is not predicted properly. However this cannot be attributed to the bias errors or the inconsistency in spectrum. The imaginary part approaches the asymptotic limit at these frequencies and hence is incapable of capturing the changes that occur in the real part.

From this analysis it is found that 4 points at the high frequency end of the spectrum fell outside the confidence interval for the model and were therefore assumed to be inconsistent with the Kramers-Kronig relations. These points were deleted for further regressions. Similar analysis was performed for the spectra collected at 600, 1200, 2400, and 3000rpm, at 1/4, 1/2, 3/4th of mass-transfer-limited current, and the portions of the spectra which are inconsistent with Kramers-Kronig relations were identified and deleted.

For the EHD data collected for treatment 1, the consistency check with Kramers-Kronig relations revealed that all the spectra collected for various conditions were completely consistent. The process model was regressed to the EIS and EHD data using the error structure weighting.

2.5 Data Analysis: Process Model

In this section the results from the regressions to the one-dimensional process model developed by Tribollet and Newman are presented. After establishing the self-consistent portion of the spectrum, the model was regressed to the data taking advantage of the established error structure for the given set of measurements. The results from one such regression to the data collected using treatment 1 are presented as impedance plane plot in Figure 2.17, and corresponding plots of the real and the imaginary parts as functions of frequency are shown in parts Figure 2.18 (a) and (b) respectively. The normalized residual errors are represented in Figure 2.19 (a) and (b). From the residual errors it can be seen that the high frequency data were not very well predicted with this model, as there is definite trending in the errors and the errors in the imaginary part are as high as 70% for very high frequencies. This resulted in a Schmidt number value of 811 ± 172 as opposed to the expected value of 1100.

In order to address the disparity between the model and the data, a constant phase element (CPE) was added to the process model [25]. The expression for the impedance given by the process model in equation (2.33) was

$$\frac{\tilde{V}}{I} = Z = R_e + \frac{R_i + Z_D}{1 + [j\omega C(R_i + Z_D)]^{-\phi}} \quad (2.41)$$

In which $1-\phi$ represents the exponent applied to the double layer capacitance. As $\phi \rightarrow 0$, the form illustrated in equation (2.33) is recovered.

Several qualitative justifications have been advanced in the literature for incorporating a CPE correction into the process model:

- (a) If the electrode surface is rough, the peaks and the valleys will be accessible to a different degree at different frequencies [26].
- (b) If the frequency becomes large relative to the kinetics of ion sorption in the double layer, then the apparent double layer capacity will depend on the frequency [27].
- (c) The occurrence of faradic reactions can cause a frequency dependence of the values in the equivalent circuit model
- (d) The current distribution can be different at different frequencies and this can lead to a frequency dispersion [28].

In essence, the CPE correction is introduced in order to address the frequency dispersion behavior. A more satisfactory regression was obtained when a constant phase element was employed, as can be seen in impedance plane representation in Figure 2.20. The regression results for the real and imaginary parts as functions of frequency are presented in Figure 2.21 (a) and (b) respectively, and the corresponding normalized residual errors are presented in Figure 2.22 (a) and (b). For the same data set that was considered earlier the normalized residual errors were now at the most 2% as compared to about 70% in extreme case when a CPE correction was not applied. The Schmidt number obtained in this case was 1073 ± 33 as opposed to 811 ± 172 obtained through the process model regression without accounting for the CPE correction, and the expected value of 1100. However, it was not always possible to obtain a CPE correction for a given

measurement. During the course of the data analysis performed for this work it was observed that a CPE correction was obtained whenever there is a significant high frequency effect which can be attributed to a surface blocking effect. The results of the regressions for treatment 1 are presented in table 2.3 (without CPE correction). Some selected results based on the lowest normalized residual sum of squares for a given condition are presented in table 2.4. Results accounting for CPE correction are presented in table 2.5 and selected results from table 2.5 are presented in table 2.6. Regressed results for treatment 2 are presented in tables 2.7 and 2.8 (without CPE correction) and in tables 2.9 and 2.10 (with CPE correction).

The process model regression for the EHD data collected for a rotation rate of 120rpm at the mass-transfer-limited current is presented in the form of an impedance plane plot in Figure 2.23. The Schmidt number obtained in this case was 1147 ± 13 . The regressions for the real and the imaginary parts as functions of frequency are presented in Figure 2.24 (a) and (b), respectively. The residual errors in this case are not normalized in these figures as for an intermediate frequency, the real part of the EHD impedance tends to 0, which results in a very high value of normalized residual error. These errors are presented in Figure 2.25 (a) and (b). These results from the EHD measurements and selected representative measurements are presented in tables 2.11 and 2.12 respectively.

2.6 Results from the Steady State Measurements

The Schmidt numbers obtained from the EIS and EHD measurements can be compared against those obtained from the steady state mass-transfer-limited current

measurements. The mass-transfer-limiting current density (i_{lim}) for the rotating disk electrode is given by

$$i_{\text{lim}} = -\frac{nFDc_{\infty}}{1-t} \left(\frac{\alpha\nu}{3D} \right)^{1/3} \sqrt{\frac{\Omega}{\nu}} \theta'_0(0) \quad (2.42)$$

where n is the number of electrons produced when one reactant ion or molecule reacts, F is the Faraday's constant, D is the diffusion coefficient of the mass-transfer-limiting species, c_{∞} is the bulk concentration of the reacting species, t is the transference number, α is the coefficient in the Cochran's velocity expansion, ν is the kinematic viscosity, Ω is the rotation speed in rad/sec, and $\theta'_0(0)$ is related to the concentration gradient in the axial direction. Three values for the mass-transfer-limited current values were obtained at each of the rotation speeds of 120, 600, 1200, 2400, and 3000 rpm, as presented in table 2.13. The diffusion coefficient values and the Schmidt number values obtained from the mass-transfer-limiting current are presented in table 2.14. The Sc values obtained at low rotation speeds are in reasonable agreement with the value 1100 that is expected for the system of interest. However the disparities grew larger with the rotation speed. These results are in agreement with the Sc values obtained from the EHD measurements.

From equation (2.42) it is evident that the relation between i_{lim} and $\sqrt{\Omega}$ is linear and the slope of the resulting plot between these two parameters should result in a value for diffusion coefficient. Such a plot is presented in Figure 2.26. The line passing through the data points was regressed ignoring the data points corresponding to the 3000rpm case. From the plot it is clear that the data corresponding to this case do not conform to the regressed straight line. The Schmidt number calculated from the slope of this straight line was 1202.

2.7 Discussion

As the system chosen for this study is traditionally used to study mass-transport phenomena, one of the interesting regressed parameters from the process model is the Schmidt number of ferricyanide ions. The schmidt number (Sc) is defined to be the ratio of kinematic viscosity (ν) to the diffusion coefficient (D) of the ionic species that is controlled by mass-transfer. The Schmidt number for the ferricyanide ions in the present system is reported to be about 1100, based on the DC and EHD measurements conducted by Robertson *et al* [23].

The regressed results of the process model as applied to the EIS data collected for the treatment 1 are presented in tables 2.3-2.6. The CPE correction was obtained only in few cases. The value NRSSQ (Residual Sum of Squares normalized with respect to the variance in the stochastic errors) is a measure of the quality of the fit. If the model describes the data adequately the NRSSQ parameter is expected to be about 1. The quality of the data for this treatment is in question as this treatment yielded the most blocked surface. The inadequacy of fit is evident here and the regressed Sc values were as much as 80% higher than the reported value of 1100 for some of the cases.

The representative regressed results of the process model based on as applied to the EIS data collected for treatment 2 are presented in tables 2.8 and 2.10, without and with a CPE correction respectively. This treatment was expected to provide the least blocked surface for the electrode based on the DC limiting current values obtained. Schmidt numbers reasonably close to the reported value of 1100 were obtained with the CPE correction. However, the quality of fit is not good, as the NRSSQ values are above

10 for most of the cases. In general, the quality of the fit is more reasonable when CPE correction was employed. However, in this case the Schmidt numbers progressively increased with an increase in rotation speed, whereas the Schmidt number should be independent of rotation speed.

The regressed values of the process model as applied to the EHD data obtained using treatment 1 and at the mass-transfer-limited current are presented in table 2.11 for rotation speeds of 120, 200, 600, and 1200 rpm. Some representative results based on normalized residual errors are presented in table 2.12. In this case, the one-dimensional model is adequate, as the current density is uniform at the mass-transfer-limited condition. However, deviations from the expected Schmidt number of 1100 were observed for these data sets also, with the extreme variation of about 25% at a rotation speed of 1200 rpm. This trend is consistent with the DC analysis results presented in table 2.14. As the non-uniform current distribution does not exist in this case, the differences should be attributed to the surface blocking effects. The R_eC values presented in the table 2.11 from the regressed values from the EHD data were consistently higher by at least an order of magnitude in all the cases. This anomaly could be attributed to surface blocking effects as discussed by Orazem *et al* [10]. EHD data collected using treatment 2 should provide Schmidt number values that are more acceptable in nature as it is observed that this is a better polishing technique and hence should provide less blocking.

From the above observations it is clear that the one-dimensional model does not provide an adequate fit to the experimental data. A more sophisticated model is necessary to understand the underlying physics of the system. The disparity in the experimental results can be attributed to two factors: non-uniform surface distributions and surface

blocking. Surface blocking effects are discussed in a greater detail in the next chapter. The main focus of this dissertation is on developing a physico-chemical impedance model accounting for the non-uniform current distributions in the frequency domain. Once a two-dimensional frequency domain model is established, the surface blocking effects can be singled out. Before fully justifying the need for a two-dimensional frequency domain model, it is necessary to understand the steady-state current distributions for the system of interest. These distributions are presented in chapter 4.

2.8 Conclusions

The applicability of the measurement model to the EIS and EHD data was demonstrated in this chapter. Generalized stochastic error structures are obtained for the two different surface treatments considered for this work. Measurement models were used to identify part of the impedance spectrum that is consistent with the Kramers-Kronig relations. A one dimensional process model was used to analyze the EIS data, and it was observed that this model does not describe the physics of the system adequately. When the one dimensional process model was applied to EHD data collected at mass-transfer limited current for various rotation rates, evidence for surface blocking was found. The process model regressions established the need for a better understanding of the current distributions in the steady state as well as in the frequency domain.

Table 2.1. The conditions and the number of repeated measurements chosen for establishing the error structure for treatment 1.

Ω , rpm	Fraction of i_{lim}	Number of replicates
120	1/4	3
600	1/2	3
1200	1/2	3
	1/4	3
2400	1/2	3
	3/4	3
3000	1/2	6

Table 2.2. The conditions and the number of repeated measurements chosen for establishing the error structure for treatment 2.

Ω , rpm	Fraction of i_{lim}	Number of replicates
120	1/2	2
	3/4	3
600	1/4	3
	1/2	3
	3/4	3
1200	1/4	3
	1/2	3
	3/4	3
2400	1/4	3
	1/2	3
	3/4	3
3000	1/4	3
	1/2	3
	3/4	3

Table 2.3. Results from the process model regression for EIS data collected using treatment 1, without CPE correction.

Condition	Data set no.	$Z(0), \Omega$	Se	$C, \mu\text{F}$	R_s, Ω	R_t, Ω	NRSSQ
120, 1/4 i_{lim}	1	160.57 ± 5.38	811 ± 172	8.04 ± 0.13	7.54 ± 0.02	4.81 ± 0.10	357.60
	2	162.15 ± 6.76	850 ± 222	7.09 ± 0.12	7.43 ± 0.02	4.21 ± 0.09	437.04
	3	162.33 ± 6.35	880 ± 212	7.07 ± 0.11	7.44 ± 0.02	4.08 ± 0.09	371.74
120, 1/2 i_{lim}	1	192.82 ± 0.57	1304 ± 24	17.40 ± 0.65	7.41 ± 0.01	0.57 ± 0.04	9.73
	1	72.04 ± 0.09	1445 ± 12	24.80 ± 1.48	7.57 ± 0.02	0.41 ± 0.01	4.48
	1	86.72 ± 0.14	1402 ± 14	18.60 ± 1.12	7.72 ± 0.02	0.59 ± 0.01	10.82
600, 1/2 i_{lim}	2	86.60 ± 0.25	1375 ± 25	15.04 ± 0.74	7.51 ± 0.02	0.55 ± 0.01	11.14
	3	86.53 ± 0.26	1385 ± 27	15.38 ± 0.73	7.46 ± 0.02	0.56 ± 0.01	12.52
	1	160.2 ± 1.29	1441 ± 76	6.44 ± 0.11	7.46 ± 0.02	2.37 ± 0.02	13.80
1200, 1/4 i_{lim}	1	52.08 ± 0.09	1383 ± 15	20.40 ± 2.36	7.54 ± 0.06	0.70 ± 0.02	10.78
	1	67.50 ± 1.76	868 ± 156	8.58 ± 0.14	7.42 ± 0.02	3.67 ± 0.09	590
	2	67.79 ± 1.70	940 ± 165	8.43 ± 0.14	7.42 ± 0.02	3.72 ± 0.09	499.83
600, 3/4 i_{lim}	3	67.69 ± 1.13	1102 ± 127	9.74 ± 0.16	7.53 ± 0.02	3.97 ± 0.07	256.84
	1	106.44 ± 0.51	1764 ± 54	6.71 ± 0.14	7.41 ± 0.02	1.72 ± 0.01	7.63
	1	35.90 ± 0.07	1550 ± 19	12.9 ± 1.00	7.23 ± 0.02	0.36 ± 0.01	1.42
1200, 1/2 i_{lim}	2	36.08 ± 0.06	1597 ± 18	17.18 ± 0.92	7.26 ± 0.012	0.35 ± 0.005	2.51
	3	36.16 ± 0.04	1643 ± 13	28.49 ± 1.10	7.37 ± 0.01	0.40 ± 0.01	2.87
	1	48.94 ± 1.36	646 ± 130	8.55 ± 0.15	7.57 ± 0.03	5.50 ± 0.14	1005.7
1200, 3/4 i_{lim}	2	49.32 ± 1.32	712 ± 138	8.41 ± 0.15	7.56 ± 0.03	5.38 ± 0.13	891.46
	3	49.59 ± 1.55	675 ± 155	7.71 ± 0.13	7.48 ± 0.02	5.06 ± 0.14	1106.8
	1	80.01 ± 1.18	1749 ± 164	9.16 ± 0.13	7.54 ± 0.02	3.36 ± 0.05	11.53
2400, 1/4 i_{lim}	2	81.52 ± 1.33	1877 ± 197	8.25 ± 0.14	7.48 ± 0.02	3.03 ± 0.04	15.08

Table 2.3—continued

	3	82.41 ± 1.32	1976 ± 199	7.91 ± 0.14	7.46 ± 0.02	2.93 ± 0.04	15.08
3000, 1/4 μ m	1	32.69 ± 0.04	1762 ± 15	0.34 ± 0.12	5.61 ± 0.34	1.64 ± 0.33	1.95
	1	39.79 ± 0.05	1859 ± 16	1.21 ± 0.45	6.40 ± 0.23	0.89 ± 0.22	2.26
	2	40.08 ± 0.06	1935 ± 17	7.18 ± 1.46	7.04 ± 0.05	0.33 ± 0.03	2.44
	3	40.19 ± 0.05	1965 ± 15	8.50 ± 1.29	7.08 ± 0.04	0.33 ± 0.01	2.00
	4	40.42 ± 0.06	2015 ± 19	4.44 ± 0.58	6.92 ± 0.04	0.41 ± 0.03	2.44
	5	40.45 ± 0.05	2044 ± 16	7.98 ± 0.91	7.06 ± 0.03	0.34 ± 0.01	1.44
1/2 μ m	6	40.50 ± 0.05	2071 ± 16	11.13 ± 1.43	7.14 ± 0.03	0.33 ± 0.01	1.94
		83.10 ± 1.85	1663 ± 237	5.68 ± 0.13	7.26 ± 0.02	2.66 ± 0.05	20.57
3/4 μ m							

Table 2.4. Selected results from the process model regression for EIS data collected using treatment 1, without CPE correction.

Condition	$Z(0), \Omega$	S_c	$C, \mu F$	R_s, Ω	R_t, Ω	NRSSQ
120, $\frac{1}{4}$ i _{lim}	160.57 ± 5.38	811 ± 172	8.04 ± 0.13	7.54 ± 0.02	4.81 ± 0.10	357.60
	192.82 ± 0.57	1304 ± 24	17.40 ± 0.65	7.41 ± 0.01	0.57 ± 0.004	9.73
600, $\frac{1}{4}$ i _{lim}	72.04 ± 0.09	1445 ± 12	24.80 ± 1.48	7.57 ± 0.02	0.41 ± 0.01	4.48
	86.72 ± 0.14	1402 ± 14	18.60 ± 1.12	7.72 ± 0.02	0.59 ± 0.01	10.82
	160.2 ± 1.29	1441 ± 76	6.44 ± 0.11	7.46 ± 0.02	2.37 ± 0.02	13.80
1200, $\frac{1}{4}$ i _{lim}	52.08 ± 0.09	1383 ± 15	20.40 ± 2.36	7.54 ± 0.06	0.70 ± 0.02	10.78
	67.69 ± 1.13	1102 ± 127	9.74 ± 0.16	7.53 ± 0.02	3.97 ± 0.07	256.84
	106.44 ± 0.51	1764 ± 54	6.71 ± 0.14	7.41 ± 0.02	1.72 ± 0.01	7.63
2400, $\frac{1}{4}$ i _{lim}	35.90 ± 0.07	1550 ± 19	12.9 ± 1.00	7.23 ± 0.02	0.36 ± 0.01	1.42
	49.32 ± 1.32	712 ± 138	8.41 ± 0.15	7.56 ± 0.03	5.38 ± 0.13	891.46
	80.01 ± 1.18	1749 ± 164	9.16 ± 0.13	7.54 ± 0.02	3.36 ± 0.05	11.53
3000, $\frac{1}{4}$ i _{lim}	32.69 ± 0.04	1762 ± 15	0.34 ± 0.12	5.61 ± 0.34	1.64 ± 0.33	1.95
	40.45 ± 0.05	2044 ± 16	7.98 ± 0.91	7.06 ± 0.03	0.34 ± 0.01	1.44
	83.10 ± 1.85	1663 ± 237	5.68 ± 0.13	7.26 ± 0.02	2.66 ± 0.05	20.57

Table 2.5. Results from the process model regression for EIS data collected using treatment 1, with CPE correction

File	Set no.	$Z(0, \Omega)$	Sc	$C, \mu F$	Re, Ω	Rt, Ω	ϕ	NRSSQ
120, $\frac{1}{4}$ illum	1	158.11 \pm 0.55	1047 \pm 24	4.59 \pm 0.05	6.92 \pm 0.01	7.85 \pm 0.05	0.28 \pm 0.003	8.26
	2	159.00 \pm 0.76	1073 \pm 33	4.19 \pm 0.05	6.88 \pm 0.01	7.06 \pm 0.06	0.29 \pm 0.004	2.35
	3	159.40 \pm 0.77	1087 \pm 33	4.17 \pm 0.06	6.88 \pm 0.01	6.73 \pm 0.06	0.29 \pm 0.004	2.43
600, $\frac{3}{4}$ illum	1	160.45 \pm 0.41	1040 \pm 30	2.59 \pm 0.10	6.71 \pm 0.03	4.90 \pm 0.10	0.35 \pm 0.008	27.68
	2	65.19 \pm 0.21	1113 \pm 26	5.05 \pm 0.07	6.86 \pm 0.01	7.41 \pm 0.08	0.32 \pm 0.004	7.56
	3	65.61 \pm 0.22	1192 \pm 30	5.02 \pm 0.07	6.87 \pm 0.05	7.13 \pm 0.07	0.30 \pm 0.004	7.40
1200, $\frac{3}{4}$ illum	1	66.00 \pm 0.13	1243 \pm 18	5.00 \pm 0.07	6.86 \pm 0.01	6.93 \pm 0.05	0.30 \pm 0.004	6.15
	2	106.84 \pm 0.38	1242 \pm 51	2.51 \pm 0.20	6.72 \pm 0.05	3.47 \pm 0.10	0.35 \pm 0.014	28.21
	3	45.94 \pm 0.12	1108 \pm 22	4.75 \pm 0.04	6.89 \pm 0.01	10.49 \pm 0.07	0.29 \pm 0.003	8.14
2400, $\frac{1}{2}$ illum	1	46.49 \pm 0.12	1156 \pm 22	4.64 \pm 0.04	6.88 \pm 0.01	10.07 \pm 0.06	0.29 \pm 0.002	7.78
	2	46.57 \pm 0.17	1187 \pm 33	4.54 \pm 0.05	6.87 \pm 0.01	9.90 \pm 0.08	0.30 \pm 0.003	7.42
	3	78.39 \pm 0.20	1691 \pm 30	6.08 \pm 0.07	7.12 \pm 0.01	5.65 \pm 0.06	0.23 \pm 0.004	1.66
2400, $\frac{3}{4}$ illum	1	79.87 \pm 0.26	1718 \pm 40	5.18 \pm 0.08	7.03 \pm 0.01	5.52 \pm 0.07	0.27 \pm 0.005	1.36
	2	80.84 \pm 0.24	1757 \pm 37	4.75 \pm 0.07	6.97 \pm 0.01	5.50 \pm 0.07	0.28 \pm 0.005	1.63
	3	39.82 \pm 0.05	1737 \pm 27	16.1 \pm 1.38	7.17 \pm 0.02	0.47 \pm 0.02	0.10 \pm 0.008	1.88
3000, $\frac{1}{2}$ illum	1	39.97 \pm 0.05	1796 \pm 27	15.9 \pm 1.29	7.17 \pm 0.02	0.46 \pm 0.02	0.09 \pm 0.008	1.73
	2	40.34 \pm 0.05	1949 \pm 27	10.9 \pm 1.18	7.10 \pm 0.02	0.41 \pm 0.02	0.07 \pm 0.014	1.35
	3	40.23 \pm 0.05	1866 \pm 25	19.8 \pm 1.13	7.22 \pm 0.01	0.52 \pm 0.02	0.09 \pm 0.007	1.62
3000, $\frac{3}{4}$ illum	1	81.59 \pm 0.56	1258 \pm 69	3.08 \pm 0.09	6.72 \pm 0.02	6.30 \pm 0.18	0.35 \pm 0.009	12.17

Table 2.6. Selected results from the process model regression for EIS data collected using treatment 1, with CPE correction

Condition	$Z(0), \Omega$	S_c	$C, \mu\text{F}$	R_s, Ω	R_t, Ω	Φ	NRSSQ
120, $V_4 \downarrow_{\text{lim}}$	159.00 ± 0.76	1073 ± 33	4.19 ± 0.05	6.88 ± 0.01	7.06 ± 0.06	0.29 ± 0.004	2.35
600, $\frac{V_2}{V_4} \downarrow_{\text{lim}}$	160.45 ± 0.41	1040 ± 30	2.59 ± 0.10	6.71 ± 0.03	4.90 ± 0.09	0.35 ± 0.01	27.68
1200, $\frac{V_2}{V_4} \downarrow_{\text{lim}}$	66.00 ± 0.13	1243 ± 18	5.00 ± 0.07	6.86 ± 0.01	6.93 ± 0.05	0.30 ± 0.004	6.15
	106.84 ± 0.38	1242 ± 51	2.51 ± 0.20	6.72 ± 0.05	3.47 ± 0.10	0.35 ± 0.01	28.21
2400, $\frac{V_2}{V_4} \downarrow_{\text{lim}}$	46.57 ± 0.17	1187 ± 33	4.54 ± 0.05	6.87 ± 0.01	9.90 ± 0.08	0.30 ± 0.003	7.42
	79.87 ± 0.26	1718 ± 40	5.18 ± 0.08	7.03 ± 0.01	5.52 ± 0.07	0.27 ± 0.01	1.36
3000, $\frac{V_2}{V_4} \downarrow_{\text{lim}}$	40.34 ± 0.05	1949 ± 27	10.90 ± 1.18	7.10 ± 0.02	0.41 ± 0.02	0.07 ± 0.01	1.35
	81.59 ± 0.56	1238 ± 69	3.08 ± 0.09	6.72 ± 0.02	6.30 ± 0.18	0.35 ± 0.01	12.17

Table 2.7. Results from the process model regression for EIS data collected using treatment 2, without CPE correction.

Condition	Set no.	$Z(0), \Omega$	S_c	$C, \mu F$	Re, Ω	R_t, Ω	NRSSQ
120, $\frac{1}{2} i_{lim}$	1	200.78 ± 0.87	1161 ± 32	11.15 ± 0.20	7.31 ± 0.008	0.85 ± 0.005	4.24
120, $\frac{3}{4} i_{lim}$	1	383.13 ± 4.45	1120 ± 77	12.77 ± 0.30	7.36 ± 0.010	0.89 ± 0.031	27.27
	2	379.17 ± 2.43	1138 ± 43	10.43 ± 0.17	7.45 ± 0.011	1.40 ± 0.016	4.32
	3	379.06 ± 3.51	1134 ± 62	8.64 ± 0.15	7.41 ± 0.012	1.46 ± 0.018	8.60
600, $\frac{1}{2} i_{lim}$	1	68.78 ± 0.22	882 ± 18	12.42 ± 0.60	7.71 ± 0.023	0.82 ± 0.012	14.12
	2	68.77 ± 0.38	852 ± 30	7.97 ± 0.35	7.52 ± 0.021	0.87 ± 0.013	32.93
	3	68.42 ± 0.24	878 ± 20	14.68 ± 0.65	7.75 ± 0.020	0.81 ± 0.010	13.23
600, $\frac{1}{4} i_{lim}$	1	90.66 ± 0.69	1099 ± 52	6.58 ± 0.23	7.36 ± 0.016	0.91 ± 0.010	45.83
	2	89.35 ± 0.36	1087 ± 28	12.46 ± 0.43	7.61 ± 0.017	0.91 ± 0.009	16.38
	3	89.65 ± 0.32	1115 ± 25	13.68 ± 0.46	7.67 ± 0.018	0.94 ± 0.009	10.71
600, $\frac{3}{4} i_{lim}$	1	153.63 ± 0.44	1262 ± 22	6.02 ± 0.17	7.34 ± 0.014	0.86 ± 0.006	2.80
	2	154.35 ± 0.78	1208 ± 38	4.41 ± 0.14	7.22 ± 0.014	0.84 ± 0.007	2.85
	3	154.05 ± 0.45	1230 ± 22	6.00 ± 0.16	7.33 ± 0.014	0.90 ± 0.006	1.70
1200, $\frac{1}{2} i_{lim}$	1	51.27 ± 0.45	980 ± 58	5.36 ± 0.06	7.49 ± 0.018	4.05 ± 0.028	105.73
	2	51.48 ± 0.76	969 ± 97	4.40 ± 0.04	7.35 ± 0.013	4.19 ± 0.043	142.11
1200, $\frac{1}{2} i_{lim}$	1	61.60 ± 0.21	1141 ± 24	14.30 ± 0.52	7.50 ± 0.016	0.77 ± 0.008	15.47
	2	61.77 ± 0.27	1141 ± 32	12.19 ± 0.44	7.45 ± 0.015	0.75 ± 0.008	26.69
	3	61.78 ± 0.24	1169 ± 30	13.75 ± 0.49	7.51 ± 0.015	0.76 ± 0.008	21.17

Table 2.7--continued

1200, 3/4 i_{lim}	1	106.66 ± 0.40	1230 ± 30	9.03 ± 0.22	7.47 ± 0.017	1.26 ± 0.012	13.98
	2	107.18 ± 0.89	1175 ± 63	5.64 ± 0.16	7.29 ± 0.015	1.13 ± 0.016	59.79
	3	107.03 ± 0.63	1221 ± 46	6.67 ± 0.18	7.39 ± 0.016	1.21 ± 0.014	32.17
2400, 1/4 i_{lim}	1	35.42 ± 0.28	972 ± 50	7.72 ± 0.53	7.46 ± 0.024	0.66 ± 0.016	41.53
	2	35.11 ± 0.19	1009 ± 35	20.16 ± 1.10	7.72 ± 0.018	0.63 ± 0.014	24.73
	3	35.18 ± 0.21	1018 ± 39	10.19 ± 0.12	6.88 ± 0.007	1.34 ± 0.009	24.45
2400, 1/2 i_{lim}	1	44.11 ± 0.12	1269 ± 22	15.00 ± 0.62	7.78 ± 0.022	0.92 ± 0.009	18.20
	2	44.08 ± 0.11	1265 ± 21	15.51 ± 0.63	7.81 ± 0.021	0.89 ± 0.009	17.99
	3	44.32 ± 0.21	1230 ± 38	8.29 ± 0.32	7.54 ± 0.020	0.95 ± 0.011	46.65
2400, 3/4 i_{lim}	1	79.49 ± 0.70	1401 ± 75	6.71 ± 0.19	7.42 ± 0.016	1.15 ± 0.017	6.71
	2	79.14 ± 0.58	1391 ± 62	7.29 ± 0.20	7.48 ± 0.016	1.13 ± 0.015	6.33
	3	79.36 ± 0.67	1392 ± 72	6.65 ± 0.20	7.45 ± 0.016	1.12 ± 0.016	7.45
3000, 1/4 i_{lim}	1	31.51 ± 0.13	1103 ± 28	29.53 ± 1.38	7.80 ± 0.017	0.66 ± 0.015	15.34
	2	31.69 ± 0.19	1068 ± 42	15.71 ± 0.91	7.61 ± 0.017	0.55 ± 0.013	27.38
	3	31.29 ± 0.13	1092 ± 28	30.82 ± 1.38	7.77 ± 0.016	0.66 ± 0.016	15.83
3000, 1/2 i_{lim}	1	42.72 ± 0.52	1101 ± 92	4.86 ± 0.05	7.66 ± 0.016	5.21 ± 0.05	116.92
	2	42.63 ± 0.58	1127 ± 105	4.38 ± 0.05	7.52 ± 0.021	5.77 ± 0.06	106.23
	3	42.47 ± 0.43	1176 ± 84	4.57 ± 0.04	7.63 ± 0.016	5.98 ± 0.04	80.58
3000, 3/4 i_{lim}	1	78.31 ± 2.12	1167 ± 205	4.86 ± 0.06	7.54 ± 0.022	6.26 ± 0.10	24.17
	2	78.22 ± 1.63	1261 ± 165	4.69 ± 0.05	7.59 ± 0.019	7.22 ± 0.08	15.68
	3	78.23 ± 1.50	1306 ± 164	4.60 ± 0.04	7.61 ± 0.019	7.76 ± 0.08	12.93

Table 2.8. Selected results from the process model regression for EIS data collected using treatment 2, without CPE correction.

Condition	$Z(0), \Omega$	S_c	$C, \mu F$	R_s, Ω	R_o, Ω	NRSSQ
120, 1/2 lim	200.78 ± 0.87	1161 ± 32	11.1 ± 0.20	7.31 ± 0.01	0.85 ± 0.01	4.2
	379.17 ± 2.43	1138 ± 43	10.4 ± 0.17	7.45 ± 0.01	1.40 ± 0.02	4.3
600, 1/4 lim	68.42 ± 0.24	878 ± 20	14.7 ± 0.65	7.75 ± 0.02	0.81 ± 0.01	13.2
	89.65 ± 0.32	1115 ± 25	13.7 ± 0.46	6.67 ± 0.02	0.94 ± 0.01	10.7
	154.05 ± 0.45	1230 ± 22	6.00 ± 0.16	7.33 ± 0.01	0.90 ± 0.01	1.7
1200, 1/4 lim	51.27 ± 0.45	980 ± 58	5.36 ± 0.06	7.49 ± 0.02	4.05 ± 0.03	105.7
	61.60 ± 0.21	1141 ± 24	14.3 ± 0.52	7.50 ± 0.02	0.77 ± 0.01	15.5
	106.66 ± 0.40	1230 ± 30	9.03 ± 0.22	7.47 ± 0.02	1.26 ± 0.01	14.0
2400, 1/4 lim	35.18 ± 0.21	1018 ± 39	10.2 ± 0.12	6.88 ± 0.01	1.34 ± 0.01	24.5
	44.08 ± 0.11	1265 ± 21	15.5 ± 0.63	7.81 ± 0.02	0.89 ± 0.01	18.0
	79.14 ± 0.58	1391 ± 62	7.29 ± 0.20	7.48 ± 0.02	1.13 ± 0.02	6.3
3000, 1/4 lim	31.51 ± 0.13	1103 ± 28	29.5 ± 1.38	7.80 ± 0.02	0.66 ± 0.02	15.3
	42.47 ± 0.43	1176 ± 84	4.57 ± 0.04	7.63 ± 0.02	5.98 ± 0.04	80.6
	78.23 ± 1.50	1306 ± 164	4.60 ± 0.04	7.61 ± 0.02	7.76 ± 0.08	12.9

Table 2.9. Results from the process model regression for EIS data collected using Treatment 2, with CPE correction.

Condition	Set no.	$Z(0), \Omega$	S_c	$C, \mu F$	R_s, Ω	R_t, Ω	Φ	NRSSQ
120, 1/2 i_{lim}	1	200.66 ± 0.77	1108 ± 31	9.69 ± 0.36	7.21 ± 0.023	1.15 ± 0.063	0.14 ± 0.026	4.38
120, 3/4 i_{lim}	3	378.86 ± 3.22	1041 ± 64	7.91 ± 0.28	7.29 ± 0.028	2.33 ± 0.184	0.16 ± 0.026	15.95
600, 1/2 i_{lim}	1	94.97 ± 0.69	677 ± 26	1.17 ± 0.18	6.61 ± 0.054	2.25 ± 0.039	0.49 ± 0.009	232.28
1200, 1/4 i_{lim}	1	50.88 ± 0.13	1074 ± 19	3.61 ± 0.05	7.05 ± 0.016	4.95 ± 0.030	0.15 ± 0.004	25.90
	2	50.94 ± 0.22	1120 ± 32	3.37 ± 0.03	7.04 ± 0.010	5.10 ± 0.032	0.15 ± 0.004	15.19
	3	51.07 ± 0.22	1111 ± 32	3.32 ± 0.03	7.04 ± 0.011	5.04 ± 0.033	0.14 ± 0.004	18.03
2400, 1/4 i_{lim}	3	35.04 ± 0.18	1024 ± 32	9.15 ± 0.18	6.80 ± 0.013	1.56 ± 0.033	0.10 ± 0.012	16.29
2400, 3/4 i_{lim}	1	82.59 ± 0.99	519 ± 49	4.44 ± 0.23	7.04 ± 0.027	3.55 ± 0.137	0.40 ± 0.012	38.57
	2	78.70 ± 0.54	1186 ± 105	6.59 ± 0.34	7.35 ± 0.043	1.83 ± 0.213	0.18 ± 0.043	7.18
	3	82.64 ± 1.01	504 ± 44	4.43 ± 0.24	7.07 ± 0.028	3.49 ± 0.132	0.40 ± 0.011	39.70
3000, 1/2 i_{lim}	1	42.14 ± 0.11	1282 ± 25	3.79 ± 0.03	7.35 ± 0.008	6.24 ± 0.027	0.13 ± 0.003	14.64
	2	41.98 ± 0.15	1337 ± 33	3.11 ± 0.04	7.08 ± 0.014	7.04 ± 0.041	0.14 ± 0.004	7.47
	3	41.98 ± 0.08	1332 ± 19	3.64 ± 0.02	7.33 ± 0.007	6.88 ± 0.021	0.10 ± 0.002	11.03
3000, 3/4 i_{lim}	1	76.43 ± 0.63	1476 ± 79	3.65 ± 0.04	7.20 ± 0.013	8.50 ± 0.088	0.16 ± 0.005	2.45
	2	76.82 ± 0.36	1543 ± 47	3.73 ± 0.02	7.29 ± 0.008	8.93 ± 0.047	0.12 ± 0.003	1.27
	3	76.87 ± 0.32	1565 ± 41	3.67 ± 0.02	7.30 ± 0.008	9.38 ± 0.043	0.11 ± 0.002	1.35

Table 2.10. Results from the process model regression for EIS data collected using Treatment 2, with CPE correction.

Condition	Z(0), Ω	Sc	C, μF	R _c	R _t	Φ	NRSSQ
120, 1/2 i_{lim}	200.66 ± 0.77	1108 ± 31	9.69 ± 0.36	7.21 ± 0.02	1.15 ± 0.06	0.14 ± 0.03	4.38
3/4 i_{lim}	378.86 ± 3.22	1041 ± 64	7.91 ± 0.23	7.29 ± 0.03	2.33 ± 0.18	0.16 ± 0.03	15.95
600, 1/2 i_{lim}	94.97 ± 0.69	677 ± 26	1.17 ± 0.18	6.61 ± 0.05	2.25 ± 0.04	0.49 ± 0.01	232.28
1200, 1/4 i_{lim}	50.94 ± 0.22	1120 ± 32	3.37 ± 0.03	7.04 ± 0.01	5.10 ± 0.03	0.15 ± 0.004	15.19
2400, 1/4 i_{lim}	35.04 ± 0.18	1024 ± 32	9.15 ± 0.18	6.80 ± 0.01	1.56 ± 0.03	0.10 ± 0.01	16.29
3/4 i_{lim}	78.70 ± 0.54	1186 ± 105	6.59 ± 0.34	7.35 ± 0.04	1.83 ± 0.21	0.18 ± 0.04	7.18
3000, 1/2 i_{lim}	41.98 ± 0.15	1337 ± 33	3.11 ± 0.04	7.08 ± 0.01	7.04 ± 0.04	0.14 ± 0.004	7.47
3/4 i_{lim}	76.82 ± 0.36	1543 ± 47	3.73 ± 0.02	7.29 ± 0.01	8.93 ± 0.05	0.12 ± 0.003	1.27

Table 2.11. Results from the process model regression for EHD data collected at the mass-transfer-limited current using treatment 1.

Ω , rpm	Set no.	A_0 , $\mu\text{A}/\text{rpm}$	Sc	$R_e C$, sec	NRSSQ
120	1	0.459 ± 0.001	1147 ± 13	0.0129 ± 0.0007	31.32
	2	0.458 ± 0.002	1162 ± 15	0.0092 ± 0.0007	32.45
	3	0.459 ± 0.002	1176 ± 19	0.0112 ± 0.0009	38.455
200	1	0.352 ± 0.001	1220 ± 16	0.0051 ± 0.0004	25.338
	3	0.345 ± 0.002	1286 ± 24	0.0061 ± 0.0006	44.037
600	1	0.199 ± 0.001	1334 ± 17	0.0012 ± 0.0002	29.522
	2	0.199 ± 0.001	1359 ± 18	0.0010 ± 0.0002	31.072
	3	0.198 ± 0.001	1377 ± 19	0.0009 ± 0.0002	34.577
1200	2	0.137 ± 0.0003	1384 ± 11	0.0006 ± 0.0001	15.674
	3	0.139 ± 0.0004	1434 ± 21	0.0002 ± 0.0001	28.567

Table 2.12. Selected results from the process model regression for EHD data collected at the mass-transfer-limited current using treatment 1.

Ω , rpm	A_0 , $\mu\text{A}/\text{rpm}$	Sc	$R_e C$, sec	NRSSQ
120 rpm	0.459 ± 0.001	1147 ± 13	0.0129 ± 0.0007	31.32
200 rpm	0.352 ± 0.001	1220 ± 16	0.0051 ± 0.0004	25.34
600 rpm	0.199 ± 0.001	1334 ± 17	0.0012 ± 0.0002	29.52
1200 rpm	0.137 ± 0.0003	1384 ± 11	0.0006 ± 0.0001	15.67

Table 2.13. Limiting current values obtained for treatment 2 at different rotation speeds.

Ω , rpm	i_{lim} , mA/cm ²			
	Measurement 1	Measurement 2	Measurement 3	Average
120	-1.8397	-1.8285	-1.8440	-1.8374
600	-3.9369	-4.0633	-4.0116	-4.0039
1200	-5.5931	-5.4990	-5.5359	-5.5426
2400	-7.6981	-7.6720	-7.7960	-7.7220
3000	-7.8231	-8.2170	-8.0617	-8.0339

Table 2.14. Schmidt numbers obtained from the i_{lim} values presented in Table 2.14.

Ω , rpm	Sc			
	Measurement 1	Measurement 2	Measurement 3	Average
120	1112	1122	1108	1114
600	1187	1132	1154	1158
1200	1179	1210	1198	1195
2400	1228	1234	1205	1222
3000	1417	1317	1355	1362

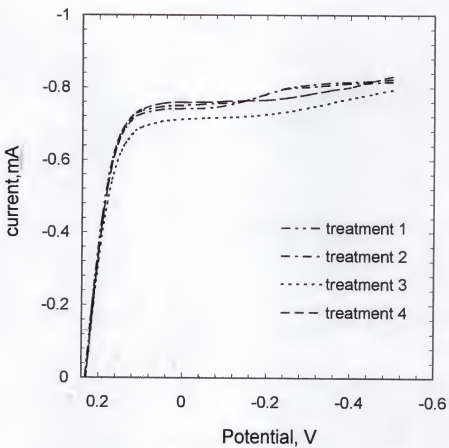


Figure 2.1. The DC polarization curves for various surface treatments. The results are presented for the cathodic region, as this is the region of interest for this work. Measurements were made at 600 rpm.

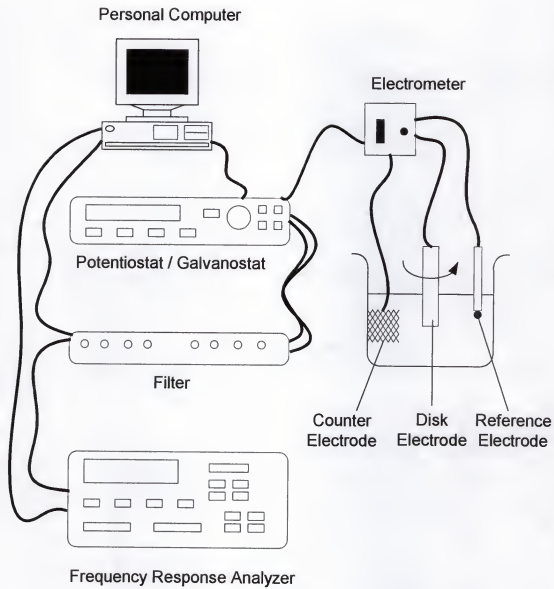


Figure 2.2. Experimental setup for the impedance measurements.

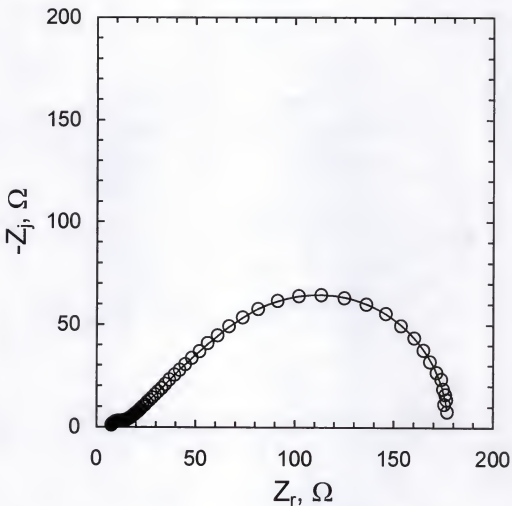


Figure 2.3. Regression of a measurement model with 8 Voigt elements to the EIS data obtained for rotating disk electrode at 120 rpm, 1/4th of the limiting current. Solid line in the figures is the measurement model fit and circles represent the data.

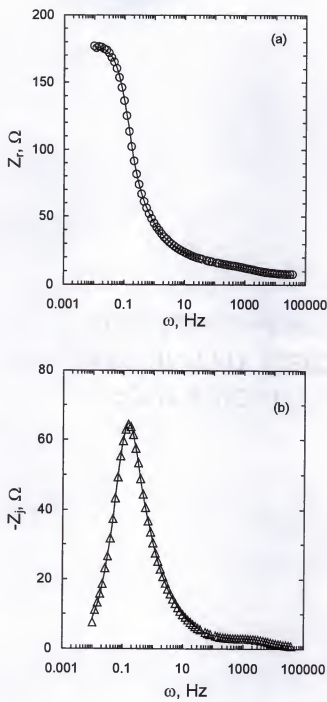


Figure 2.4. Regression of a measurement model with 8 Voigt elements to the EIS data obtained for rotating disk electrode at 120 rpm, 1/4th of the limiting current, corresponding to the condition in Figure 2.3. (a) real part as a function of frequency and (b) imaginary part as a function of frequency.

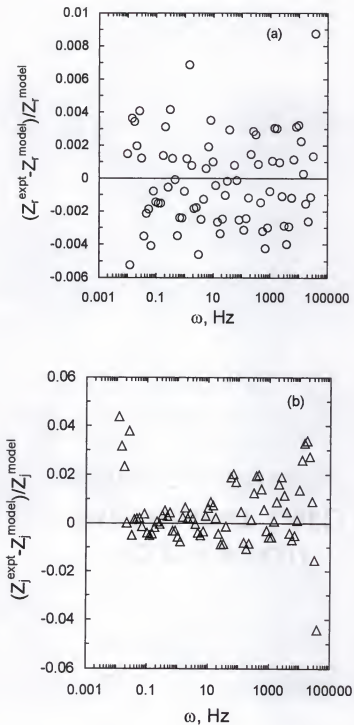


Figure 2.5. Normalized residual errors in the (a)real and (b)imaginary parts as functions of frequency for the regression of a measurement model with 8 Voigt elements to the EIS data obtained for rotating disk electrode at 120 rpm, 1/4th of the limiting current.

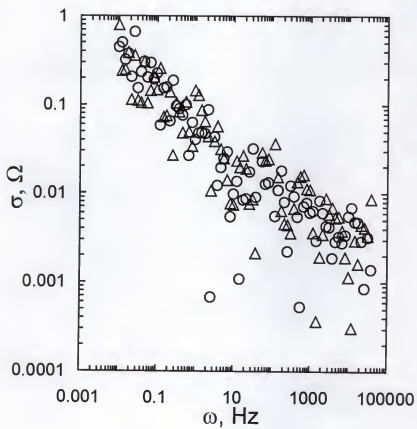


Figure 2.6. Standard deviations in the real (O) and imaginary (Δ) parts calculated using measurement models with modulus weighting for the 3 replicates of EIS data collected at 120rpm, 1/4th of limiting current case for the rotating disk electrode system.

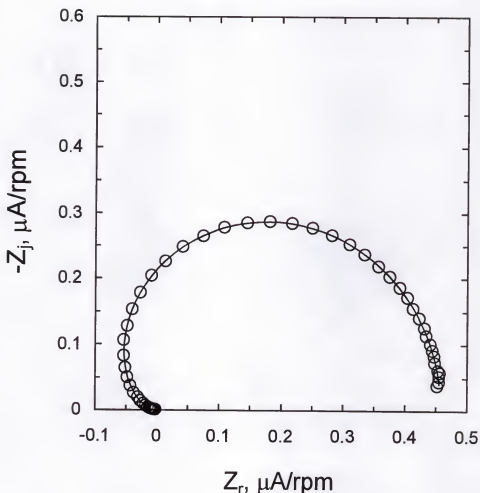


Figure 2.7. Regression of a measurement model with 2 Voigt elements to the EHD data obtained for rotating disk electrode at 120 rpm, mass-transfer-limited current using treatment 1. Solid line in the figures is the measurement model fit and circles represent the data.

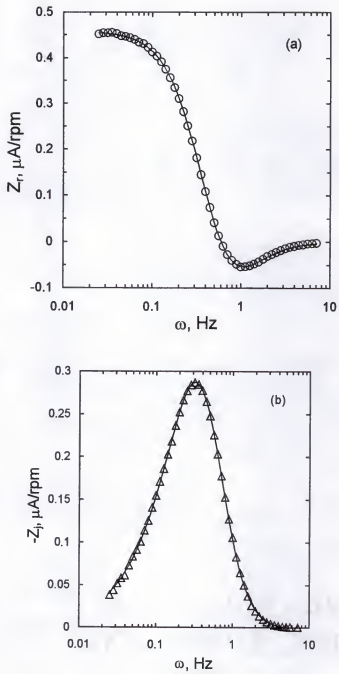


Figure 2.8. Regression of a measurement model with 2 Voigt elements to the EHD data obtained for rotating disk electrode at 120 rpm, mass-transfer-limited current. This corresponds to that in Figure 2.7. Solid line in the figures is the measurement model fit. (a) real and (b) imaginary parts as functions of frequency.

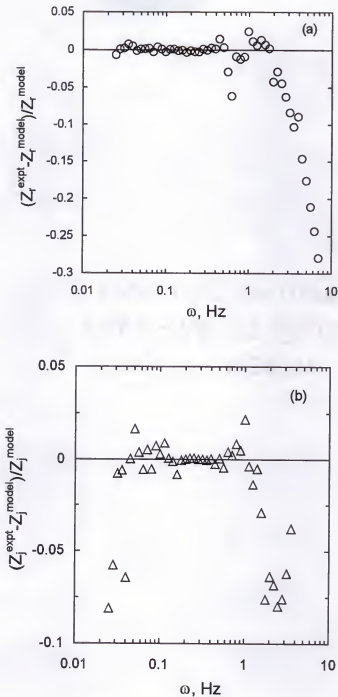


Figure 2.9. Normalized residual errors in the (a) real and (b) imaginary parts as functions of frequency from the regression of a measurement model with 2 Voigt elements to the EHD data obtained (corresponding to Figure 2.7) for rotating disk electrode at 120 rpm, mass-transfer-limited current.

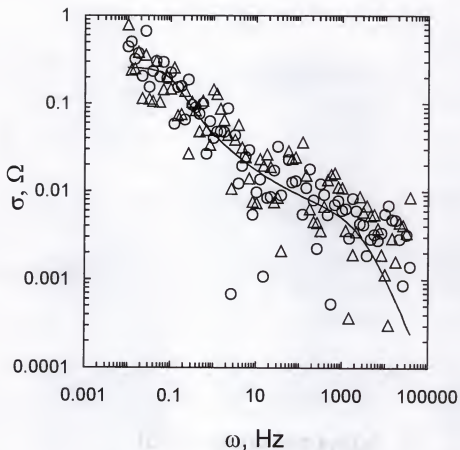


Figure 2.10. The solid line represents the error structure model obtained by accounting for various conditions for the rotating disk electrode, using treatment 1. The (O)s and the (Δ)s represent the standard deviations of the stochastic noise obtained by using the measurement model approach applied to 120rpm, $1/4^{\text{th}}$ of limiting current.

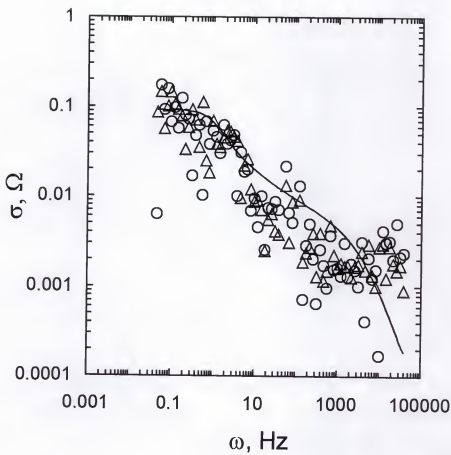


Figure 2.11. The solid line represents the error structure model obtained by accounting for various conditions for the rotating disk electrode, using treatment 1. The (O)s and the (Δ)s represent the standard deviations of the stochastic noise obtained by using the measurement model approach applied to 1200 rpm, 1/2 of limiting current.

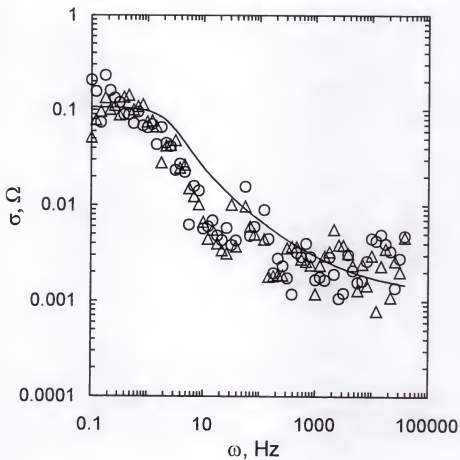


Figure 2.12. The solid line represents the error structure model obtained by accounting for various conditions for the rotating disk electrode, using treatment 1. The (O)s and the (Δ)s represent the standard deviations of the stochastic noise obtained by using the measurement model approach applied to 3000 rpm, 1/2 of limiting current.

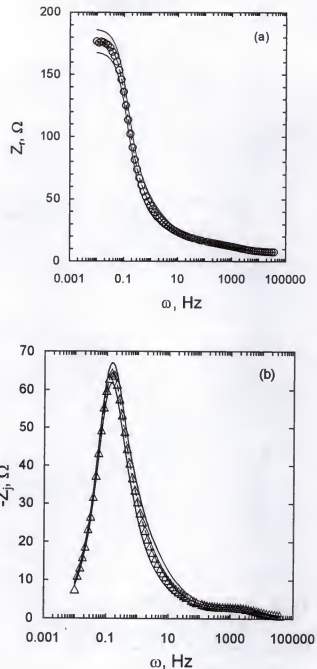


Figure 2.13. Checking for consistency with the Kramers-Kronig relations. EIS data collected for 120 rpm, 1/4th of the limiting current case for the rotating disk electrode system. Measurement model was regressed to the (a)real part and (b)imaginary part was predicted based on the 10 lineshape parameters obtained. The outer lines represent the 95.4% confidence limits and the line through the data is the measurement model fit.

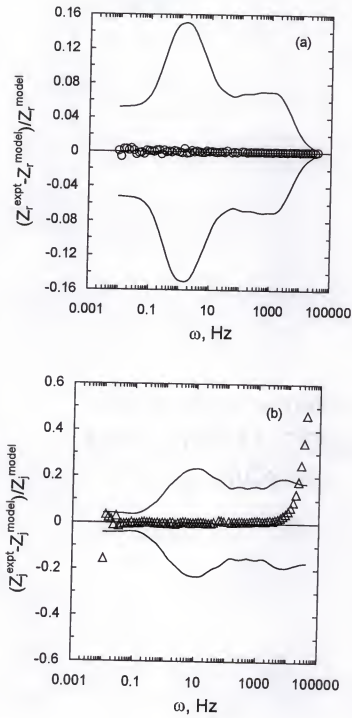


Figure 2.14. Normalized residual errors in (a) real and (b) imaginary parts corresponding to the regression results presented in Figure 2.13. The outer lines represent the 95.4% confidence limits and the line through the data is the measurement model fit.

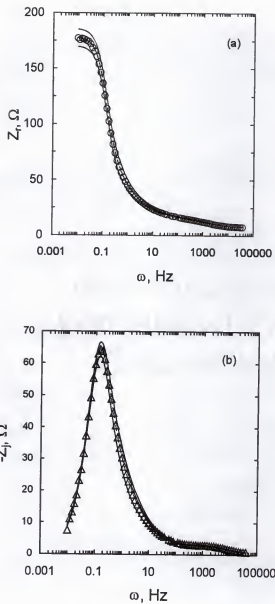


Figure 2.15. Checking for consistency with the Kramers-Kronig relations. 120 rpm, 1/4th of the limiting current case for the rotating disk electrode system. Measurement model was (a) regressed to the imaginary part and (b) real part is predicted based on the 11 lineshape parameters obtained. The outer lines represent the 95.4% confidence limits and the line through the data is the measurement model fit.

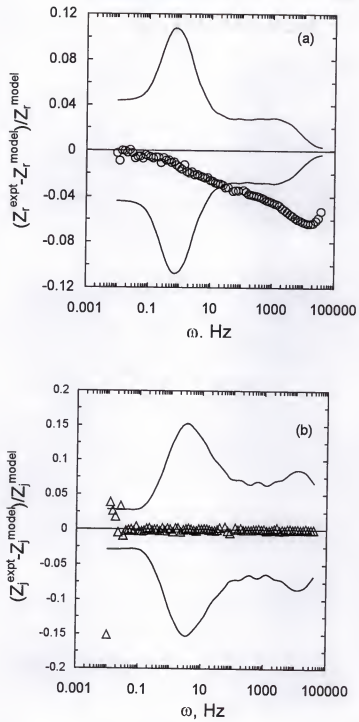


Figure 2.16. Normalized residual errors in (a) real and (b) imaginary parts corresponding to the regression results presented in Figure 2.15. The outer lines represent the 95.4% confidence limits and the line through the data is the measurement model fit.

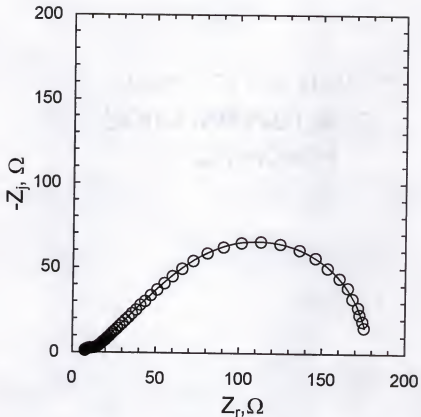


Figure 2.17. Process model regression (with error structure weighting) for 120 rpm, $1/4^{\text{th}}$ of the limiting current case for the rotating disk electrode system. Error structure was used to fit the data to the model. The solid line represents fit of the model to the data.

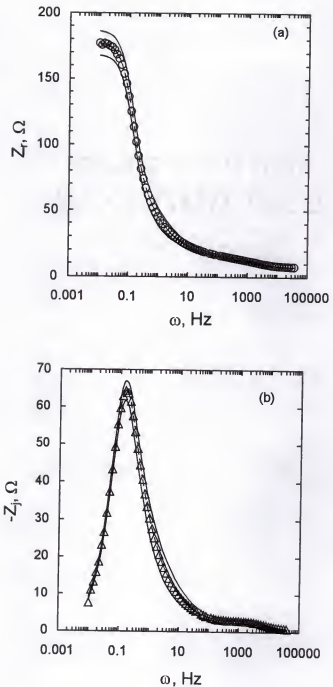


Figure 2.18. Process model regression (with error structure weighting) for EIS data collected at 120 rpm, $1/4^{\text{th}}$ of the limiting current case for the rotating disk electrode system, corresponds to Figure 2.17. Error structure was used to fit the data to the model. The solid line represents fit of the model to the data. Outer lines represent the 95.4% confidence limits.

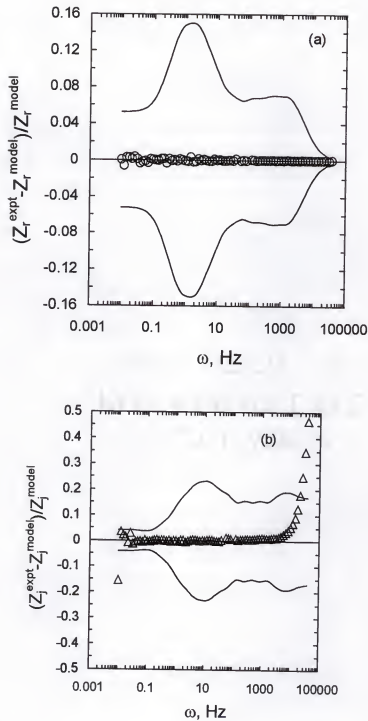


Figure 2.19. Normalized residual errors in (a) real and (b) imaginary parts corresponding to the regression results presented in Figure 2.17. The outer lines represent the 95.4% confidence limits.

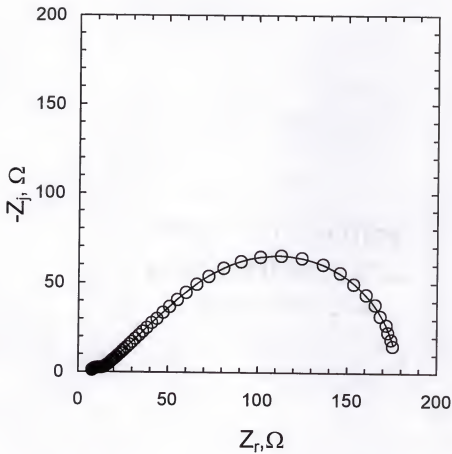


Figure 2.20. Process model regression (with error structure weighting) accounting for CPE correction for the EIS data collected for 120 rpm, 1/4th of the mass-transfer-limited current case for the rotating disk electrode system using treatment 1. The solid line represents fit of the model to the data.

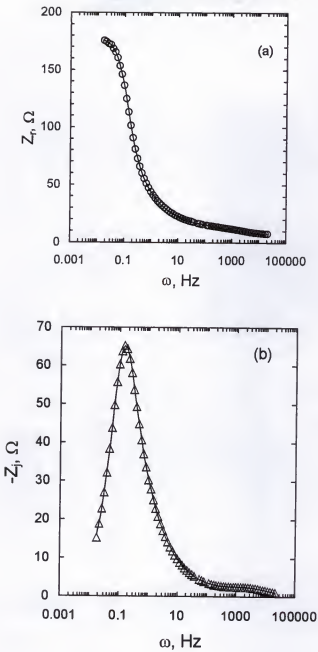


Figure 2.21. Process model regression (with error structure weighting) accounting for CPE correction for the EIS data collected for 120 rpm, 1/4th of the mass-transfer-limited current case for the rotating disk electrode system using treatment 1, corresponding to Figure 2.20. The solid line represents fit of the model to the data. (a) real and (b) imaginary parts as functions of frequency.

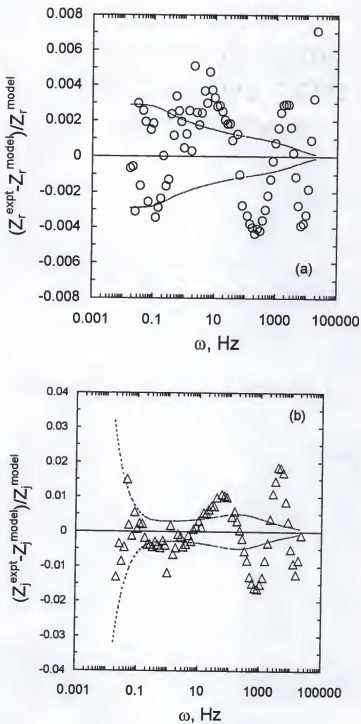


Figure 2.22. Normalized residual errors in (a) real and (b) imaginary parts corresponding to the regression results presented in Figure 2.20. The dashed lines represent the normalized noise level.

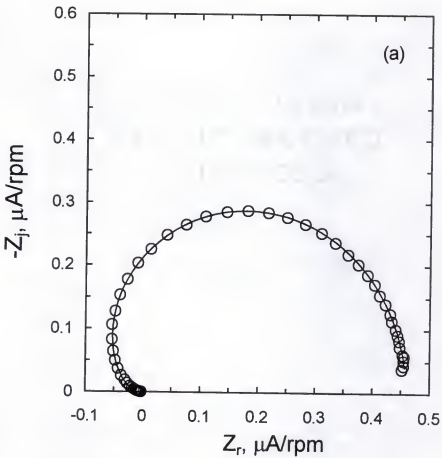


Figure 2.23. Process model regression (with error structure weighting) for the EHD data collected for 120 rpm, at the mass-transfer-limited current case for the rotating disk electrode system using treatment 1. The solid line represents fit of the model to the data.

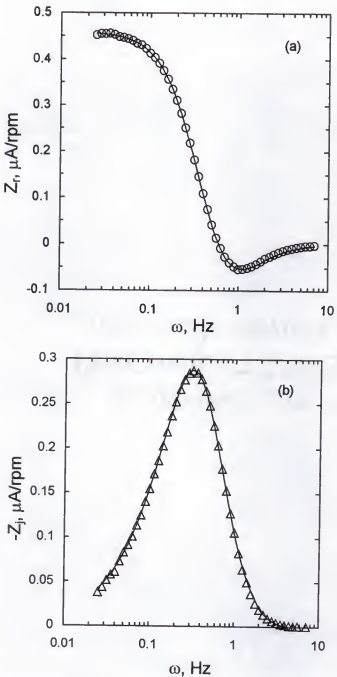


Figure 2.24. Process model regression (with error structure weighting) for the EHD data collected for 120 rpm, at the mass-transfer-limited current case for the rotating disk electrode system using treatment 1, corresponds to Figure 2.23. The solid line represents fit of the model to the data. (a) Real part and (b) Imaginary part as functions of frequency.

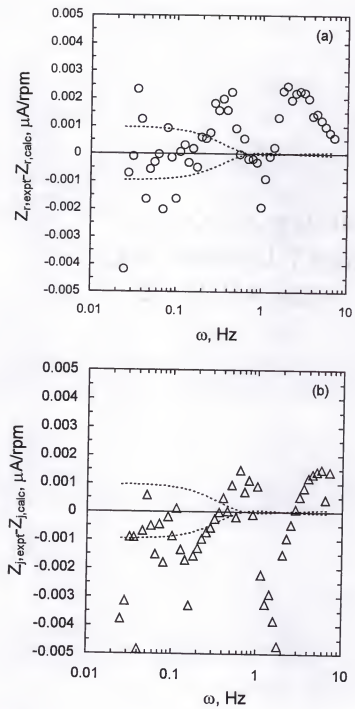


Figure 2.25. Residual errors in (a) real and (b) imaginary parts corresponding to the regression results presented in Figure 2.23. The dashed lines represent the noise level.

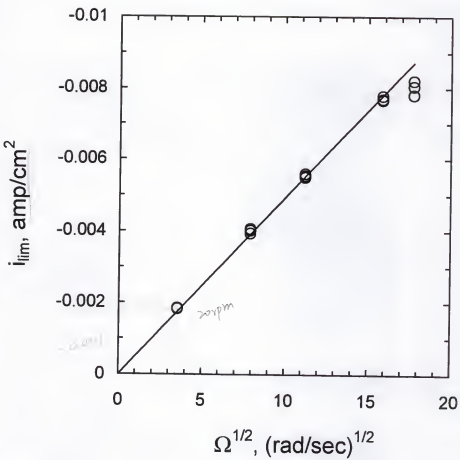


Figure 2.26: The square root of the rotation speed plotted against the mass-transfer-limiting current value. The line passing through is regressed ignoring the 3000rpm case.

CHAPTER 3

INFLUENCE OF SURFACE PHENOMENA ON THE IMPEDANCE RESPONSE OF A ROTATING DISK ELECTRODE

In chapter 2 it was shown that the one-dimensional frequency domain model proposed by Tribollet and Newman is inadequate to describe the system of interest for most of the cases studied, either because the quality of regressed fits is low or because the determined Schmidt numbers are very high. High Sc values may be resulting from the partial blocking of the electrode surface to the mass transport phenomena, as a large Sc value can be caused by a reduced apparent diffusion coefficient.

The role of the surface blocking for the system of interest was discussed earlier by a number of researchers. Stieble and Jüttner reported that, depending on the defined prepolarization conditions, a partial blocking of the electrode surface was observed as indicated by distinct changes of the impedance spectra [29]. They reported blocking index values as high as 30 in some cases, which results in just about 3% of the total surface area of the electrode being active. The blocking index is defined as the ratio of the area of inactive portion of the surface to the area of active portion. Voltammetric techniques were applied to study the effect of surface blocking [30,31,32]. It was observed that the irreversibility of the heterogeneous kinetics increased with the surface coverage, and the apparent charge transfer resistance was found to be higher. The film formation was attributed to the adsorption of certain compounds onto the surface of the Pt disc electrode. However there is no agreement between the authors about the composition and

structure of the compounds adsorbed onto the electrode surface. Some suggested that ferri and ferrocyanide ions are adsorbed on the Pt surface [33,34,35]. Others suggested that iron cyanide complexes are decomposed resulting in the formation of species that are adsorbed on the electrode surface (*e.g.* CN⁻ and Fe(CN)₅) [36,37,38]. It was also believed that coexistence of different oxidation states of iron as in ferri and ferrocyanide may lead to a bonding between the two species thus forming a prussian blue layer on the electrode surface.

The influence of the blocking effect is evident on the charge transfer resistance as well as the associated mass-transfer phenomena. In the present work, application of a process model to one of the data sets with 27 repeated measurements revealed a temporal evolution which is attributed to the surface blocking.

3.1 Experimental Protocol

The electrolyte for this study consisted of 0.01M K₃Fe(CN)₆ and 0.01M K₄Fe(CN)₆ in 1M KCl. Roughness of the surface can influence the charge transfer process and could be strongly associated with the frequency dispersion behavior. Hence the preparation of electrode surface before each experiment is a very important factor. It is also believed that the partial blocking of the electrode surface could be a function of the surface treatment used. Hence the best possible surface treatment is needed in order to obtain reliable information from the system under consideration. The treatment that yielded the maximum value for the limiting current, as illustrated in Figure 2.1, was chosen for the data analysis presented in this section. The electrode was pretreated with wet polishing on a 1200 grit emery cloth, washed in de-ionized water, polished using alumina

paste and then placed in an equivolume mixture of water and ethanol and subjected to ultra sound cleaning. Following the ultra-sound cleaning, the electrode was washed in de-ionized water. Under microscopic observation the surface of the electrode appeared to be significantly different from one surface treatment to the other. For the case presented in this chapter, the most "mirrorlike" surface was obtained. The data sets considered in this chapter were collected at 120rpm and at $1/4^{\text{th}}$ of limiting current. Repeated measurements were made in order to facilitate the use of measurement model to determine the stochastic contribution of errors. However the spectra were collected overnight with no polishing in between measurements, thus making this set of measurements very interesting to study the evolution of surface blocking effects.

3.2 Results and Discussion

Impedance spectroscopy results presented in Figure 3.1 and Figure 3.2 for $1/4^{\text{th}}$ of the mass transfer limited current and for a disk rotation speed of 120rpm demonstrate the time-dependent poisoning of the Pt surface. From these figures it can readily be seen that the high frequency phenomena which correspond to the charge transfer become more and more significant with an increased experimental time. The error structure for these measurements as given by equation (2.39) was obtained using the measurement model approach [9,10]. The corresponding error structure parameters are $\beta = 1.44138 \times 10^{-3}$, $\gamma = 1.47696 \times 10^{-4}$, and $\delta = 1.96453 \times 10^{-3}$. The regression strategy used in this work took full account of the error structure of the measurements following the procedure presented in chapter 2. The quality of the regression and the value obtained for the Schmidt number was found to be a strong function of the mathematical treatment used to describe

convective diffusion. The model that accounted for a 3-term expansion of the axial velocity in the convective diffusion equation and CPE correction provided the smallest residual sum of squares for the regression of the impedance data.

The standard deviations of the repeated measurements given in Figure 3.3 reflect contributions from bias errors caused by transient changes in electrode conditions. The real and imaginary parts of the standard deviation calculated directly were correlated but are not equal. The standard deviations of the stochastic part of the measurement, obtained by use of the measurement model to filter bias errors, were much smaller, and the real and imaginary parts of the standard deviation were statistically equal. This result is found to be a direct consequence of the way Kramers-Kronig relations transform the stochastic noise in the measurement, as presented in chapter 7. The standard deviation of the stochastic part of the measurement (open symbols in Figure 3.3) ranged from 0.2 to 0.01 percent of the modulus. The stochastic noise level of the measurements shown in Figure 3.1 and Figure 3.2 was therefore much less than the 3-5 percent of the modulus (often assumed to be the noise level for impedance measurements). The residual sum of squares normalized by the sum of variances for the measurement given in Figure 3.4 represents an F-Test for comparison of variance. The dashed lines are limits for accepting the hypothesis that the residual sum of squares differs from the sum of variances for the measurement. In spite of the low noise levels evident in Figure 3.3, with the exception of the first two measurements the process model yielded residual errors that fell within the noise level of the measurement. The larger residual errors seen for the first two scans were found to be the result of inconsistency of the data with the Kramers-Kronig relations. The success of the regression for the subsequent measurements allowed determination of the role of the

poisoning reaction evident in Figure 3.1 and Figure 3.2. The Schmidt number obtained by regression is presented in Figure 3.5. For the first two hours of the sequential impedance scans, the Schmidt number obtained was in good agreement with the value of 1100 obtained by DC techniques given by the dashed line in Figure 3.5. After this, the Schmidt number increased with time. As the residual errors for these regressions (Figure 3.4) were of the order of the noise of the measurement, the increase of Schmidt number suggests that the effective diffusion coefficient decreases with time. The charge transfer resistance also increased with time, as shown in Figure 3.6. The increase of the mass transfer resistance shown in Figure 3.7 is consistent with the decrease of effective diffusion coefficient or increase in the value of the Schmidt number suggested by Figure 3.5. The double layer capacitance, shown in Figure 3.8, and the exponent for the constant phase element shown in Figure 3.9 approached a constant value. These results show that the poisoning of platinum which occurs with prolonged experimentation, contributes to both a decrease of rate constant that hinders electrode kinetics and a blocking of the electrode surface that hinders mass transfer. This necessitates accounting for the blocking effects in modeling impedance spectroscopy.

Another possible factor, as mentioned earlier, is the radial dependence of the current distributions. The process model that is currently used is one-dimensional in nature and this may yield regressed parameters that are significantly different from what is expected when the current distributions are highly non-uniform in nature. The main focus of this work is in understanding the issues associated with the non-uniform current distributions.

3.3 Conclusions

The results presented in this chapter are in agreement with the previous observations regarding the surface blocking phenomena. The resistance to the mass-transport and the charge transfer were observed to be increasing with the duration of the experiment. Surface treatment in between measurements is very important in order to obtain reliable information from the impedance spectroscopy data.

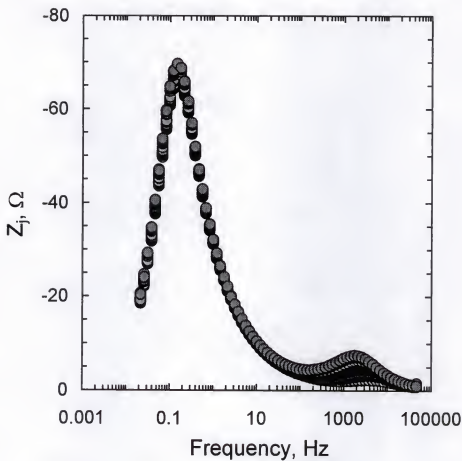


Figure 3.1. Imaginary part of the impedance for reduction of ferricyanide on a Pt disk rotating at 120 rpm and at $1/4^{\text{th}}$ of the limiting current. The time trending between the spectra can be seen very clearly.

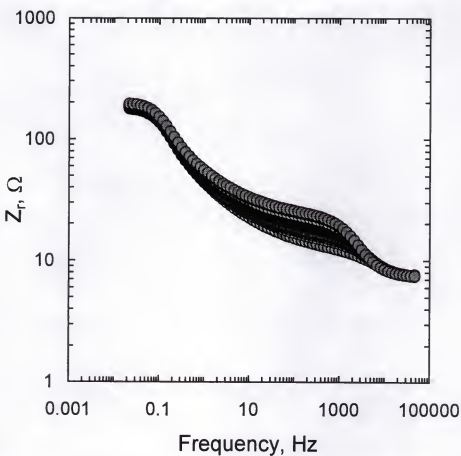


Figure 3.2. Real part of the impedance for the repeated measurements with time as a parameter.

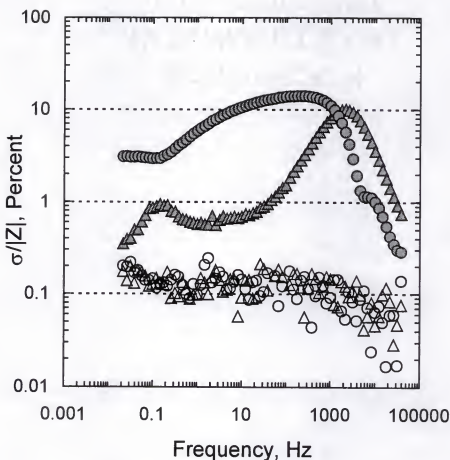


Figure 3.3. Error structure for the data presented in Figure 3.1 and Figure 3.2: filled symbols represent the statistically calculated standard deviations of repeated measurements; open symbols are the standard deviations of the stochastic noise calculated using the measurement model approach.

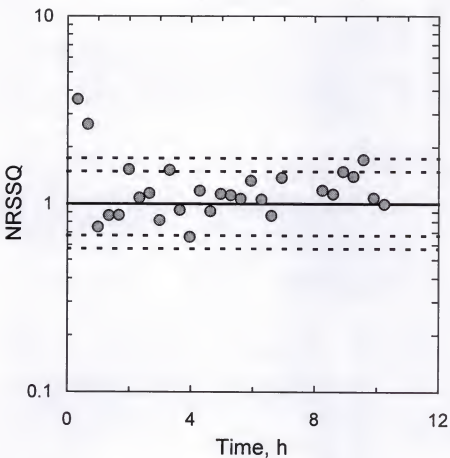


Figure 3.4. Normalized residual sum of squares for regression of a process model to the data presented in Figure 3.1 and Figure 3.2. The inner and outer dashed lines correspond to the 0.05 and 0.01 levels of significance for the F-test.

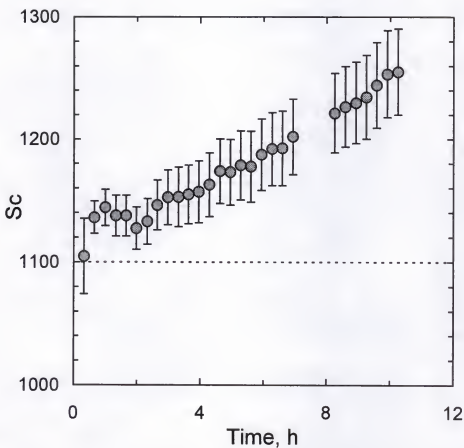


Figure 3.5. Schmidt number obtained by regression of process model to the data.

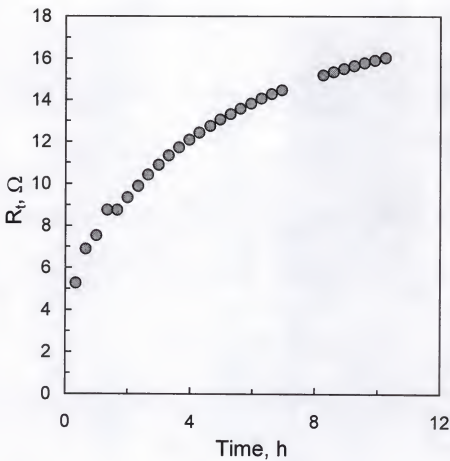


Figure 3.6. Charge transfer resistance obtained by regression of process model to the data.

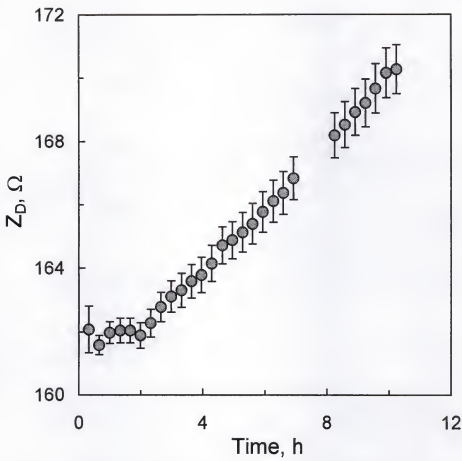


Figure 3.7. Mass transfer resistance obtained by regression of a process model to the data.

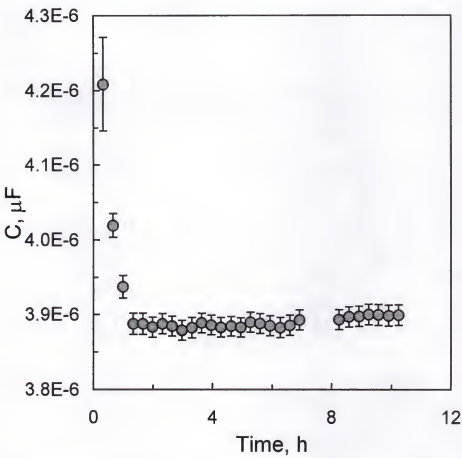


Figure 3.8. Double layer capacitance obtained by regression of process model to the data.

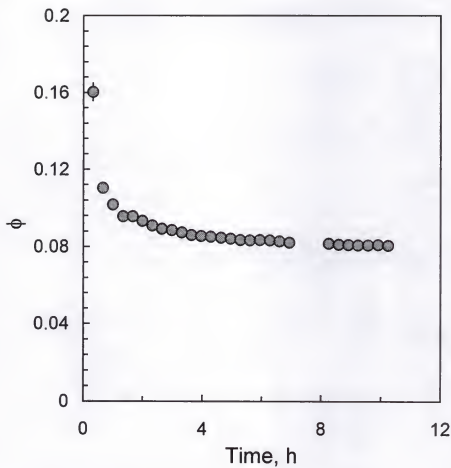


Figure 3.9. Exponent in the CPE element obtained by regression of process model to the data.

CHAPTER 4
STEADY STATE MODEL FOR A ROTATING DISK ELECTRODE BELOW THE
MASS-TRANSFER LIMITED CURRENT

The need for a better understanding of the current distributions is presented in chapter 2. The development of a steady state model for current distributions accounting for a finite Schmidt number correction and the charge distribution within the diffuse part of the double layer is presented in this chapter.

The popularity of the rotating disk for experimental electrochemistry has motivated development of numerous mathematical models that describe the physics of the system. The Levich equation for mass-transfer-limited current was obtained under the assumption that the Schmidt number is infinitely large [39]. As the axial velocity is uniform for the rotating disk electrode there is no radial distribution of current under the mass transfer limitation. Newman provided a correction to the Levich equation, which accounted for a finite value of the Schmidt number [40]. This correction amounted to a 3 percent reduction in the value of the mass-transfer-limited current obtained for a Schmidt number of 1000, typical of electrolytic systems. In subsequent work, he relaxed the assumption of a mass-transfer-limited condition by coupling convective diffusion in radial and axial directions in an inner diffusion-layer region with Laplace's equation for potential in an outer domain [41]. The cathodic Tafel limit of a Butler-Volmer expression was used to account for metal deposition kinetics. Appel extended this model to account for redox reactions as, in principle, Newman's model was developed for deposition reactions [42].

The focus in later years was on frequency-domain techniques. Significant effort has been expended on developing analytic formulae for the impedance response of a rotating disk electrode [43-54]. A comparative study of the application of these models to interpretation of impedance spectra has been presented by Orazem *et al.* [55]. A one-dimensional numerical model for the impedance response of a rotating disk electrode which accounted for the influence of a finite Schmidt number was presented by Tribollet and Newman [5]. The first two terms in the Cochran expansion for the axial component of fluid velocity were included in the convective diffusion equation [56]. Tribollet *et al.* reported that for a Schmidt number of 1000 the errors caused by neglecting the second term in the axial velocity expansion could be as high as 24 percent [53]. This result was confirmed by regression of various mass-transfer models to impedance data [55]. Mathematical models have been developed which account for frequency dispersion associated with the non-uniform potential distribution on the disk electrode [57-60], but, to date, no comparable model has been developed for the influence of non-uniform mass-transfer on the impedance response. Appel and Newman provided a preliminary mathematical development that they proposed would be used to develop a model for the influence of radially-dependent convective diffusion on the impedance response under the assumption that the Schmidt number is infinitely large [61]. Later Appel provided a model to calculate the radial distribution of impedance under the assumption that the Schmidt number is infinitely large [42]. However he was able to generate the radial distribution of impedances over a very limited frequency range due to numerical difficulties.

Though the errors resulting from neglecting the finite Schmidt number correction are not so significant for steady state calculations, they have been shown to be significant

in the frequency domain [53,55]. The objective of the work presented in this chapter is to develop a steady state treatment of current and potential distributions on a rotating disk electrode that accounts for a finite Schmidt number and for the distribution of charge in the diffuse part of the double layer. This provides a foundation for the development of a mathematical model that accounts for the influence of non-uniform mass transfer on the impedance response of a rotating disk electrode (presented in the next chapter). This work also provides a means of interpreting anomalous values of Schmidt numbers obtained from impedance data collected for the reduction of ferricyanide on a Pt disk electrode, as shown in chapter 2, in terms of the competing roles of surface poisoning and the influence of non-uniform current distribution [6,45].

4.1 Theoretical Development

The domain of interest was divided into an outer region where the concentration was assumed to be uniform, an inner boundary-layer region where electroneutrality and the convective diffusion equation for the reacting species were assumed to apply, and an inner diffuse part of the double layer where the assumption of electroneutrality was relaxed. The entire electrode surface was assumed to be active; thus, local passivation and partial blocking phenomena were not included in the model.

4.1.1 Diffusion Layer

The development in this part follows that presented by Newman with the exception that correction is made for a finite Schmidt number by incorporating 3-term expansions appropriate near the electrode surface for axial and radial velocity [41]. A critical assumption in the development of this work was that the current densities at the inner limit

of the diffusion layer and at the inner limit of the outer region are equal to the current density at the electrode surface. This assumption is valid if the diffusion layer is thin compared to the electrode radius. The validity of this assumption is implicit for an infinite Schmidt number because the diffusion layer is infinitely thin.

For a finite Schmidt number, the diffusion layer is still small compared to typical disk dimensions. The thickness of the boundary layer δ is given by

$$\delta = \left(\frac{3D_i}{\alpha\nu} \right)^{1/3} \left(\frac{\nu}{\Omega} \right)^{1/2} \quad (4.1)$$

where D_i is the diffusion coefficient of the species of interest, ν is the kinematic viscosity coefficient, Ω is the rotation speed of the disk electrode in radians/sec, and α is the coefficient in the expansion for the radial velocity term in equation (4.6) and has a value of 0.51023. The boundary layer thickness for the copper deposition system considered by Newman [41] is determined by the diffusivity of the cupric ion ($D_{Cu^{2+}} = 0.642 \times 10^{-5} \text{ cm}^2/\text{s}$) and by the kinematic viscosity ($\nu = 0.94452 \times 10^{-2} \text{ cm}^2/\text{s}$). For a rotation rate of 300 rpm, δ has a value of 13.76 μm which is small compared to the disc radius of 0.25cm, yielding an aspect ratio $\delta r_0 = 0.0055$, where r_0 is the radius of the disk. The corresponding value for the ferricyanide system treated in a later section of this chapter is 0.012. The solution of the convective diffusion equation can, in these cases, be decoupled from the solution of Laplace's equation for potential in the region of uniform composition.

Under the assumption of a steady state, the convective diffusion equation is given by

$$\nu_r \frac{\partial c_R}{\partial r} + \nu_z \frac{\partial c_R}{\partial z} = D_R \frac{\partial^2 c_R}{\partial z^2} \quad (4.2)$$

where ν_r and ν_z are the radial and axial components of velocity, c_R is the concentration of the reacting species, and D_R is the diffusion coefficient of the reacting species. A separation of variables can be applied as shown below:

$$c_R = c_\infty \left[1 + \sum_{m=0}^{\infty} \left(A_m (r/r_0)^{2m} \theta_m(\xi) \right) \right] \quad (4.3)$$

where c_∞ is the bulk concentration of the reacting species, A_m are the coefficients which correspond to the radial dependent part of the concentration, and $\theta_m(\xi)$ is the axial dependent part, where ξ is the scaled axial distance given by

$$\xi = z \left(\sqrt{av/(3D_R)} \right) \sqrt{\Omega/\nu} \quad (4.4)$$

For $\theta_m=1$ at $\xi=0$, the radial concentration distribution on the electrode surface can be written as

$$c_0 = c_\infty \left[1 + \sum_{m=0}^{\infty} \left(A_m (r/r_0)^{2m} \right) \right] \quad (4.5)$$

The expressions for the radial and axial components of the velocity resulting from Cochran's 3-term expansion [56] are given by

$$\nu_r = arz \frac{\Omega^{3/2}}{\nu^{1/2}} - \frac{1}{2} rz^2 \frac{\Omega^2}{\nu} - \frac{b}{3} rz^3 \frac{\Omega^{5/2}}{\nu^{3/2}} \quad (4.6)$$

and

$$\nu_z = -az^2 \frac{\Omega^{3/2}}{\nu^{1/2}} + \frac{1}{3} z^3 \frac{\Omega^2}{\nu} + \frac{b}{6} z^4 \frac{\Omega^{5/2}}{\nu^{3/2}} \quad (4.7)$$

respectively, where b is a constant with a value of -0.61592 . Application of equations (4.3), (4.4), (4.6), and (4.7) in equation (4.2) yields

$$\sum_{m=0}^{\infty} A_m (r/r_0)^{2m} \theta_m''(\xi) + \frac{3\xi^2}{a} \left\{ a - \frac{\xi}{3} \left(\frac{3D_R}{av} \right)^{1/3} - \frac{b\xi^2}{6} \left(\frac{3D_R}{av} \right)^{2/3} \right\} \sum_{m=0}^{\infty} A_m (r/r_0)^{2m} \theta_m'(\xi) \\ - \frac{3\xi}{a} \left\{ a - \frac{\xi}{2} \left(\frac{3D_R}{av} \right)^{1/3} - \frac{b\xi^2}{3} \left(\frac{3D_R}{av} \right)^{2/3} \right\} \sum_{m=0}^{\infty} 2mA_m (r/r_0)^{2m} \theta_m(\xi) = 0 \quad (4.8)$$

By equating the coefficients of $(r/r_0)^{2m}$ equation (4.8) can be rewritten as

$$\theta_m'' - \frac{3}{a} \xi^2 \left[-a + \frac{1}{3} \xi \left(\frac{3}{a} \right)^{1/3} Sc^{-1/3} + \frac{b}{6} \xi^2 \left(\frac{3}{a} \right)^{2/3} Sc^{-2/3} \right] \theta_m' \\ - \frac{6m\xi}{a} \left[a - \frac{1}{2} \xi \left(\frac{3}{a} \right)^{1/3} Sc^{-1/3} - \frac{b}{3} \xi^2 \left(\frac{3}{a} \right)^{2/3} Sc^{-2/3} \right] \theta_m = 0 \quad (4.9)$$

The primes in the superscripts refer to derivatives with respect to ξ . Equation (4.9) can be compared to

$$\theta_m'' + 3\xi^2 \theta_m' - 6m\xi \theta_m = 0 \quad (4.10)$$

obtained by Newman for an infinite Schmidt number. The boundary conditions for equation (4.9) are $\theta_m = 1$ at $\xi = 0$ and $\theta_m = 0$ at $\xi = \infty$. For the numerical calculation presented here, a value of $\xi = 20$ was used for approximation of the boundary condition at ∞ . The choice of this value is justified as a value of $\xi = 10$ resulted in the same values of θ_m to within 15 significant digits and the derivative of θ_m with respect to ξ at $\xi = 20$ yielded a value identically equal to 0. Equation (4.9) exhibits functional dependence on the Schmidt number. The numerical procedure that was used to solve the convective diffusion equation is presented in a subsequent section.

The current distribution on the electrode surface at steady state depends only on the dimensionless concentration gradient at electrode surface $\theta_m'(0)$ and not on the θ_m values at the other axial positions, that is,

$$\frac{i}{nF} = \frac{D_R}{1-t_R} \left. \frac{\partial c_R}{\partial z} \right|_{z=0} = \frac{D_R c_\infty}{1-t_R} \left(\frac{aV}{3D} \right)^{1/3} \sqrt{\frac{\Omega}{V}} \sum_{m=0}^{\infty} A_m (r/r_0)^{2m} \theta'_m(0) \quad (4.11)$$

where t_R is the transference number of the reacting species, n is the number of electrons produced when one reactant ion or molecule reacts, F is the Faraday's constant. The interfacial overpotential resulting from convective diffusion is the concentration overpotential given by

$$\eta_c = -\frac{RT}{ZF} \left[\ln \left(\frac{c_\infty}{c_0} \right) - t_R \left(1 - \frac{c_0}{c_\infty} \right) \right] \quad (4.12)$$

where η_c is the concentration overpotential, R is the universal gas constant, T is the temperature of the electrolyte in Kelvin, and Z is the number of equivalents of reactant used up per one electron produced/consumed.

4.1.2 Outer Region: Laplace's Equation

The approach taken in this region followed that developed by Newman [41]. In the outer region, concentrations were assumed to be uniform, and, under the assumption that there is no charge distribution within the bulk of the solution, the potential in this region satisfies Laplace's equation. Hence

$$\nabla^2 \Phi = 0 \quad (4.13)$$

where Φ is the potential referenced to infinity. The solution of equation (4.13) after transformation to rotational elliptic coordinates (η, μ) where $z = r_0 \mu \eta$ and $r = r_0 \sqrt{(1 + \mu^2)(1 - \eta^2)}$ and after applying appropriate boundary conditions is

$$\Phi_0 = \frac{RT}{ZF} \sum_{n=0}^{\infty} B_n P_{2n}(\eta) \quad (4.14)$$

where Φ_0 is the ohmic drop on the electrode surface as a function of radial position, $P_{2n}(\eta)$ is a Legendre polynomial of order $2n$ on the electrode surface ($\mu = 0$), $Z = -z_+ z_- / (z_+ - z_-)$ for single salt and $Z = -n$ with supporting electrolyte, and B_n 's are the constant coefficients to be determined. The current density obtained from the derivative of the potential just outside the diffusion layer is assumed to be equal to that obtained from equation (4.11); thus a relationship between coefficients B_n and A_m is found as

$$B_n = \frac{\pi}{4} N \sum_{m=0}^{\infty} \{Q_{n,m} A_m\} \quad (4.15)$$

where

$$Q_{n,m} = (4n+1) \frac{4\theta'_m(0)}{\pi M'_{2n}(0)} \int_0^1 \eta (1-\eta^2)^m P_{2n}(\eta) d\eta \quad (4.16)$$

$$M'_{2n}(0) = -\frac{2}{\pi} \frac{(2^n n!)^4}{[(2n)]^2} \quad (4.17)$$

and

$$N = -\sqrt{\frac{r_0^2 \Omega}{v}} \left(\frac{av}{3D} \right)^{1/3} \frac{n Z F^2 D c_\infty}{R T (1-t) \kappa_\infty} \quad (4.18)$$

The A_m coefficients were determined using an iterative procedure. A more detailed discussion of the solution procedure can be found in [41].

4.1.3 Diffuse Part of the Double Layer

The method used to account for the two-dimensional diffuse part of the double layer followed the approach suggested by Frumkin [62] in which the kinetic expression was written in terms of a surface overpotential adjusted by the zeta potential and the

concentrations were replaced by the concentrations at the inner limit of the diffuse double layer.

4.1.3a Solution of Poisson's equation

Under the assumption that the double layer is unaffected by the passage of current (see, e.g., [63]) the concentration at the inner limit of the diffuse part of the double layer is given by

$$c_{i,\text{iddl}} = c_{i,0} \exp\left(-\frac{z_i F \zeta}{RT}\right) \quad (4.19)$$

where $c_{i,0}$ is the concentration of species i at the outermost part of the diffuse part of the double layer (the innermost part of the diffusion layer), $c_{i,\text{iddl}}$ is the concentration of species i at the innermost part of the diffuse part of the double layer (the plane of closest approach to the metal surface), ζ is the zeta potential, and z_i is the charge number of species i . The values of concentration at the inner limit of the diffusion layer $c_{i,0}$ were obtained under the assumptions that the solution at this location is electrically neutral, that the diffusion coefficients of the reactant and product ions are equal, and that the diffusion coefficients of the cation and anion from the supporting electrolyte are equal. Thus, a decrease in the concentration of the reactants was offset by an equal increase in the product concentration. The above assumptions are appropriate for the case of the reduction of ferricyanide on Pt electrode discussed in a subsequent section. The diffusion coefficients of the ferri and ferrocyanide are 0.896×10^{-5} cm²/sec and 0.739×10^{-5} cm²/sec respectively, and the diffusion coefficients for K⁺ and Cl⁻ ions are 1.957×10^{-5} cm²/sec and 2.032×10^{-5} cm²/sec, respectively. The above assumptions could be relaxed following the ordinary perturbation approach of Levich [39],[64].

Under the assumption that the diffuse part of the double layer is thin, Poisson's equation

$$\frac{d^2\psi}{dz^2} = -\frac{F}{\varepsilon} \sum_i z_i c_{i0} \exp\left(-\frac{z_i F \psi}{RT}\right) \quad (4.20)$$

can be solved in the axial dimension subject to the boundary conditions

$$\psi \rightarrow 0 \text{ as } z \rightarrow \infty \text{ and } \frac{d\psi}{dz} = \frac{q_2}{\varepsilon} \text{ at } z = z_2 \quad (4.21)$$

where ψ is the potential within the diffuse part of the double layer measured relative to the outermost region of this diffuse part, q_2 is the charge held within the diffuse part of the double layer at a given radial position, and ε is the permittivity of the electrolyte. The use of equation (4.21) requires introduction of a geometric parameter z_2 corresponding to the distance between the electrode surface and the plane of closest approach for ionic species.

Solution of equation (4.20) yields

$$q_2 = \left\{ 2RT\varepsilon \sum_i c_{i0} \left[\exp\left(-\frac{z_i F \zeta}{RT}\right) - 1 \right] \right\}^{1/2} \quad (4.22)$$

where ζ is the zeta potential given by the value of ψ at $z=z_2$.

The total applied potential

$$V - \Phi_{ref} = \Phi_0 + \eta_c + \eta_s^* + \zeta \quad (4.23)$$

is sum of the ohmic potential drop (Φ_0), concentration overpotential (η_c), surface overpotential (η_s^*), and zeta potential (ζ). The Butler-Volmer expression for the normal current density as a function of surface overpotential and concentration was modified to account for the potential and concentration of reacting species at the plane of closest approach; thus,

$$i = i_0 \left\{ \frac{c_0 \exp(-z_r F \zeta / RT)}{c_\infty} \right\}^\gamma \left[\exp \left\{ \frac{\alpha ZF}{RT} \eta_s^* \right\} - \exp \left\{ -\frac{\beta ZF}{RT} \eta_s^* \right\} \right] \quad (4.24)$$

where z_r is the charge number of the reacting species, i_0 is the exchange current density, α and β are the anodic and cathodic transfer coefficients, and γ is the exponent for composition dependence of the exchange current density. In principle such an expression for the reaction kinetics is valid only in case of deposition reactions. However Appel showed that this expression can still be used for redox reactions when the current is a significant fraction of the mass-transfer limiting current [42].

Within this approach, q_2 , c_{io} , $c_{i,iddl}$, i , ζ , η_s , Φ_{ohmic} and η_s^* are functions of radial position. Assumption that the interface taken as a whole is electrically neutral yields

$$q_m = -q_2 \quad (4.25)$$

where q_m is the charge density associated with the concentration of electrons on the metal surface. Because the diffuse double layer is thin in comparison to electrode dimensions, equation (4.25) was assumed to apply at each radial position. Under the assumption that specific adsorption can be neglected, charge is not present between the metal surface and the plane of closest approach of the solvated ions. The potential profile in this region can be assumed to be linear with respect to the axial position; hence,

$$\frac{\eta_s^*}{z_2} = \frac{q_m}{\epsilon} \quad (4.26)$$

The development presented to this point constitutes the mathematical model for convective diffusion to a rotating disk electrode that accounts for finite Schmidt numbers, the influence of the diffuse double layer, and currents below the mass transfer limited

current. Solution of this set of equations can be used to obtain such measurable properties as the double-layer capacitance.

4.1.3b Calculation of double-layer capacitance

The double layer capacitance (C_{dl}) is given by

$$\begin{aligned} C_{dl} &= \frac{dq_m}{d(\eta_s^* + \zeta)} \\ &= \frac{1}{(d\eta_s^*/dq_m) + (d\zeta/dq_m)} \\ &= \frac{1}{(1/C_2) + (1/C_{ddl})} \end{aligned} \quad (4.27)$$

where C_2 is the capacitance between the electrode surface and the plane of closest approach and C_{ddl} is the capacitance across the diffuse part of the double layer. From equation (4.26),

$$C_2 = \frac{dq_m}{d\eta_s^*} = \frac{\epsilon}{y_2} \quad (4.28)$$

C_{ddl} can be calculated as $C_{ddl} = \frac{dq_m}{d\zeta}$. The double layer capacitance can be expressed as a

function of zeta potential by introducing equations (4.22) and (4.25)

$$\begin{aligned} C_{ddl} &= -\{2RT\epsilon\}^{1/2} \frac{d}{d\zeta} \left[\sum_i c_{io} \left[\exp\left\{-\frac{z_i F \zeta}{RT}\right\} - 1 \right] \right]^{1/2} \\ &= F \sqrt{\frac{\epsilon}{RT}} \frac{\sum_i z_i c_{io} \exp\left\{-\frac{z_i F \zeta}{RT}\right\}}{\sqrt{\sum_i 2c_{io} \left[\exp\left\{-\frac{z_i F \zeta}{RT}\right\} - 1 \right]}} \end{aligned} \quad (4.29)$$

An explicit treatment of the double layer in the model facilitates the calculation of charge distribution. This information can be used to determine the influence of charge distribution on the steady state and frequency domain response of disk electrode.

4.2 Numerical Procedure

In the following sections the numerical procedure employed to solve the convective diffusion equation and a step-by-step algorithm for the implementation of the steady state model are presented.

4.2.1 Solution to the Convective Diffusion Equation

Calculation of the steady state current and potential distributions on the electrode surface requires accurate values for $\theta'_m(0)$. A finite difference scheme using central difference formulae accurate to the order of the square of the element length was used to solve equation (4.9) for $m=0$ to 10 at different values of Schmidt number. A tri-diagonal system of equations was obtained and solved by employing the Thomas algorithm [65]. To reduce the error caused by the choice of the step size, calculated values of $\theta'_m(0)$ for different element lengths were extrapolated to zero element length by linear regression. One such regression for an infinite Schmidt number and $m=0$ is presented in Figure 4.1. The 95 percent confidence interval for the intercept was used to estimate the precision of the result. In all cases, 9 significant digits were obtained. For example, the value for $\theta'_m(0)$ obtained by extrapolation was -1.119846522. This result is consistent with the corresponding value of -1.11984652 reported by Newman [41]. The same results were obtained by approximating the solution by a series of Chebyshev polynomials, as illustrated in chapter 6. For the number of significant digits reported here, $\theta'_m(0)$ was not sensitive to the use of more decimal places for constants a and b in Cochran's velocity expansions [56].

Similar extrapolations were made for m=1 to 10 and for various values of Schmidt number. The $\theta'_m(0)$ values obtained for m=0 are given as functions of $Sc^{-1/3}$ in Figure 4.2. The $\theta'_m(0)$ values obtained for different values of m were regressed to a sixth degree polynomial as given by

$$\theta'_m(0) = \sum_{k=0}^6 a_{m,k} Sc^{-k/3} \quad (4.30)$$

where Sc is the Schmidt number of the reacting ions and $a_{m,k}$ are the polynomial coefficients to be determined from the polynomial regression. A sixth-order expansion was used because the 95% confidence intervals for the regressed parameters did not include zero and because smaller order expansions did not provide a sufficiently accurate representation of the numerical results. The residual errors for the expansion were randomly distributed and had magnitudes of roughly 10^{-11} as shown in Figure 4.3.

The mass-transfer limited current density is uniform and is given by

$$i_{lim} = -\frac{nFD_i c_\infty}{1-t} \left(\frac{av}{3D}\right)^{1/3} \sqrt{\frac{\Omega}{v}} \theta'_0(0) \quad (4.31)$$

Equation (4.30) yields a value for $\theta'_0(0)$ at a Schmidt number of 1000 of -1.085880341 as compared to -1.119846522 for an infinite Schmidt number. Assumption of an infinite Schmidt number results in a relative error of 3.1% which is in agreement with the value reported by Newman [40]. The largest error expected for aqueous electrolytes may be seen for hydrogen ion which yields a Schmidt number of the order of 100, resulting in a relative error of 7.1% in the calculated value of the mass-transfer-limited current. While the influence of the finite Schmidt number correction on the calculated mass-transfer-

limited current is small, the errors associated with neglecting this correction are more significant in the frequency domain [53,55].

4.2.2 Algorithm for Implementation of the Model

The numerical procedure employed in this work to handle the diffusion layer and the outer region with the Ohmic drop is similar to the one implemented by Newman [41]; however, introduction of the diffuse part of the double layer required modification of the kinetic boundary condition in order to accommodate the zeta-potential. An algorithm for implementation of the numerical scheme is provided below:

1. The values for $\theta'_m(0)$ resulting from the convective diffusion equation were determined for a given value of Schmidt number from the polynomial expression in equation (4.30) and by using Table 4.1 for the values of $a_{m,k}$.
2. A value for A_m coefficients was assumed, or, in other words, the concentration distribution was assumed on the electrode surface as per equation (4.5).
3. The current distribution resulting from mass-transport was calculated as per equation (4.11).
4. The current distribution obtained from the derivative of the potential just outside the diffusion layer was equated to that from step (3) to obtain the B_n coefficients. The relation used to obtain these coefficients was provided in equation (4.15).
5. The Φ_0 distribution was obtained from equation (4.14).
6. A value for η^* was substituted in terms of ζ from the equations (4.22), (4.25), and (4.26), and the value of ζ was obtained by using a Newton-Raphson technique to solve the non-linear equation (4.24).

7. The η_s^* distribution was calculated from the ζ -potential distribution obtained from step (5) by employing equations (4.22), (4.25), and (4.26).
8. The η_c distribution was calculated from equation (4.23).
9. The concentration distribution was calculated from equation (4.12).
10. The A_m coefficients were obtained again from the concentration distribution from step (8). The new values for the A_m coefficients are the weighted sum of those obtained from the present iteration and from the previous iteration.
11. Steps (3) through (10) were repeated until convergence was achieved.
12. Once the convergence criteria were met, the charge distribution was obtained from equation (4.22), and the double layer capacitance was obtained from equations (4.27), (4.28), and (4.29).

A FORTRAN program used in implementing this algorithm is presented in Appendix A.

4.3 Application to Experimental Systems

The systems treated in this work include electrodeposition of copper and reduction of ferricyanide on platinum.

4.3.1 Electrodeposition of Copper

To validate the numerical approach used in this work, calculations were performed for the 0.1M copper sulfate system studied by Newman [41]. This part of the study did not incorporate the diffuse part of the double layer. Newman's results for an infinite Schmidt number were reproduced. The concentration and current distributions obtained for infinite and finite Schmidt number for this system are compared in Figure 4.4 with applied potential as a parameter. For a given value of applied potential, the distributions

resulting from both these cases differed most significantly as the mass-transfer-limited condition was approached. The largest deviation was seen at the center of the disk. The differences seen between the calculated distributions for infinite and finite Schmidt number are due to differences in the corresponding values of the mass-transfer-limited current. When distributions were presented at the same fraction of the mass-transfer-limited current, the differences were not perceptible.

4.3.2 Reduction of Ferricyanide on Pt

The motivation for this study was to explore the influence of the non-uniform current and potential distributions on the interpretation of the impedance data obtained for the reduction of ferricyanide on a Pt rotating disk electrode. The electrolytic solution consisted of 0.01 M $K_3Fe(CN)_6$, 0.01 M $K_4Fe(CN)_6$, and 1M KCl. Experimental details are presented in chapter 2. The one-dimensional impedance model developed by Tribollet and Newman was used to analyze the data obtained [5]. It was observed that the regressed values for Schmidt number increased with an increase in rotation speed. As the Schmidt number is an electrolytic property independent of rotation speed, this result points to the inadequacy of the one-dimensional model used. To motivate development of a two-dimensional model, current, potential, and charge distributions for this system were obtained as functions of rotation speed and as fractions of the mass-transfer-limited current.

4.3.2a Current, Potential, and Charge Distributions

The numerical values of various parameters used for this particular system are listed in Table 4.2. The rate constant for reduction of ferricyanide on Pt is very large [37], [66]; thus, the surface overpotential can be expected to be small. Due to the use of excess

supporting electrolyte, the contribution of ohmic drop can also be expected to be small. Thus, mass transport being the predominate factor, the current distribution is expected to be uniform. Calculated current distributions are presented in Figure 4.5 for rotation rates of 120 and 3000 rpm. A uniform calculated current distribution was indeed observed at low rotation speeds, but at large rotation speeds the current distribution was more nonuniform. These distributions can be contrasted with the extreme case of a primary current distribution where $i_{\text{sur}}/i_{\text{avg}}=0.5$ at the center of the electrode and is equal to ∞ at the periphery. As shown in Figure 4.5(b) for 1/4th of the limiting current at 3000rpm, the current distribution varies from a value of 0.88 at the center to 1.23 at the edge of the electrode.

The non-uniformity in calculated current distribution shown in Figure 4.5b was obtained in spite of the use of excess supporting electrolyte. From the calculated overpotentials shown in Figure 4.6 and Figure 4.8 it can be seen that at both 120 and 3000rpm, the surface overpotential, and the zeta potential are small. The applied potential, by virtue of the large metal conductivity, is uniform. Thus, a non-uniform distribution in ohmic potential is compensated by an opposing distribution in concentration overpotential. The potential distributions are more uniform for the 120rpm case and are less so for the 3000rpm case. A large rotation speed increases the value of the mass-transfer limited current and, therefore, increases the influence of the ohmic potential drop. The concentration overpotential increases to be a more significant fraction of the applied potential as current approaches mass-transfer limitation. The ohmic potential drop, therefore, becomes less significant. Thus, the current distribution is more uniform at 3/4 of the mass-transfer-limited current than at 1/4 (see Figure 4.5).

Although, as seen in Figure 4.6 and Figure 4.8 the zeta potential obtained does not contribute significantly to the overall potential, calculation of the zeta potential allows determination of the charge distribution from equation (4.22). As can be seen from Figure 4.10, the charge distribution calculated for this system is more non-uniform at 3000rpm than at 120rpm. The charge distribution follows the distribution of surface overpotential (see equation (4.26)).

The charge distribution thus obtained was used to calculate the radial distribution of the double layer capacitance from equations (4.27) and (4.29). The calculated capacitance was found to be independent of rotation rate and to be uniformly distributed with a value of $55\mu\text{F}/\text{cm}^2$ for $y_2 = 10\text{A}^\circ$. This value is in reasonable agreement with the experimental value of $35\mu\text{F}/\text{cm}^2$ obtained by Deslouis and Tribollet for the same system [67]. They obtained the same value of capacitance from measurements on disk and ring-disk electrodes. This result is in agreement with the calculations from the present work which showed that the capacitance has no radial distribution. The value of the double layer capacitance is sensitive to the choice of y_2 . By choosing $y_2 = 17\text{A}^\circ$ a value of $35\mu\text{F}/\text{cm}^2$ was obtained for the double layer capacitance.

4.3.2b Zero Frequency Asymptotes of Local Impedance

As a preliminary step towards formulating a detailed two-dimensional model for the impedance analysis explicitly accounting for various phenomena, the zero frequency asymptotes for the local impedances for the ferri/ferrocyanide system were obtained from steady state distributions calculated at two applied potentials separated by 5mV. The ratio of the difference in overpotential with respect to the difference in current density calculated locally provides the contribution of the respective phenomena to overall

impedance response. The radial distributions of these values are presented in Figure 4.11 and Figure 4.12 for 120 and 3000rpm respectively. The zero frequency asymptotes for the local impedance are more uniform for the case of 120rpm and are less so for 3000rpm. This is a strong indication that a two-dimensional model is necessary to obtain reliable information from impedance data. At higher fractions of the limiting current, the local impedance resulting from the concentration overpotential dominates. The local impedance values resulting from the ohmic drop are estimated to be about $2\Omega\text{-cm}^2$, which corresponds to 10Ω for a disc with a surface area of 0.2cm^2 , in agreement with experiment. Appel reported the radial distributions of the impedance calculations for a single dimensionless frequency of 0.1 applied to 0.0001 equimolar solution of sodium ferrocyanide and sodium ferricyanide with a 0.1M sodium fluoride supporting electrolyte [42]. Similar non-uniformities were observed from his calculations.

4.4 Conclusions

In this chapter, a finite Schmidt number correction was applied to the steady state model for the rotating disc electrode below the mass transfer limited current. The result of the convective diffusion equation accounting for this correction was expressed as a polynomial expansion of $\text{Sc}^{-1/3}$, and the coefficients of the polynomial expansion were tabulated. The model was then extended to incorporate the diffuse part of the double layer. Results provided by Newman for deposition of copper were reproduced. The distributions of current, potential, and charge were assessed for the reduction of ferricyanide on Pt. The double layer capacitance and the zero frequency asymptotes of the local impedances were evaluated. Surface non-uniformities were observed for the

distribution of various parameters. The zero frequency asymptotes of the local impedances were calculated and non-uniformities were observed. These asymptotic calculations show that non-uniformity effects are significant, especially at higher rotation rates. These non-uniformities in fact could cause the anomalous Schmidt number values that were observed in chapter 2. This points to the need for a two-dimensional impedance model accounting for a finite Schmidt number correction. Development of such a two-dimensional impedance model is presented in the next chapter.

Table 4.1. Polynomial coefficients in the expansion for $\theta'_m(0)$ resulting from the solution of the convective diffusion equation. The number of significant digits reported are based on the respective confidence intervals from the regression.

	a_0	a_1	a_2	a_3	a_4	a_5	a_6
m=0	-1.119846522	0.333723494	0.0630655	-0.02483	-0.1009	-0.1539	-0.361
1	-1.532987928	0.348508169	0.0563987	-0.01244	-0.0557	-0.0760	-0.184
2	-1.805490584	0.351502095	0.0501466	-0.008443	-0.03678	-0.0463	-0.1034
3	-2.015723734	0.352526040	0.0456708	-0.006567	-0.02707	-0.0321	-0.0647
4	-2.189982747	0.352984907	0.0423604	-0.005472	-0.02132	-0.0240	-0.0441
5	-2.340450747	0.353227157	0.0398003	-0.004743	-0.01758	-0.0187	-0.0323
6	-2.473842754	0.353369827	0.0377463	-0.004220	-0.01493	-0.0153	-0.0247
7	-2.594287242	0.353460658	0.03605028	-0.003823	-0.01295	-0.0128	-0.0194
8	-2.704520850	0.353521951	0.03461769	-0.0035106	-0.01141	-0.01114	-0.0154
9	-2.806460253	0.35356522	0.0333854	-0.00326	-0.0102	-0.010	-0.013
10	-2.901505453	0.3535688	0.03230943	-0.003038	-0.00927	-0.00841	-0.0109

Table 4.2. Input parameters used for the ferri/ferro cyanide in 1M KCl system reacting on the Pt disc electrode

$v = 0.951 \times 10^{-2} \text{ cm}^2/\text{sec}$	$D = 0.896 \times 10^{-5} \text{ cm}^2/\text{sec}$
$F = 96487 \text{ coul}/\text{eq}$	$c_{\infty} = 10^{-5} \text{ mol/c.c.}$
$Z = 1$	$T = 298K$
$\alpha = 0.5$	$\beta = 0.5$
$\epsilon = 6.933 \times 10^{-12} \text{ C/V/cm}$	$n = 1$
$r_0 = 0.25 \text{ cm}$	$t = 0.04$
$R = 8.314 \text{ J/mol/K}$	$i_0 = 0.3 \text{ amp/cm}^2$
$\kappa_{\infty} = 0.1 \text{ ohm}^{-1} \text{ cm}^{-1}$	$y_2 = 10 \text{ A}^\circ$
$\gamma = 1.0$	

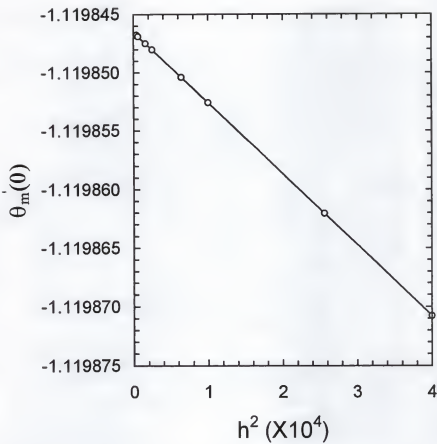


Figure 4.1. Determination of the accurate value for $\theta'_m(0)$ for infinite Schmidt number, making use of the values obtained from the FDM scheme using varying step-sizes.

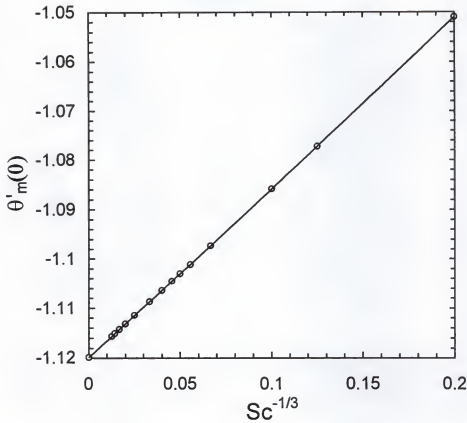


Figure 4.2. A sixth degree polynomial fit for $\theta_m(0)$ vs. $Sc^{-1/3}$

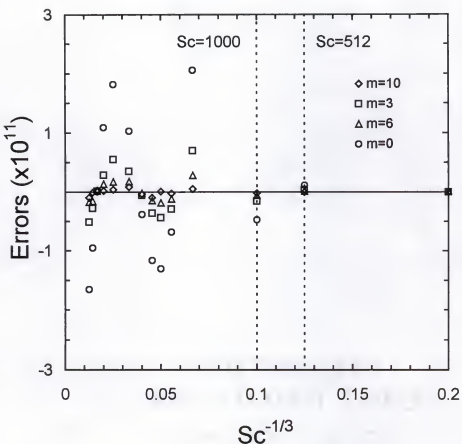


Figure 4.3. Errors in $\theta_m(0)$ values between polynomial fits and the values calculated from the FDM scheme

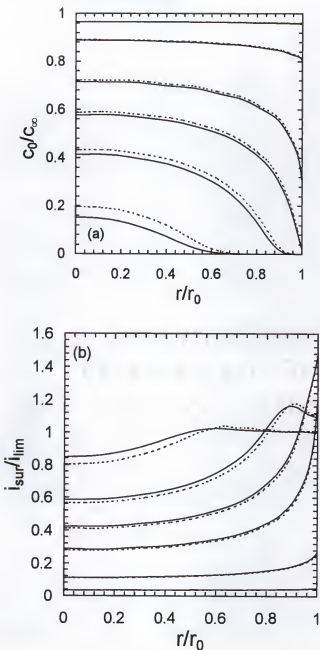


Figure 4.4. Calculated (a) concentration and (b) current distribution on the surface of the disk electrode for deposition of copper under the condition corresponding to figures (6) and (7) of reference (41) with $N=50$. Adjacent infinite Sc (dashed lines) and finite Sc (solid lines) are for same applied potential. In the order of decreasing concentration, the applied potentials ($V-\Phi_{ref}$) used were $-0.08V$, $-0.28V$, $-0.68V$, $-0.98V$, $-1.28V$, and $-1.58V$.

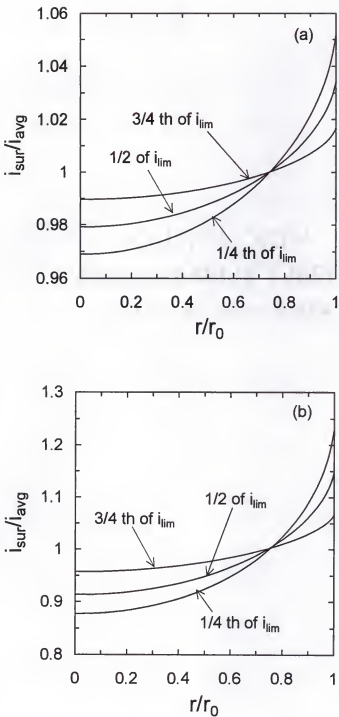


Figure 4.5. Calculated current distributions for the reduction of ferricyanide on a Pt disk electrode rotating at (a) 120 rpm and (b) 3000 rpm. System properties are given in Table 4.2.

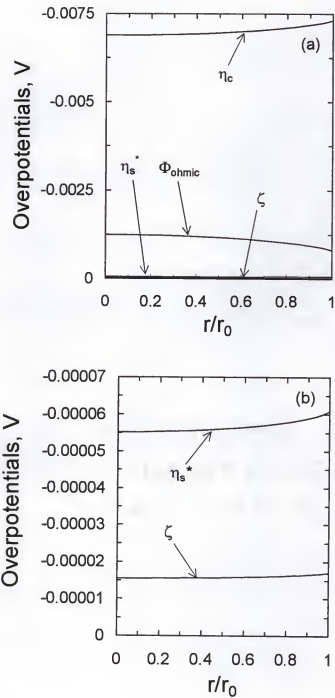


Figure 4.6. Calculated overpotentials for the case of Figure 4.5a (120rpm) at (a) 1/4th of i_{lim} , (b) 1/4 of i_{lim} on an enlarged scale to show the distributions of η_s^* and ζ .

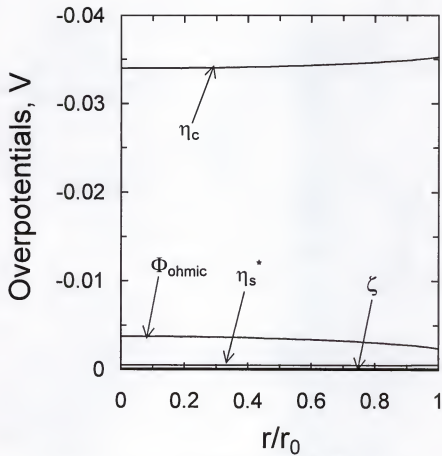


Figure 4.7. Calculated overpotentials for the case of Figure 4.5a (120rpm) at 3/4th of i_{lim} .

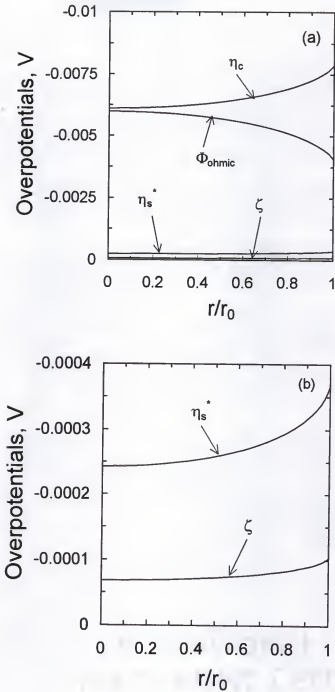


Figure 4.8. Calculated overpotentials for the case of Figure 4.5b (3000rpm) at (a) 1/4th of i_{lim} , (b) 1/4 of i_{lim} on an enlarged scale to show the distributions of η_s^* and ζ .

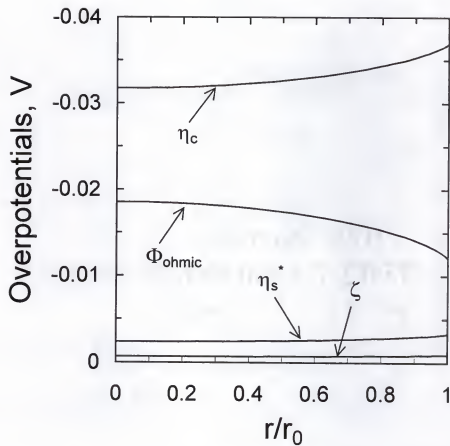


Figure 4.9. Calculated overpotentials for the case of Figure 4.5b (3000rpm) at 3/4th of i_{lim} .

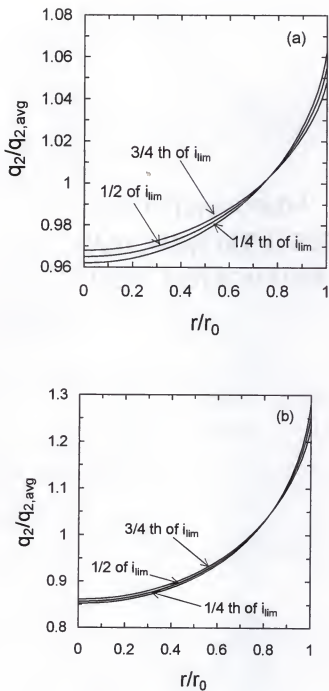


Figure 4.10. Calculated charge distributions for the cases of (a) Figure 4.5a (120rpm) and (b) Figure 4.5b (3000rpm).

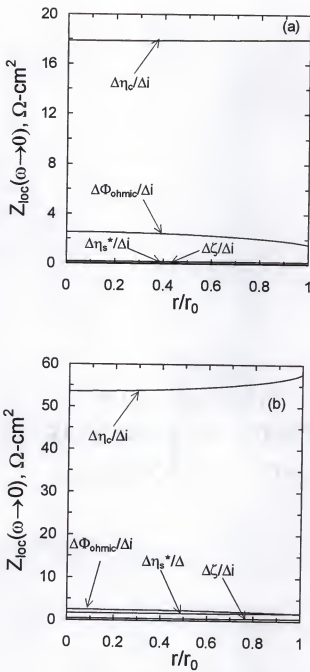


Figure 4.11. Calculated local impedance distributions corresponding to Figure 4.5a (120 rpm) for (a) 1/4th of i_{lim} , and (b) 3/4th of i_{lim} .

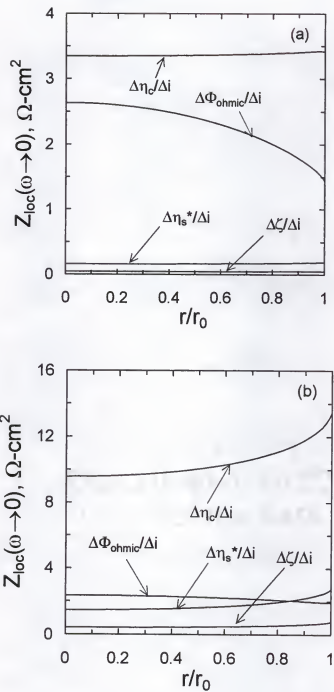


Figure 4.12. Calculated local impedance distributions corresponding to Figure 4.5b (3000 rpm) for (a) 1/4th of i_{lim} , and (b) 3/4th of i_{lim} .

CHAPTER 5

A MATHEMATICAL MODEL FOR THE RADIALLY DEPENDENT IMPEDANCE OF A ROTATING DISK ELECTRODE

The need for a two-dimensional frequency domain model accounting for a finite Schmidt number correction is established in the previous chapter. The development of such a model, application to the ferricyanide reduction on platinum electrode, and a comparison with the existing one-dimensional frequency domain model is presented in this chapter.

Frequency domain techniques are commonly employed in the study of electrode kinetics and mass transfer in electrolytic solutions. While the information obtained is similar to that from transient techniques, better resolution of physical processes can be achieved because the noise level in frequency-domain measurements can be made to be extremely small [10,19,68]. A second advantage of the frequency domain techniques over transient techniques is that the Kramers-Kronig relations can be used to identify instrumental artifacts or changes in baseline properties [11], [69-71].

Due to the growing popularity of the rotating disk electrode, significant effort has been expended on developing analytic formulae for the impedance response of this system [43-54]. A comparative study of the application of these models to interpretation of impedance spectra has been presented by Orazem *et al.* [55]. A one-dimensional numerical model for the impedance response of a rotating disk electrode which accounted for the influence of a finite Schmidt number was presented by Tribollet and Newman [5]. This

model accounts for effects associated with kinetics, mass-transport, and ohmic potential drop within the bulk of the solution under the assumption of uniform radial distributions of current, concentration, and overpotentials. The first two terms in the Cochran expansion [56] for the axial component of fluid velocity were included in the convective diffusion equation. Tribollet *et al.* reported that the errors caused by neglecting the second term in the axial velocity expansion could be as high as 24 percent for a Schmidt number of 1000 [53]. This result was confirmed by regression of various mass-transfer models to impedance data [55].

Mathematical models have been developed which account for frequency dispersion associated with the non-uniform potential distribution on the disk electrode [57-60]. But, to date, no comparable model has been developed for the influence of non-uniform mass-transfer on the impedance response. Appel and Newman provided a preliminary mathematical development [61], valid for an infinite Schmidt number, that they proposed would be used to develop a model for the influence of radially-dependent convective diffusion on the impedance response. Later, Appel used this approach to calculate the radial distribution of impedance, but results were presented only for a single dimensionless frequency due to numerical difficulties associated with implementation of the model [42].

For some systems, even in the presence of excess supporting electrolyte, the distributions of current and overpotential on the electrode surface can be significantly non-uniform in the steady state domain as illustrated in the previous chapter (refer to Figure 4.5 (b)). For such cases, the available one-dimensional model can be inadequate to describe the physics of the system. The objective of this work is to provide a development of a two-dimensional model for electrochemical impedance response of a rotating disk

electrode that accounts for non-uniform ohmic potential drop, surface and concentration overpotentials.

5.1 Theoretical Development

The formulation for the two-dimensional impedance model results from applying a sinusoidal perturbation about the steady-state solution presented in the previous chapter. The capacitance was assumed to be uniformly distributed across the surface of the disk electrode. This assumption is justified by the results of steady state calculations valid in the absence of specific adsorption. Assumption of uniform capacitance is also consistent with the experimental results presented by Deslouis and Tribollet [67]. The development of a two-dimensional frequency domain model is presented in this chapter.

5.1.1 Convective Diffusion

For a small sinusoidal perturbation of frequency ω in potential, the response can be assumed to be linear, and all associated variables will oscillate at the same frequency ω . Thus; each variable can be written in the form

$$\chi = \bar{\chi} + \text{Re}\{\tilde{\chi} \exp(j\omega t)\} \quad (5.1)$$

where χ is the variable under consideration, $\bar{\chi}$ is the corresponding steady state or baseline value of χ , $\tilde{\chi}$ is the complex amplitude of perturbation, t is the time, ω is frequency, and $j = \sqrt{-1}$. As defined, $\tilde{\chi}$ is a function only of position. The same notation is used for the other parameters considered in this chapter.

On the basis of equation (5.1), the concentration of the reacting species can be written as

$$c(r, z, t) = \bar{c}(r, z) + \operatorname{Re}\{\tilde{c}(r, z) \exp(j\omega t)\} \quad (5.2)$$

where \bar{c} and \tilde{c} are functions of radial and axial position. Incorporation of concentration perturbation terms in the unsteady state convective diffusion equation and cancellation of the steady state terms yields

$$j\omega \tilde{c} + v_r \frac{\partial \tilde{c}}{\partial r} + v_z \frac{\partial \tilde{c}}{\partial z} = D \frac{\partial^2 \tilde{c}}{\partial z^2} \quad (5.3)$$

where v_r and v_z are the radial and axial components of the velocity of the fluid and D is the diffusion coefficient of the species of interest. The velocity components, v_r and v_z , account for the first three terms of Cochran's expansion as given by

$$v_r = az \frac{\Omega^{3/2}}{\nu^{1/2}} - \frac{1}{2} rz^2 \frac{\Omega^2}{\nu} - \frac{b}{3} rz^3 \frac{\Omega^{5/2}}{\nu^{3/2}} \quad (5.4a)$$

and

$$v_z = -az^2 \frac{\Omega^{3/2}}{\nu^{1/2}} + \frac{1}{3} z^3 \frac{\Omega^2}{\nu} + \frac{b}{6} z^4 \frac{\Omega^{5/2}}{\nu^{3/2}} \quad (5.4b)$$

where a and b are the coefficients from Cochran's expansion for the radial and axial velocities for the rotating disk electrode system, Ω is the rotation rate of the disk electrode, and ν is the kinematic viscosity of the electrolyte. For the steady state case, a variable-separable form was used for the expression of concentration of the reacting species, c , that is,

$$c = c_\infty \left[1 + \sum_{m=0}^{\infty} \left\{ A_m \left(\frac{r}{r_0} \right)^{2m} \theta_m(\xi) \right\} \right] \quad (5.5)$$

where c_∞ is the bulk concentration of the reacting species, A_m values are the coefficients to be determined from the steady state calculations, and $\theta_m(\xi)$ is the axial dependent term

which can also be determined from the steady state values. The dimensionless axial distance ξ is given by

$$\xi = z \left(\frac{\alpha v}{3D} \right)^{1/3} \sqrt{\frac{\Omega}{v}} \quad (5.6)$$

The resulting perturbation in concentration c from equation (5.5) can be written as

$$\tilde{c} = c_{\infty} \sum_{m=0}^{\infty} \left\{ [\tilde{A}_m \theta_m(\xi) + A_m \tilde{\theta}_m(\xi)] \left(\frac{r}{r_0} \right)^{2m} \right\} \quad (5.7)$$

Substitution of equations (5.4a), (5.4b), and (5.6) in equation (5.3) yields

$$\begin{aligned} jK\tilde{c} + & \left(3r\xi - \frac{3}{2}r\xi^2 BSc^{-1/3} - 2Cr\xi^3 Sc^{-2/3} \right) \frac{\partial \tilde{c}}{\partial r} \\ & + \left(-3\xi^2 + B\xi^3 Sc^{-1/3} + C\xi^4 Sc^{-2/3} \right) \frac{\partial \tilde{c}}{\partial \xi} = \frac{\partial^2 \tilde{c}}{\partial \xi^2} \end{aligned} \quad (5.8)$$

where Sc is the Schmidt number of the species controlled by mass transfer, and

$$K = \frac{\omega}{\Omega} \left(\frac{9v}{a^2 D} \right)^{1/3} \quad (5.9)$$

$$B = \left(\frac{3}{a^4} \right)^{1/3} \quad (5.10)$$

and

$$C = \frac{b}{6} \left(\frac{3}{a} \right)^{5/3} \quad (5.11)$$

where K is the dimensionless frequency of perturbation. Combination of equations (5.7) and (5.8), cancellation of terms resulting from the steady state part of the convective diffusion,

$$\begin{aligned} & \theta_m'' + (3\xi^2 - B\xi^3 Sc^{-1/3} - C\xi^4 Sc^{-2/3})\theta_m' \\ & + 2m\left(-3\xi + \frac{3}{2}\xi^2 B Sc^{-1/3} + 2C\xi^3 Sc^{-2/3}\right)\theta_m = 0 \end{aligned} \quad (5.12)$$

yields

$$A_m \left\{ \begin{aligned} & \tilde{\theta}_m'' + (3\xi^2 - B\xi^3 Sc^{-1/3} - C\xi^4 Sc^{-2/3})\tilde{\theta}_m' \\ & + 2m\left(-3\xi + \frac{3}{2}\xi^2 B Sc^{-1/3} + 2C\xi^3 Sc^{-2/3}\right)\tilde{\theta}_m \end{aligned} \right\} - jK\tilde{A}_m\theta_m = 0 \quad (5.13)$$

where primes in the superscripts refer to derivative with respect to ξ . The real and imaginary parts of equation (5.13) provide two ordinary differential equations which must be solved simultaneously.

Solution of equation (5.13) requires that boundary conditions on $\tilde{\theta}_m$ be established. From the steady state case, the concentration at the surface is given by

$$c_0 = c_\infty \left[1 + \sum_{m=0}^{\infty} \left\{ A_m \left(r/r_0 \right)^{2m} \right\} \right] \quad (5.14)$$

Hence, the perturbation in concentration of reacting species on the electrode surface is given by

$$\tilde{c}_0 = c_\infty \sum_{m=0}^{\infty} \tilde{A}_m \left(r/r_0 \right)^{2m} \quad (5.15)$$

However, from equation (5.7),

$$\tilde{c}_0 = c_\infty \sum_{m=0}^{\infty} \left[[\tilde{A}_m \theta_m(0) + A_m \tilde{\theta}_m(0)] \left(r/r_0 \right)^{2m} \right] \quad (5.16)$$

As $\theta_m(0) = 1$ from steady state calculations, comparison of equations (5.15) and (5.16) reveals the boundary conditions for equation (5.13) to be

$$\tilde{\theta}_m = 0 \text{ at } \xi = 0 \quad (5.17)$$

and

$$\tilde{\theta}_m = 0 \text{ at } \xi = \infty \quad (5.18)$$

The boundary condition at $\xi = \infty$ results from the observation that the imposed perturbation does not have any effect on the parameter values far away from the electrode surface. The simultaneous equations resulting from the equation (5.13) can be solved by the reduction-in-order method. The solution for equation (5.13) can be written as

$$\begin{aligned} \tilde{\theta}_m &= \tilde{\theta}_{mh} \left[\frac{\int_{\xi}^{\xi'} \left[\frac{jK\tilde{A}_m \theta_m \tilde{\theta}_{mh}}{A_m} \exp \left(\xi'^3 - \frac{B\xi'^4}{4} Sc^{-1/3} - \frac{C\xi'^5}{5} Sc^{-2/3} \right) \right] d\xi'}{\tilde{\theta}_{mh}^2 \exp \left(\xi'^3 - \frac{B\xi'^4}{4} Sc^{-1/3} - \frac{C\xi'^5}{5} Sc^{-2/3} \right)} \right. \\ &\quad \left. + K_1 \tilde{\theta}_{mh} \int_{\xi}^{\xi'} \frac{1}{\tilde{\theta}_{mh}^2 \exp \left(\xi'^3 - \frac{B\xi'^4}{4} Sc^{-1/3} - \frac{C\xi'^5}{5} Sc^{-2/3} \right)} d\xi' + K_2 \tilde{\theta}_{mh} \right] \end{aligned} \quad (5.19)$$

where $\tilde{\theta}_{mh}$ is the solution to the homogeneous part of the differential equation, and K_1 and K_2 are arbitrary constants that need to be determined based on the boundary conditions. Equation (5.19) can be written as

$$\tilde{\theta}_m = \tilde{\theta}_{mh} \left[K_2 + \int_{\xi}^{\xi'} \tilde{\theta}_{mh}^{-2} \exp \left(-\xi'^3 + \frac{B\xi'^4}{4} Sc^{-1/3} + \frac{C\xi'^5}{5} Sc^{-2/3} \right) t_1(\xi') d\xi' \right] \quad (5.20)$$

where

$$t_1(\xi') = K_1 + j \int_{\xi}^{\xi'} \frac{K\tilde{A}_m \theta_m \tilde{\theta}_{mh}}{A_m} \exp \left(\xi^3 - \frac{B\xi^4}{4} Sc^{-1/3} - \frac{C\xi^5}{5} Sc^{-2/3} \right) d\xi \quad (5.21)$$

From the boundary condition $\tilde{\theta}_m = 0$ at $\xi = 0$ and equation (5.20), $K_2 = 0$. From the boundary condition $\tilde{\theta}_m = 0$ at $\xi = \infty$,

$$K_1 = -j \frac{K\tilde{A}_m}{A_m} \int_0^\infty \theta_m \tilde{\theta}_{mh} \exp\left(\xi^3 - \frac{B\xi^4}{4} Sc^{-1/3} - \frac{C\xi^5}{5} Sc^{-2/3}\right) d\xi \quad (5.22)$$

Equation (5.22) is a direct consequence of the observation that the factor $\tilde{\theta}_{mh}^{-2} \exp\left(-\xi'^3 + \frac{B\xi'^4}{4} Sc^{-1/3} + \frac{C\xi'^5}{5} Sc^{-2/3}\right)$ approaches infinity as ξ' becomes large (the rate at which $\tilde{\theta}_{mh}^2$ approaches $0+j0$ is much faster than the rate at which $\exp\left(-\xi'^3 + \frac{B\xi'^4}{4} Sc^{-1/3} + \frac{C\xi'^5}{5} Sc^{-2/3}\right)$ approaches 0). Hence, in order for a stable solution to exist, $t_1(\xi')$ must be zero. One of the parameters of great interest is the derivative of $\tilde{\theta}_m$ with respect to ξ at the electrode surface, as this will be used at a later stage to calculate the perturbation in current resulting from mass transport:

$$\tilde{\theta}'_m(0) = \left. \frac{d\tilde{\theta}_m}{d\xi} \right|_{\xi=0} = K_1 = -j \frac{K\tilde{A}_m}{A_m} \int_0^\infty \theta_m \tilde{\theta}_{mh} \exp\left(\xi^3 - \frac{B\xi^4}{4} Sc^{-1/3} - \frac{C\xi^5}{5} Sc^{-2/3}\right) d\xi \quad (5.23)$$

The homogeneous part of the convective diffusion equation is given by

$$\left[\begin{aligned} & \tilde{\theta}_{mh}'' + (3\xi^2 - B\xi^3 Sc^{-1/3} - C\xi^4 Sc^{-2/3}) \tilde{\theta}_{mh}' \\ & + 2m \left(-3\xi + \frac{3}{2}\xi^2 B Sc^{-1/3} + 2C\xi^3 Sc^{-2/3} \right) \tilde{\theta}_{mh} - jK\tilde{\theta}_{mh} \end{aligned} \right] = 0 \quad (5.24)$$

and the boundary conditions to solve this equation can be chosen to be

$$\tilde{\theta}_{mh} = 1 \text{ at } \xi = 0 \quad (5.25)$$

and

$$\tilde{\theta}_{mh} = 0 \text{ at } \xi \rightarrow \infty \quad (5.26)$$

The boundary conditions of Equations (5.25) and (5.26) are used for solving the homogeneous part of the convective diffusion equation, and the boundary conditions for the overall solution are provided by equations (5.17) and (5.18). Following Levart and Schuhmann's approach, the solution to the homogeneous part can be expressed as a polynomial series of $Sc^{-1/3}$ [72]. Hence, by retaining two terms accounting for the finite Sc correction, $\tilde{\theta}_{mh}$ can be represented by

$$\tilde{\theta}_{mh} = \tilde{\theta}_{0,mh} + \tilde{\theta}_{1,mh} Sc^{-1/3} + \tilde{\theta}_{2,mh} Sc^{-2/3} \quad (5.27)$$

Thus, equation (5.24) can be rewritten as

$$\left[\begin{array}{l} \left(\tilde{\theta}_{0,mh}'' + \tilde{\theta}_{1,mh}'' Sc^{-1/3} + \tilde{\theta}_{2,mh}'' Sc^{-2/3} \right) \\ + \left(3\xi^2 - B\xi^3 Sc^{-1/3} - C\xi^4 Sc^{-2/3} \right) \left(\tilde{\theta}_{0,mh}' + \tilde{\theta}_{1,mh}' Sc^{-1/3} + \tilde{\theta}_{2,mh}' Sc^{-2/3} \right) \\ + 2m \left(-3\xi + \frac{3}{2}\xi^2 B Sc^{-1/3} + 2C\xi^3 Sc^{-2/3} \right) \left(\tilde{\theta}_{0,mh} + \tilde{\theta}_{1,mh} Sc^{-1/3} + \tilde{\theta}_{2,mh} Sc^{-2/3} \right) \\ - jK \left(\tilde{\theta}_{0,mh} + \tilde{\theta}_{1,mh} Sc^{-1/3} + \tilde{\theta}_{2,mh} Sc^{-2/3} \right) \end{array} \right] = 0 \quad (5.28)$$

Collection of real and imaginary terms of the same order of Sc yields six simultaneous ordinary differential equations:

$$\tilde{\theta}_{0,mh,r}'' + 3\xi^2 \tilde{\theta}_{0,mh,r}' - 6m\xi \tilde{\theta}_{0,mh,r} + K \tilde{\theta}_{0,mh,j} = 0 \quad (5.29a)$$

$$\tilde{\theta}_{0,mh,j}'' + 3\xi^2 \tilde{\theta}_{0,mh,j}' - 6m\xi \tilde{\theta}_{0,mh,j} - K \tilde{\theta}_{0,mh,r} = 0 \quad (5.29b)$$

$$\tilde{\theta}_{1,mh,r}'' + 3\xi^2 \tilde{\theta}_{1,mh,r}' - 6m\xi \tilde{\theta}_{1,mh,r} + K \tilde{\theta}_{1,mh,j} = B\xi^3 \tilde{\theta}_{0,mh,r}' - 3m\xi^2 B \tilde{\theta}_{0,mh,r} \quad (5.29c)$$

$$\tilde{\theta}_{1,mh,j}'' + 3\xi^2 \tilde{\theta}_{1,mh,j}' - 6m\xi \tilde{\theta}_{1,mh,j} - K \tilde{\theta}_{1,mh,r} = B\xi^3 \tilde{\theta}_{0,mh,j}' - 3m\xi^2 B \tilde{\theta}_{0,mh,j} \quad (5.29d)$$

$$\begin{aligned} \tilde{\theta}_{2,mh,r}'' + 3\xi^2\tilde{\theta}_{2,mh,r}' - 6m\xi\tilde{\theta}_{2,mh,r} + K\tilde{\theta}_{2,mh,r} \\ = B\xi^3\tilde{\theta}_{1,mh,r}' - 3m\xi^2B\tilde{\theta}_{1,mh,r} + C\xi^4\tilde{\theta}_{0,mh,r}' - 4mC\xi^3\tilde{\theta}_{0,mh,r} \end{aligned} \quad (5.29e)$$

$$\begin{aligned} \tilde{\theta}_{2,mh,j}'' + 3\xi^2\tilde{\theta}_{2,mh,j}' - 6m\xi\tilde{\theta}_{2,mh,j} - K\tilde{\theta}_{2,mh,j} \\ = B\xi^3\tilde{\theta}_{1,mh,j}' - 3m\xi^2B\tilde{\theta}_{1,mh,j} + C\xi^4\tilde{\theta}_{0,mh,j}' - 4mC\xi^3\tilde{\theta}_{0,mh,j} \end{aligned} \quad (5.29f)$$

This system was solved using Newman's BAND algorithm. The boundary conditions are

$$\tilde{\theta}_{0,mh} = 1 \text{ at } \xi = 0 \text{ and } \tilde{\theta}_{0,mh} \rightarrow 0 \text{ as } \xi \rightarrow \infty \quad (5.30a)$$

$$\tilde{\theta}_{1,mh} = 0 \text{ at } \xi = 0 \text{ and } \tilde{\theta}_{1,mh} \rightarrow 0 \text{ as } \xi \rightarrow \infty \quad (5.30b)$$

and

$$\tilde{\theta}_{2,mh} = 0 \text{ at } \xi = 0 \text{ and } \tilde{\theta}_{2,mh} \rightarrow 0 \text{ as } \xi \rightarrow \infty \quad (5.30c)$$

5.1.2 Conditions on Current

The current density on the electrode surface is constrained by mass transfer and kinetic considerations.

5.1.2a Mass transport

The normal Faradic current density i_f must satisfy

$$\frac{i_f}{nF} = \frac{D}{1-t_R} \frac{\partial c}{\partial z} \Big|_{z=0} = \frac{Dc_\infty}{1-t_R} \left(\frac{av}{3D} \right)^{1/3} \sqrt{\frac{\Omega}{\nu}} \sum_{m=0}^{\infty} A_m (r/r_0)^{2m} \theta_m'(0) \quad (5.31)$$

where t is the transference number of the reacting species, n is the number of electrons produced when one reactant ion or molecule reacts, and F is Faraday's constant. The oscillation in normal current density is related to the derivative of oscillation in the concentration by

$$\begin{aligned}\frac{\tilde{i}_f}{nF} &= \frac{D}{1-t_R} \left. \frac{\partial \tilde{c}}{\partial z} \right|_{z=0} \\ &= \frac{Dc_\infty}{1-t_R} \left(\frac{av}{3D} \right)^{1/3} \sqrt{\frac{\Omega}{\nu}} \sum_{m=0}^{\infty} \left\{ \tilde{A}_m \theta'_m(0) + A_m \tilde{\theta}'_m(0) \right\} (r/r_0)^{2m}\end{aligned}\quad (5.32)$$

The interfacial overpotential resulting from convective diffusion is the concentration overpotential (η_c) given by

$$\eta_c = -\frac{RT}{ZF} \left[\ln \left(\frac{c_\infty}{c_0} \right) - t_R \left(1 - \frac{c_0}{c_\infty} \right) \right] \quad (5.33)$$

where R is the universal gas constant, T is the temperature of the electrolyte in Kelvin, and Z is the number of equivalents of reactant used up per one electron produced/consumed. For the case of sinusoidal perturbation

$$\tilde{\eta}_c = \frac{RT}{ZF} \left[\frac{1}{c_0} - \frac{t_R}{c_\infty} \right] \tilde{c}_0 \quad (5.34)$$

5.1.2b Kinetics

The current resulting from the kinetic contribution can be equated to the current resulting from the mass transport, as was done for the steady-state case. The steady-state expression for the current due to kinetic contribution is

$$i_f = i_0 \left(\frac{c_0}{c_\infty} \right)^\gamma \left[\exp \left(\frac{\alpha ZF}{RT} \eta_s \right) - \exp \left(-\frac{\beta ZF}{RT} \eta_s \right) \right] \quad (5.35)$$

where i_0 is the exchange current density, α and β are the anodic and cathodic transfer coefficients, γ is the composition dependence of the exchange current density, and η_s is the surface overpotential. The oscillation in Faradic current is given by

$$\tilde{i}_f = \frac{\gamma i_f}{c_0} \tilde{c}_0 + i_0 \left(\frac{c_0}{c_\infty} \right)^\gamma \frac{ZF}{RT} \left[\alpha \exp\left(\frac{\alpha ZF}{RT} \eta_s\right) + \beta \exp\left(-\frac{\beta ZF}{RT} \eta_s\right) \right] \tilde{\eta}_s \quad (5.36)$$

The capacitive contribution to the current density is given by

$$\tilde{i}_c = j\omega C (\tilde{\eta}_c + \tilde{\eta}_s) \quad (5.37)$$

where C is the double layer capacitance.

5.1.3 Potential

Under the assumptions of the absence of concentration gradients within the bulk of the solution,

$$\nabla^2 \Phi = 0 \quad (5.38)$$

where Φ is the ohmic potential. Hence when a sinusoidal perturbation is imposed, the equation is transformed to

$$\nabla^2 \tilde{\Phi} = 0 \quad (5.39)$$

It should be noted that Laplace's equation does not have time dependence, even for the unsteady-state case. The rotational elliptic coordinate transformation applied for the steady state problem can be applied to equation (5.39), that is,

$$\frac{\partial}{\partial \mu} \left[(1 + \mu^2) \frac{\partial \tilde{\Phi}}{\partial \mu} \right] + \frac{\partial}{\partial \eta} \left[(1 - \eta^2) \frac{\partial \tilde{\Phi}}{\partial \eta} \right] = 0 \quad (5.40)$$

where $y = r_0 \mu \eta$ and $r = r_0 \sqrt{(1 + \mu^2)(1 - \eta^2)}$. The boundary conditions for equation (5.40) were that $\partial \tilde{\Phi} / \partial \eta = 0$ at $\eta = 0$ (on the annulus), $\tilde{\Phi} = 0$ at $\mu = \infty$ (far from the disk), and $\tilde{\Phi}$ is well defined at $\eta = 1$ (on the axis of disk). The solution of equation (5.40) satisfying these boundary conditions can be expressed as,

$$\tilde{\Phi} = \frac{RT}{ZF} \sum_{n=0}^{\infty} \tilde{B}_n P_{2n}(\eta) M_{2n}(\mu) \quad (5.41)$$

where \tilde{B}_n are coefficients to be determined, $P_{2n}(\eta)$ are Legendre polynomials of order $2n$, and $M_{2n}(\mu)$ are Legendre polynomials of an imaginary argument satisfying

$$\frac{d}{d\mu} \left[(1 + \mu^2) \frac{dM_{2n}}{d\mu} \right] = 2n(2n+1)M_{2n} \quad (5.42)$$

with the boundary condition $M_{2n} = 0$ at $\mu = 0$ and $M_{2n} = 0$ at $\mu = \infty$. On the surface of the disk electrode, that is, at $\mu = 0$,

$$\tilde{\Phi}_0 = \frac{RT}{ZF} \sum_{n=0}^{\infty} \tilde{B}_n P_{2n}(\eta) \quad (5.43)$$

The current density at steady state is related to the derivative of the potential just outside the diffusion layer by

$$i = -\kappa_\infty \frac{\partial \Phi}{\partial z} \Big|_{z=0} = -\frac{\kappa_\infty}{r_0 \eta} \frac{\partial \Phi}{\partial \mu} \Big|_{\mu=0} \quad (5.44)$$

In terms of oscillating variables,

$$\tilde{i} = -\kappa_\infty \frac{\partial \tilde{\Phi}}{\partial z} \Big|_{z=0} = -\frac{\kappa_\infty}{r_0 \eta} \frac{\partial \tilde{\Phi}}{\partial \mu} \Big|_{\mu=0} \quad (5.45)$$

or, from equation (5.41),

$$\tilde{i} = \frac{-\kappa_\infty}{r_0 \eta} \frac{RT}{ZF} \sum_{n=0}^{\infty} \tilde{B}_n P_{2n}(\eta) M'_{2n}(0) \quad (5.46)$$

From the properties of the Legendre functions it can be seen that

$$M'_{2n}(0) = -\frac{2}{\pi} \frac{(2^n n!)^4}{[(2n)!]^2} \quad (5.47)$$

The total current density is given by

$$\tilde{i} = \tilde{i}_c + \tilde{i}_f \quad (5.48)$$

where \tilde{i}_c and \tilde{i}_f are the oscillations in capacitive and Faradic currents and

$$\tilde{V} = \tilde{\Phi}_0 + \tilde{\eta}_z + \tilde{\eta}_c \quad (5.49)$$

where \tilde{V} is the oscillation in potential applied to the system.

5.2 Numerical Procedure

The numerical procedure adopted for solving for the current and potential distributions in the frequency domain is discussed in this section. The steps provided in this section were used to obtain distributions for a given frequency, and calculations were repeated over a range of frequencies to provide a spectrum:

1. The steady state distributions for concentration, current, various overpotentials, and other parameters of interest such as A_m , $\theta'_m(0)$ and so on, were calculated using the steady state model without accounting explicitly for the charge distribution. Correction for a finite Sc was used in obtaining these results.
2. The solution to the homogeneous part of the convective diffusion equation was obtained adopting Newman's BAND algorithm for a given set of frequencies. A Simpson's $1/3^{\text{rd}}$ rule in combination with Simpson's $3/8^{\text{th}}$ rule was used to evaluate the integrals involved in equation (5.23) and a value of $\mu = 10.0$ was used to represent the value for ∞ , as the perturbations dissipate at this distance. The accuracy of the solution could be increased using an adaptive integration technique. Use of adaptive integration should be especially important for calculations at high frequencies.

3. Guess values for \tilde{A}_m were introduced. The power series was truncated at $m = 10$.
4. The values for \tilde{c}_0 were calculated from equation (5.15) for a specified number of radial positions r/r_0 . The values of r/r_0 were chosen to be the values of abscissa ranging between 0 and 1 used for the Gauss-Legendre quadrature.
5. The values for $\tilde{\theta}'_m(0)$ were determined from equation (5.23).
6. The \tilde{i}_r distribution was obtained from equation (5.32) using values for \tilde{A}_m and $\tilde{\theta}'_m(0)$.
7. The $\tilde{\eta}_s$ distribution was calculated using equation (5.36).
8. The total current density \tilde{i} was determined from equation (5.48).
9. The \tilde{B}_n coefficients were calculated by expressing \tilde{i} resulting from the above step as a linear combination of Legendre polynomials of η , the rotational elliptic transformation variable, that is,

$$\tilde{i} = \sum_{l=0}^{\infty} \tilde{r}_l P_{2l}(\eta) \quad (5.50)$$

where l is varied from 0 to 10 and \tilde{r}_l are complex coefficients. By making use of the orthogonal properties of Legendre polynomials, \tilde{r}_l coefficients were obtained as

$$\tilde{r}_l = (4l+1) \int_0^1 \tilde{i} P_{2l}(\eta) d\eta \quad (5.51)$$

From equations (5.46) and (5.50)

$$\frac{-\kappa_\infty}{r_0 \eta} \frac{RT}{ZF} \sum_{n=0}^{\infty} \tilde{B}_n P_{2n}(\eta) M'_{2n}(0) = \sum_{l=0}^{\infty} \tilde{r}_l P_{2l}(\eta) \quad (5.52)$$

From equation (5.52)

$$\tilde{B}_n = -\frac{r_0 \eta}{\kappa_\infty RT} \frac{ZF}{M'_{2n}(0)} \tilde{r}_n \quad (5.53)$$

10. From the values of \tilde{B}_n coefficients thus obtained, the $\tilde{\Phi}_0$ values were found from the equation (5.43).

11. The $\tilde{\eta}_c$ distribution was obtained from (5.49).

12. The \tilde{c}_0 distribution was recalculated from equation (5.34). At convergence, the distribution obtained during this step should match with that obtained from step 4.

13. The \tilde{c}_0 distribution resulting from the above step was expressed as a linear combination of Legendre polynomials of η , the rotational elliptic transformation variable, *that is*,

$$\tilde{c}_0 = c_\infty \sum_{l=0}^{\infty} \tilde{a}_l P_{2l}(\eta) \quad (5.54)$$

where l is varied from 0 to 10 and \tilde{a}_l are complex coefficients. By making use of the orthogonal properties of Legendre polynomials, \tilde{a}_l coefficients were obtained as

$$\tilde{a}_l = (4l+1) \int_0^1 (\tilde{c}_0 / c_\infty) P_{2l}(\eta) d\eta \quad (5.55)$$

14. From equations (5.15) and (5.50), a relationship between \tilde{A}_m and \tilde{a}_l was established and a new set of \tilde{A}_m values were obtained.

15. The new set of \tilde{A}_m values were averaged with the \tilde{A}_m values from previous iteration by using a weighting factor.

16. Steps 5 through 15 were repeated until convergence was obtained.

A FORTRAN program used in implementing the frequency domain calculations using this algorithm is presented in Appendix B. Using a 300 MHz Digital Equipment Corporation (DEC)'s Alpha processor (model no. DEC-221164), the CPU time needed to generate a typical spectrum with about 60 frequency points obtained within a tolerance limit of 1 in 10^8 is about 5 minutes. However the calculations can be made faster by compromising on the tolerance limit. An improvement in the integration scheme will result in significant decrease in the time needed to generate the spectrum.

5.3 Results and Discussion

Direct comparison can be made between the one-dimensional and two-dimensional models for a specified condition. Agreement between the two models is expected under conditions for which the current distribution is uniform (slow kinetics or near mass transfer limitation). The one-dimensional model is expected to be inadequate for non-uniform current distributions.

5.3.1 Uniform Current Distribution

From steady state calculations, an *a priori* assessment of the uniformity of current distribution can be obtained from dimensionless parameters

$$J = \frac{i_0 r_0 ZF}{RT\kappa_\infty} \quad (5.56)$$

which provides the relative value of kinetic and ohmic contributions to the system resistance, and

$$N = -\sqrt{\frac{r_0^2 \Omega}{\nu}} \left(\frac{av}{3D} \right)^{1/3} \frac{nZF^2 Dc_\infty}{RT(1-t)\kappa_\infty} \quad (5.57)$$

which provides the relative value of mass transfer and ohmic contributions. The influence of these parameters on the uniformity of distributions can be seen in Figure 8 of [41]. The current distribution is uniform for small values of J and N .

Calculated results are presented in Figure 5.1 for an exchange current density of $3\text{mA}/\text{cm}^2$ and a diffusion coefficient value of $0.3095 \times 10^{-5}\text{cm}^2/\text{sec}$. Other parameters used in these simulations are those corresponding to the values for the reduction of ferricyanide system as reported in chapter 4. Equations (5.56) and (5.57) yield $J = 0.225$ and $N = 0.0695$. From the results presented in Figure 5.1, it can be seen that a significant high frequency loop results due to the kinetic effect. In this case, steady state calculations show that the current distribution has less than 1% variation across the electrode surface.

In this case it is expected that the two-dimensional model that is developed here should be in agreement with the calculations performed for the one-dimensional case. Comparison between the one and two-dimensional models are presented Figure 5.1a and Figure 5.1b. The discrepancy between the two models at high frequencies could be attributed to the numerical instabilities in the two-dimensional model at high frequencies. However, for most part of the frequency spectrum the normalized differences are less than 3%. This result illustrates that one dimensional model is adequate for cases where kinetic effects play a dominant role. Similar agreement between the one and two-dimensional models is seen for larger exchange current densities (larger values of J) as the mass-transfer-limited current density is approached.

5.3.2 Non-Uniform Current Distribution

The one-dimensional model does not provide an adequate representation of the impedance response for a disk electrode below the mass-transfer-limited current for large

exchange current densities. The values for the exchange current densities and the diffusion coefficients used in this section are those required to match the values of experimentally obtained impedance spectra.

A comparison between the two models is presented in Figure 5.2 and Figure 5.3 for a rotation speed of 120rpm, at $i/i_{lim}=0.25$ ($J = 2.25$ and $N = 0.0695$). Even at this low rotation speed, where the steady-state current density at the center of the disk is 97 percent of the average value, considerable disparity is observed between the one-dimensional and two-dimensional models. This is consistent with the observation that even small non-uniformities in the steady-state domain could become significantly important in the frequency domain. The one-dimensional model does not adequately describe the system behavior as reaction kinetics become fast. A similar comparison is presented in Figure 5.4 and Figure 5.5 for 3000rpm at 1/4th of the mass-transfer-limited current ($J = 7.489$ and $N = 0.3552$). The discrepancy is larger due to the increased value of N .

For the same values of J and N as was used in Figure 5.4, the disparity between the two models for a rotation speed of 120rpm was reduced significantly when calculations were obtained at 3/4th of the mass-transfer-limited current, as shown in Figure 5.6 and Figure 5.7. The agreement is observed because the distributions are more uniform near mass-transfer limitation. At 3000 rpm, however, the two models do not agree, even near the mass-transfer-limited current (see Figure 5.8 and Figure 5.9). In this case, $J = 5.617$, and $N = 0.5874$. The discrepancy between the two models can be attributed to the larger value of N . The influence of non-uniformities becomes more significant with an increase in rotation speed.

Another perspective on the two-dimensional character of the disk impedance response at large N can be seen from the radial distributions of the real and imaginary parts of local impedance given in Figure 5.10 for the conditions of Figure 5.6 and Figure 5.8. The distributions are shown for dimensionless frequencies of 1 and 2.8. The increased non-uniformity of the local impedance at 3000rpm results in the discrepancy seen between the one and two-dimensional models.

A surprising result of the work presented by Orazem *et al.* [55] was that the one-dimensional model of Tribollet and Newman for impedance of a rotating disk fit the data to within the noise level of the measurement, even for conditions where the present work would indicate that a two-dimensional model would be required. Their result can be explained by regressing the one-dimensional model to impedance spectra calculated using the two-dimensional model presented in the present work. The results of the regression are presented in Figure 5.11 for the 120rpm, $3/4^{\text{th}}$ of mass transfer limited current comparison shown in Figure 5.6. The quality of the fit is extremely good with residual sum of square to noise ratio of about 2.0. The quality of the fit is such that it would be difficult to use regression to experimental data to distinguish between the two-dimensional and one-dimensional models. The principal difference between the two models is that the one-dimensional model provided a Schmidt number 7 percent higher (1780 as opposed to 1660 for the two-dimensional model). Results from the one-dimensional model regression for the two dimensional model calculations for 3000rpm, $3/4^{\text{th}}$ of the mass-transfer-limited current are presented in Figure 5.12. In this case the one-dimensional model provided a Schmidt number 22 percent higher (1530 as opposed to 1250 for the two dimensional model). Similar results were obtained for other cases

Similar analysis was performed for the impedance spectra generated using the two-dimensional model for a Schmidt number of 1100 and for an exchange current value of 50mA/cm^2 for various rotation rates and for various fractions of mass-transfer limited current. Regressions were done using a no weighting strategy. The Schmidt number values obtained through this analysis are presented in table 5.1. The value of the parameter J is constant as the exchange current density value is fixed for generating these values.

The kinetic effects are more prominent in the high frequency region, and the two-dimensional model results presented in this work encountered numerical instabilities at very high frequencies. This could be a reason for the disagreement between the two models for the charge transfer resistance. The problem of numerical instabilities at very high frequencies could be addressed by using adaptive integration schemes for calculating the integrals involved. The present work illustrates that a good fit for the one-dimensional model does not imply that the model is adequate to describe the physics of the system. Due importance should be attached to the role of non-uniform current distributions for the assessment of electrochemical impedance data for cases where J and N are large.

5.4 Conclusions

A two-dimensional mathematical model for the impedance response of a disk electrode was developed on the basis of the coupling among the convective diffusion in a thin diffusion layer, the Laplace's equation for potential in an outer region, and the Butler-Volmer expression for the electrode kinetics. The influence of a finite Schmidt number, which is critical in the frequency domain, was taken into account by including three terms in the axial and radial velocity expansions. A uniform distribution of capacitance was

assumed in the development of the model, and this assumption was supported by experimental observations reported in the literature for ring-disk measurements [67] and by preliminary calculations presented in chapter 4. Reliable results were obtained for dimensionless frequencies less than 1000. Use of improved integration strategies could extend the frequency range.

The non-uniform current distribution observed below the mass-transfer-limited current has a significant effect on the impedance response of a rotating disk electrode when electrode kinetics are fast. One-dimensional models apply when kinetic or mass transfer limitations make the current distribution more uniform. Discrepancies between the one and two-dimensional models were observed under conditions where the steady-state current density at the center of the disk was 97 percent or less of the average value.

Under conditions yielding a non-uniform current distribution, the one-dimensional model may provide an adequate fit to the data, but the physical parameters obtained by regression will be incorrect. In such cases, non-uniform current distributions should be taken into account. The effect of non-uniform current distributions on impedance was seen at 120rpm and is even greater at larger rotation speeds.

Table 5.1. One-dimensional frequency domain process model regressions for the two-dimensional model calculations for a Sc value of 1100 and for an exchange current density of 50mA/cm^2 . Dimensionless parameter $J = 3.7445$.

	N	$Z(w=0, \Omega)$	Sc	$C (\mu\text{F})$	R_e, Ω	R_s, Ω	NRSSQ
120, 5% i_{lim}	0.1276	69.47 ± 0.03	1122 ± 3	7.10 ± 0.15	6.29 ± 0.03	2.71 ± 0.03	2.2257
10% i_{lim}	0.1276	73.42 ± 0.03	1125 ± 3	7.08 ± 0.14	6.28 ± 0.03	2.86 ± 0.03	2.2629
25% i_{lim}	0.1276	89.71 ± 0.04	1134 ± 3	7.02 ± 0.11	6.28 ± 0.03	3.45 ± 0.02	2.3953
50% i_{lim}	0.1276	139.58 ± 0.08	1151 ± 4	9.15 ± 1.34	7.04 ± 0.39	4.47 ± 0.37	2.8841
75% i_{lim}	0.1276	301.69 ± 0.20	1166 ± 4	8.29 ± 0.89	7.32 ± 0.62	9.44 ± 0.55	3.2026
90% i_{lim}	0.1276	909.22 ± 0.50	1171 ± 4	6.91 ± 0.03	6.29 ± 0.06	25.73 ± 0.04	3.1211
95% i_{lim}	0.1276	2281.4 ± 1.25	1168 ± 4	6.89 ± 0.01	6.25 ± 0.03	49.44 ± 0.13	3.0585
96% i_{lim}	0.1276	3109.8 ± 1.75	1165 ± 4	6.89 ± 0.02	6.24 ± 0.05	60.00 ± 0.22	3.0046
600, 25% i_{lim}	0.2854	40.67 ± 0.04	1147 ± 3	9.66 ± 3.94	6.87 ± 0.74	2.86 ± 0.71	2.1774
50% i_{lim}	0.2854	65.16 ± 0.06	1179 ± 3	7.51 ± 2.28	6.47 ± 0.94	4.96 ± 0.90	2.5536
75% i_{lim}	0.2854	151.39 ± 0.13	1209 ± 4	7.03 ± 0.76	6.35 ± 0.66	10.17 ± 0.58	2.9478
90% i_{lim}	0.2854	520.67 ± 0.32	1211 ± 4	6.91 ± 0.06	6.29 ± 0.11	24.38 ± 0.06	2.9705
1200, 25% i_{lim}	0.4036	29.15 ± 0.02	1157 ± 3	7.40 ± 1.02	6.37 ± 0.26	3.34 ± 0.25	1.9813
50% i_{lim}	0.4036	47.59 ± 0.04	1200 ± 3	6.47 ± 1.08	6.04 ± 0.52	5.35 ± 0.50	2.4255
75% i_{lim}	0.4036	115.91 ± 0.14	1240 ± 4	5.61 ± 0.99	4.87 ± 1.23	11.37 ± 1.12	2.7498
2400, 25% i_{lim}	0.5708	20.92 ± 0.02	1169 ± 3	5.73 ± 1.24	5.85 ± 0.48	3.83 ± 0.46	1.7698
50% i_{lim}	0.5708	35.19 ± 0.04	1228 ± 4	3.84 ± 1.16	4.15 ± 1.25	7.13 ± 1.21	2.1352
75% i_{lim}	0.5708	89.91 ± 0.08	1265 ± 5	8.49 ± 0.13	7.6 (fixed)	8.74 ± 0.04	2.855
3000, 25% i_{lim}	0.6382	18.79 ± 0.01	1168 ± 3	15.13 ± 0.24	7.6 (fixed)	2.15 ± 0.01	2.0504
50% i_{lim}	0.6382	31.95 ± 0.04	1237 ± 4	4.16 ± 0.98	4.51 ± 0.92	6.75 ± 0.89	2.087
75% i_{lim}	0.6382	83.61 ± 0.08	1275 ± 5	8.43 ± 0.14	7.6 (fixed)	8.67 ± 0.05	2.7159

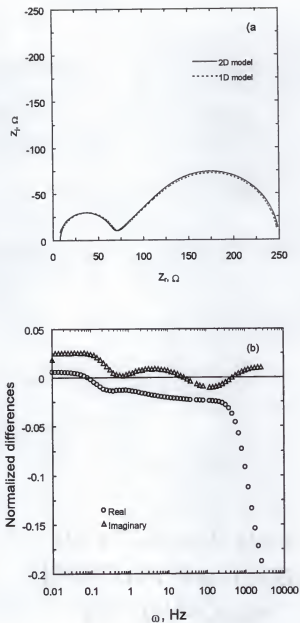


Figure 5.1(a) Comparison between one-dimensional and two-dimensional models for the slow kinetics case at 1/4th of i_{lim} and $\Omega = 120\text{rpm}$ with $i_0 = 3 \text{ mA/cm}^2$, $D = 0.3095 \times 10^{-5} \text{ cm}^2/\text{sec}$, $J = 0.225$, $N = 0.0695$, and $Sc = 2730$. In this case steady-state distributions tend to be highly uniform. (b) Differences between the calculations from two-dimensional and one-dimensional model normalized with respect to the two-dimensional model as a function of frequency.

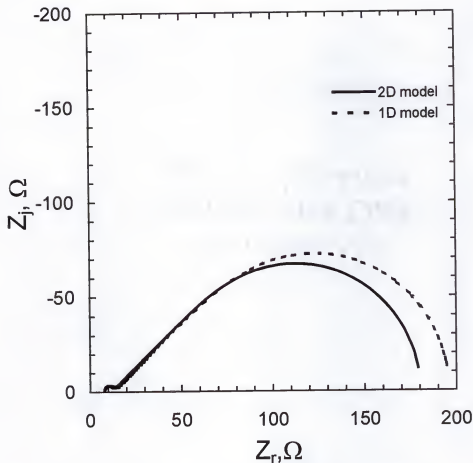


Figure 5.2. Comparison between the impedance spectra generated by 1D and 2D models for 120rpm, $1/4^{th}$ of i_{lim} , $i_0 = 30 \text{ mA/cm}^2$, $D = 0.3095 \times 10^{-5} \text{ cm}^2/\text{sec}$, $J = 2.247$, $N = 0.0695$, and $Sc = 2730$. Results presented for impedance plane plot.

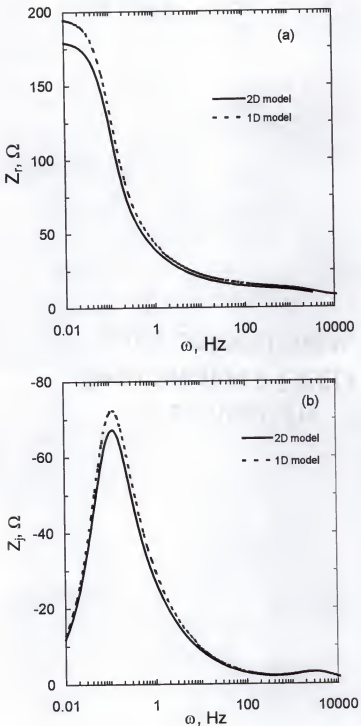


Figure 5.3. Comparison between the impedance spectra generated by 1D and 2D models for 120rpm, $1/4^{\text{th}}$ of i_{lim} , $i_0 = 30 \text{ mA/cm}^2$, $D = 0.3095 \times 10^{-5} \text{ cm}^2/\text{sec}$, $J = 2.247$, $N = 0.0695$, and $Sc = 2730$ (corresponds to Figure 5.2). Results presented for (a) real part as a function of frequency (b) imaginary part as a function of frequency.

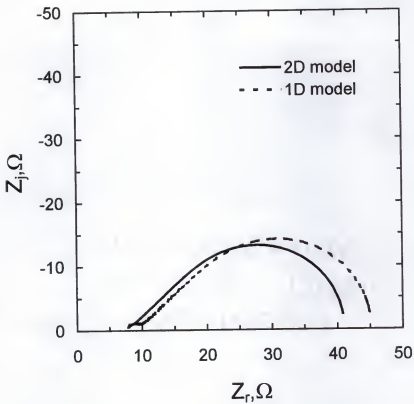


Figure 5.4. Comparison between the impedance spectra generated by 1D and 2D model for 3000rpm, $1/4^{\text{th}}$ of i_{lim} , $i_0 = 100 \text{ mA/cm}^2$, $D = 0.3195 \times 10^{-5} \text{ cm}^2/\text{sec}$, $J = 7.489$, $N = 0.3552$, and $Sc = 2650$.

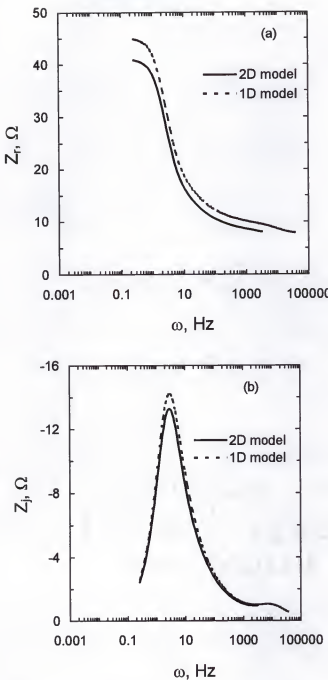


Figure 5.5. Comparison between the impedance spectra generated by 1D and 2D model for 3000rpm, $1/4^{\text{th}}$ of i_{lim} , $i_0 = 100 \text{ mA/cm}^2$, $D = 0.3195 \times 10^{-5} \text{ cm}^2/\text{sec}$, $J = 7.489$, $N = 0.3552$, and $Sc = 2650$ (corresponds to Figure 5.4). Results presented for (a) real part as a function of frequency (b) imaginary part as a function of frequency.

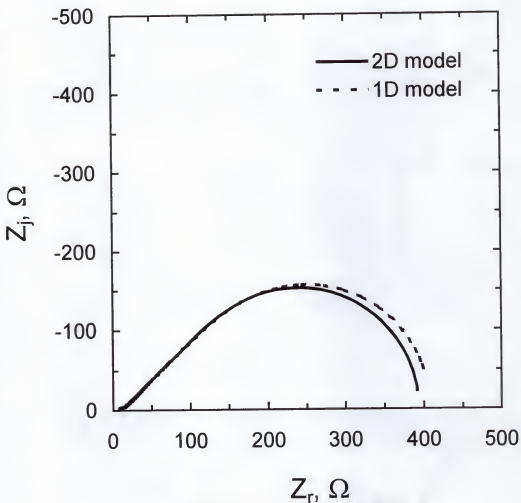


Figure 5.6. Comparison between the impedance spectra generated by 1D and 2D model for 120rpm, $3/4^{th}$ of i_{lim} , $i_0 = 100$ mA/cm 2 , $D = 0.5095 \times 10^{-5}$ cm 2 /sec, $J = 7.489$, $N = 0.0970$, and Sc = 1660. Results presented for impedance plane plot.

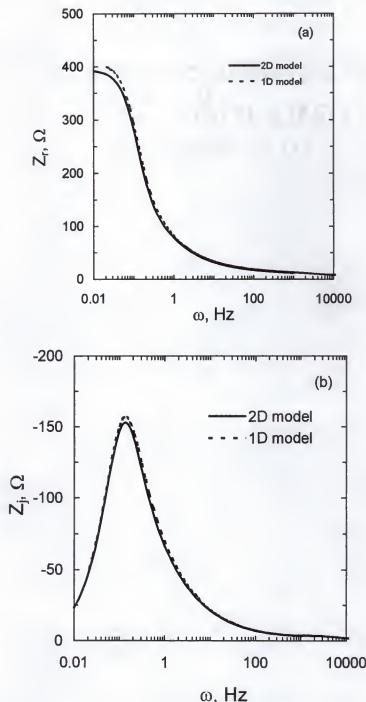


Figure 5.7. Comparison between the impedance spectra generated by 1D and 2D model for 120rpm, $3/4^{th}$ of i_{lim} , $i_0 = 100$ mA/cm 2 , $D = 0.5095 \times 10^{-5}$ cm 2 /sec, $J = 7.489$, $N = 0.0970$, and $Sc = 1660$ (corresponds to Figure 5.6). Results presented for (a) real part as a function of frequency (b) imaginary part as a function of frequency.

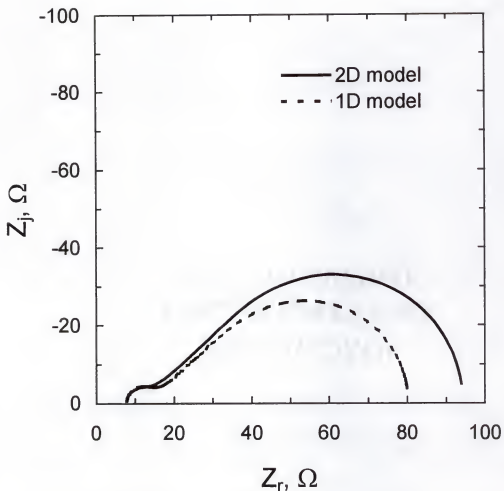


Figure 5.8. Comparison between the impedance spectra generated by 1D and 2D model for 3000rpm, $3/4^{\text{th}}$ of i_{lim} , $i_0 = 75\text{mA/cm}^2$, $D = 0.6795 \times 10^{-5}\text{ cm}^2/\text{sec}$, $J = 5.617$, $N = 0.5874$, and $\text{Sc} = 1250$. Results presented for impedance plane plot.

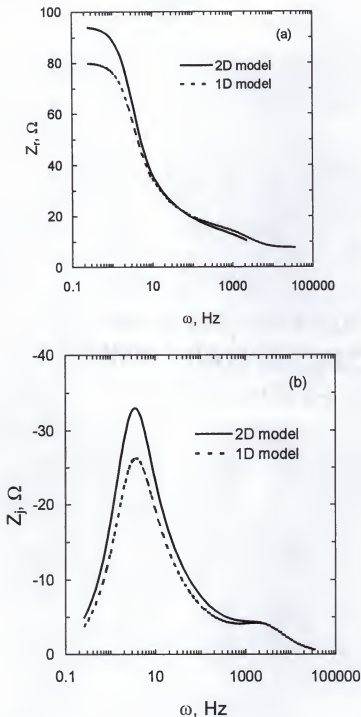


Figure 5.9. Comparison between the impedance spectra generated by 1D and 2D model for 3000rpm, $3/4^{\text{th}}$ of i_{lim} , $i_0 = 75 \text{ mA/cm}^2$, $D = 0.6795 \times 10^{-5} \text{ cm}^2/\text{sec}$, $J = 5.617$, $N = 0.5874$, and $\text{Sc} = 1250$ (corresponds to the condition of Figure 5.8). Results presented for (a) real part as a function of frequency (b) imaginary part as a function of frequency.

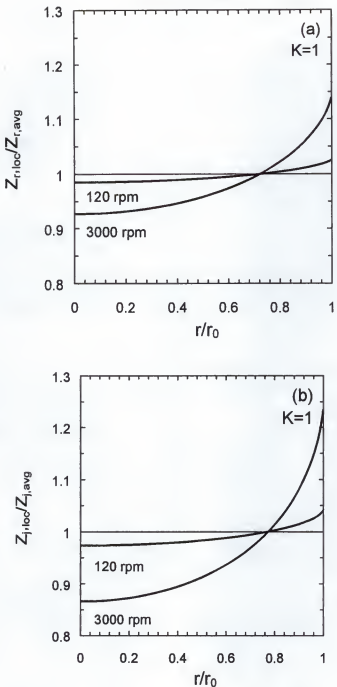


Figure 5.10. Distributions for local impedance values for a dimensionless frequencies of $K=1$ and $K=2.8$. The parameter values are those given in Figure 5.6 and Figure 5.8.

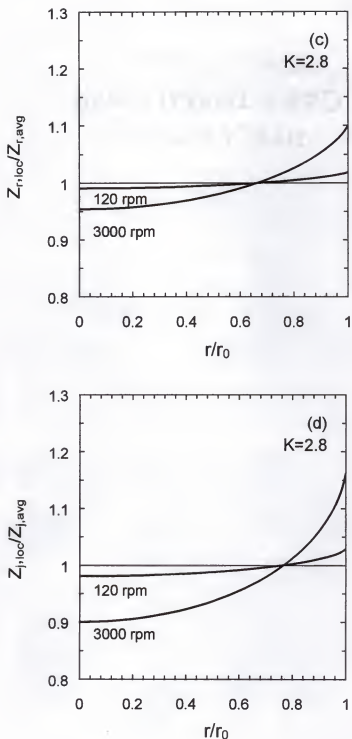


Figure 5.10-- continued

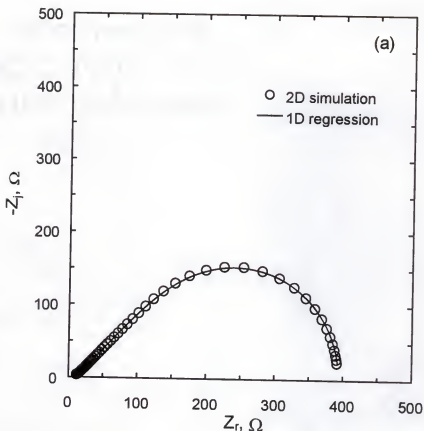


Figure 5.11. Results for regression of the 1D model to a 2D model simulation for 120rpm, $3/4^{\text{th}}$ of i_{lim} . An input value of $Sc = 1660$ for 2D model resulted in a regressed Sc of 1780 for the 1D model case. (a) complex plane plot (b) real impedance as a function of frequency (c) imaginary impedance as a function of frequency

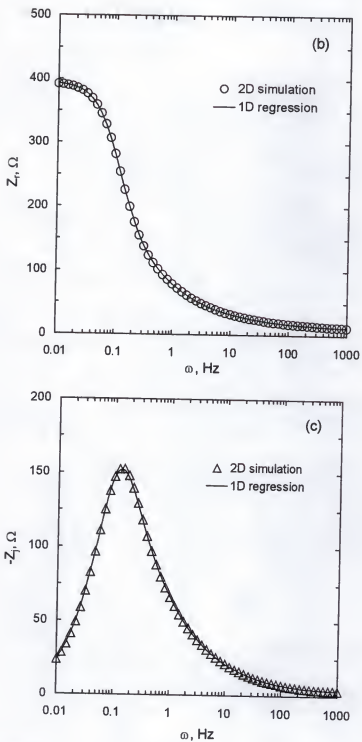


Figure 5.11-- continued

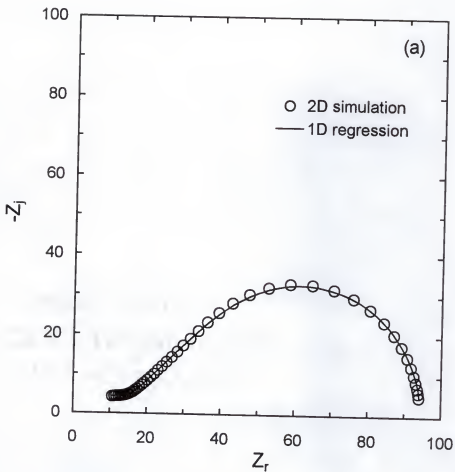


Figure 5.12. Results for regression of the 1D model to a 2D model simulation for 3000rpm, $3/4^{\text{th}}$ of i_{lim} . An input value of $Sc = 1250$ for 2D model resulted in a regressed Sc of 1530 for the 1D model case. (a) complex plane plot (b) real impedance as a function of frequency (c) imaginary impedance as a function of frequency

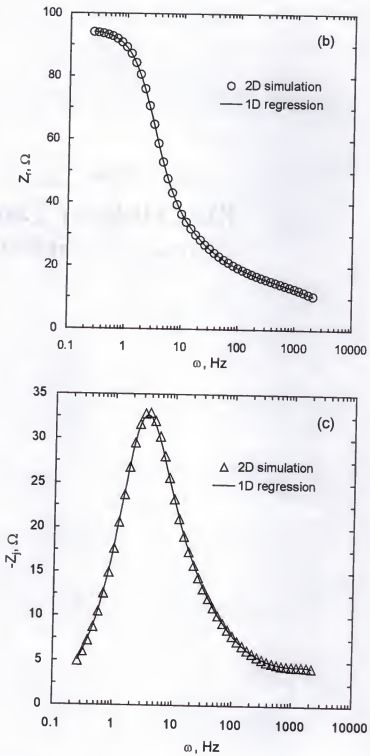


Figure 5.12—continued.

CHAPTER 6
CHEBYSHEV POLYNOMIAL SOLUTION FOR THE STEADY STATE
CONVECTIVE DIFFUSION FOR A ROTATING DISC ELECTRODE

In this chapter, the applicability of the Chebyshev polynomials in solving differential equations is illustrated in the case of convective diffusion equation for the rotating disc electrode system for the infinite Schmidt number assumption. A comparison is drawn here between the solution obtained by this approach and that from a finite difference scheme. It is shown that the Chebyshev polynomial approximation provides results with good accuracy and fewer calculations.

Chebyshev polynomials are the solutions of the differential equation

$$\sqrt{1-x^2} \frac{d}{dx} \left[\sqrt{1-x^2} \frac{dT_n}{dx} \right] + n^2 T_n = 0 \quad (6.1)$$

where $T_n(x)$ is a Chebyshev polynomial in x of n th degree given by

$$T_n(x) = \cos [n \arccos x] \quad (6.2)$$

and x varies between -1 and +1, as the value of arccos is defined for arguments with absolute value of less than 1. Chebyshev polynomials of various orders as functions of x are shown in Figure 6.1. Let $x = \cos \theta$. Then equation (6.2) can be written as

$$T_n(\cos \theta) = \cos n\theta \quad (6.3)$$

Thus,

$$T_0(x) = 1, T_1(x) = x, T_2(x) = 2x^2 - 1, T_3(x) = 4x^3 - 3x, T_4(x) = 8x^4 - 8x^2 + 1, \dots \quad (6.4)$$

One of the most important properties of Chebyshev polynomials is that they satisfy the orthogonality relation

$$\int_{-1}^1 T_n(x)T_m(x)(1-x^2)^{-1/2} dx = \frac{\pi}{2} c_n \delta_{nm} \quad (6.5)$$

where $c_0=2$, $c_n=1$ for $n>0$, and δ_{nm} is the Dirac delta function given by

$$\delta_{nm} = \begin{cases} 1 & \text{if } n = m \\ 0 & \text{if } n \neq m \end{cases} \quad (6.6)$$

Extensive use was made of the orthogonal property of Legendre polynomials in the steady state and frequency domain modeling (see chapters 4 and 5). These polynomials were used in approximating various distributions across the electrode surface. In this chapter the use of the orthogonal property of Chebyshev polynomials is illustrated.

The use of Chebyshev polynomials in the series approximation of various analytic functions is well established. The particular method of solution using Chebyshev polynomials described in this work is also known as the tau method, initially devised by Lanczos [73]. The procedure used for this work is a variation of this original method [74]. In the remaining part of this section a more detailed discussion on the use of various solution techniques is provided.

The tau method in turn belongs to the class of spectral methods [75]. Other than the tau method, spectral methods consist of Galerkin and collocation methods. In all these methods the solution to the differential equation of interest is approximated by a linear combination of globally smooth functions. This is the most important distinction of these methods in comparison with finite difference and finite element methods. In finite difference and finite element schemes the basis functions are local in nature. Very often it

is convenient to choose the basis functions for spectral methods to be orthogonal functions so that the orthogonal property can be exploited in the solution process. Hence the choice of basis functions in the tau method is not restricted to Chebyshev polynomials. Other family of orthogonal functions such as Legendre polynomials, Fourier series, and Laguerre series can also be used.

Spectral method can be viewed to be a development of the method of weighted residuals (MWR) [76]. The key elements of the MWR are the trial functions (basis functions used for approximating the solution) and the test functions (also known as weight functions). The test functions are used to enforce the minimization of the residual. The choice of weighting function distinguishes Galerkin, collocation, and tau methods. In the Galerkin approach, the test functions and the trial functions are the same. In the method of collocation, the test functions are the Dirac delta functions. To state it more explicitly, in case of the Galerkin methods, the governing differential equation is valid through the whole domain in an averaged sense where as in case of the collocation techniques, the differential equation should be satisfied exactly at the collocation points. Tau methods are closer to Galerkin methods but they differ in the treatment of the boundary conditions. The tau approach is the most difficult to rationalize within the context of the MWR.

Clenshaw proposed the use of Chebyshev polynomials in the solution of linear differential equations [77]. In this work he provided various examples for solving first and second order linear equations and an eigenvalue problem by using Chebyshev polynomial approach. Later Clenshaw and Norton extended the Chebyshev series approximation to a broader class of boundary value problems [78], by using the Picard iteration scheme [79].

This allowed them to solve linear differential equations with non-polynomial coefficients as well as nonlinear differential equations.

6.1 Transformation of the Convective Diffusion Equation

To provide a clear understanding of the solution process of differential equations with the use of spectral Chebyshev techniques, Johnson treated ordinary differential equations with constant coefficients and documented the approach in a detailed manner [80]. In case of many engineering problems, the governing equations contain variable coefficients. In order to demonstrate the applicability of Chebyshev polynomials in such cases, the steady state convective diffusion equation in two dimensions for a rotating disk electrode is considered in this chapter. The solution to convective diffusion is important in case of several electrochemical systems with forced convection where the goal is to calculate the current distribution. There are very efficient finite difference codes with excellent convergence, such as the BAND algorithm developed by Newman, to address the boundary value problems [20]. For problems of the nature considered in this work, the Chebyshev polynomial approximation has a much faster convergence compared to the traditional finite difference methods. This feature is of great use in problems where the boundary value problems need to be solved for a number of times. An example is the non-uniform current distribution calculations on rotating disk electrode in the frequency domain shown in chapter 5, where the homogeneous part of the convective diffusion needs to be solved for a number of frequencies.

In the Chebyshev spectral tau method, the solution to the differential equation is written as a summation of Chebyshev polynomials multiplied by unknown weighting

coefficients which need to be determined. This summation is also assumed to satisfy the boundary conditions. (This is an important difference between the tau method and the Galerkin method. In the Galerkin approach each of the basis functions must satisfy the boundary conditions whereas in the tau approach it is sufficient if the approximated function satisfies the boundary conditions.) The unknown coefficients are determined using the orthogonality of the Chebyshev polynomials.

The convective diffusion for the rotating disk electrode is given by

$$v_r \frac{\partial c}{\partial r} + v_z \frac{\partial c}{\partial z} = D \frac{\partial^2 c}{\partial z^2} \quad (6.7)$$

where v_r and v_z are the radial and axial velocity components, r and z are the radial and axial components. A scaled axial distance is defined to be

$$\zeta = z \left(\frac{a \nu}{3D} \right)^{1/3} \sqrt{\frac{\Omega}{\nu}} \quad (6.8)$$

The concentration in the diffusion layer can be expressed as a series solution

$$c_0 = c_\infty \left[1 + \sum_{m=0}^{\infty} A_m (r / r_0)^{2m} \theta_m(\zeta) \right] \quad (6.9)$$

where c_0 is the concentration of the reactant on the electrode surface, A_m are constant coefficients, $\theta_m(\zeta)$ are the axial dependent terms in the concentration series. Using this expression in equation (6.7) the axial dependence can be separated as

$$\theta_m'' + 3\zeta^2 \theta_m' - 6m\zeta \theta_m = 0 \quad (6.10)$$

Primes in the superscripts of equation (6.10) refer to the derivatives with respect to ζ . The boundary conditions for this equation are given by $\theta_m = 1$ at $\zeta = 0$ and $\theta_m' = 0$ at

$\zeta \rightarrow \infty$. For the purpose of numerical calculations, as shown in chapter 4, $\zeta = 20$ can be used instead of $\zeta \rightarrow \infty$. Hence the boundary conditions transform to

$$\theta_m = 1 \text{ at } \zeta = 0 \text{ and } \theta_m = 0 \text{ at } \zeta = 20 \quad (6.11)$$

The domain of interest is $\zeta \in [0, 20]$. In order to apply the Chebyshev polynomial approximation, this domain should be transformed to $[-1, 1]$. Hence, a linear transformation

$$x = 0.1\zeta - 1 \quad (6.12)$$

is applied to the system of interest, where x is the transformed variable. $\theta_m(\zeta)$ is transformed to $y(x)$. The convective diffusion equation in terms of x and y is given by

$$0.01y'' + 30(x+1)^2 y' - 60m(x+1)y = 0 \quad (6.13)$$

or

$$0.01y'' + 30x^2 y' + 60xy' + 30y' - 60m(x+1)y = 0 \quad (6.14)$$

and the boundary conditions are given by

$$x(-1) = 1 \text{ and } x(1) = 0 \quad (6.15)$$

The domain of integration as well as the governing differential equation is transformed to fit into the domain of interest. At this stage series approximations in terms of Chebyshev polynomials are introduced for various terms involved in equation (6.14).

6.1.1 Series Approximations

Let

$$y = \sum_{n=0}^{\infty} a_n T_n(x) \quad (6.16a)$$

where a_n represents the associated weighting factor which needs to be determined. Other terms resulting from (6.14) can also be expressed as summations of Chebyshev polynomials as given below.

$$y' = \sum_{n=0}^{\infty} a_n^{(1)} T_n(x) \quad (6.16b)$$

$$y'' = \sum_{n=0}^{\infty} a_n^{(2)} T_n(x) \quad (6.16c)$$

$$x^2 y' = \sum_{n=0}^{\infty} b_n T_n(x) \quad (6.16d)$$

$$xy' = \sum_{n=0}^{\infty} e_n T_n(x) \quad (6.16e)$$

$$xy = \sum_{n=0}^{\infty} f_n T_n(x) \quad (6.16f)$$

The coefficients $a_n^{(1)}$, $a_n^{(2)}$, b_n , d_n , and e_n need to be expressed in terms of a_n . These relations can be obtained in a recursive fashion and the formulae for the above mentioned functions are provided in literature [75]. In order to validate the expressions provided in this reference, these recursion relations were rederived and the relation provided for $x^2 y'$ was found to be incorrect. These relations are provided in the following set of equations including the one corrected for $x^2 y'$.

$$c_n a_n^{(1)} = 2 \sum_{\substack{p=n+1 \\ p+n \text{ odd}}}^{\infty} p a_p \quad (6.17a)$$

$$c_n a_n^{(2)} = 2 \sum_{\substack{p=n+2 \\ p+n \text{ even}}}^{\infty} p(p^2 - n^2) a_p \quad (6.17b)$$

$$c_n b_n = \frac{1}{2} \left[(n-1)a_{n-1} + (n+1)(1+c_n+d_n)a_{n+1} + 4 \sum_{\substack{p=n+3 \\ p \text{ odd}}}^{\infty} pa_p \right] \quad (6.17c)$$

$$c_n e_n = na_n + 2 \sum_{\substack{p=n+2 \\ p \text{ even}}}^{\infty} pa_p \quad (6.17d)$$

$$c_n f_n = \frac{1}{2} (c_{n-1} a_{n-1} + a_{n+1}) \quad (6.17e)$$

where $c_n=0$ ($n<0$), $c_0=2$, $c_n=1$ ($n>0$), $d_n=0$ ($n<0$), $d_0=-1$, and $d_n=1$ ($n>0$). As an illustration, the derivation of the recursion relation for x^2y' is provided in the next subsection.

6.1.2 Recursion Relation for x^2y'

The key to deriving the recursion relations depends upon identifying the equivalent trigonometric function for the term that is under consideration. Since

$$x = \cos \theta \quad (6.18)$$

x can be substituted by $\cos \theta$. Also, since

$$y = \sum_{n=0}^{\infty} a_n T_n(x) \text{ and } T_n(x) = \cos n\theta \quad (6.19)$$

The derivative of $T_n(x)$ with respect to x yields

$$T'_n(x) = \frac{n \sin n\theta}{\sin \theta} \quad (6.20)$$

Similarly, obtaining the derivatives of $T_n(x)$ and $T_m(x)$, and application of the principles of trigonometry yields

$$T_n(x) = \frac{1}{2} \left[\frac{T'_{n+1}(x)}{n+1} - \frac{T'_{n-1}(x)}{n-1} \right] \quad (6.21)$$

and

$$\begin{aligned} x^2 y &= \sum_{n=1}^{\infty} a_n x^2 T'_n(x) \\ &= \sum_{n=1}^{\infty} a_n \cos^2 \theta \frac{n \sin n\theta}{\sin \theta} \end{aligned} \quad (6.22)$$

where

$$\cos^2 \theta \frac{\sin n\theta}{\sin \theta} = \frac{1}{4} \left[\frac{\sin(n+2)\theta}{\sin \theta} + \frac{2 \sin n\theta}{\sin \theta} + \frac{\sin(n-2)\theta}{\sin \theta} \right] \quad (6.23)$$

Hence from equation (6.20)

$$x^2 T'_n(x) = \frac{n}{4} \left[\frac{T'_{n+2}(x)}{n+2} + \frac{2T'_n(x)}{n} + \frac{T'_{n-2}(x)}{n-2} \right] \quad (6.24)$$

However, since $y = \sum_{n=0}^{\infty} a_n T_n(x)$

$$\begin{aligned} x^2 y' &= \sum_{n=0}^{\infty} b_n T_n(x) \\ &= \sum_{n=1}^{\infty} a_n x^2 T'_n(x) \\ &= \sum_{n=1}^{\infty} \frac{n a_n}{4} \left[\frac{T'_{n+2}(x)}{n+2} + \frac{2T'_n(x)}{n} + \frac{T'_{n-2}(x)}{n-2} \right] \end{aligned} \quad (6.25)$$

From equations (6.21) and (6.25)

$$\sum_{n=0}^{\infty} b_n \left[\frac{T'_{n+1}(x)}{n+1} - \frac{T'_{n-1}(x)}{n-1} \right] = \sum_{n=1}^{\infty} \frac{n a_n}{4} \left[\frac{T'_{n+2}(x)}{n+2} + \frac{2T'_n(x)}{n} + \frac{T'_{n-2}(x)}{n-2} \right] \quad (6.26)$$

It should be noted that $T'_{-m}(x) = T'_m(x)$ and $\lim_{m \rightarrow 0} \frac{T'_m(x)}{m} = \lim_{m \rightarrow 0} \frac{\sin m\theta}{\sin \theta} = 0$.

Expansion of these series and regrouping various terms multiplying various $T'_m(x)$ terms and simplifying yields equation (6.17c).

6.1.3 Substitution into the Convective Diffusion Equation

Substitution of equations (6.16) into the convective diffusion equation given by (6.13) yields

$$\left\{ \begin{array}{l} 0.01 \sum_{n=0}^{\infty} a_n^{(2)} T_n(x) + 30 \sum_{n=0}^{\infty} b_n T_n(x) + 60 \sum_{n=0}^{\infty} e_n T_n(x) \\ + 30 \sum_{n=0}^{\infty} a_n^{(1)} T_n(x) - 60m \sum_{n=0}^{\infty} f_n T_n(x) - 60m \sum_{n=0}^{\infty} a_n T_n(x) \end{array} \right\} = 0 \quad (6.27)$$

In a practical situation the series has to be truncated to a finite number of terms. Hence, if y is being estimated by a truncated Chebyshev polynomial series with the highest power of value N (an N^{th} degree polynomial), then y'' can be estimated only by a polynomial of degree $N-2$. An algebraic relationship for the unknown coefficients is obtained from the inner product of $T_n(x)$ and $T_p(x)$ where $T_p(x)$ is defined in accordance with equation (6.5).

$$\langle T_n(x), T_p(x) \rangle = \frac{2}{\pi c_n} \int_{-1}^1 T_n(x) T_p(x) (1-x^2)^{-1/2} dx = \delta_{np} \quad (6.28)$$

where $\delta_{np} = 1$ where $n = p$ and is zero when $n \neq p$.

By taking the inner product of equation (6.27) with respect to $T_p(x)$

$$0.01a_n^{(2)} + 30b_n + 60e_n + 30a_n^{(1)} - 60m(f_n + a_n) = 0 \quad (6.29)$$

where $n = 0, 1, 2, \dots, n-3, n-2$. The inner product is taken only for n varying from 0 to $n-2$. If y is an n^{th} degree polynomial, then y'' is of degree $n-2$.

Coefficients $a_n^{(1)}, a_n^{(2)}, b_n, e_n$, and f_n can be expressed in terms of a_n through the recursive relations (6.17), yielding $n-1$ equations. However, there are $n+1$ unknowns (a_0 to a_n) to be determined. The two additional equations can be obtained from the boundary

conditions $x(-1) = 1$ and $x(1) = 0$. This method of writing the solution as a series even at the boundary is known as the Tau method. This is different from the Galerkin method in the sense that the basis functions $T_n(x)$ are not individually required to satisfy the boundary conditions. Hence,

$$\sum_{n=0}^N a_n T_n(-1) = 1 \quad (6.30a)$$

$$\sum_{n=0}^N a_n T_n(1) = 0 \quad (6.30b)$$

From the properties of Chebyshev polynomials, $T_n(-1) = (-1)^n$ and $T_n(1) = 1$. Hence from (6.30a) and (6.30b)

$$\sum_{n=0}^N a_n (-1)^n = 1 \quad (6.31a)$$

$$\sum_{n=0}^N a_n = 0 \quad (6.31b)$$

6.1.4 Non Homogeneous Equations

The differential equation considered for this work was homogeneous. Non homogeneous equations can also be solved by the use of Chebyshev polynomials. The added term can be expressed as a linear combination of Chebyshev polynomials. For example

$$1 = T_0(x) \quad (6.32a)$$

$$x = T_1(x) \quad (6.32b)$$

$$x^2 = \frac{1}{2} [T_2(x) + T_0(x)] \quad (6.32c)$$

$$x^3 = \frac{1}{4} [T_3(x) + 3T_1(x)] \quad (6.32d)$$

$$x^4 = \frac{1}{8} [T_4(x) + 4T_2(x) + 3T_0(x)] \quad (6.32e)$$

and so on. After this inner products can be taken on the right hand side also.

6.2 Results and Discussion

Equations (6.29), (6.31a), and (6.31b) need to be solved for simultaneously to obtain a_n coefficients and hence the solution. For the purpose of the present study, the convective diffusion is solved for using the Chebyshev polynomial expansions as well as a finite difference scheme with varying step sizes for the case of infinite Schmidt numbers. A comparison is made in order to emphasize the superiority of the Chebyshev polynomial approximation over the finite difference scheme in case of the present problem. The parameter that is of practical importance is $\theta'_m(0)$ as this signifies the rate of mass transport. This is the parameter that is obtained for this comparative study. The values of this parameter for $m=0$, 5, and 10 are presented in Table 6.1, Table 6.2, & Table 6.3 respectively. As it can be seen from these results, the convergence is much faster in case of Chebyshev polynomials.

From this it was observed that the convergence is much faster by the application of Chebyshev polynomials. One drawback of this approach is that the convergence criteria for this approach is not well established. When higher order cross product terms such as x^3y^n are involved the resulting algebraic equations are ill conditioned in nature which results in lack of accuracy of the solution. This problem was encountered when the approach was applied to solving the convective diffusion equation accounting for finite

Schmidt number. However by choosing an efficient numerical scheme for the solution of the linear system of equations that results from this approach, this method can be used even for complicated linear differential equations.

6.3 Conclusions

The applicability of Chebyshev polynomials in solving the steady state convective diffusion equation for a rotating disc electrode was illustrated. For the problem that was considered in this work, the convergence obtained by using Chebyshev approximation is found to be very fast in comparison with that from the finite difference scheme.

Table 6.1. Comparison between the Chebyshev approximation and the FDM scheme for $m = 0$ in the convective diffusion equation. Value of $\theta'_m(0)$ obtained by extrapolation to a step size of zero value is -1.119846522021

No. of terms in Chebyshev approx.	Value of $\theta'_m(0)$	No. of nodes in FDM scheme	Value of $\theta'_m(0)$
11	-1.03094588111193	101	-1.13553825010888
26	-1.11909234991382	1001	-1.11988421505475
51	-1.11984784688562	1251	-1.11986892628523
101	-1.11984652169427	2501	-1.11985126312467
151	-1.11984652172219	5001	-1.11984759958694
201	-1.11984652172219	10001	-1.11984677775223

Table 6.2. Comparison between the Chebyshev approximation and the FDM scheme for $m = 5$ in the convective diffusion equation. Value of $\theta'_m(0)$ obtained by extrapolation to a step size of zero value is -2.340450747254

No. of terms in Chebyshev approx.	Value of $\theta'_m(0)$	No. of nodes in FDM scheme	Value of $\theta'_m(0)$
11	-2.09070385994810	101	-2.57827669933820
26	-2.34308047335845	1001	-2.34499997552230
51	-2.34045102991164	1251	-2.34339455441446
101	-2.34045075950235	2501	-2.34120286825501
151	-2.34045075950242	5001	-2.34064080790497
201	-2.34045075950242	10001	-2.34049852431772

Table 6.3. Comparison between the Chebyshev approximation and the FDM scheme for $m = 10$ in the convective diffusion equation. Value of $\theta'_m(0)$ obtained by extrapolation to a step size of zero value is -2.901505452807

No. of terms in Chebyshev approx.	Value of $\theta'_m(0)$	No. of nodes in FDM scheme	Value of $\theta'_m(0)$
11	-2.47551374048620	101	-3.25312335973968
26	-2.90563022533799	1001	-2.91044576289627
51	-2.90150518991599	1251	-2.90731168783412
101	-2.90150549289233	2501	-2.90299930892293
151	-2.90150549289233	5001	-2.90188423570831
201	-2.90150549289233	10001	-2.90160083994728

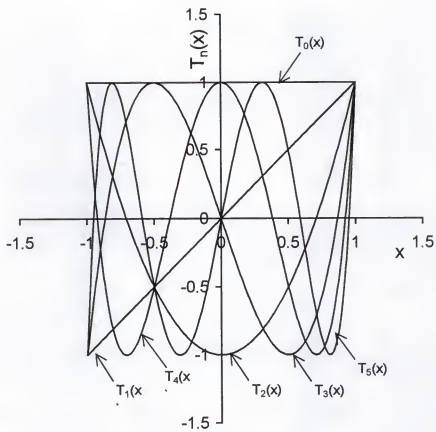


Figure 6.1. Chebyshev polynomials as functions of x .

CHAPTER 7

SPECTROSCOPY APPLICATIONS OF THE KRAMERS-KRONIG TRANSFORMS: IMPLICATIONS FOR ERROR STRUCTURE IDENTIFICATION

It is well established that the use of weighting strategies that account for the stochastic error structure of measurements enhances the information that can be extracted from regression of spectroscopic data [15]-[18],[23],[81]-[86]. Hence the independent assessment of the error structure is needed. The error structure for most radiation-based spectroscopic measurements such as absorption spectroscopy and light scattering can be readily identified [87],[88]. The error analysis approach has been successful for some optical spectroscopy techniques because these systems lend themselves to replication and, therefore, to the independent identification of the different errors that contribute to the total variance of the measurements. In contrast, the stochastic contribution to the error structure of electrochemical impedance spectroscopy measurements cannot generally be obtained from the standard deviation of repeated measurements because even a mild non-stationary behavior introduces a non-negligible time-varying bias contribution to the error. Recent advances in the use of measurement models for filtering lack of replicacy have made possible experimental determination of the stochastic and bias contributions to the error structure for impedance measurements [7-11].

The measurement model approach for identification of error structures is widely used (see, for example, [87] and [88] for applications to optical spectroscopies and [89] for general application to spectroscopy). The measurement model approach has recently

been applied to identify the error structures of impedance spectra collected for a large variety of electrochemical systems [7-11]. Use of measurement models in identifying the noise level in the impedance measurements for the reduction of ferricyanide is illustrated in chapter 2. One striking result of the application of measurement models to impedance spectroscopy has been that the standard deviation of the real and imaginary components of the impedance spectra were found to be equal, even where the two components differed by several orders of magnitude. The only exception was found when the data did not conform to the Kramers-Kronig relations or when the precision of the measurement did not allow calculation of the standard deviation of one of the components (*i.e.*, all significant digits reported by the instrumentation for the replicated measurements were equal [19]). The equality of standard deviations in the stochastic noise will be illustrated with examples from a number of frequency domain techniques in chapter 8. The objective of the present chapter is to explore whether the equality of the noise levels in the real and imaginary parts of electrochemical impedance spectra can be attributed to the manner in which errors propagate through the Kramers-Kronig relations when both real and imaginary components are obtained from the same measurement.

7.1 Experimental Motivation

Spectroscopic measurements, which yield complex variables, are illustrated in hierarchical form in Figure 7.1. Spectrophotometric techniques such as absorption spectroscopy and light scattering record the light intensity as a function of the wavelength of the incident radiation used to interrogate the sample. The frequency dependence arises from the wavelength of light employed. Electrochemical and mechanical spectroscopic

techniques employ a modulation of a system variable such as applied potential, and the frequency dependence arises from the frequency of the modulation. In electrochemical, mechanical, and some spectrophotometric techniques, both real and imaginary (or modulus and phase angle) components are obtained from a single measured variable (e.g., the impedance).

To date, the equality of the standard deviations for real and imaginary components was observed for a number of such systems which are highlighted in Figure 7.1. The equality of the standard deviation for real and imaginary components was observed for:

- Electro-Hydrodynamic Impedance Spectroscopy (EHD): Electro-Hydrodynamic Impedance Spectroscopy is a coupled mechanical/electrochemical measurement in which the rotation rate of a disk electrode is modulated about a pre-selected value. The impedance response at a fixed potential is given by $\Delta I/\Delta\Omega$, where I is the current through the disk electrode and Ω is the rotation speed of the disk [10].
- Electrochemical Impedance Spectroscopy: The database now includes measurements for electrochemical and solid-state systems under both potentiostatic and galvanostatic modulation [7-9]. The equality of the standard deviation for real and imaginary components was observed, even for systems with a very large solution resistance [19].
- Optically-Stimulated Impedance Spectroscopy: Impedance measurements were obtained for solid-state systems under monochromatic illumination [90].

The contention that the variances of the real and imaginary parts of Kramers-Kronig transformable complex variables are equal is supported by experimental evidence and has been validated statistically, as discussed in a subsequent section.

In contrast to results found for electrochemical and mechanical spectroscopies, the standard deviations for the real and imaginary components of the complex refractive index from spectrophotometric measurements were found to be correlated but not necessarily equal [91]. However, for measurement of optical properties (*e.g.*, the real and imaginary components of the complex refractive index) over a sufficiently broad range of frequencies, different instruments with their particular error structures have to be used; whereas, in electrochemical and mechanical spectroscopies a single instrument is used to measure simultaneously both the real and imaginary components.

For electrochemical and mechanical/electrochemical spectroscopies, the experimental evidence for the equality of the standard deviation of real and imaginary components is compelling and suggests that there may be a fundamental explanation for the observed relationship between the noise level of real and imaginary components of the impedance response.

7.2 Application of the Kramers-Kronig Relations

The Kramers-Kronig relations are integral equations which constrain the real and imaginary components of complex quantities for systems that satisfy conditions of causality, linearity, and stability [92-95]. The Kramers-Kronig transforms arise from the constitutive relations associated with the Maxwell equations for the description of an electromagnetic field at interior points in matter. Bode extended the concept to electrical impedance and tabulated various forms of the Kramers-Kronig relations [95].

An application of the Kramers-Kronig relations to variables containing stochastic noise was presented by Macdonald, who showed, through a Monte Carlo analysis with

synthetic data and an assumed error structure, that the standard deviation of the impedance component predicted by the Kramers-Kronig relations was equal to that of the input component [96]. The analysis was incomplete because it did not identify correctly the conditions under which the variances of the real and imaginary components of experimental impedance data are equal, and the author continued to use a weighting strategy in his regressions based upon a modified proportional error structure for which the variances of the real and imaginary components of experimental impedance data are different [96,98].

The objective of the present work is to identify the error structure for frequency-dependent measurements. Herein an explicit relationship between the variances of the real and imaginary components of the error is reported without *a priori* assumption of the error structure. The only requirements are that the Kramers-Kronig relations be satisfied, that the errors be stationary in the sense of replication at the measurement frequency, that the derivative of the variance with respect to frequency exists, and that the errors be uncorrelated with respect to frequency. In the subsequent section, stochastic error terms are incorporated into the derivation of Kramers-Kronig relations in order to examine how the errors for the real and imaginary terms are propagated.

7.3 Absence of Stochastic Errors

The Kramers-Kronig transforms can be derived under the assumptions that the system is linear, stable, stationary, and causal. The system is assumed to be stable in the sense that response to a perturbation to the system does not grow indefinitely and linear in the sense that the response is directly proportional to an input perturbation at each

frequency. Thus, the response to an arbitrary perturbation can be treated as being composed of a linear superposition of waves. The response is assumed to be analytic at frequencies of zero to infinity. The statement that the response must be analytic in the domain of integration may be viewed as being a consequence of the condition of primitive causality, *that is*, that the effect of a perturbation to the system cannot precede the cause of the perturbation [99].

The starting point in the analysis is that the integral around the closed loop (see Figure 7.2) must vanish by Cauchy's integral theorem [100],

$$\oint (Z(x) - Z_{\infty}) dx = 0 \quad (7.1)$$

where Z is the impedance response and x is the complex frequency. Equation (7.1) yields (see, for example, [95])

$$Z_j(\omega) = \frac{2\omega}{\pi} \int_0^\infty \frac{Z_r(x) - Z_r(\omega)}{x^2 - \omega^2} dx \quad (7.2a)$$

and

$$Z_r(\omega) = Z_r(\infty) + \frac{2\omega}{\pi} \int_0^\infty \frac{-x Z_j(x) + \omega Z_j(\omega)}{x^2 - \omega^2} dx \quad (7.2b)$$

where ω is the frequency of interest. r and j in the subscripts refer to real and imaginary parts respectively. Only the principal value of the respective integrals is considered. The terms $Z_r(\omega)$ and $\omega Z_j(\omega)$ in equations (7.2a) and (7.2b), respectively, facilitate numerical evaluation of the singular integrals, but do not contribute to the numerical value of the

integrals as $\int_0^\infty \frac{1}{x^2 - \omega^2} dx = 0$ for $\omega \neq 0$ [101].

A similar development cannot be used to relate the real and imaginary parts of stochastic quantities because equation (7.1) is not satisfied except in an expectation sense.

7.4 Propagation of Stochastic Errors

The stochastic error can be defined by

$$Z_{\text{ob}}(\omega) = Z(\omega) + \varepsilon(\omega) = (Z_r(\omega) + \varepsilon_r(\omega)) + j(Z_j(\omega) + \varepsilon_j(\omega)) \quad (7.3)$$

where $Z_{\text{ob}}(\omega)$ is the observed value of the impedance at any given frequency ω , $Z(\omega)$, $Z_r(\omega)$, and $Z_j(\omega)$ represent the error-free values of the impedance which conform exactly to the Kramers-Kronig relations, and j is the imaginary number $\sqrt{-1}$. The measurement error $\varepsilon(\omega)$ is a complex stochastic variable such that $\varepsilon(\omega) = \varepsilon_r(\omega) + j\varepsilon_j(\omega)$. Clearly, at any frequency ω

$$E(Z(\omega)_{\text{ob}}) = Z(\omega) \quad (7.4)$$

only if

$$E(\varepsilon_r(\omega)) = 0 \quad (7.5a)$$

and

$$E(\varepsilon_j(\omega)) = 0 \quad (7.5b)$$

where $E(\cdot)$ refers to the expectation of the argument. $E(x)$ represents the expected value of random variable x where by definition

$$E(x) = \sum_{\text{All } x} xP(x) \quad (7.6)$$

where $P(x)$ is the probability for the random variable to have a value of x . Equations (7.5a) and (7.5b) are satisfied for errors that are stochastic and do not include the effects of bias.

7.4.1 Transformation from Real to Imaginary

The Kramers-Kronig relations can be applied to obtain the imaginary part from the real part of the impedance spectrum only in an expectation sense, *that is*,

$$E(Z_i(\omega)) = \frac{2\omega}{\pi} E \left(\int_0^{\infty} \frac{Z_r(x) - Z_r(\omega) + \varepsilon_r(x) - \varepsilon_r(\omega)}{x^2 - \omega^2} dx \right) \quad (7.7)$$

It is evident from equation (7.7) that, for the expected value of the observed imaginary component to approach its true value in the Kramers-Kronig sense, it is necessary that equation (7.5a) be satisfied and that

$$E \left(\frac{2\omega}{\pi} \int_0^{\infty} \frac{\varepsilon_r(x)}{x^2 - \omega^2} dx \right) = 0 \quad (7.8)$$

For the first condition to be met, it is necessary that the process be stationary in the sense of replication at every measurement frequency. The second condition can be satisfied in two ways: In the hypothetical case where all frequencies can be sampled, the expectation can be carried to the inside of the integral, and equation (7.8) results directly from equation (7.5a). In the more practical case where the impedance is sampled at a finite number of frequencies, $\varepsilon_r(x)$ represents the error between an interpolated function and the “true” impedance value at frequency x . This term is composed of contributions from the quadrature and/or interpolation errors and from the stochastic noise at the applied frequency ω . In the latter case, equation (7.8) represents a constraint on the integration procedure. In the limit that quadrature and interpolation errors are negligible, the residual errors $\varepsilon_r(x)$ should be of the same magnitude as the stochastic noise $\varepsilon_r(\omega)$.

Under the conditions that equations (7.5a) and (7.8) are satisfied and for a given evaluation of equation (7.7)

$$Z_j(\omega) + \varepsilon_j^*(\omega) = \frac{2\omega}{\pi} \left\{ E \left(\int_0^\infty \frac{Z_r(x) - Z_r(\omega) + \varepsilon_r(x) - \varepsilon_r(\omega)}{x^2 - \omega^2} dx \right) + \int_0^\infty \frac{\varepsilon_r(x)}{x^2 - \omega^2} dx \right\} \quad (7.9)$$

where $\varepsilon_j^*(\omega)$ represents the error in the evaluation of the Kramers-Kronig relations caused by the second integral on the right-hand side. The variance of the transformed imaginary variable can be shown by the following development to be equal to the variance of the real variable. From equation (7.9)

$$\text{var}(\varepsilon_j^*(\omega)) = \left(\frac{2\omega}{\pi} \right)^2 \frac{1}{N-1} \sum_{k=1}^N \left[\int_0^\infty \frac{\varepsilon_r(x)}{x^2 - \omega^2} dx - \overline{\int_0^\infty \frac{\varepsilon_r(x)}{x^2 - \omega^2} dx} \right]^2 \quad (7.10)$$

where N is the number of replicate measurements which is assumed to be large. Under the assumption that equation (7.8) is satisfied

$$\text{var}(\varepsilon_j^*(\omega)) = \frac{1}{N-1} \sum_{k=1}^N \left(\frac{2\omega}{\pi} \int_0^\infty \frac{\varepsilon_{r,k}(x)}{x^2 - \omega^2} dx \right)^2 \quad (7.11)$$

As only the principal values of the integrals are considered, it is appropriate to approach the point of singularity at $x=\omega$ equally from both sides. In terms of the principal value, for specific values of k , the integral in equation (7.11) becomes

$$\frac{2\omega}{\pi} \int_0^\infty \frac{\varepsilon_{r,k}(x)}{x^2 - \omega^2} dx = \frac{2\omega}{\pi} \int_0^{\omega^-} \frac{\varepsilon_{r,k}(x)}{x^2 - \omega^2} dx + \frac{2\omega}{\pi} \int_{\omega^+}^\infty \frac{\varepsilon_{r,k}(x)}{x^2 - \omega^2} dx \quad (7.12)$$

Under the transformations $x=\omega y$ in the domain $[0, \omega^-]$ and $x=\omega y$ in the domain $[\omega^+, \infty]$ (reference [96]),

$$\frac{2\omega}{\pi} \int_0^{\infty} \frac{\varepsilon_{r,k}(x)}{x^2 - \omega^2} dx = -\frac{2}{\pi} \int_0^1 \frac{(\varepsilon_{r,k}(\omega y) - \varepsilon_{r,k}(\omega/y))}{1 - y^2} dy \quad (7.13)$$

Equation (7.13) can be expressed in a summation sense as

$$-\frac{2}{\pi} \int_0^1 \frac{(\varepsilon_{r,k}(\omega y) - \varepsilon_{r,k}(\omega/y))}{1 - y^2} dy = -\frac{2}{\pi} \sum_{m=1}^M \left[\frac{\varepsilon_{r,k}(\omega y_m) - \varepsilon_{r,k}(\omega/y_m)}{1 - y_m^2} W(y_m) \right] \quad (7.14)$$

where M is large, $M-1$ represents the number of intervals for the domain of integration, or M is the number of nodes used for numerical evaluation of integrals, and $W(y_m)$ is the weighing factor which can be a function of the integration procedure chosen. From equations (7.11), (7.13), and (7.14)

$$\text{var}(\varepsilon_j^*(\omega)) = \frac{4}{\pi^2} \frac{1}{N-1} \sum_{k=1}^N \left(\sum_{m=1}^M \left[\frac{\varepsilon_{r,k}(\omega y_m) - \varepsilon_{r,k}(\omega/y_m)}{1 - y_m^2} W(y_m) \right] \right)^2 \quad (7.15)$$

A general expression for the errors is given by $\varepsilon_{r,k}(x) = P_k(0,1)\sigma_r(x)$ where $P_k(0,1)$ is the k^{th} observation of a symmetrically distributed random number with a mean value of zero and a standard deviation of 1, and $\sigma_r(x)$ is the standard deviation for the errors which is representative of the error structure for the spectroscopy measurements and is assumed to be a continuous function of frequency. Under the assumption that the errors are uncorrelated with respect to frequency,

$$\sigma_j^{*2}(\omega) = \sum_{m=1}^M \left\{ a_m [\sigma_r^2(\omega y_m) + \sigma_r^2(\omega/y_m)] \right\} \quad (7.16)$$

where a_m is the weighting factor given by

$$a_m = \left[\frac{W(y_m)}{1 - y_m^2} \right]^2 \quad (7.17)$$

In the limit that $M \rightarrow \infty$, the trapezoidal rule yields

$$a_m = \frac{4}{\pi^2} \frac{1}{(2m-1)^2} \quad (7.18)$$

and

$$\sum_{m=1}^{\infty} a_m = 0.5 \quad (7.19)$$

As shown in Figure 7.3, the a_m coefficients decay rapidly away from $y=1$. Beyond the first five terms, the individual contribution of each term is less than 1% of the first term. The series approaches its limiting value to within 1 percent when 20 terms are used. The error associated with using a finite number of terms in equation (7.16) can be made therefore to be negligibly small.

Under the assumption that $\sigma_r^2(x)$ is continuous at $x=\omega$, a Taylor series expansion can be written in terms of frequency x which, when expressed in terms of the transformation variable $x = \omega y_m$ (valid for $x < \omega$), yields

$$\sigma_r^2(x) = \sigma_r^2(\omega) + \left(\frac{d\sigma_r^2(x)}{dx} \right)_{x=\omega} (\omega(y_m - 1)) + O\left((\omega(y_m - 1))^2\right) \quad (7.20)$$

Similarly, for the variable transformation $x = \omega/y_m$ valid for $x > \omega$,

$$\sigma_r^2(x) = \sigma_r^2(\omega) + \left(\frac{d\sigma_r^2(x)}{dx} \right)_{x=\omega} \omega \left(\frac{1}{y_m} - 1 \right) + O\left(\left(\omega \left(\frac{1}{y_m} - 1 \right)\right)^2\right) \quad (7.21a)$$

In the vicinity of $y_m=1$, equation (7.21a) can be expressed in a form similar to equation (7.20), that is,

$$\sigma_r^2(x) = \sigma_r^2(\omega) - \left(\frac{d\sigma_r^2(x)}{dx} \right)_{x=\omega} \omega(y_m - 1) + O((\omega(y_m - 1))^2) \quad (7.21b)$$

Equation (7.21b) is justified because the major part of the contribution to the integral occurs within the range of $y=1$ to roughly $y=1-10^{-6}$. The assumption that higher order terms in the expansion for $\sigma_r^2(x)$ can be neglected is justified because the region over which linearization is assumed to apply extends only 1/1000 of the frequency ω , e.g., 1 Hz at a frequency ω of 1000 Hz.

Substitution of equations (7.20) and (7.21) into equation (7.16) yields

$$\sigma_j^{*2}(\omega) = \sigma_r^2(\omega) \sum_{m=1}^p 2a_m \quad (7.22)$$

where $p < M$ and accounts for intervals in the vicinity of $y=1$. Following equation (7.19)

$$\sigma_j^{*2}(\omega) = \sigma_r^2(\omega) \quad (7.23)$$

This result is consistent with the results of Monte Carlo calculations for assumed error structures but was obtained here without explicit assumption of an error structure [91],[96]. The only requirements are that the Kramers-Kronig relations be satisfied, that the errors be stationary in the sense of replication at each measurement frequency, that the errors be uncorrelated with respect to frequency, and that the derivative of the variance with respect to frequency exists.

7.4.2 Transformation from Imaginary to Real

The Kramers-Kronig relations for obtaining the real part from the imaginary part of the spectrum can be expressed as equation (7.2b), which, in terms of expectations becomes

$$E(Z_r(\omega) - Z_r(\infty)) = E\left(\frac{2}{\pi} \int_0^\infty \frac{-xZ_j(x) + \omega Z_j(\omega) - x\varepsilon_j(x) + \omega\varepsilon_j(\omega)}{x^2 - \omega^2} dx\right) \quad (7.24)$$

Following the discussion in the earlier section, the necessary conditions for Kramers-Kronig transformability become equation (7.5b) and

$$E\left(\frac{2}{\pi} \int_0^\infty \frac{x\varepsilon_j(x)}{x^2 - \omega^2} dx\right) = 0 \quad (7.25)$$

The variance of the error in the evaluation of equation (7.24) is given by

$$\text{var}\left(\varepsilon_r^*\right) = \frac{1}{N-1} \sum_{k=1}^N \left(\frac{2}{\pi} \int_0^\infty \frac{-x\varepsilon_{j,k}(x)}{x^2 - \omega^2} dx \right)^2 \quad (7.26)$$

Under the transformation used in the earlier section,

$$\int_0^\infty \frac{x\varepsilon_{j,k}(x)}{x^2 - \omega^2} dx = - \int_0^1 \frac{y\varepsilon_{j,k}(\omega y)}{1-y^2} dy + \int_{y_2}^1 \frac{(1/y)\varepsilon_{j,k}(\omega/y)}{1-y^2} dy + \int_{x(y_2)}^\infty \frac{x\varepsilon_{j,k}(x)}{x^2 - \omega^2} dx \quad (7.27)$$

where a point of singularity at $y_m=0$ (at $\omega=\infty$) introduced by the transformation $x = \omega/y$ was avoided by further subdivision of the integral. Since y_2 can be chosen such that the third integral of equation (7.27) has negligible value and that the first integral has a negligible contribution from the range $y=0$ to y_2 , equation (7.27) can be solved by following a procedure similar to what was adopted in the earlier section. A form similar to equation (7.15) is obtained,

$$\text{var}\left(\varepsilon_r^*(\omega)\right) = \frac{4}{\pi^2} \frac{1}{N-1} \sum_{k=1}^N \left(\sum_{m=1}^M \left[\frac{y_m \varepsilon_{j,k}(\omega y_m) - (1/y_m) \varepsilon_{j,k}(\omega/y_m) W(y_m)}{1-y_m^2} \right] \right)^2 \quad (7.28)$$

In the region of interest ($y_m \rightarrow 1$), $\frac{y_m}{1-y_m^2}$ and $\frac{1}{y_m(1-y_m^2)}$ tend toward $\frac{1}{1-y_m^2}$. Hence,

$$\text{var}\left(\varepsilon_r^*(\omega)\right) = \frac{4}{\pi^2} \frac{1}{N-1} \sum_{k=1}^N \left(\sum_{m=1}^p \left[\frac{\varepsilon_{j,k}(\omega y_m) - \varepsilon_{j,k}(\omega / y_m)}{1 - y_m^2} W(y_m) \right] \right)^2 \quad (7.29)$$

where $p < M$ and accounts for the intervals in the region of $y \rightarrow 1$. Equation (7.29) is directly analogous to equation (7.15). Following the discussion in the previous section,

$$\sigma_r^{*2}(\omega) = \sigma_j^2(\omega) \quad (7.30)$$

Thus, the variance of the real part of the impedance is equal to the variance of the imaginary part of the impedance, independent of the direction of the transformation, if the Kramers-Kronig relations are satisfied in an expectation sense. In order for the Kramers-Kronig relations to be satisfied, the conditions stated through equations (7.5), (7.8), and (7.25) must be satisfied. Equations (7.5a) and (7.5b) represent the usual constraints on the experimental stochastic errors; whereas, equations (7.8) and (7.25) represent constraints on the integration procedure.

As summarized in the following section, the theoretical development presented here is supported by experimental observations for various physical systems that satisfy the conditions of Kramers-Kronig relations.

7.5 Experimental Verification

The equality of the standard deviations for real and imaginary parts of the impedance has been observed for the impedance response of solid state systems (GaAs Schottky diodes, ZnO varistors, ZnS electroluminescent panels) [8,9,14], corrosion of copper in sea-water (under either potentiostatic or galvanostatic modulation) [9,14,69], electrochemistry at metal hydride electrodes (LaNi₅ and Mischmetal) [14,70], the electrohydrodynamic impedance response for reduction of ferricyanide and oxidation of

ferrocyanide on Pt rotating disks [10,102], the impedance response of membranes for which the solution resistance is large [19], and the impedance response of electrical circuits with a large leading resistance [19]. Some examples are illustrated in detail in the next chapter.

7.6 Implications for the Error Structure

The result of the development presented here is that, for data that are consistent with the Kramers-Kronig relations in an expectation sense, the standard deviation of the real part of a complex spectrum at a given frequency must be equal to the standard deviation of the imaginary part. The development did not require any assumptions concerning analyticity of the stochastic noise with respect to frequency; therefore, the result applies to spectra in which data are collected sequentially as well as to spectra in which a single observation is used to resolve a spectrum, as is done, for example, by Fourier transformation of transient data.

The implications of this result are illustrated in Figure 7.4, where the real and imaginary parts of an impedance spectrum are presented as functions of frequency. The probability distribution function for the data, corresponding to an equal standard deviation for the real and imaginary parts, is shown at a frequency of 0.03 Hz. The real part of the impedance at this frequency is roughly 100Ω as compared to -3Ω for the imaginary part, and the noise level therefore represents a much larger percentage of the imaginary signal than the real. This result, which has also been observed in a large number of experimental systems [7-11,14,19,69,70,102] is now shown to have a fundamental basis.

While the development presented here shows that the standard deviations for the real and imaginary parts of a Kramers-Kronig-transformable complex quantity are equal, the instantaneous realizations of the stochastic errors for the respective components has been shown experimentally to be uncorrelated [9,69]. The errors were also found to be uncorrelated with respect to frequency [9,69], an observation that supports a key assumption made in the present work. The assumption of the existence of the first derivative of the variance is supported by the identification of error structures presented in the figures for the error structures for various systems, presented in the next chapter.

The need to identify an appropriate form for the impedance $Z(x)$ in the presence of stochastic errors (see, for example, equations (7.9) and (7.24)) supports the use of measurement models composed of lineshapes that themselves satisfy the Kramers-Kronig relations. The use of such measurement models is superior to the use of polynomial fitting because fewer parameters are needed to model complex behavior. Experimental data seldom contain a frequency range sufficient to approximate the range of integration of 0 to ∞ required to evaluate the Kramers-Kronig integrals; therefore, extrapolation of the data set is required. Measurement models can be used to extrapolate the experimental data set, and the implications of the extrapolation procedure are quite different than from extrapolations with polynomials. The extrapolations done with measurement models are based on a common set of parameters for the real and imaginary parts and on a model structure that has been shown to represent adequately the observations. The confidence in the extrapolation using measurement models is, therefore, higher. In addition, as the lineshapes used satisfy the Kramers-Kronig relations, experimental data can be checked for consistency with the Kramers-Kronig relations without actually integrating the equations

over frequency, avoiding the concomitant quadrature errors [11,69,70,71,98,102]. The correlation and bias errors introduced by quadrature errors are discussed further in [91]. The results presented here also indicate clearly the importance of identifying the nature of the error structure prior to application of the Kramers-Kronig transforms.

The analytic approach presented here establishes an explicit relationship between σ_r and σ_i with the only requirement that the errors be stationary in the sense of replication at each measurement frequency, that errors be uncorrelated with respect to frequency, that the derivative of the variance with respect to frequency exists, and that the Kramers-Kronig relations be satisfied. In addition, the conditions for the applicability of the Kramers-Kronig relations to experimental data have been identified, that is, equations (7.5), (7.8), and (7.25) be satisfied.

The observation regarding the equality of the standard deviations in the real and imaginary parts of the stochastic noise received some criticism in the recent past based on the work performed by Macdonald and Pieterbarg [103]. Their conclusions are based only on numerical simulations conducted on synthetic data. However, the result presented in this chapter is very general in nature and is applicable for all spectroscopic measurements obeying Kramers-Kronig transforms with real and imaginary components obtained simultaneously using the same instrumentation. Huge amount of experimental evidence is available to support this result, some examples of which are presented in chapter 8.

7.7 Conclusions

Knowledge of the error structure plays a critical role in interpreting spectroscopic measurements. An assessment of the stochastic (or noise) component of the errors allows

refinement of regression strategies and can guide design of experiments to improve signal-to-noise ratios. Assessment of consistency of data with the Kramers-Kronig relations is also important because inconsistencies can be attributed to experimental bias errors that must be accounted for during interpretation of measurements.

In this work, the experimental observation that real and imaginary parts of the impedance have the same standard deviation was found to have a fundamental basis for stationary error structures. The propagation of stochastic errors through the Kramers-Kronig relations in both directions (real-to-imaginary and imaginary-to-real) yielded standard deviations that were equal. Thus, the observations concerning the error structure of electrochemical, optical-electrochemical, and mechanical-electrochemical impedance spectra should apply as well to purely mechanical spectroscopic measurements.

This work suggests also that evaluation of stochastic errors could provide insight into the degree of consistency with the Kramers-Kronig relations. The concept that there exists a relationship between stochastic error structure and bias errors is supported by repeated experimental observation that the standard deviation of real and imaginary parts of the impedance were equal except for spectra that were found to be inconsistent with the Kramers-Kronig relations.

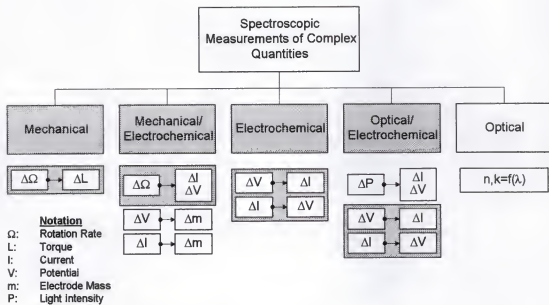


Figure 7.1. Hierarchical representation of spectroscopic measurements. The shaded boxes represent measurement strategies for which the real and imaginary parts of Kramers-Kronig-transformable impedance were found to have the same standard deviation. Following completion of the analysis reported here, an experimental investigation was begun which showed that the real and imaginary parts of complex viscosity also have the same standard deviation if the spectra are consistent with the Kramers-Kronig relations.

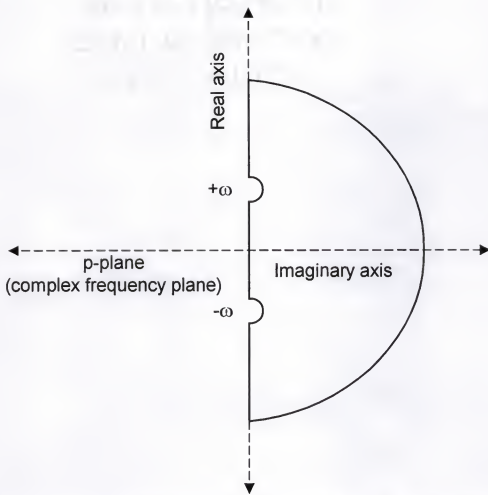


Figure 7.2. Path of integration for the contour integral in the complex-frequency plane.

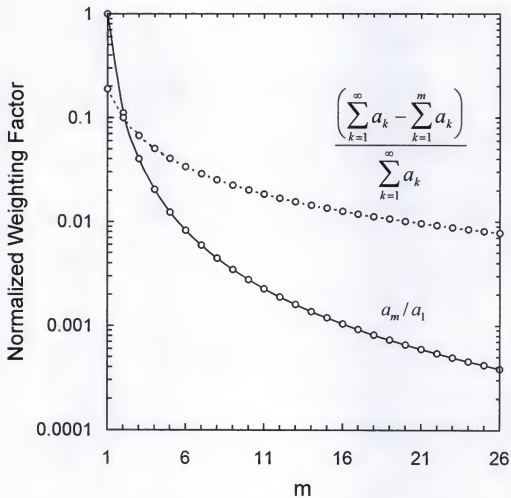


Figure 7.3. Weighting factor for Eq. (7.17) as a function of m normalized to show relative contributions to the integral.

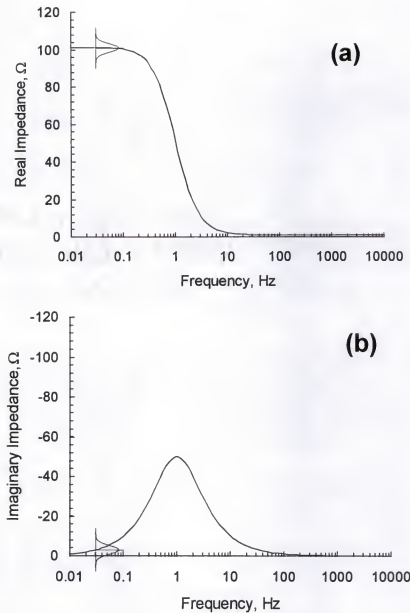


Figure 7.4. Real (a) and imaginary (b) parts of a typical electrochemical impedance spectrum as a function of frequency. The normal probability distribution function, shown at a frequency of 0.03 Hz, shows that one consequence of the equality of the standard deviations for real and imaginary components is that the level of stochastic noise as a percentage of the signal can be much larger for one component than the other.

CHAPTER 8

COMMON FEATURES FOR FREQUENCY DOMAIN MEASUREMENTS

Spectroscopy techniques involving measurement of a frequency-dependent complex quantity are commonly used to identify material properties. Spectrophotometric techniques such as absorption spectroscopy and light scattering record the light intensity as a function of the wavelength of the incident radiation used to interrogate the sample. The frequency dependence arises from the wavelength of light employed. Electrochemical and mechanical spectroscopic techniques employ modulation of a system variable such as applied potential, and the frequency dependence arises from the frequency of the modulation. Interpretation of the resulting spectra in terms of material properties usually requires regression of a process model that describes the physics of the system.

Knowledge of the error structure plays a critical role in interpreting spectroscopic measurements. A discussion on error structure can be found in chapter 2. Use of weighting strategies that account for the stochastic error structure of measurements enhances the information that can be extracted from regression of a model to the spectroscopic data. The advantage of weighting the regressions with respect to the error structure is that part of the spectrum where the noise level is high is assigned lesser weight and part of the spectrum where noise level is low is assigned more weight in the regressions. This enhances the information content that can be obtained from the impedance measurements. In addition, through identification of the error structure, inconsistencies can be attributed to experimental bias errors that might otherwise be

interpreted as needing refinement of the process model. However, for many spectroscopic measurements, (e.g., impedance spectroscopy) the long time required to collect a spectrum interferes with identification of the error structure because even a mild non-stationary behavior introduces a non-negligible time-varying bias contribution to the error.

The central idea of this chapter is to illustrate the extension of the measurement model concept from electrochemical impedance spectroscopy to other spectroscopy measurements. There are several features of impedance spectra that should be seen as well in other spectroscopy measurements. It was shown in the previous chapter that the variances of the real and imaginary components of impedance spectra are equal if the Kramers-Kronig relations are satisfied. This result has been observed experimentally for electrochemical impedance measurements. It should be observed as well for any spectroscopy measurement in which a single instrument is used to obtain both real and imaginary components of a complex quantity simultaneously and for which the system under study satisfies the constraints of causality, linearity, and stability.

The spectroscopic techniques discussed in this chapter share similarities in terms of lineshapes which can be used to describe the frequency dependence of the measured quantity, in terms of the Kramers-Kronig relations which constrain the real and imaginary parts of the measured quantity, and the error structure. The common features exploited by measurement model analysis will be supported with experimental data from the electrochemical impedance spectroscopy (electrochemical), test circuits (electrical), rheology of viscoelastic fluids (mechanical), electrohydrodynamic impedance spectroscopy (mechanical/electrical), and acoustophoretic spectroscopy (mechanical/electrical). It is

worth noting that the similarities are seen despite the inherently different physical principles upon which these different techniques are based.

8.1 Similarity in Terms of Line Shapes

Spectroscopic measurements which yield complex variables are illustrated in hierarchical form in Figure 7.1. In electrochemical, mechanical, and some spectrophotometric techniques, both real and imaginary components are obtained from a single measured variable (*e.g.*, impedance).

The measurement model technique was widely used for identification of error structure associated with spectroscopic measurements [87-89]. It has been applied to optical spectroscopy [88], electrochemical [7-9,11,69,104] and electrohydrodynamic impedance spectroscopy [10], and recently, to rheology of viscoelastic fluids [105]. The similarity between different spectroscopic techniques is evident from the fact that line-shapes containing the same mathematical structure can be applied to each of the spectroscopies.

The measurement model [7-11,69,104] used to determine the error structure of electrochemical impedance data was given by a generalized Voigt model, *that is*,

$$Z(\omega) = Z_0 + \sum_k \frac{\Delta_k}{(1 + j\tau_k \omega)} \quad (8.1)$$

Equation (8.1) represents a superposition of line shapes (*i.e.*, a series arrangement of circuits involving dissipative elements Δ_k in parallel with oscillating elements with time constants τ_k) that has been applied in the fields of optics, solid mechanics, rheology and in

electrochemistry (where, for AC impedance, Δ_k 's are resistances and Z_0 is the resistance associated with ohmic drop).

8.2 Similarity in Terms of Transfer Function

In this section, the similarity between various frequency domain techniques is established based on the transfer function used to describe the frequency response of the systems considered.

8.2.1 Electrochemical Impedance Spectroscopy

The Voigt model as used in electrochemistry is presented in Figure 8.1a. The current-voltage relationship for a resistor is given by

$$I = \frac{1}{R}V \quad (8.2)$$

where I is the current, R is the resistance, and V is the potential drop across the resistor. The corresponding relationship for the capacitor is

$$I = C \frac{dV}{dt} \quad (8.3)$$

where C is the capacitance. The response of the Voigt model (Figure 8.1a) to a sinusoidal current or potential perturbation is given in terms of impedance $Z = \Delta\tilde{V} / \Delta\tilde{I}$ by (8.1).

8.2.2 Rheology of Viscoelastic Fluids

The rheological model related to the Voigt model used in electrochemistry is the Kelvin-Voigt model presented in Figure 8.1b [106]. The stress-strain relationship for a spring is given by

$$\sigma = G\gamma \quad (8.4)$$

where S is the stress, G is the Hookian spring constant, and γ is the strain. The corresponding relationship for the dashpot is

$$S = \eta\dot{\gamma} \quad (8.5)$$

where η is the viscosity for the dashpot and $\dot{\gamma}$ is the rate of strain (e.g., dv_x/dy). The response of the Kelvin-Voigt model shown in Figure 8.1b to a sinusoidal stress is given by

$$J(\omega) = \frac{1}{G_0} + \sum_k \frac{1/G_k}{1 + j\omega\lambda_k} \quad (8.6)$$

where $J(\omega)$ is the complex compliance of the system, G_k is the Hookian spring constant for spring k , and λ_k is the time constant given by $\lambda_k = \eta_k/G_k$. The complex compliance is related to the complex viscosity η by

$$J = \frac{j}{\omega\eta} \quad (8.7)$$

The line-shape represented by equation (8.1) can be applied to the complex viscosity as well as the complex compliance.

8.2.3 Optical Spectroscopy

The form of equation (8.1) applied to optical spectroscopies is the Debye model, which represents a special case of the Lorentz oscillator [87]. The Lorentz oscillator treats charged particles in the medium as harmonic oscillators;

$$\varepsilon(\omega) = \varepsilon_0 + \sum_k \frac{\omega_{p,k}^2}{\omega_{0,k}^2 - \omega^2 - j\omega\gamma_k} \quad (8.8)$$

where ε is the dielectric permittivity and ε_0 , $\omega_{p,k}^2$, $\omega_{0,k}^2$ and γ_k are adjusted parameters.

The natural frequency for the undamped oscillator is $\omega_{0,k}^2$ and $\omega_{p,k}^2$ is proportional to the concentration of charged particles per unit volume. The damping constant γ_k depends on

the width of the ground state which is narrow, and the width of state k , which depends on the transition probabilities to all other states. Summation over the different oscillators accounts for multiple discrete energy levels, and provides agreement with quantum mechanical results.

The Drude model applies to free electrons (metals) and appears as a special case of the Lorenz oscillator for which the spring constant of the oscillator is equal to zero:

$$\varepsilon(\omega) = \varepsilon_0 - \sum_k \frac{\omega_{p,k}^2}{\omega^2 + j\omega\gamma_k} \quad (8.9)$$

Combined models could, in principle, be developed to account for bound and free electrons. An example of a combined model is given by

$$\varepsilon(\omega) = \varepsilon_0 - \sum_e \frac{\omega_{p,e}^2}{\omega^2 + j\omega\gamma_e} + \sum_k \frac{\omega_{p,k}^2}{\omega_{0,k}^2 - \omega^2 - j\omega\gamma_k} \quad (8.10)$$

The Debye model accounts for a linear response of a charged particle to a time-dependent field. The multiple Debye model is given by

$$\varepsilon(\omega) = \varepsilon_0 + \sum_k \frac{\Delta_k}{1 - j\omega\tau_k} \quad (8.11)$$

where Δ_k describes the maximum value of the real part of the function (seen at $\omega \rightarrow 0$) and τ_k is the characteristic time constant for element k . The Debye model could be regarded to be a low frequency limit to the Lorenzian model. Equation (8.1) can be written as

$$\varepsilon(\omega) = \varepsilon_0 + \sum_k \frac{\frac{\omega_{p,k}^2}{\omega_{0,k}^2 - \omega^2}}{1 - j\omega \frac{\gamma_k}{\omega_{0,k}^2 - \omega^2}} \quad (8.12)$$

which approaches equation (8.11) under the assumption that $\omega_{0,k}^2 \gg \omega^2$.

8.2.4 Acoustophoretic Spectroscopy

Acoustophoretic spectroscopy capitalizes on two types of electroacoustic effects. One is the generation of sound waves by an alternating electric field. As an applied electric field is alternated, the polar attractions of the charged particles will oscillate, that is, the particles will at one moment be attracted to one pole and in the next moment be attracted to the opposite pole. This particle movement creates pressure disturbances, although small, which propagate out from the surface. The second electroacoustic effect is the generation of an alternating electric field by the application of an ultrasonic beam. The propagating sound waves impart motion to the particles and surrounding liquid. The relative motion between the phases creates alternating dipoles, the sum of which creates a detectable alternating electric field.

The acoustosizer can measure both types of electroacoustic effects although the instrument is usually operated to measure the generated sound waves resulting from an alternating applied electric field, as the signal to noise ratio is larger for this mode of operation. The electroacoustic signal is related to the size and charge of the suspended particles. The determination of particle size and charge is a two step process in which the dynamic mobility is first calculated and subsequently the size and shape are determined. There exist multiple techniques for the determination of these properties however all are limited to systems of rather dilute suspensions. Acoustophoresis has the advantage in that it is possible to measure electroacoustic effects in suspensions of any concentration [107, 108]. Acoustophoresis data collected [109] for a suspension of polyacrylic acid, 0.062g/L, pH of 10 and molecular weight 5,000 (*Polyacrylic Acid*) is analyzed by the measurement model to support the presence of the common features in acoustophoretic spectra.

8.3 Similarity in Terms of the Kramers-Kronig Relations

The Kramers-Kronig transforms, as discussed in chapter 7, are integral equations that constrain the real and imaginary components of complex quantities for systems that satisfy conditions of causality, linearity, and stability [92-95],[99],[110]. These transforms arise from the constitutive relations associated with the Maxwell equations for description of an electromagnetic field at interior points in matter. A contour integral approach can also be used to derive the Kramers-Kronig relations [95]. In effect, the Kramers-Kronig relations constrain the complex properties associated with propagation of a wave through matter under assumptions of primitive causality, linearity, and stability [99]. As the constraints required for satisfaction of the Kramers-Kronig relations are not very stringent, the Kramers-Kronig relations can be expected to apply to each of the spectroscopic techniques described here.

8.4 Similarity in Terms of Error Structure

In addition to similarities in various aspects shared by a number of transfer functions, a significant similarity exists in terms of the stochastic error structure of the measurements.

The error structure for most radiation-based spectroscopic measurements such as absorption spectroscopy and light scattering can be readily identified [87,88]. The error analysis approach has been successfully used for some optical spectroscopy techniques because these systems lend themselves to replication and, therefore, to the independent identification of the different errors that contribute to the total variance of the

measurements. In contrast, the stochastic contribution to the error structure of electrochemical impedance spectroscopy measurements cannot generally be obtained from the standard deviation of repeated measurements because even a mild non-stationary behavior introduces a non-negligible time-varying bias contribution to the error. Recent advances in the use of measurement models for filtering lack of replicacy have made experimental determination of the stochastic and bias contributions to the error structure for impedance measurements possible [7-10,69,104].

The generalized measurement model increases stepwise the number of line shapes used to regress the experimental data until a maximum is obtained. The data are regressed using a weighted least squares technique which minimizes the residual errors in the real and imaginary components of the measurement according to

$$J = \sum_k \frac{(Z_{r,k} - \hat{Z}_{r,k})^2}{\sigma_{r,k}^2} + \sum_k \frac{(Z_{j,k} - \hat{Z}_{j,k})^2}{\sigma_{j,k}^2} \quad (8.13)$$

where $Z_{r,k}$ and $Z_{j,k}$ are the real and imaginary components of the k^{th} data point, respectively and $\hat{Z}_{r,k}$ and $\hat{Z}_{j,k}$ are the corresponding model values. Once the model is regressed to fit the data, residual errors are calculated as

$$Z - \hat{Z} = \varepsilon_{\text{residual}} = \varepsilon_{\text{lif}} + \varepsilon_{\text{bias}} + \varepsilon_{\text{stochastic}} \quad (8.14)$$

where Z is the experimental value and \hat{Z} is the model value. The residual errors are composed of errors from lack of fit, *lif*, systematic *bias* and *stochastic* noise. Lack of fit errors are minimized by maximizing the number of line shapes to obtain a good fit to the experimental data. Specific criterion for a “good fit” cannot be explicitly stated, as the

quality of a fit depends on the noise level of the measurement itself [9]. One can say that a fit is "good" if the resulting residual errors are within the noise level of the data.

One striking result of application of measurement models to impedance spectroscopy has been that the standard deviation of the real and imaginary components of the impedance spectra were found to be equal, even where the two components differed by several orders of magnitude. The only exception was found when the data did not conform to the Kramers-Kronig relations or when the precision of the measurement did not allow calculation of the standard deviation of one of the components (*i.e.*, all significant digits reported by the instrumentation for the replicated measurements were equal [19]). In chapter 7 it was shown that, in addition to constraining the values of complex properties, the Kramers-Kronig relations constrain the error structure such that the variances of the real and imaginary components are equal.

The experimental support that is presented in the next section illustrates the common features shared by various spectroscopic techniques in terms of the applicability of measurement models and in terms of the measured error structure.

8.5 Experimental Results and Discussion

8.5.1 Electrochemical Impedance Spectroscopy

Potential was controlled by a Solartron 1286 potentiostat and driven by a Solartron 1250 frequency response analyzer. Impedance measurements were collected frequency by frequency from high frequency to low. The long-integration feature of the frequency response analyzer was used, which terminated measurement at a given frequency when a 1% closure error was achieved on the measured channel (potential when

galvanostatic modulation is employed and current when potentiostatic modulation is employed).

Typical results are presented in Figure 8.2a for the impedance response of a Pt disk electrode rotating at 120rpm and at 1/4th of the limiting current for reduction of ferricyanide in a 1M KCl supporting electrolyte at 25°C. Impedance measurements were conducted under potentiostatic modulation. The open circles and triangles represent the standard deviation of the stochastic noise in the repeated impedance measurements. The measurement model approach described by Agarwal *et al.* was used to filter lack of replicacy [9]. The real and imaginary parts of the impedance are seen to have the same standard deviation, even at frequencies where the two components differ by over one order of magnitude. Data collected at certain frequencies were found to be corrupted in the frequency scans collected for this work. The very high frequency end point in each spectrum was eliminated for the data analysis and subsequent regressions, as this point was found to be effected by startup transients associated with the measurement. These impedance data were collected at the CNRS, Paris and the in line frequency for the power supply is 50Hz. During the data analysis it was observed that the data collected close to 50Hz and 100Hz (a harmonic of 50Hz) were found to be outliers. The measurement model approach is very sensitive to outliers and it was observed that the inclusion of the data points close to these two frequencies resulted in significant distortion of error structure. Hence, the points with in $\pm 5\text{Hz}$ of these two points were eliminated for the data analysis conducted.

In order to verify the equality of standard deviations of the stochastic noise in the measurement a statistical F-test was conducted, the results of which are presented in

Figure 8.2b and Figure 8.2c. The F-test involves calculating the ratio of the variances of the two quantities of interest, in this case the real and the imaginary parts, and verifying the bounds of this ratio over a number of frequencies. This ratio is expected to be randomly scattered around a value of 1. In Figure 8.2b the circles represent the ratio of standard deviations of the real and imaginary parts the experimental data without using any filtering technique. 28 replicates were used for this case. These ratios are either extremely high or extremely low for most of the frequencies and there is a definite trending as the bias errors are not filtered. The 'x's represent the ratio of the variances of the stochastic errors after the bias errors are filtered and the dashed lines represent the confidence limits for the F-test. In this case the two data points that fall within $\pm 5\text{Hz}$ of the 50Hz and 100Hz points are not deleted. This caused visible trending especially in intermediate to high frequency ranges. The ratio calculated in this case is not randomly scattered around 1. Figure 8.2c is for the case where these two high frequency end points are deleted. In this case the errors are randomly scattered around 1. However, one may question the equality of the standard deviations since for some frequency ranges the points are scattered beyond the confidence limits. Observation of Figure 8.2a reveals that the standard deviations of the stochastic noise for parts of the frequencies are less than 3 orders of magnitude as compared to the parameter that is being measured and only 5 decimal places of the real and the imaginary parts were reported by the instrument. This may lead to uncertainties in the measured errors. A quantitative way of determining whether the equality of standard deviation is observed is by conducting a two-tailed *t*-test.

As the ratio of the variances is expected to be 1, the value of $\log(\sigma_r / \sigma_i)^2$ is expected to be randomly scattered around a mean value of 0. A histogram for the relative

frequency of occurrence of the value of $\log(\sigma_r / \sigma_j)^2$ is presented in Figure 8.2d. The t-test parameter which is given by $(\bar{X} - \mu) / (s_x / \sqrt{n})$, where \bar{X} is the sample mean, that is, the mean value of $\log(\sigma_r / \sigma_j)^2$ over the available range of frequencies, μ is the ensemble mean, s_x is the sample variance, and n is the number of available data points, in this case 74 frequency points. The t-test parameter in this case yielded a value of 0.63. This is very well acceptable for the hypothesis that the ratio of variances in the real and imaginary parts of the stochastic noise is equal to 1, or the standard deviations of the stochastic components are equal, as this value is within 1.99, the confidence limit for t-test for a level of significance $\alpha=0.05$. In this case it can be seen that the equality of standard deviations is satisfied.

8.5.2 Test Circuit

In the initial stages when the equality of standard deviations was observed for the electrochemical systems, in order to convince ourselves that this is a fundamental property of the systems under consideration due to the applicability of Kramers-Kronig relations, we sought verification by analyzing test circuit measurements conducted by T. El Moustafid of CNRS, Paris [19]. This system is very ideal as there is no time-dependent bias contribution, in other words the system is not evolving with time. Impedance measurements were collected under galvanostatic modulation at the open-circuit condition for a circuit composed of a resistor R_0 in series with a parallel resistor/capacitor combination, R_1C_1 . Potential was controlled by a Solartron 1186 potentiostat and driven by a Solartron 1250 frequency response analyzer. Replication was achieved for these

measurements so that the standard deviation of the real and imaginary parts of the impedance could be calculated directly, without use of the measurement model.

The data obtained are presented in Figure 8.3a. The ratio R_0/R_1 was equal to 10, which meant that the real part of the impedance was at least 20 times larger than the imaginary part of the impedance at all frequencies and was almost 2,000 times larger at the lowest frequency measured (0.1Hz). The significant departure from RC circuit behavior seen at frequencies above 2,000Hz was attributed to potentiostatic limitations. The data at frequencies above this point were found by the methods discussed in chapter 2 to be inconsistent with the Kramers-Kronig relations.

In spite of the three orders of magnitude difference between the real and imaginary parts of the impedance, the standard deviations of the repeated measurements were indistinguishable except in two frequency regimes. The standard deviations were found to be different in value in the higher (greater than 2,000Hz) frequency range where instrumental limitations affected the measurement. The standard deviations were also found to be different in value in the frequency range between 10 and 200Hz. In this frequency range, the calculation of the standard deviation of the real part was constrained by the 5 digits reported by the FRA. The dashed line in Figure 8.3a represents a value corresponding to 0.5 parts in 10^5 . This line drops an order of magnitude at the frequency of 180 Hz where the measured real part of the impedance changes from 1000.0 to 999.99 ohms. For data points marked by an \times , all 5 digits for six repeated measurements were identical, and a standard deviation of 0 was calculated. In other words, the standard deviations for the real and the imaginary parts of the impedance were equal unless the number of significant digits reported by the FRA were inadequate to calculate σ , or unless

potentiostatic limitations influenced the result. The results of a statistical F-test are presented in Figure 8.3b. The equality of standard deviations was verified by conducting a t-test as illustrated in Figure 8.3c.

8.5.3 Electrohydrodynamic Impedance Spectroscopy

In the usual application of electrochemical impedance spectroscopy, a complex impedance is calculated as the ratio of potential to current under a small perturbation of current (galvanostatic regulation) or potential (potentiostatic regulation). The impedance is measured as a function of the frequency of the perturbation, and regression of models to the resulting spectra yields values for physical properties. In recent years generalized impedance techniques have been introduced in which a non-electrical quantity such as pressure, temperature, magnetic field, and light intensity is modulated to give a current or potential response [2,3]. Electrohydrodynamic Impedance Spectroscopy (EHD) is one such generalized impedance technique in which sinusoidal modulation of disk rotation rate drives a sinusoidal current or potential. The technique has been applied to surface or electrode processes that are under mass transport control, and it has been used to obtain diffusivities of ionic species by the determination of the Schmidt number ($Sc=v/D$) [10,54,110-122].

Electrohydrodynamic impedance experiments are performed by modulating the rotation speed Ω of the rotating disk electrode with a fixed amplitude of perturbation $\Delta\Omega$ around a mean rotation speed of Ω_0 . The perturbation frequency ω is varied to obtain the widest possible range. The angular velocity can thus be written as

$$\Omega = \Omega_0 + \Delta\Omega \cos(\omega t) \quad (8.15)$$

The resulting current I , at fixed potential, can be expressed as

$$I = I_0 + \Delta I \cos(\omega t + \phi) \quad (8.16)$$

where I_0 is the average current, ΔI is the amplitude of the sinusoidal current response, and ϕ is the phase shift. The EHD impedance, given by

$$Z_{ehd} = \frac{\Delta \tilde{I}}{\Delta \tilde{\Omega}} \quad (8.17)$$

has the structural form of an admittance. Typical EHD data are presented in Figure 8.4 as a function of frequency. The measurement model approach was used to extract values for the standard deviation of repeated measurements, given as open symbols in Figure 8.4.

The open circles and triangles represent the real part and the imaginary part respectively of the standard deviation. The corresponding closed symbols represent the standard deviations of the repeated measurements. The line in Figure 8.4 corresponds to a model for the error structure given by

$$\sigma_r = \sigma_i = \alpha |Z_j| + \beta |Z_r - Z_\infty| + \gamma \frac{|Z|^2}{R_m} + \delta \quad (8.18)$$

where α , β , γ , and δ are parameters determined by regression. The parameter R_m accounts for the current-measuring resistor, and Z_∞ is the high-frequency asymptote for the real part of the impedance. For this case $\gamma=0$ and $Z_\infty=0$. The standard deviations of the real and imaginary parts of the noise are equal, a result that is consistent with observations made in the previous section for EIS. The results presented in Figure 8.4a also suggest that the noise level becomes a significant fraction of the signal at higher frequencies, a characteristic that influences the regression of models to EHD data. The ratio of variances of the real and imaginary parts of the noise and corresponding F-test limits are presented

in Figure 8.4b and the equality of standard deviation using t-test is illustrated in Figure 8.4c.

8.5.4 Rheology of Viscoelastic Fluids

The experiments were performed using a parallel plate rheometer [121]. In the parallel plate system, the lower plate is forced to oscillate sinusoidal and the other is stationary. The amplitude of the oscillation is given by [106],[122]

$$\Theta = \Theta_0 \sin(\omega t) \quad (8.19)$$

The torque needed to hold the lower plate in a fixed mean position is measured as

$$T = T_0 \sin(\omega t + \alpha) \quad (8.20)$$

Under the assumptions that inertia can be neglected, the free surface is cylindrical with radius R , edge and surface tension effects can be neglected, and Θ_0 is small, the complex viscosity has components

$$\eta'(\omega) = \frac{2HT_0 \sin(\alpha)}{\pi R^4 \omega \Theta_0} \quad (8.21a)$$

and

$$\eta''(\omega) = \frac{2HT_0 \cos(\alpha)}{\pi R^4 \omega \Theta_0} \quad (8.21b)$$

for the real and imaginary parts, respectively, where H is the gap height and α is the measured phase lag between T and Θ .

An example is given in Figure 8.5a for the complex viscosity of high density polyethylene melt. The open circles and triangles represent the real part and the imaginary part respectively of the standard deviation of the complex viscosity. The corresponding closed symbols represent the standard deviations of the repeated measurements. The line

given in Figure 8.5a is the fitted model for the error structure which is the same as presented as equation (8.18) with the exception that $R_m=1$ and $Z_\infty=0$. The ratio of variances of the real and imaginary parts of the noise and corresponding F-test limits are presented in Figure 8.5b and the equality of standard deviation using t-test is illustrated in Figure 8.5c. This result is consistent with observations made in the previous sections for EIS and EHD.

8.5.5 Acoustophoretic spectroscopy

Acoustophoretic spectra were collected for a suspension of polyacrylic acid (PAA) with a density of 0.062 g/L, a pH of 10, and a molecular weight of 5000 and the complex data thus obtained was analyzed using measurement model approach. More details regarding the acoustophoretic spectroscopy technique and the data analysis can be found in reference 108. The standard deviations in the stochastic noise obtained through this analysis are presented in Figure 8.6a and the F-test results are presented in Figure 8.6b. In case of this data the t-test results indicated that the equality of standard deviations in the real and imaginary parts is not satisfied. For analyzing this spectrum only 13 data points are available. However a more complete spectrum would have resulted in data that would have yielded to the hypothesis.

8.6 Conclusions

Spectroscopic techniques share similarities in terms of line-shapes which can be used to describe the frequency dependence of the measured quantity, in terms of the Kramers-Kronig relations which constrain the real and imaginary parts of the measured quantity, and the error structure, which is shown here to share common features.

Knowledge of the error structure plays a critical role in interpreting spectroscopic measurements. Use of weighting strategies that account for the stochastic error structure of measurements enhances the information that can be extracted from regression of a model to spectroscopic data. In addition, through identification of the error structure, inconsistencies can be attributed to experimental bias errors that might otherwise be interpreted as needing refinement of the process model.

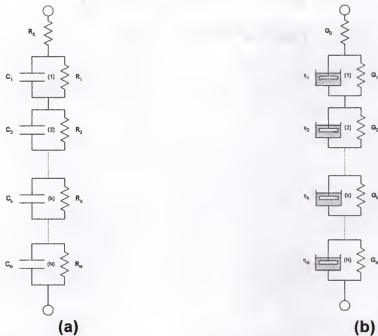


Figure 8.1. Line-shape models yielding the same mathematical structure for spectroscopic response: a) Voigt model for electrochemical systems; b) Kelvin-Voigt model for rheology of viscoelastic fluids.

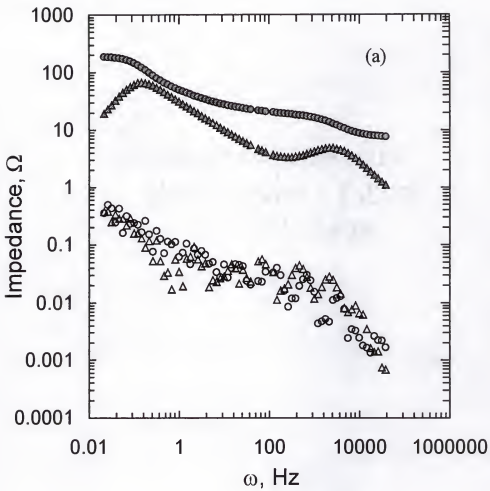


Figure 8.2. (a)The impedance response obtained under potentiostatic modulation for reduction of ferricyanide on a Pt disk electrode rotating at 120 rpm, at 1/4th of mass-transfer limited current in a 1M KCl aqueous solution. Closed symbols represent the impedance values and open symbols represent the corresponding standard deviation. O) Real part and Δ) Imaginary part. (b) F-test parameters. The inner dashed lines represent the 95% confidence limits for the F-test parameter and the outer lines represent the 99% confidence limits. Circles represent the F-test parameters for the raw standard deviations. (c) F-test parameters after deleting the point close to 50Hz and 100Hz. (d) Histogram with *t*-test results.

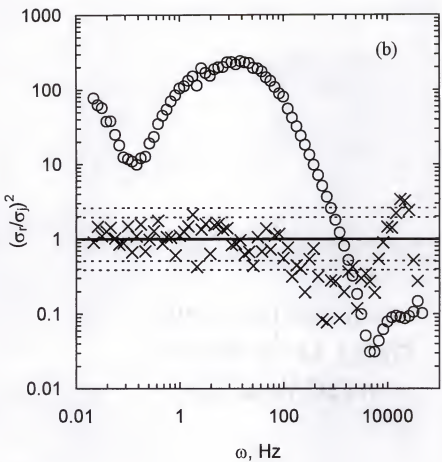


Figure 8.2--continued

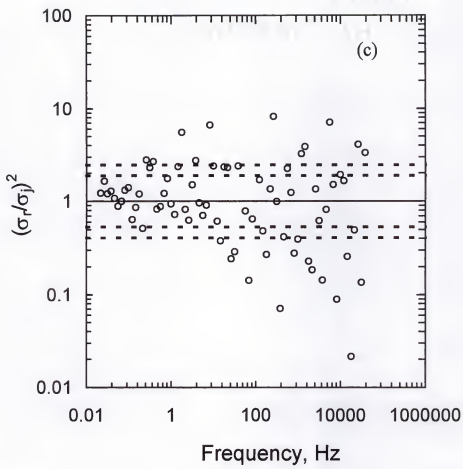


Figure 8.2--continued

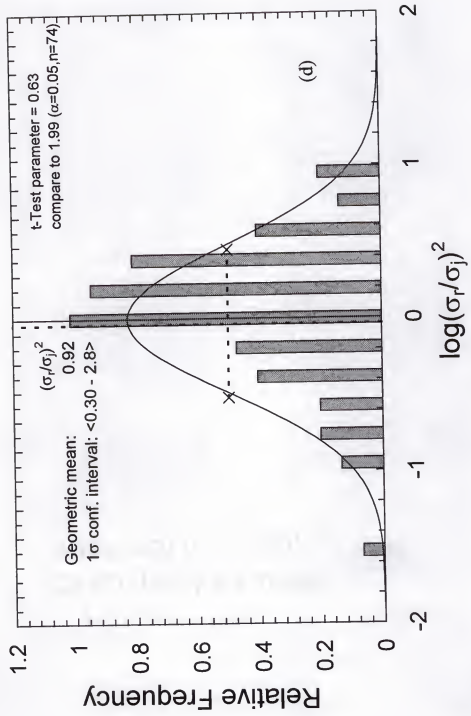


Figure 8.2--continued.

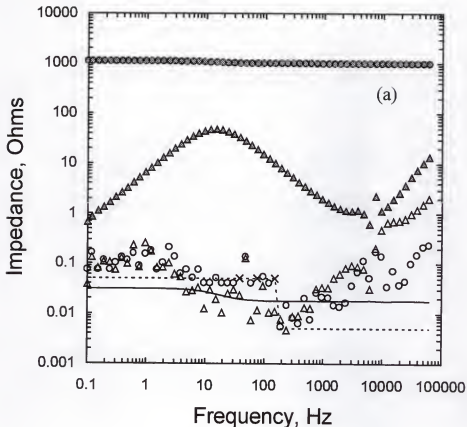


Figure 8.3. (a)The impedance response obtained under galvanostatic modulation for a parallel R_1C_1 circuit in series with a resistor R_0 ($R_0/R_1=10$). Closed symbols represent the impedance values and open symbols represent the corresponding standard deviation. The line represents the model for the error structure given as equation (8.18). O) Real part and Δ) Imaginary part. (b) F-test corresponding to the variances of stochastic noise (c) Histogram with t -test results corresponding to the variance of stochastic noise

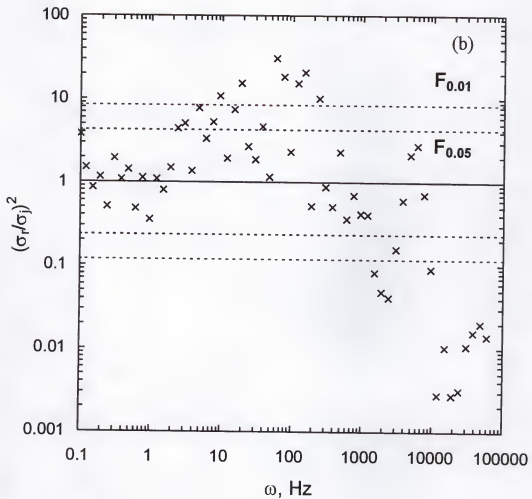


Figure 8.3--continued.

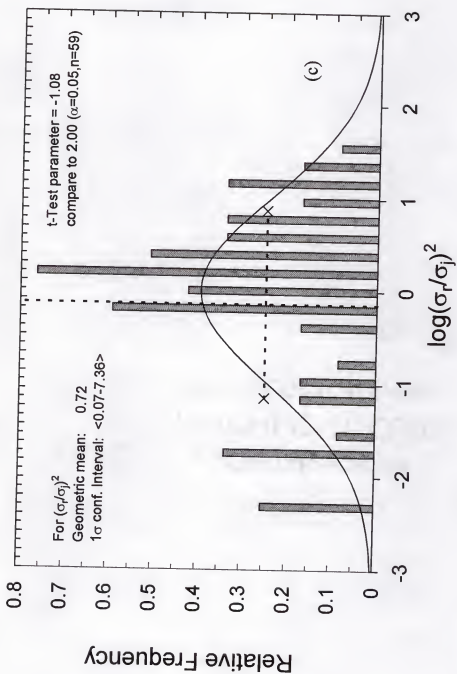


Figure 8.3--continued.

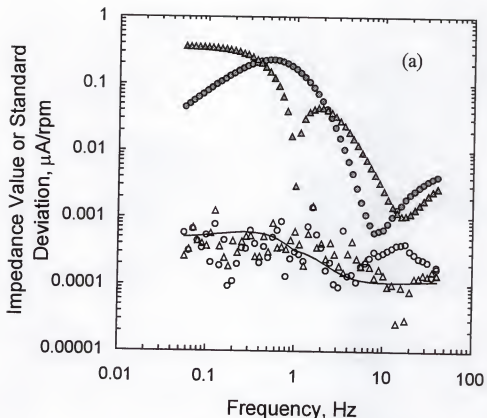


Figure 8.4. (a) The EHD impedance response obtained for reduction of ferricyanide on a Pt disk electrode rotating at 200 rpm in a 1M KCl aqueous solution. Closed symbols represent the electro-hydrodynamic impedance values and open symbols represent the corresponding standard deviation. The line represents the model for the error structure given as equation (8.18). O) Real part and Δ) Imaginary part. (b) Statistical F-test to verify the equality of standard deviations in the stochastic noise (c) Histogram with *t*-test results corresponding to the variance of stochastic noise

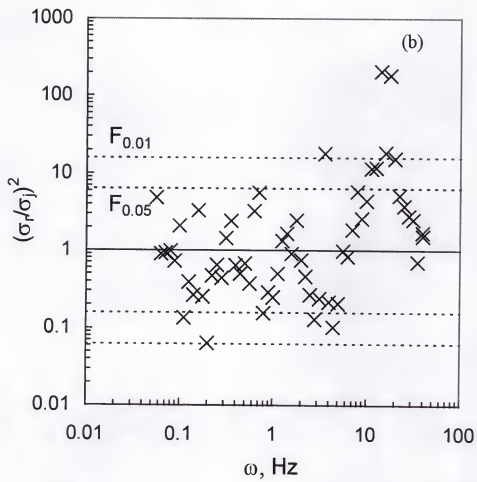


Figure 8.4--continued

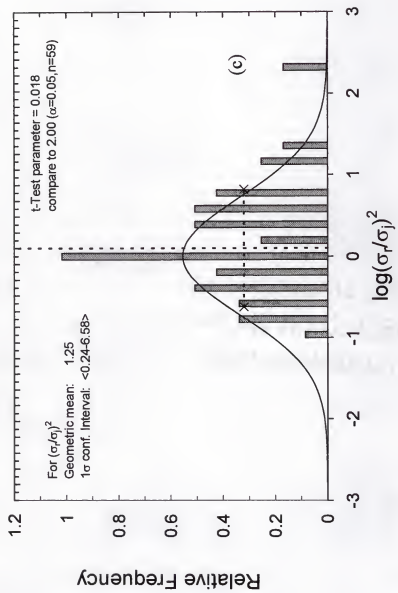


Figure 8.4--continued.

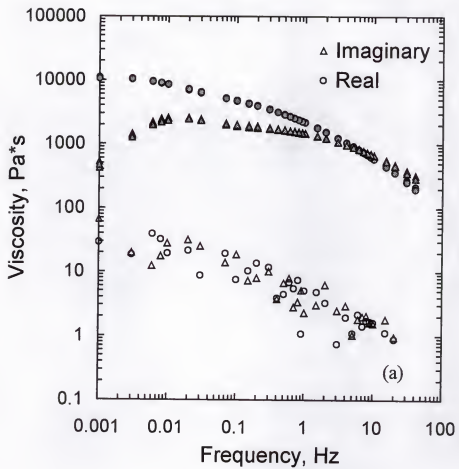


Figure 8.5. (a)The complex viscosity for high density polyethylene melt. Closed symbols represent the viscosity values and open symbols represent the corresponding standard deviation. O) Real part and Δ) Imaginary part. (b) F-test corresponding to the variances of stochastic noise (c) Histogram with *t*-test results corresponding to the variance of stochastic noise

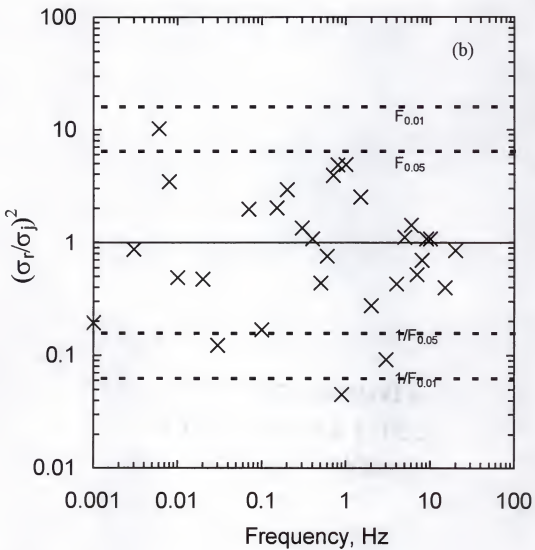


Figure 8.5--continued.

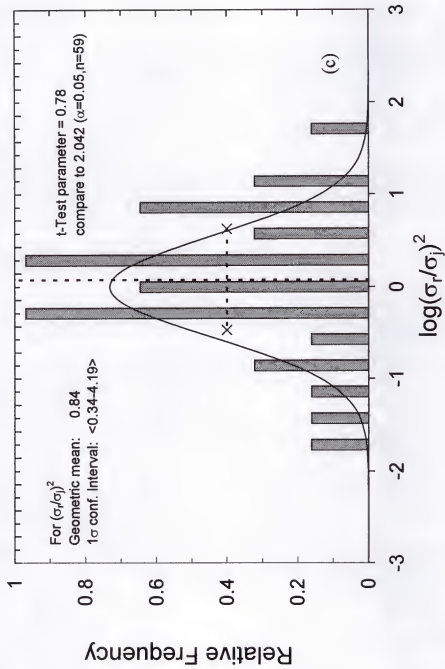


Figure 8.5--continued.

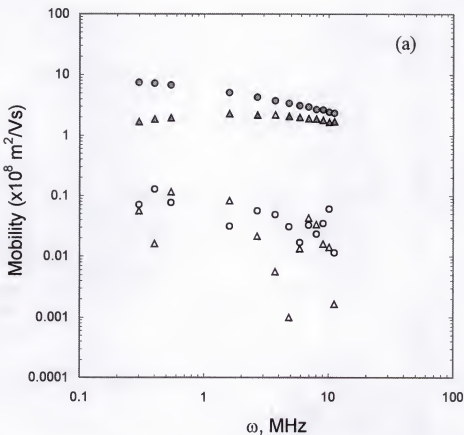


Figure 8.6. (a) The complex mobility for a suspension of polyacrylic acid (PAA) with a density of 0.062 g/L, a pH of 10, and a molecular weight of 5000. Closed symbols represent the mobility values and open symbols represent the corresponding standard deviation. O) Real part and Δ) Imaginary part. (b) F-test corresponding to the variances of stochastic noise (c) Histogram with *t*-test results corresponding to the variance of stochastic noise

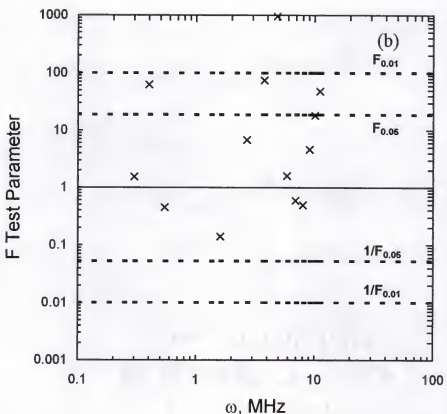


Figure 8.6--continued.

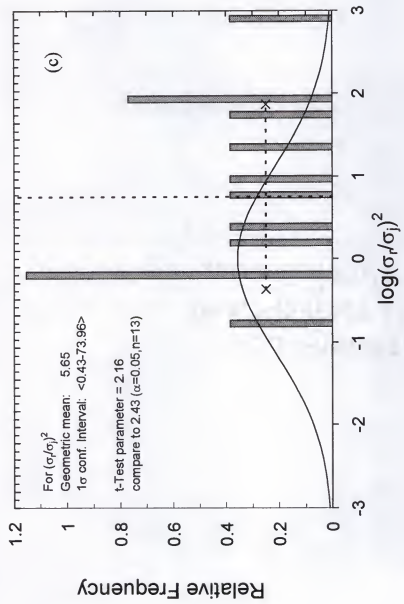


Figure 8.6--continued.

CHAPTER 9 CONCLUSIONS

The influence of the current and potential distributions as well as that of the surface phenomena on the interpretation of impedance data was presented in this thesis. A model system of potassium ferri/ferrocyanide reacting on the surface of a platinum rotating disk electrode was chosen for the purpose of this study. Experiments were conducted in the steady state domain in order to determine the best possible surface treatment. Repeated electrochemical impedance measurements were made to facilitate the study of the stochastic error structure. In all the cases it was observed that the standard deviations in the real and imaginary parts of the stochastic noise were equal. This result was proved to be a direct consequence of the applicability of Kramers-Kronig transforms to this system. The equality of standard deviations was also observed for a number of other frequency domain techniques and the results were reported in this thesis.

The frequency domain model developed by Tribollet and Newman was used to determine the Schmidt number of the ferricyanide ions using the measurement model regression strategy that employs the stochastic error structure weighting. It was observed that the Schmidt number increased with the rotation speed of the electrode. Also, when the repeated measurements were made with no surface polishing between the measurements, it was observed that the Schmidt number increased with the duration of the experiment. This was a strong evidence for the blocking phenomena.

An impedance model that accounts for the radial dependence of current, concentration, and overpotentials was developed in order to account for the non-uniformity related issues in the frequency domain. From this model it was observed that the non-uniform distributions become more significant at high rotation speeds as well as at high frequencies. A comparison is made between the one-dimensional model that was developed earlier and the two-dimensional model developed for this work. Significant differences were obtained between the result generated using the two models, especially for cases where non-uniform distributions are more prominent.

From this work it could conclusively be stated that both non-uniform distributions as well as surface phenomena should be accounted for in interpreting the impedance data.

CHAPTER 10 SUGGESTIONS FOR FUTURE WORK

There are numerous significant contributions in the broad area of electrochemical engineering made during the course of this work. This work leads to some new exciting research problems. For example, the frequency domain model developed for this work should be reformed in order to facilitate the regression of the experimental data to determine the Schmidt numbers. A two-dimensional model accounting for the distributions in case of electrohydrodynamic impedance conducted below the mass transfer limitation can be developed based on the model presented for this work. The boundary conditions can be modified in order to account for the surface passivation reactions occurring in systems such as the corrosion of copper in seawater environment. It would be interesting to explicitly account for the charge distribution within the diffuse part of the double layer to study how this will influence the result, though the impact may not be very significant. An explicit treatment for the surface blocking phenomena in the model would be an interesting and challenging problem.

With respect to the statistical aspects, an error structure should be obtained for transient measurements. Propagation of these errors when the transient data is transformed into the frequency domain would be an interesting study.

APPENDIX A STEADY STATE MODEL FOR THE ROTATING DISK ELECTRODE

```
C ****
PROGRAM DDLSS3DIS
C
C Program written by Madhav Durbha and Mark E. Orazem, documented
C into this final form on 11th June 1998. The mathematical model
C on which this program is based, is presented in detail in
C The Journal of the Electrochemical Society (June 1998), Vol. 145,
C No. 6, pp 1940-1949.
C
C Program to simulate the steady state current distributions for a
C rotating disk electrode system. The model on which the computer
C program is based explicitly accounts for the effects of mass
C transfer, kinetics, and ohmic drop within the bulk of the
C solution. This model also exclusively accounts for charge
C distribution in the diffuse part of the double layer and a finite
C schmidt number correction is incorporated into the solution for
C the convective diffusion equation.
C
C This program outputs the radial distributions of current, potential,
C concentration, charge distribution, and double layer capacitance
C on the surface of the disk electrode.
C Details of various branches of the program are explained in individual
C subroutines. In order to obtain accurate solutions, all the calculations
C were performed using double precision throughout the program.
C DDLDATA is the input file, and VOLTS, AMTHP, and SSOUT are the output
C files.
C
      INTEGER K,NMAX,MMAX,NO,IZ,IDRAMAX,I,L,IT,ITTOL,NL,LO
C
      PARAMETER(IDRAMAX=30)
C
C IDRAMAX is the variable corresponding to the number of radial positions
C used for the calculations performed. These dimensionless radial
C coordinates are generated to be the abscissa for the Gauss-Legendre
C quadrature.
C
```

```

DOUBLE PRECISION CINF, CCENT, AL(20), Q(20,20), XMPR(20), TEMP, T,
+ UPR(20), PI, XN, R, OM, R0, XNU, D, A, F, B(20), XILIM, ALPHA, BETA,
+ XKINF, XN1, XN2, XN3, ETA(IDRAMAX), C1, XI0, AMTOL, XJ0, GA,
+ PHI(IDRAMAX), V, SUMP(IDRAMAX), AM(20), csurg2(IDRAMAX),
+ XIDEN(IDRAMAX), XN4, CSURGI(IDRAMAX), CSUR(IDRAMAX),
+ RAMTOL, AMST(20), SUMRAM, W2, XINT(20,20), XLEGP,
+ WE(IDRAMAX), DRA(IDRAMAX), RERAM(IDRAMAX), X1, X2, error,
+ XIAV, XJ, SC, X, ETAC(IDRAMAX), ZETA(IDRAMAX), PERM, Y2,
+ CPOT(IDRAMAX), CFERRO(IDRAMAX), CCL(IDRAMAX),
+ CFERRI(IDRAMAX), ETAST(IDRAMAX), Q2(IDRAMAX), STEP, FAKE0,
+ FAKE1, FAKE2, INVCPD, CAPD(IDRAMAX), Q2AV

C
OPEN(UNIT=13,FILE='DDLDATA',STATUS='UNKNOWN')
READ(13,38)XNU
38 FORMAT(39X,F19.16)
C
C XNU is kinetic viscosity in (cm)**2/sec
C
READ(13,41)D
41 FORMAT(39X,F19.16)
C
C D is the diffusion coefficient in (cm)**2/sec
C
READ (13,23)LO
23 FORMAT(33X,II)
IF (LO .EQ. 0) THEN
  SC = XNU/D
  X = 1/(SC)**(1.0D0/3.D0)
  PRINT *, 'THE CALCULATIONS ARE DONE WITH FINITE SCHMIDT
+           NUMBER CORRECTION'
ELSE
  PRINT *, 'THE CALCULATIONS ARE DONE WITH INFINITE SCHMIDT
+           NUMBER ASSUMPTION'
  X = 0.D0
ENDIF
NL = IDRAMAX
X1 = 0.0D0
X2 = 1.0D0
C
CALL GAULEG(X1,X2,DRA,WE,NL)
C
C This is the subroutine that is used for generating the necessary
C abscissas and weighting factors used for the Gauss-Legendre quadrature
C integration procedure.
C

```

NMAX = 11
C
C NMAX is the maximum value of N+1 used in Q(N,M)in the steady state
C model.
C
MMAX = 11
C
C MMAX is the maximum value of M+1, M is the degree of the polynomial
C used to estimate the concentration of the reactant as a function of
C the normal distance from the surface of the disc electrode.
C
UPR(1) = -1.119846522026D0+0.333723493681D0*X
+ +0.063065495796D0*X**2
+ -0.024831364762*X**3-0.100924424861*X**4
+ -0.153916634180*X**5-0.361110032914*X**6
UPR(2) = -1.532987928427+0.348508168763*X+0.056398738367*X**2
+ -0.012443161467*X**3-0.055731225137*X**4
+ -0.075985761086*X**5-0.184336630530*X**6
UPR(3) = -1.805490583604+0.351502095496*X+0.050146600384*X**2
+ -0.008443399975*X**3-0.036778525256*X**4
+ -0.046258489551*X**5-0.103363494337*X**6
UPR(4) = -2.015723734147+0.352526039999*X+0.045670783752*X**2
+ -0.006567389500*X**3-0.027072177649*X**4
+ -0.032082498207*X**5-0.064688069153*X**6
UPR(5) = -2.189982747231+0.352984907151*X+0.042360393354*X**2
+ -0.005472434784*X**3-0.021316136406*X**4
+ -0.024033824753*X**5-0.044058591888*X**6
UPR(6) = -2.340450747257+0.353227157058*X+0.039800253199*X**2
+ -0.004743049979*X**3-0.017577424448*X**4
+ -0.018741170708*X**5-0.032338077692*X**6
UPR(7) = -2.473842753935+0.353369826902*X+0.037746320639*X**2
+ -0.004219897577*X**3-0.014925747091*X**4
+ -0.015256845657*X**5-0.024676089933*X**6
UPR(8) = -2.594287242379+0.353460658362*X+0.036050283712*X**2
+ -0.003822713947*X**3-0.012953807670*X**4
+ -0.012811642639*X**5-0.019394632191*X**6
UPR(9) = -2.704520850202+0.353521950785*X+0.034617693958*X**2
+ -0.003510623955*X**3-0.011410194860*X**4
+ -0.011135715480*X**5-0.015353967373*X**6
UPR(10)= -2.806460252572+0.353565215382*X+0.033385436778*X**2
+ -0.003255643179*X**3-0.010205811988*X**4
+ -0.009703503554*X**5-0.012705306833*X**6
UPR(11)= -2.901505452808+0.353596877262*X+0.032309432319*X**2
+ -0.003038288308*X**3-0.009267906946*X**4
+ -0.008414271284*X**5-0.010937287457*X**6

C

C One dimensional array UPR is the required value that is ,derivative of
C THETA(M) at the surface of the disc electrode. The coefficients for
C the polynomial expansion are provided by the polynomial regressions
C performed as described in the model.

C

PI = 3.141592654D0

C

C One dimensional array MPR is used to store the value of M(2N)PRIME.
C

CALL INTEGRAL(MMAX,NMAX,XINT)
CALL MPRIME(NMAX,PI,XMPR)
CALL CALCQ(MMAX,NMAX,PI,UPR,XMPR,XINT,Q)

C

C CINF is the concentration of the species in the bulk of the solution.
C

READ(13,35)R0

35 FORMAT(39X,F19.16)

C

C R0 is the radius of the disk electrode in cm

C

READ(13,37)OM

37 FORMAT(39X,F19.16)

OM = OM*PI/30

C

C OM is the angular speed of the disk electrode in rad/sec

C

READ(13,40)A

40 FORMAT(39X,F19.16)

C

C A is coefficient in series for the expansion of velocity terms

C

READ(13,42)NO

42 FORMAT(39X,I2)

C

C -NO is the number of equivalents

C

READ(13,43)IZ

43 FORMAT(35X,I2)

C

C IZ corresponds to the number of equivalents

C

READ(13,44)F

44 FORMAT(39X,F19.16)

C

C F is the Faraday's constant in Coulomb/equivalent
C

```

READ(13,45)CINF
45 FORMAT(39X,F19.16)
C
C CINF is the concentration of the species at infinite distance in moles/c.c.
C
```

READ(13,46)R
46 FORMAT(39X,F19.16)
C
C R is universal gas constant in J/mol./Kelvin.
C

```

READ(13,47)TEMP
47 FORMAT(39X,F19.16)
C
C TEMP is the temperature of the system in Kelvin.
C
```

READ(13,48)T
48 FORMAT(39X,F19.16)
C
C T is the transference number of the reactant.
C

```

READ(13,49)XKINF
49 FORMAT(39X,F19.16)
C
C XKINF is the conductivity of the solution in 1/(ohm.cm)
C
```

C1 = IZ*F/(R*TEMP)
XN1 = -(R0**2*OM/XNU)**0.5
XN2 = (A*XNU/(3*D))**1.3
XN3 = NO*C1*F*D*CINF/((1-T)*XKINF)
XN = XN1*XN2*XN3

C

READ(13,50)V
50 FORMAT(39X,F19.16)
C
C V is the applied potential in volts.
C

READ(13,51)W2
51 FORMAT(39X,F19.16)
C
C W2 is the weighting factor used in the iterations.
C

READ(13,52)CCENT
52 FORMAT(39X,F19.16)

```

C
DO 85 L=1,IDRAMAX
CSUR(L) = CCENT
85 CONTINUE
C
AL(1) = CCENT/CINF - 1
C
C AL is the one-dimensional array of the coefficients a(l) in the
C Legendre polynomial expansion for concentration terms.
C DRA is the dimensionless radial position, that is, (r/r0)
C IDRAMAX is the total number of DRA values chosen excluding 0.
C
DO 10 I = 1,IDRAMAX
ETA(I) = (1-(DRA(I))**2)**0.5
10 CONTINUE
PRINT *, ' PROGRAM IS RUNNING '
XILIM = -(NO*F*D*CINF)/(1-T)*XN2*((OM/XNU)**0.5)*UPR(1)
C
C XILIM refers to the limiting current density value in amp./(cm)**2
C
READ(13,53)GA
53 FORMAT(33X,F19.16)
C
C GA is the value of Gamma.
C
READ(13,54)XI0
54 FORMAT(38X,F19.16)
C
C XI0 is the exchange current density in amp/(cm)**2
C
READ(13,55)ALPHA
55 FORMAT(36X,F19.16)
READ(13,56)BETA
56 FORMAT(22X,F19.16)
AM(1) = AL(1)
XN4 = (NO*F*D*CINF*XN2*(OM/XNU)**0.5)/(1-T)
READ(13,57)ITTOL
57 FORMAT(39X,16)
READ(13,58)RAMTOL
58 FORMAT(39X,F19.16)
READ(13,59)AMTOL
59 FORMAT(38X,F19.16)
READ(13,60)PERM
60 FORMAT(38X,F19.16)
READ(13,61)Y2

```

```

61 FORMAT(38X,F19.16)
  READ(13,61)STEP
62 FORMAT(38X,F19.16)
C
  PRINT *, 'PLEASE NOTE:-'
  PRINT *, 'THIS PROGRAM IS SPECIFIC TO THE SYSTEM CONSIDERED.'
C

  DO 16 IT = 1,ITTOL
    CALL CALCB(XN,Q,AM,MMAX,NMAX,PI,B)
    CALL CALPHI(C1,NMAX,IDRAMAX,ETA,B,PHI)

C
C PHI is the potential just "outside" the diffusion layer.
C V is the potential applied to the disk electrode measured with
C respect to a reference electrode. This is constant through out.
C and is equal to the sum of the ohmic potential, surface
C overpotential, zeta potential, and concentration overpotential.
C
  CALL CALIDEN(XN4,AM,DRA,IDRAMAX,MMAX,UPR,XIDEN)
C
  DO 29 I = 1,IDRAMAX
    CCL(I) = 0.995D-3 + 0.5*CSUR(I)
    CPOT(I) = 1.075D-3 - 0.5*CSUR(I)
    CFERRO(I) = 0.020D-3 - CSUR(I)
    CFERRI(I) = CSUR(I)
29  CONTINUE
C
C Subroutine SPLITETAS is the one that determines the relative
C contributions of surface overpotetial and the potential drop across
C the diffuse part of the double layer.
C
  CALL SPLITETAS(CCL, CPOT, CFERRO, CFERRI, IDRAMAX, C1, F, R, TEMP,
  +   IZ, PERM, Y2, CINF, CSUR, ALPHA, BETA, GA, XI0, XIDEN, ETAST,
  +   RAMTOL, ITTOL, V, STEP, ZETA, IT, PHI)
C
  DO 334 I = 1,IDRAMAX
    ETAC(I) = V - PHI(I) - ETAST(I) - ZETA(I)
334 CONTINUE
C
C Calculates the concentration of the reacting species on the surface
C of the disk electrode.
C
  CALL CALCSUR(IDRAMAX,C1,T,CINF,ETAC,RAMTOL,ITTOL,CSUR)
C

```

```

DO 36 L = 1,MMAX
  AMST(L) = AM(L)
36 CONTINUE
C
  CALL CALAL(CSUR,CINF,DRA,IDRAMAX,WE,MMAX,AL)
C
  CALL CALAM(MMAX,AL,AM)
C
  SUMRAM = 0
  do 39 i = 1,mmax
    RERAM(I) = ABS((AM(I)-AMST(I))/AM(I))
    SUMRAM = SUMRAM + RERAM(I)
    AM(I) = W2*AM(I) + (1-W2)*AMST(I)
39 CONTINUE
IF (SUMRAM .LE. AMTOL .OR. IT .EQ. ITTOL) THEN
  XIAV = 0.D0
  Q2AV = 0.D0
  DO 434 I = 1,DRAMAX
    XIAV = XIAV + XIDEN(I)*DRA(I)*WE(I)
    Q2(I) = ETAST(I)*PERM/Y2
    Q2AV = Q2AV + Q2(I)*DRA(I)*WE(I)
434 CONTINUE
  XIAV = 2.D0*XIAV
  Q2AV = 2.D0*Q2AV
  DO 584 I = 1,DRAMAX
    FAKE0 = F*ZETA(I)/(R*TEMP)
    FAKE1 = CPOT(I)*(DEXP(-FAKE0)-1.D0)+CCL(I)*(DEXP(FAKE0)-1.D0)
    +      +CFERRI(I)*(DEXP(3.D0*FAKE0)-1.D0)
    +      +CFERRO(I)*(DEXP(4.D0*FAKE0)-1.D0)
    FAKE1 = DSQRT(2.D0*FAKE1)
    FAKE2 = CPOT(I)*DEXP(-FAKE0)-CCL(I)*DEXP(FAKE0)
    +      -3.D0*CFERRI(I)*DEXP(3.D0*FAKE0)
    +      -4.D0*CFERRO(I)*DEXP(4.D0*FAKE0)
    FAKE1 = (FAKE1/FAKE2)*DSQRT(R*TEMP/PERM)/F
    INVCPD = (Y2/PERM)+FAKE1
    CAPD(I) = 1/INVCPD
584 CONTINUE
  XJ = XIAV*R0*BETA*F/(R*TEMP*XKINF)
  XJI0 = XJ0*R0*IZ*F/(R*TEMP*XKINF)
  PRINT *,XILIM,XILIM
  print *,XIAV,XIAV
  print *,xn,XN
  PRINT *,XJ,XJ
  PRINT *,XJ0,R0,IZ,F,R,TEMP,XKINF
  PRINT *,XJI0,XJI0

```

```

print *, 'pot. diff', PHI(IDRAMAX)-PHI(1)
Print *, 'error', SUMRAM
PRINT *, 'curr @ r=0', XIDEN(1)
print *, 'c(0)/c_inf', CSUR(1)/CINF
print *, 'i(0)/i_avg', XIDEN(1)/XIAV
print *, 'XIAV/XILIM', XIAV/XILIM

c
OPEN(UNIT = 3,FILE='VOLTS',STATUS='UNKNOWN')
CLOSE(UNIT = 3,STATUS = 'DELETE')
OPEN(UNIT = 3,FILE='VOLTS',STATUS='UNKNOWN')
    WRITE(3,173)
OPEN(UNIT = 13,FILE='AMTHP',STATUS='UNKNOWN')
CLOSE(UNIT = 13,STATUS = 'DELETE')
OPEN(UNIT = 13,FILE='AMTHP',STATUS='UNKNOWN')

c
OPEN(UNIT = 33,FILE='SSOUT',STATUS='UNKNOWN')
CLOSE(UNIT = 33,STATUS = 'DELETE')
OPEN(UNIT = 33,FILE='SSOUT',STATUS='UNKNOWN')
    WRITE(33,174)
DO 597 K = 1, IDRAMAX
    WRITE(3,111)DRA(K),ETAST(K),ZETA(K),ETAC(K),PHI(K),Q2(K)
+        ,CSUR(K)/CINF,XIDEN(K)/XIAV,XIDEN(K)/XILIM,
+        CAPD(K),Q2(K)/Q2AV
    WRITE(33,116)DRA(K),ETAST(K),ZETA(K),ETAC(K),PHI(K),Q2(K)
+        ,CSUR(K),XIDEN(K)
597 CONTINUE
c
PRINT *, 'Y2 is ', Y2
print *, 'IT is ', IT
WRITE(13,*)'The values for Am coefficients are'
112 FORMAT(6X,E20.14)
DO I = 1,11
    WRITE(13,112)AM(I)
ENDDO
WRITE(13,*)
WRITE(13,*)'The values for thmpr coefficients are'
DO I = 1,11
    WRITE(13,112)UPR(I)
ENDDO
WRITE(13,*)
WRITE(13,*)'The values for the Q(N,M) coefficients are'
DO I = 1,NMAX
    DO J = 1,MMAX
        WRITE(13,112)Q(I,J)
    ENDDO

```

```

ENDDO
WRITE(13,*)
173 FORMAT(2X,'RADIAL POSITION',9X,'ETAS STAR',12X,'ZETA POT.',10X,
+CONC OVERPOT.',9X,'OHMIC DROP',14X,'Q2',18X,'CSUR/CINF',11X,
+'ISUR/IAVG',12X,'ISUR/LIM',10X,'CAPACITANCE',10X,'Q2/Q2AVG')
174 FORMAT(2X,'RADIAL POSITION',12X,'ETAS STAR',14X,'ZETA POT.',12X,
+CONC OVERPOT.',12X,'OHMIC DROP',16X,'Q2',20X,'CSUR',19X,'ISUR')
111 FORMAT(E18.12,3X,E18.12,3X,E18.12,3X,E18.12,3X,E18.12,3X,E18.12,
+      3X,E18.12,3X,E18.12,3X,E18.12,3X,E18.12)
116 FORMAT(E20.14,3X,E20.14,3X,E20.14,3X,E20.14,3X,E20.14,3X,E20.14,
+      3X,E20.14,3X,E20.14)

C
CLOSE(33)
CLOSE(13)
CLOSE(3)

C
STOP
ENDIF
16 CONTINUE
STOP
END

C
C-----
SUBROUTINE GAULEG(X1,X2,X,W,NL)
C-----
C
C Source: Numerical Recipes in FORTRAN, 2nd ed.
C
C Given the lower and upper limits of integration X1 and X2, and given
C NL, this routine returns arrays X(1:NL) and W(1:NL) of length NL,
C containing the abscissas and weights of the Gauss Legendre NL-point
C quadrature formula.
C
C
DOUBLE PRECISION XM,XL,Z,P1,P2,P3,PP,EPS
DOUBLE PRECISION X1,X2,W(NL),X(NL),Z1,DUMMY
INTEGER M,NL,I,J
EPS = 1.D-14
M = (NL+1)/2
XM = 0.5*(X2+X1)
XL = 0.5*(X2-X1)
DUMMY=1.0/(NL+0.5)
DO 12 I = 1,M
    Z = COS(3.141592654*(I-0.25)*DUMMY)
1   CONTINUE

```

```

P1 = 1.0
P2 = 0.0
DO 11 J = 1,NL
    P3 = P2
    P2 = P1
    P1 = ((2**J-1)*Z**P2-(J-1)*P3)/DFLOAT(J)
11   CONTINUE
    PP = NL*(Z**P1-P2)/(Z**Z-1)
    Z1 = Z
    Z = Z1-P1/PP
    IF (ABS(Z-Z1) .GT. EPS) GO TO 1
    X(I) = XM - XL*Z
    X(NL+1-I) = XM + XL*Z
    W(I) = 2*XL/((1-Z**Z)**PP*PP)
    W(NL+1-I) = W(I)
12   CONTINUE
    RETURN
    END

```

C-----
C DOUBLE PRECISION FUNCTION FACT(N)
C-----
C
C Function subprogram to calculate the factorial of a given number
C

```
INTEGER N
IF (N .GE. 2) THEN
FACT = 1.
DO 15 I = 1,N
FACT = FACT*DFLOAT(I)
15 CONTINUE
ELSE
    FACT = 1.
ENDIF
RETURN
END
```

```
C
C-----  
SUBROUTINE MPRIME(NMAX,PI,XMPR)
C-----  
C
C Subroutine subprogram that evaluates the value of M(2N)PRIME at 0.
```

```
INTEGER NMAX,I,IDRAMAX  
DOUBLE PRECISION XMPR(20),PI  
DOUBLE PRECISION FACT,PROD,INVPI
```

```

INVPI=1.0/PI
DO 10 I = 1,NMAX
  XMPR(I) = -2*(2**((I-1)*FACT(I-1)/PROD(2*(I-1),I-1))**2*INVPI
10 CONTINUE
RETURN
END
C
C-----
SUBROUTINE INTEGRAL(MMAX,NMAX,Y)
C-----
C
C Subroutine subprogram that evaluates the integral that is involved in
C calculating Q(N,M).
C Please note that the values of the definite integral are exact.
C There is no approximation involved.
C
INTEGER MMAX,NMAX,M,N,K,L,IB,IA,IC
DOUBLE PRECISION D,XNUM,DIN,Y(20,20),SUM,A1
DOUBLE PRECISION FACT,PROD
DO 10 N = 1,NMAX
  DO 21 M = 1,MMAX
    SUM = 0
    DO 30 K = 0,M-1
      DO 40 L = 0,N-1
        A1 = PROD(M-1,M-K-1)/FACT(K)
        XNUM = A1*(PROD(4*(N-1)-2*L,2*(N-1)-L)/FACT(2*(N-1)-2*L))
        DIN = FACT(L)
        IA = 2**((2*N-1)
        IB = N-L+K
        IC = (-1)**(L+K)
        D = (IC*XNUM/IA)*1/(DIN*IB)
        SUM = SUM + D
40    CONTINUE
30    CONTINUE
      Y(N,M) = SUM
C
21    CONTINUE
10    CONTINUE
RETURN
END
C
C-----
DOUBLE PRECISION FUNCTION PROD(M,N)
C-----
C

```

C Function PROD(M,N) gives the value of FACT(M)/FACT(N).

C

```
INTEGER M,N
IF (M.GE.1 .AND. N.LT.M) THEN
PROD = 1.
DO 20 I = N+1,M
    PROD = PROD*DFLOAT(I)
```

20 CONTINUE

```
ELSE
    PROD = 1.
```

ENDIF

RETURN

END

C

C-----

SUBROUTINE CALCQ(MMAX,NMAX,PI,UPR,XMPR,XINT,Q)

C-----

C

C This subroutine calculates the value of Q(N,M) for different values of
C N and M.

C

INTEGER N,M,MMAX,NMAX

DOUBLE PRECISION PI,UPR(20),XMPR(20),XINT(20,20),Q(20,20)

DO 10 N = 1,NMAX

DO 20 M = 1,MMAX

Q(N,M) = (4*N-3)*4*UPR(M)*XINT(N,M)/(PI*XMPR(N))

20 CONTINUE

10 CONTINUE

RETURN

END

C

C-----

SUBROUTINE CALCB(XN,Q,AM,MMAX,NMAX,PI,B)

C-----

C

C This subroutine calculates the values for B making use of Q and AL.

C

INTEGER MMAX,NMAX,I,J

DOUBLE PRECISION XN,Q(20,20),AM(20),PI,B(20)

DO 10 I = 1,NMAX

B(I) = 0

DO 20 J = 1,MMAX

B(I) = B(I) + Q(I,J)*AM(J)

20 CONTINUE

B(I) = PI*XN*B(I)*.25

```

10 CONTINUE
    RETURN
    END
C
C-----SUBROUTINE CALPHI(C1,NMAX,IDRAMAX,ETA,B,PHI)
C-----
C
C This subroutine calculates the values of PHI
C
    INTEGER NMAX, IDRAMA X, I, J
    DOUBLE PRECISION C1, ETA(IDRAMAX), B(20), PHI(IDRAMAX)
    DOUBLE PRECISION XLEGP, INVCI
    INVCI=1.0/C1
    DO 10 I = 1, IDRAMAX
        PHI(I) = 0
        DO 20 J = 1, NMAX
            PHI(I) = PHI(I)+B(J)*XLEGP(J-1,ETA(I))
20    CONTINUE
    PHI(I) = PHI(I)*INVCI
10    CONTINUE
    RETURN
    END
C
C-----DOUBLE PRECISION FUNCTION XLEGP(N,XIN)
C-----
C
C This function calculates the Legendre polynomial expansion for P(2*N,X)
C
    INTEGER N, I, IA, IB, IC
    DOUBLE PRECISION XIN, XNUM, DIN
    DOUBLE PRECISION FACT, PROD, SUM
    SUM = 0.
    NP1=N+1
    DO 10 K = 1, NP1
        I=K-1
        IA = 4*N-2*I
        IB = 2*N-I
        IC = 2*N-2*I
        IF (N .EQ. 0) THEN
            XLEGP = 1
            RETURN
        ENDIF

```

```

IF (XIN.EQ.0 .AND. IC.EQ.0) THEN
    XNUM = ((PROD(IA,IB)/FACT(IC))/FACT(I))
ELSE
    XNUM = ((PROD(IA,IB)/FACT(IC))/FACT(I))*XIN**IC
ENDIF
    DIN = DFLOAT(2**((2*N)))
    SUM = SUM + (-1)**I*XNUM/DIN
10 CONTINUE
    XLEGP = SUM
    RETURN
END
C
C-----  

SUBROUTINE CALIDEN(XN4,AM,DRA,DRAMAX,MMAX,UPR,XIDEN)
C-----  

C
C This subroutine calculates the current density at various points on the
C disk from using various input parameters.
C
    DOUBLE PRECISION XN4, AM(20), DRA(DRAMAX), UPR(20),
+      XIDEN(DRAMAX)
    INTEGER MMAX,DRAMAX,I,J
    DO 10 I = 1,DRAMAX
        XIDEN(I) = 0
        DO 20 J = 1,MMAX
            XIDEN(I) = XIDEN(I) + AM(J)*(DRA(I))**((2*(J-1))*UPR(J)
20    CONTINUE
        XIDEN(I) = XN4*XIDEN(I)
10    CONTINUE
    RETURN
END
C
C-----  

SUBROUTINE SPLITETAS (CCL, CPOT, CFERRO, CFERRI, DRAMAX, C1,
+      F, R, TE, IZ, PERM, Y2, CINF, CSUR, ALPHA, BETA, GA, XI0,
+      XIDEN, ETAST, RAMTOL, ITTOL, V, STEP, ZETA, IT, PHI)
C-----  

C
C Subroutine to calculate the individual contributions of surface
C overpotential and zeta potential. Uses a combination of Newton-Raphson
C and bisection schemes. Source code taken from the 2nd edition of
C numerical recipes in FORTRAN and is adapted for solving the present
C problem.
C
    INTEGER IDRAMAX,IZ,ITTOL,IT

```

```

DOUBLE PRECISION CCL(IDRAMAX), CPOT(IDRAMAX),
+ CFERRO(IDRAMAX), CFERRI(IDRAMAX), C1, F, R, TE, PERM, Y2, CINF,
+ CSUR(IDRAMAX), XI0, ALPHA, BETA, GA, XIDEN(IDRAMAX),
+ ETAST(IDRAMAX), ZETA(IDRAMAX), DUM0, DUM1, DUM2, DUM3,
+ DUM4, DUM5, SQR, RTSAFE(IDRAMAX), XL, XH, DF, X, X1, X2,
+ RAMTOL, DXOLD, V, TEMP, FL, FH, F1, PHI(IDRAMAX), STEP
DOUBLE PRECISION FUN,FD
C
C DO 10 I = 1, IDRAMAX
C
C COMPUTE SEQUENCE OF POINTS CONVERGING TO THE ROOT
C
X1 = 0.
H = STEP*(V-PHI(I))
X2 = H
FL=FUN(C1,IZ,ALPHA,BETA,GA,R,TE,CINF,PERM,Y2,CPOT(I),CCL(I),
+ CFERRI(I),CFERRO(I),CSUR(I),XI0,XIDEN(I),X1)
FH=FUN(C1,IZ,ALPHA,BETA,GA,R,TE,CINF,PERM,Y2,CPOT(I),CCL(I),
+ CFERRI(I),CFERRO(I),CSUR(I),XI0,XIDEN(I),X2)
C
DO WHILE (FL*FH .GT. 0. .AND. DABS(X2) .LT. DABS(V))
X1 = X1 + H
X2 = X1 + H
C
FL=FUN(C1,IZ,ALPHA,BETA,GA,R,TE,CINF,PERM,Y2,CPOT(I),CCL(I),
+ CFERRI(I),CFERRO(I),CSUR(I),XI0,XIDEN(I),X1)
FH=FUN(C1,IZ,ALPHA,BETA,GA,R,TE,CINF,PERM,Y2,CPOT(I),CCL(I),
+ CFERRI(I),CFERRO(I),CSUR(I),XI0,XIDEN(I),X2)
END DO
C
IF ((FL.GT.0..AND.FH.GT.0.) OR.(FL.LT.0..AND.FH.LT.0.)) THEN
PAUSE 'ROOT MUST BE BRACKETED IN RTSAFE'
ENDIF
IF (FL.EQ.0.) THEN
RTSAFE(I) = X1
GO TO 10
ELSE IF (FH.EQ.0.) THEN
RTSAFE(I) = X2
GO TO 10
ELSE IF (FL.LT.0.) THEN
XL = X1
XH = X2
ELSE
XH = X1
XL = X2

```

```

ENDIF
RTSAFE(I) = 0.5*(X1+X2)
C
DXOLD = ABS(X2-X1)
DX = DXOLD
F1=FUN(C1,IZ,ALPHA,BETA,GA,R,TE,CINF,PERM,Y2,CPOT(I),CCL(I),
+ CFERRI(I),CFERRO(I),CSUR(I),XI0,XIDEN(I),RTSAFE(I))
DF=FD(C1,IZ,ALPHA,BETA,GA,R,TE,PERM,Y2,F,CPOT(I),CCL(I),
+ CFERRI(I),CFERRO(I),RTSAFE(I))
DO 11 J = 1,ITTL
    IF(((RTSAFE(I)-XH)*DF-F1)*((RTSAFE(I)-XL)*DF-F1).GE.0.
+ .OR.ABS(2.0*F1).GT.ABS(DXOLD*DF)) THEN
        DXOLD = DX
        DX = 0.5*(XH-XL)
        RTSAFE(I)= XL+DX
        IF(XL.EQ.RTSAFE(I))GO TO 10
    ELSE
        DXOLD = DX
        DX = F1/DF
        TEMP = RTSAFE(I)
        RTSAFE(I)= RTSAFE(I)-DX
        IF (TEMP.EQ.RTSAFE(I))GO TO 10
        ENDIF
        IF (ABS(DX).LT.RAMTOL) GO TO 10
        F1=FUN(C1,IZ,ALPHA,BETA,GA,R,TE,CINF,PERM,Y2,CPOT(I),CCL(I),
+ CFERRI(I),CFERRO(I),CSUR(I),XI0,XIDEN(I),RTSAFE(I))
        DF=FD(C1,IZ,ALPHA,BETA,GA,R,TE,PERM,Y2,F,CPOT(I),CCL(I),
+ CFERRI(I),CFERRO(I),RTSAFE(I))
        IF (F1.LT.0.) THEN
            XL = RTSAFE(I)
        ELSE
            XH = RTSAFE(I)
        ENDIF
    11 CONTINUE
    PAUSE 'RTSAFE EXCEEDING MAXIMUM ITERATIONS'
10  CONTINUE
DO 20 I=1,IDRAMAX
    ZETA(I) = RTSAFE(I)
    DUM0 = ZETA(I)*C1/IZ
    DUM1 = CPOT(I)*(DEXP(-DUM0)-1.0)
    DUM2 = CCL(I)*(DEXP(DUM0)-1.0)
    DUM3 = CFERRI(I)*(DEXP(3.0*DUM0)-1.0)
    DUM4 = CFERRO(I)*(DEXP(4.0*DUM0)-1.0)
    DUM5 = 2.0*R*TE/PERM
    SQR = (DUM5*(DUM1+DUM2+DUM3+DUM4))**0.5

```

```

      ETAST(I) = -Y2*SQR
20  CONTINUE
      RETURN
      END
C-----
C----- DOUBLE PRECISION FUNCTION FUN(C1, IZ, ALPHA, BETA, GA, R, TEMP,
+    CINF, PERM, Y2, CPOT, CCL, CFERRI, CFERRO, CSUR, XI0, XIDEN,
+    ZETA)
C-----
C----- INTEGER IZ
C----- DOUBLE PRECISION C1, ALPHA, BETA, GA, R, TEMP, PERM, Y2, CPOT,
+    CCL, CINF, CFERRI, CFERRO, ZETA, XIDEN, XI0, CSUR, DUM0, DUM1,
+    DUM3, DUM4, DUM5,DUM6,DUM7,DUM8,SQR
      DUM0 = ZETA*C1/IZ
C----- DUM1 = DEXP(DUM0*GA*3.0)
      DUM3 = CPOT*(DEXP(-DUM0)-1.0)
      DUM4 = CCL*(DEXP(DUM0)-1.0)
      DUM5 = CFERRI*(DEXP(3.0*DUM0)-1.0)
      DUM6 = CFERRO*(DEXP(4.0*DUM0)-1.0)
      DUM7 = 2.0*R*TEMP/PERM
      DUM8 = (XIDEN/XI0)*(CINF/CSUR)**GA
C----- SQR = (DUM7*(DUM3+DUM4+DUM5+DUM6))**0.5
      FUN = DUM1*(DEXP(-ALPHA*C1*Y2*SQR)-DEXP(BETA*C1*Y2*SQR))-+
        DUM8
C----- RETURN
      END
C-----
C----- DOUBLE PRECISION FUNCTION FD(C1, IZ, ALPHA, BETA, GA, R, TEMP,
+    PERM, Y2, F, CPOT, CCL, CFERRI, CFERRO, ZETA)
C-----
C----- INTEGER IZ
C----- DOUBLE PRECISION C1,ALPHA,BETA,GA,R,TEMP,PERM,Y2,CPOT,CCL,F,
+    CFERRI,CFERRO,ZETA,VAR0,VAR1,VAR2,VAR3,VAR4,VAR5,
+    VAR6,VAR7,VAR8,FIRST,SECOND,FIRST1,SECOND1,SQR
      VAR0 = ZETA*C1/IZ
C----- VAR2 = DEXP(VAR0*(BETA*IZ-GA*3.0))
      VAR3 = CPOT*(DEXP(-VAR0)-1.0)
      VAR4 = CCL*(DEXP(VAR0)-1.0)
      VAR5 = CFERRI*(DEXP(3.0*VAR0)-1.0)

```

```

VAR6 = CFERRO*(DEXP(4.0*VAR0)-1.0)
VAR7 = 2.0*R*TEMP/PERM
SQR = (VAR7*(VAR3+VAR4+VAR5+VAR6))**0.5
FIRST = DEXP(-ALPHA*C1*Y2*SQR)
SECOND = DEXP(BETA*C1*Y2*SQR)
FIRST1 = (3.0*GA*C1/IZ)*DEXP(3.0*GA*VAR0)*(FIRST-SECOND)
VAR8 = CPOT*DEXP(-VAR0)-CCL*DEXP(VAR0)
+ -3.0*CFERRI*DEXP(3.0*VAR0)-4.0*CFERRO*DEXP(4.0*VAR0)
VAR8 = F*VAR8/PERM
SECOND1 = C1*Y2*(VAR8/SQR)*(ALPHA*FIRST+BETA*SECOND)*
+ DEXP(3.0*GA*VAR0)
FD = FIRST1 + SECOND1
RETURN
END
C
C-----SUBROUTINE CALCSUR (IDRAMAX, C1, T, CINF, ETAC, RAMTOL, ITTOL,
+ CSUR)
C-----C
C
        INTEGER IDRAMAX,I,ITTOL
        DOUBLE PRECISION C1, T, CINF, ETAC(IDRAMAX), CSUR(IDRAMAX), X,
+ X1, X2, RTSAFE(IDRAMAX),DX,DXOLD,F,XL,XH,RAMTOL,FL,FH
        DOUBLE PRECISION FUN1,FD1
C
        DO 10 I = 1, IDRAMAX
C
C COMPUTE SEQUENCE OF POINTS CONVERGING TO THE ROOT
C
        X1 = 1.0D-250
        X2 = 1.0D0
        FL=FUN1(ETAC(I),C1,T,X1)
        FH=FUN1(ETAC(I),C1,T,X2)
C
        IF ((FL.GT.0..AND.FH.GT.0.) .OR. (FL.LT.0..AND.FH.LT.0.))
+ PAUSE 'ROOT MUST BE BRACKETED IN RTSAFE'
        IF (FL.EQ.0.) THEN
            RTSAFE(I) = X1
            GO TO 10
        ELSE IF (FH.EQ.0.) THEN
            RTSAFE(I) = X2
            GO TO 10
        ELSE IF (FL.LT.0.) THEN
            XL = X1
            XH = X2

```

```

        ELSE
        XH = X1
        XL = X2
ENDIF
RTSAFE(I) = 0.5*(X1+X2)
DXOLD = ABS(X2-X1)
DX = DXOLD
F=FUN1(ETAC(I),C1,T,RTSAFE(I))
DF=FD1(C1,T,RTSAFE(I))
DO 11 J = 1,ITOL
IF(((RTSAFE(I)-XH)*DF-F)*((RTSAFE(I)-XL)*DF-F).GE.0.
+     .OR.ABS(2.0*F).GT.ABS(DXOLD*DF)) THEN
    DXOLD = DX
    DX = 0.5*(XH-XL)
    RTSafe(I)= XL+DX
    IF(XL.EQ.RTSAFE(I))GO TO 10
ELSE
    DXOLD = DX
    DX = F/DF
    TEMP = RTSAFE(I)
    RTSafe(I)= RTSAFE(I)-DX
    IF (TEMP.EQ.RTSAFE(I))GO TO 10
ENDIF
IF (ABS(DX).LT.RAMTOL) GO TO 10
F=FUN1(ETAC(I),C1,T,RTSAFE(I))
DF=FD1(C1,T,RTSAFE(I))
IF (F.LT.0.) THEN
    XL = RTSAFE(I)
ELSE
    XH = RTSAFE(I)
ENDIF
11 CONTINUE
PAUSE 'RTSAFE EXCEEDING MAXIMUM ITERATIONS'
10 CONTINUE
DO 20 I=1,IDRAMAX
    CSUR(I) = CINF*RTSAFE(I)
20 CONTINUE
RETURN
END
C
C-----
DOUBLE PRECISION FUNCTION FUN1(ETAC,C1,T,X)
C-----
C
DOUBLE PRECISION ETAC,C1,T,X

```

```

FUN1 = (DLOG(X)+T*(1-X))/C1 - ETAC
RETURN
END
C
C----- DOUBLE PRECISION FUNCTION FD1(C1,T,X)
C----- C
C----- DOUBLE PRECISION C1,T,X
FD1 = (1/X - T)/C1
RETURN
END
C
C----- SUBROUTINE CALAL(CSUR,CINF,DRA,IDRAMAX,WE,MMAX,AL)
C----- C
C----- This subroutine calculates the AL coefficients using trapezoidal rule.
C----- C
      DOUBLE PRECISION CSUR(IDRAMAX),CINF,DRA(IDRAMAX),
+      AL(20),SUM,WE(IDRAMAX),A
      INTEGER IDRAMAX,I,J,MMAX
      DOUBLE PRECISION XLEGP,INVCF
      INVCF=1.0/CINF
      DO 10 I = 1,MMAX
         SUM = 0
         DO 20 J = 1,IDRAMAX
            A = ((CSUR(J))*INVCF - 1)*XLEGP(I-1,DRA(J)))
            SUM = SUM + A*WE(J)
20      CONTINUE
         AL(I) = (4*I - 3)*SUM
10      CONTINUE
      RETURN
      END
C
C----- SUBROUTINE CALAM(MMAX,AL,AM)
C----- C
C----- This subroutine calculates the AM coefficnts using AL coefficnts.
C----- C
      INTEGER MMAX,I,J
      DOUBLE PRECISION AL(20),AM(20),SUM
      DOUBLE PRECISION COEFF

```

```
DO 10 I = 1,MMAX
    SUM = 0
        DO 20 J = I,MMAX
            SUM = SUM + AL(J)*COEFF(J-1,J-I)
20    CONTINUE
    AM(I) = SUM
10    CONTINUE
    RETURN
END

C
C----- DOUBLE PRECISION FUNCTION COEFF(N,IR)
C----- C This function subprogram calculates the coefficients in the legendre
C polynomial expansion.
C
    INTEGER N,IR,IA,IB,IC
    DOUBLE PRECISION FACT,PROD
    DOUBLE PRECISION XNUM,DIN
    IA = 4*N - 2*IR
    IB = 2*N - IR
    IC = 2*N - 2*IR
    XNUM = (PROD(IA,IB)/FACT(IC))/FACT(IR)
    DIN = 2**((2*N)
    COEFF = ((-1)**IR)*XNUM/DIN
    RETURN
END

C
C----- C
```

APPENDIX B
FREQUENCY DOMAIN MODEL FOR THE ROTATING DISK ELECTRODE

PROGRAM CAPIMP8_LDIS

C

C Model formulated and program written by Madhav Durbha and Mark E. Orazem.
C DATE LAST MODIFIED: June 11th, 1998. The theoretical development of the
C Mathematical model is presented in Chapter 5. Model is also presented in the
C manuscript "A Mathematical Model for the Radially Dependent Impedance
C of a Rotating Disk Electrode," to be published in the conference
C proceedings volume of the 1998 Electrochemical Society meeting
C (May 3rd, 1998) held in San Diego, California.

C

C

C This program calculates the local impedances for a specified frequency.
C By specifying a number of frequencies, impedance spectrum can be obtained.
C All the computations are performed using double precision. Baseline
C values for impedance calculations are obtained by using the steady state
C program without explicitly accounting for the double layer capacitance.
C Capacitance is assumed to be uniformly distributed across the surface
C of the electrode. A finite Schmidt number correction is incorporated.
C John Newman's BAND algorithm is employed to solve for the homogenous
C part of the convective diffusion equation in the frequency domain.

C

IMPLICIT DOUBLE PRECISION (A-H,O-Z)

IMPLICIT INTEGER*8 (I-N)

COMMON/BA/ A(6,6),B(6,6),C(6,10001),D(6,13),G(6),X(6,6),Y(6,6)

COMMON/NS/ NVAR,NJ,LFREQ,NMAXP1,MMAXP1,NFRE

COMMON/AA/ XNU,DIF,FRK(90),BK,CK,MA1,CBULK(6),CONC(6,10001),

+ CONV(6,10001),AMTG,AMSS(11),THMPRSS(11),CINF,TRAN,

+ AAL,OM,NO,FA,QSS(11,11),R0,IZ,TEMP,XN,R,XKINF,WW(90),

+ CDDL

COMMON/BB/ H,DEL

COMMON/CC/ SUMH

COMMON/SIMP/ XI(10001)

COMMON/GAUQUA/ DRA(60),WE(60),IDRAMAX,YINT(11,11),ETA(60)

COMMON/OP/CURFRTIL(60),CURFTIL(60),THPTR(11),

+ THPTJ(11),AMTR(11),AMTJ(11),CSURTILR(60),

+ CSURTILJ(60)

COMMON/QTIL/QRTILDA(11,11),QJTLDA(11,11)

```

DIMENSION THMREAP(11,10001),THMIMAP(11,10001),
+    FRKHSQR(90),THMREAPSS(11,10001),
+    FUNCR(10001),FUNCJ(10001),AMTRST(11),AMTJST(11),
+    OUTR(11),OUTJ(11),ZR(90),ZJ(90),ZLocr(60),
+    ZLOCJ(60),DUMETC(60),CURPRESR(60),CURPRESJ(60),
+    ALTRST(11),ALTJST(11)
COMMON/BTIL/BRTILDA(11),BJTILDA(11),C1
COMMON/PHI/PHITR(60),PHITJ(60)
COMMON/SS/ ETASTSS(60),ZETASS(60),ETACSS(60),PHISS(60),
+    Q2SS(60),CSURSS(60),XIDENSS(60)
COMMON/ETAS/ ALPHA,BETA,GAMMA,
+    XZ(60),YZ(60),VAR0(60),DNRZ(60),XI0,
+    ZETTILR(60),ZETTILJ(60),ETASTILR(60),
+    ETASTILJ(60),BZ(60),Y2
COMMON/CONC/ ETACTILR(60),ETACTILJ(60)
COMMON/AL/ ALTR(11),ALTJ(11)
COMMON/AV/ CURTILAVR(90),CURTILAVJ(90)
COMMON/CUR/CURTILR(60),CURTILJ(60)
COMMON/CL/ CLTR(11),CLTJ(11)
COMMON/CM/ CMTR(11),CMTJ(11)

C      NMAXP1 = 11
      MMAXP1 = 11
      IDRMAX = 30
C 30 radial positions are used
      PI = 22.D0/7.0D0
C      CALL INIT
C      VTILR = -0.01
      VTILJ = 0.
      open(unit=96,file='RESULTS',STATUS='UNKNOWN')
      close(unit=96,status='delete')
      open(unit=96,file='RESULTS',STATUS='UNKNOWN')
C      WRITE (96,107)
C      C1 = IZ*FA/(R*TEMP)
      DUMT = TRAN/CINF
C      DO 10 I =1,IDRAMAX
      XZ(I) = ALPHA*C1*DEXP(ALPHA*C1*ETASTSS(I))
      +        +BETA*C1*DEXP(-BETA*C1*ETASTSS(I))
      DUMETC(I) = (1/CSURSS(I) - TRAN/CINF)/C1
10    CONTINUE

```

```

C
C
C XNU is the kinematic viscosity and DIF is the diffusion coefficient.
C SC is the schmidt number of the reacting species.
C
C
SC = XNU/DIF
1209 format (i4,3x,i4,3X,11(E22.14,3x))

X1      = 0.0D0
X2      = 1.0D0
CALL GAULEG(X1,X2,IDRAMAX)

C
CALL INTEGRAL
C
ITMAX = 3000
AMTOL = 1.D-8
W2    = 1.D0
C
C W2 is the weighting factor used in performing the iterations.
C
DO 487 LFREQ =1,NFRE
C
C NFRE is the total number of frequencies in the impedance spectrum.
C
W2    = W2*0.9
AMTOL = AMTOL*0.9
DO 12 MA1 = 1,MMAXP1
AMTR(MA1) = AMTG
AMTJ(MA1) = AMTG
J=0
C
C Initialize coefficient matrices for derivative boundary conditions.
C This is for setting up the matrices that are needed for implementation
C of BAND algorithm.
C
DO I=1,NVAR
  DO K=1,NVAR
    Y(I,K)=0.0
    X(I,K)=0.0
  ENDDO
ENDDO
C
SUMH=0.0
C

```

```

C Initialize all coefficient matrices to zero
C
351   J=J+1
      SUMH=SUMH+H
      DO I=1,NVAR
         G(I)=0.0
         DO K=1,NVAR
            A(I,K)=0.0
            B(I,K)=0.0
            D(I,K)=0.0
         ENDDO
      ENDDO

C
C Boundary conditions for bulk solution
C
C      IF (J.EQ.1) CALL BC1(J)
C
C EQUATIONS FOR INTERIOR DOMAIN
C
C      IF ((J.GT.1).AND.(J.LT.NJ)) CALL INNER(J)
C
C Equtions for second Boundary conditions
C
C      IF (J.EQ.NJ) Call BC2(J)
C
C      CALL BAND(J)
C
C      IF (J.NE.NJ) GOTO 351
C
      FRKHSQR(LFREQ) = (FRK(LFREQ)/2.D0)**0.5
      DO 99 J = 1,NJ
         XI(J)      = (J-1)*H
         THMREAP(MA1,J) = C(1,J)+C(3,J)*SC**(-1./3.)
         +
         +C(5,J)*SC**(-2./3.)
         +
         THMIMAP(MA1,J) = C(2,J)+C(4,J)*SC**(-1./3.)
         +
         +C(6,J)*SC**(-2./3.)
99      CONTINUE
         IF (LFREQ .EQ. 1) THEN
            DO 991 J =1,NJ
               THMREAPSS(MA1,J) = THMREAP(MA1,J)
            CONTINUE
991      ENDIF
C
12      CONTINUE

```

```

IF (LFREQ .EQ. 1) THEN
GOTO 487

ENDIF

C
DO 27 I = 1, IDRAMAX
CSURTILR(I) = 0.
CSURTILJ(I) = 0.
DO 28 K = 1, MMAXP1
    CSURTILR(I) = CSURTILR(I)
    +      +AMTR(K)*(DRA(I))**2*(K-1))
    CSURTILJ(I) = CSURTILJ(I)
    +      +AMTJ(K)*(DRA(I))**2*(K-1))
28    CONTINUE
C
27    CONTINUE

C
DO 26 MA1 = 1, 11
DO J = 1, 2001
C
C Depending on the upper limit of J Simpsons rule subroutine should be
C adjusted
C
    FUNCR(J) = THMREAPSS(MA1,J)*THMREAP(MA1,J)
    +      *DEXP(XI(J)**3-0.25*BK*XI(J)**4*SC**(-1./3.))
    +      -0.2*CK*XI(J)**5*SC**(-2./3.))
    FUNCJ(J) = THMREAPSS(MA1,J)*THMIMAP(MA1,J)
    +      *DEXP(XI(J)**3-0.25*BK*XI(J)**4*SC**(-1./3.))
    +      -0.2*CK*XI(J)**5*SC**(-2./3.))
    ENDDO
    CALL SIMPSONSRULE(FUNCR, OR)
    CALL SIMPSONSRULE(FUNCJ, OJ)
C
C Combination of Simpson's 1/3rd and 3/8th rule is used in order to
C evaluate the integrals that are involved.
C
    OUTR(MA1) = OR*FRK(LFREQ)
    OUTJ(MA1) = OJ*FRK(LFREQ)
C
    OUTR(MA1) = OUTR(MA1)/AMSS(MA1)
    OUTJ(MA1) = OUTJ(MA1)/AMSS(MA1)
26    CONTINUE
C
DO 394 ITER = 1, ITMAX

```

```

DO 291 MA1 = 1,11
    THPTR(MA1) = AMTJ(MA1)*OUTR(MA1)
    +           + AMTR(MA1)*OUTJ(MA1)
    THPTJ(MA1) = AMTJ(MA1)*OUTJ(MA1)
    +           - AMTR(MA1)*OUTR(MA1)
C
291     CONTINUE
C
CALL CURFTILDA
C
CALL ETASTILDA
C
DO I = 1,IDRAMAX
    CURPRESR(I) = CURTILR(I)
    CURPRESJ(I) = CURTILJ(I)
    D2R = ETASTILR(I)+ETACTILR(I)
    D2J = ETASTILJ(I)+ETACTILJ(I)
C
    CURTILR(I) = CURFRTR(I)-2.*PI*WW(LFREQ)*CDDL*D2J
    CURTILJ(I) = CURFJTR(I)+2.*PI*WW(LFREQ)*CDDL*D2R
C
ENDDO
    CALL CALCLTILDA
    CALL CALCMTILDA
    DO I = 1,IDRAMAX
        DUMMR = 0
        DUMMJ = 0
        DO M = 1,MMAXP1
            DUMMR = DUMMR+CMTR(M)*DRA(I)**(2*(M-1))
            DUMMJ = DUMMJ+CMTJ(M)*DRA(I)**(2*(M-1))
        ENDDO
C
        ENDDO
C
CALL BTILDA
C
CALL PHITILDA
C
DO I = 1,IDRAMAX
    ETACTILR(I)=VTILR-ETASTILR(I)-PHITR(I)
    ETACTILJ(I)=VTILJ-ETASTILJ(I)-PHITJ(I)
C

```

```

ENDDO
CALL CONCTIL
C
DO 36 M = 1,MMAXP1
AMTRST(M) = AMTR(M)
AMTJST(M) = AMTJ(M)
C
36    CONTINUE
C
CALL CALALTILDA
C
CALL CALAMTILDA
C
SUMRAM = 0
do 39 i = 1,mmaxP1
C
RERAMR = ABS((AMTR(I)-AMTRST(I))/AMTR(I))
RERAMJ = ABS((AMTJ(I)-AMTJST(I))/AMTJ(I))
SUMRAM = SUMRAM + RERAMR + RERAMJ
AMTR(I) = W2*AMTR(I) + (1-W2)*AMTRST(I)
AMTJ(I) = W2*AMTJ(I) + (1-W2)*AMTJST(I)
39    CONTINUE
C
IF (SUMRAM .LE. AMTOL .OR. ITER .EQ. ITMAX) THEN
PRINT *,'CONVERGENCE MET AT',ITER,SUMRAM,LFREQ
C
CURTILAVR(LFREQ) = 0.
CURTILAVJ(LFREQ) = 0.
DO I = 1,IDRAMAX
CURTILAVR(LFREQ) = CURTILAVR(LFREQ)+CURTILR(I)
+      *DRA(I)*WE(I)
CURTILAVJ(LFREQ) = CURTILAVJ(LFREQ)+CURTILJ(I)
+      *DRA(I)*WE(I)
ENDDO
CURTILAVR(LFREQ) = 2.*CURTILAVR(LFREQ)
CURTILAVJ(LFREQ) = 2.*CURTILAVJ(LFREQ)
C
C 'RATCOMP' calculates the ratio of two complex numbers
C
CALL RATCOMP(VTILR,VTILJ,CURTILAVR(LFREQ),
+             CURTILAVJ(LFREQ),ZR(LFREQ),ZJ(LFREQ))
C
DO I=1,IDRAMAX
C
CALL RATCOMP(VTILR,VTILJ,CURFRTIL(I),

```

```

+      CURFJTIL(I),ZLOCR(I),ZLOCJ(I))
C
C One should decide between the two WRITE statements that follow. For
C somone interested in studying the radial distributions, first WRITE
C is appropriate to use and the second WRITE is appropriate to generate
C impedance values at different frequencies.
C
        WRITE (96,113) DRA(I),CSURTILR(I),CSURTILJ(I),
+      CURTILR(I),CURTILJ(I),PHITR(I),
+      PHITJ(I),ETACTILR(I),ETACTILJ(I),
+      ETASTILR(I),ETASTILJ(I),ZLOCR(I),
+      ZLOCJ(I)

        ENDDO
C
C      WRITE (96,115) DRA(20),CSURTILR(20),CSURTILJ(20),
C +    CURFRTR(20),CURFJTIL(20),PHITR(20),
C +    PHITJ(20),ETACTILR(20),ETACTILJ(20),
C +    ETASTILR(20),ETASTILJ(20),ZR(LFREQ),ZJ(LFREQ)
C +    ,WW(LFREQ)
C
107   FORMAT(2X'RADIAL POSITION',17X,'CONCR',22X,'CONCJ',22X,'IR',22X,
+      'IJ',22X,'PHIR',22X,'PHIJ',22X,'ETACR',22X,'ETACJ',22X,
+      'ETASR',22X,'ETASJ',22X,'ZR',22X,'ZJ',22X,'FREQUENCY')
115   FORMAT(E20.14,6X,E20.14,6X,E20.14,6X,E20.14,6X,E20.14,6X,
+      E20.14,6X,E20.14,6X,E20.14,6X,E20.14,6X,E20.14,6X,E20.14,6X,
+      E20.14,6X,E20.14,6X,E20.14,6X)
113   FORMAT(E20.14,6X,E20.14,6X,E20.14,6X,E20.14,6X,E20.14,6X,
+      E20.14,6X,E20.14,6X,E20.14,6X,E20.14,6X,E20.14,6X,E20.14,6X,
+      E20.14,6X,E20.14)
C      CLOSE(96)
C
        GOTO 487
      ENDIF

394   CONTINUE
487   CONTINUE
      CLOSE(96)
      STOP
      END
C
C-----
      SUBROUTINE GAULEG(X1,X2)
C-----
```

C

C Subroutine used to generate the weighting factors and abscissas for
 C the Gauss-Legendre quadrature. Adapted from the 2nd edition of
 C "Numerical Recipes in FORTRAN".

C

```

IMPLICIT DOUBLE PRECISION (A-H,O-Z)
IMPLICIT INTEGER*8 (I-N)
COMMON/GAUQUA/ DRA(60),WE(60),IDRAMAX
EPS = 1.D-14
M = (IDRAMAX+1)/2
XM = 0.5*(X2+X1)
XL = 0.5*(X2-X1)
DUMMY=1.0/(IDRAMAX+0.5)
DO 12 I = 1,M
    Z = COS(3.141592654*(I-0.25)*DUMMY)
1  CONTINUE
    P1 = 1.0
    P2 = 0.0
    DO 11 J = 1,IDRAMAX
        P3 = P2
        P2 = P1
        P1 = ((2*J-1)*Z*P2-(J-1)*P3)/DFLOAT(J)
11   CONTINUE
    PP = IDRAMAX*(Z*P1-P2)/(Z*Z-1)
    Z1 = Z
    Z = Z1-P1/PP
    IF (ABS(Z-Z1) .GT. EPS) GO TO 1
    DRA(I)      = XM - XL*Z
    DRA(IDRAMAX+1-I) = XM +XL*Z
    WE(I)       = 2*XL/((1-Z*Z)*PP*PP)
    WE(IDRAMAX+1-I) = WE(I)
12   CONTINUE
    RETURN
    END

```

C

C -----
 C Subroutine that reads the input variables
 Subroutine INIT

C -----

```

IMPLICIT DOUBLE PRECISION (A-H,O-Z)
IMPLICIT INTEGER*8 (I-N)
COMMON/BA/ A(6,6),B(6,6),C(6,10001),D(6,13),G(6),X(6,6),Y(6,6)
COMMON/NS/ NVAR,NJ,LFREQ,NMAXP1,MMAXP1,NFRE
COMMON/AA/ XNU,DIF,FRK(90),BK,CK,MA1,CBULK(6),CONC(6,10001),

```

```

+ CONV(6,10001),AMTG,AMSS(11),THMPRSS(11),CINF,TRAN,AAL,OM,
+ NO,FA,QSS(11,11),R0,IZ,TEMP,XN,R,XKINF,WW(90),CDDL
COMMON/BB/ H,DEL
COMMON/GAUQUA/ DRA(60),WE(60),IDRAMAX,YINT(11,11),ETA(60)
COMMON/SS/ ETASTSS(60),ZETASS(60),ETACSS(60),PHISS(60),
+ Q2SS(60),CSURSS(60),XIDENSS(60)
COMMON/ETAS/ ALPHA,BETA,GAMMA,
+ XZ(60),YZ(60),VAR0(60),DNRZ(60),XI0,
+ ZETTILR(60),ZETTILJ(60),ETASTILR(60),
+ ETASTILJ(60),BZ(60),Y2

C
C Input file from which various parameters are being read is called
C 'SSUNDAT'.
C
C      open(unit=136,file='d:\users\DUARBHA\SSMODEL\SSUNDAT',
+           STATUS='UNKNOWN')
C
C      PI = 3.141592654D0
C      READ(136,35)XNU
35   FORMAT(39X,F19.16)
C
C XNU is kinetic viscosity in (cm)**2/sec
C
C      READ(136,35)DIF

C
C D is the diffusion coefficient in (cm)**2/sec
C
C      READ (136,*)
23   FORMAT(39X,I2)

C
C      READ(136,23) IDRAMAX

      READ(136,35)R0
C
C R0 is the radius of the disk electrode in cm
C
C      READ(136,35)OM

C
C OM is the angular speed of the disk electrode in rPM
C
C      READ(136,35)AAL
C

```

C AAL is coefficient in series for the expansion of velocity terms
C
READ(136,42)NO
42 FORMAT(39X,I2)

C
C -NO is the number of equivalents
C
READ(136,43)IZ
43 FORMAT(35X,I2)

C
C IZ corresponds to the number of equivalents
C
READ(136,35)FA

C
C F is the Faraday's constant in Coulomb/equivalent
C
READ(136,35)CINF

C
C CINF is the concentration of the species at infinite distance in moles/c.c.
C
READ(136,35)R

C
C R is universal gas constant in J/mol./Kelvin.

C
READ(136,35)TEMP

C
C TEMP is the temperature of the system in Kelvin.

C
READ(136,35)TRAN

C
C T is the transference number of the reactant.

C
READ(136,35)XKINF

C
C XKINF is the solution conductivity in 1/(ohm.cm)

READ (136,*)
READ (136,*)
READ (136,*)
READ (136,35) GAMMA
READ (136,35) XI0
READ (136,35) ALPHA
READ (136,35) BETA
READ (136,143) ITTOL

```

143 FORMAT(39X,I4)
  READ (136,*)
  READ (136,*)
  READ (136,*)
  READ (136,*)
  READ (136,*)
  READ (136,35) AMTG
  READ (136,35) CDDL
  print *,XNU,Dif,DRAMAX,LO,R0,OM,AAL,NO,IZ,FA,CINF,R,TEMP,TRAN,
+ XKINF,VSS,W2,CCENT,GAMMA,XI0,Alpha,Beta,ITTOL,RAMTOL,AMTOL,
+ PERM,Y2,STEP,AMTG,CDDL
C
C      PAUSE
C      PRINT *,'AMTG',AMTG
C
C      CLOSE(136)
C

C  N is the NUmber of unknowns= NUmber of species +1(Voltage)
C      NVAR=6

C  NJ=NUMBER OF NODES
C      NJ=10001
C  DOMAIN LENGTH # OF DEBYE LENGTHS
C      DEL = 10.0
C  H=Stepsize
C      H=DEL/(NJ-1)
C  WW = frequency of perturbation (Hz)
C      WW(2) = 1.43
C      NFRE = 2
C  NFRE is the variable that sets the number of frequency points
C that are needed
DO I = 2,NFRE
  WW(I) = WW(2)*10.**((I-2)/12.)
ENDDO
C
C  OMEGA = rotational speed (cycles/s)
C      OMEGA=OM/60.
C      OM = OM*PI/30.D0
C  XNU =
BBL=-0.61592201
DO L = 1,nfre
  FRK(L)=(WW(L)/OMEGA)*(((9.*XNU)/((AAL**2)*DIF))**(.1/3.))
ENDDO
C

```

```

BK    = (3./AAL**4)**(1./3.)
CK   = (BBL/6.)*((3./AAL)**(5./3.))
C
OPEN(UNIT=24,FILE='d:\USERS\DURBHA\SSMODEL\AMTHP',
+ STATUS='UNKNOWN')
READ(24,*)
DO I=1,MMAXP1
  READ(24,112)AMSS(I)
ENDDO
READ(24,*)
READ(24,*)
DO I=1,MMAXP1
  READ(24,112)THMPRSS(I)
ENDDO
READ(24,*)
READ(24,*)
DO I = 1,NMAXP1
  DO J = 1,MMAXP1
    READ(24,112)QSS(I,J)
  ENDDO
ENDDO
C
112  FORMAT(6X,E20.14)
CLOSE(24)
C
OPEN(UNIT=33,FILE='D:\USERS\DURBHA\SSMODEL\SSOUT',
+ STATUS='UNKNOWN')
READ(33,*)
DO K=1,DRAMAX
  READ(33,116)DRA(K),ETASTSS(K),ETACSS(K),PHISS(K),CSURSS(K),
+ XIDENSS(K)
ENDDO
116  FORMAT(E20.14,3X,E20.14,3X,E20.14,3X,E20.14,3X,E20.14)
CLOSE(33)
C
C      BULK SOLUTION CONCENTRATIONS MOL/LITER
C
CBULK(1)=1.0
DO I = 2,NVAR
  CBULK(I) = 0.
ENDDO
C
C Initialize entire domain of the array by assigning
C Bulk Concentration values at all nodes
C

```

```

DO I=1,NVAR
  DO J=1,NJ
    C(I,J)=0.0
    CONC(I,J)=CBULK(I)
  ENDDO
ENDDO
RETURN
END

```

C

C-----

Subroutine BC1(J)

C-----

IMPLICIT DOUBLE PRECISION (A-H,O-Z)

IMPLICIT INTEGER*8 (I-N)

COMMON/BA/ A(6,6),B(6,6),C(6,10001),D(6,13),G(6),X(6,6),Y(6,6)

COMMON/NS/ NVAR,NJ,LFREQ,NMAXP1,MMAXP1

COMMON/AA/ XNU,DIF,FRK(90),BK,CK,MA1,CBULK(6),CONC(6,10001),
+ CONV(6,10001),AMSS(11),THMPRSS(11),CINF,TRAN,AAL,OM,
+ NO,FA,QSS(11,11),R0,IZ,TEMP,XN,R,XKINF,WW(90),CDDL

COMMON/BB/ H,DEL

C Boundary conditionS for bulk solution

```

DO I=1,NVAR
  B(I,I)=H
  G(I)=(CBULK(I)*H)
ENDDO
RETURN
END

```

C

C-----

Subroutine Inner(J)

C-----

C-----

IMPLICIT DOUBLE PRECISION (A-H,O-Z)

IMPLICIT INTEGER*8 (I-N)

COMMON/BA/ A(6,6),B(6,6),C(6,10001),D(6,13),G(6),X(6,6),Y(6,6)

COMMON/NS/ NVAR,NJ,LFREQ,NMAXP1,MMAXP1

COMMON/AA/ XNU,DIF,FRK(90),BK,CK,MA1,CBULK(6),CONC(6,10001),
+ CONV(6,10001),AMSS(11),THMPRSS(11),CINF,TRAN,AAL,OM,
+ NO,FA,QSS(11,11),R0,IZ,TEMP,XN,R,XKINF,WW(90),CDDL

COMMON/BB/ H,DEL

DIMENSION AD(6,6),BD(6,6),DD(6,6)

H2=H**2.

XI = (J-1)*DEL/(NJ-1)

DO I = 1,NVAR

```

DO K = 1,NVAR
  AD(I,K) = 0.
  BD(I,K) = 0.
  DD(I,K) = 0.
ENDDO
ENDDO
C
DO I = 1,NVAR
  AD(I,I) = 1.
  BD(I,I) = 3.*XI**2
  DD(I,I) = -6.*(MA1-1)*XI
ENDDO
DO I = 3,NVAR
  BD(I,I-2) = -BK*XI**3
  DD(I,I-2) = 3.*(MA1-1)*BK*XI**2
ENDDO
DO I = 5,NVAR
  BD(I,I-4) = -CK*XI**4
  DD(I,I-4) = 4*(MA1-1)*CK*XI**3
ENDDO
DO I = 2,2,NVAR
  DD(I-1,I) = FRK(LFREQ)
  DD(I,I-1) = -FRK(LFREQ)
ENDDO
DO I = 1,NVAR
  DO K =1,NVAR
    A(I,K) = AD(I,K) - H*BD(I,K)*0.5D0
    B(I,K) = 2*AD(I,K)+H2*DD(I,K)
    D(I,K) = AD(I,K)+H*BD(I,K)*0.5D0
  ENDDO
  G(I) = 0.
ENDDO
RETURN
END

```

C-----

Subroutine BC2(J)
 IMPLICIT DOUBLE PRECISION (A-H,O-Z)
 IMPLICIT INTEGER*8 (I-N)
 COMMON/BA/ A(6,6),B(6,6),C(6,10001),D(6,13),G(6),X(6,6),Y(6,6)
 COMMON/NS/ NVAR,NI,LFREQ,NMAXP1,MMAXP1
 COMMON/AA/ XNU,DIF,FRK(90),BK,CK,MA1,CBULK(6),CONC(6,10001),
+ CONV(6,10001),AMSS(11),THMPRSS(11),CINF,TRAN,AAL,OM,

+ NO,FA,QSS(11,11),R0,IZ,TEMP,XN,R,XKINF,WW(90),CDDL
 COMMON/BB/ H,DEL

C-----
 C Boundary conditions at inner boundary
 C-----

```
do i=1,NVAR
B(i,i)= H
G(i)=0.0
enddo
```

```
RETURN
END
```

C-----

```
SUBROUTINE MATINV(N,M,DETERM)
IMPLICIT DOUBLE PRECISION (A-H,O-Z)
IMPLICIT INTEGER*8 (I-N)
COMMON/BA/ A(6,6),B(6,6),C(6,10001),D(6,13),G(6),X(6,6),Y(6,6)
COMMON/NS/ NTEMP,NJ,LFREQ,NMAXP1,MMAXP1
DIMENSION ID(6)
```

```
DETERM=1.01
DO 1 I=1,N
```

```
1 ID(I)=0
DO 18 NN=1,N
BMAX=1.1
DO 6 I=1,N
IF(ID(I).NE.0) GOTO 6
BNEXT=0.0
BTRY=0.0
DO 5 J=1,N
IF (ID(J).NE.0) GOTO 5
IF (DABS(B(I,J)).LE.BNEXT) GOTO 5
BNEXT=DABS(B(I,J))
IF (BNEXT.LE.BTRY) GOTO 5
BNEXT=BTRY
BTRY=DABS(B(I,J))
JC=J
```

```
5 CONTINUE
IF(BNEXT.GE.BMAX*BTRY) GOTO 6
BMAX=BNEXT/BTRY
IROW=I
JCOL=JC
6 CONTINUE
```

```

IF (ID(JC).EQ.0) GOTO 8
DETERM=0.0
RETURN
8 ID(JCOL)=1
IF (JCOL.EQ.IROW) GO TO 12
DO 10 J=1,N
SAVE=B(IROW,J)
B(IROW,J)=B(JCOL,J)
10 B(JCOL,J)=SAVE
DO 11 K=1,M
SAVE=D(IROW,K)
D(IROW,K)=D(JCOL,K)
11 D(JCOL,K)=SAVE
12 FF=1.0/B(JCOL,JCOL)
DO 13 J=1,N
13 B(JCOL,J)=B(JCOL,J)*FF
DO 14 K=1,M
14 D(JCOL,K)=D(JCOL,K)*FF
DO 18 I=1,N
IF (I.EQ.JCOL) GO TO 18
FF=B(I,JCOL)
DO 16 J=1,N
16 B(I,J)=B(I,J)-FF*B(JCOL,J)
DO 17 K=1,M
17 D(I,K)=D(I,K)-FF*D(JCOL,K)
18 CONTINUE
RETURN
END

```

C-----

```

SUBROUTINE BAND(J)
IMPLICIT DOUBLE PRECISION (A-H,O-Z)
IMPLICIT INTEGER*8 (I-N)
DIMENSION E(6,7,10001)
COMMON/BA/A(6,6),B(6,6),C(6,10001),D(6,13),G(6),X(6,6),Y(6,6)
COMMON/NS/ NVAR,NJ,LFREQ,NMAXP1,MMAXP1
101 FORMAT(15H DETERM=0 AT J=,I4)
IF (J-2) 1,6,8
1 NP1=NVAR+1
DO 2 I=1,NVAR
D(I,2*NVAR+1)=G(I)
DO 2 L=1,NVAR
LPN=L+NVAR
2 D(I,LPN)=X(I,L)
CALL MATINV(NVAR,2*NVAR+1,DETERM)

```

```

IF (DETERM) 4,3,4
3 PRINT 101,J
4 DO 5 K=1,NVAR
   E(K,NP1,1)=D(K,2*NVAR+1)
   DO 5 L=1,NVAR
   E(K,L,1)= -D(K,L)
   LPN=L+NVAR
5 X(K,L)= -D(K,LPN)
   RETURN
6 DO 7 I=1,NVAR
   DO 7 K=1,NVAR
   DO 7 L=1,NVAR
7 D(I,K)=D(I,K)+A(I,L)*X(L,K)
8 IF (J-NJ) 11,9,9
9 DO 10 I=1,NVAR
   DO 10 L=1,NVAR
   G(I)=G(I)-Y(I,L)*E(L,NP1,J-2)
   DO 10 M=1,NVAR
10 A(I,L)=A(I,L)+Y(I,M)*E(M,L,J-2)
11 DO 12 I=1,NVAR
   D(I,NP1)=-G(I)
   DO 12 L=1,NVAR
   D(I,NP1)=D(I,NP1)+A(I,L)*E(L,NP1,J-1)
   DO 12 K=1,NVAR
12 B(I,K)=B(I,K)+A(I,L)*E(L,K,J-1)
   CALL MATINV(NVAR,NP1,DETERM)
   IF (DETERM) 14, 13, 14
13 PRINT 101,J
14 DO 15 K=1,NVAR
   DO 15 M=1,NP1
15 E(K,M,J)= -D(K,M)
   IF (J-NJ) 20,16,16
16 DO 17 K=1,NVAR
17 C(K,J)=E(K,NP1,J)
   DO 18 JJ=2,NJ
   M=NJ-JJ+1
   DO 18 K=1,NVAR
   C(K,M)=E(K,NP1,M)
   DO 18 L=1,NVAR
18 C(K,M)=C(K,M)+E(K,L,M)*C(L,M+1)
   DO 19 L=1,NVAR
   DO 19 K=1,NVAR
19 C(K,1)=C(K,1)+X(K,L)*C(L,3)
20 RETURN
END

```

```

C
C-----
      SUBROUTINE SIMPSONSRULE(FUNC,OUTPUT)
C-----
C Combination of Simpson's 1/3rd and 3/8th rule to evaluate the
C integral involved in solving the convective diffusion equation.
C
      IMPLICIT DOUBLE PRECISION (A-H,O-Z)
      IMPLICIT INTEGER*8 (I-N)
      COMMON/BB/ H,DEL
      COMMON/SIMP/ XI(10001)
      COMMON/NS/ NVAR,NJ,LFREQ,NMAXP1,MMAXP1
      DIMENSION FUNC(10001)

C
      NJU = 2001
      M = NJU
C M is the upper limit of J where simpson's routine is called in the
C main program
C
      OUTPUT = 0.0
      IF (MOD(NJU,2).NE.0 .AND. NJU.GT.1) THEN
          OUTPUT = OUTPUT+3*H*(FUNC(NJU-3)+3*(FUNC(NJU-2)
          +           +FUNC(NJU-1))+FUNC(NJU))/8.0
          M = NJU-3
      ENDIF

C
      IF (M .GT. 1) THEN
          SUM1 = 0
          DO 20 J = 1,M-1,2
              SUM1 = SUM1 + FUNC(J+1)
20      CONTINUE
          SUM2 = 0
          DO 30 K = 2,M-2,2
              SUM2 = SUM2 + FUNC(K+1)
30      CONTINUE
          OUTPUT = OUTPUT + H*(FUNC(1)+4*SUM1+2*SUM2+FUNC(M+1))/3.
      ENDIF
      RETURN
END

C
C-----
      SUBROUTINE CURFTILDA
C-----

```

```

IMPLICIT DOUBLE PRECISION (A-H,O-Z)
IMPLICIT INTEGER*8 (I-N)
COMMON/NS/ NVAR,NJ,LFREQ,NMAXP1,MMAXP1
COMMON/AA/ XNU,DIF,FRK(90),BK,CK,MA1,CBULK(6),CONC(6,10001),
+      CONV(6,10001),AMTG,AMSS(11),THMPRSS(11),CINF,TRAN,
+      AAL,OM,NO,FA,QSS(11,11),R0,IZ,TEMP,XN,R,XKINF,WW(90),
+      CDDL
COMMON/OP/CURFRITIL(60),CURFJITIL(60),THPTR(11),
+      THPTJ(11),AMTR(11),AMTJ(11)
COMMON/GAUQUA/ DRA(60),WE(60),IDRAMAX,YINT(11,11),ETA(60)
C
C      DUM = (NO*FA*DIF*CINF/(1.-TRAN))*(AAL*XNU/(3.*DIF))**(.1/3.)
C      DUM = DUM*(OM/XNU)**0.5
C
C      DO 10 I = 1, IDRAMAX
C          CR = 0.
C          CJ = 0.
C      DO M1 = 1, MMAXP1
C
C          DR = AMTR(M1)*THMPRSS(M1)+AMSS(M1)*THPTR(M1)
C          DR = DR*(DRA(I))**((2*(M1-1)))
C          CR = CR + DR
C
C          DJ = AMTJ(M1)*THMPRSS(M1)+AMSS(M1)*THPTJ(M1)
C          DJ = DJ*(DRA(I))**((2*(M1-1)))
C          CJ = CJ + DJ
C      ENDDO
C
C          CURFRITIL(I) = DUM*CR
C          CURFJITIL(I) = DUM*CJ
10    CONTINUE
C
C      RETURN
END
C-----
C----- DOUBLE PRECISION FUNCTION FACT(N)
C-----
C
C      Function subprogram to calculate the factorial of a given number
C
C      INTEGER N
C      IF (N .GE. 2) THEN
C          FACT = 1.
C          DO 15 I = 1,N

```

```

      FACT = FACT*DFLOAT(I)
15    CONTINUE
      ELSE
          FACT = 1.
      ENDIF
      RETURN
      END

C
C----- DOUBLE PRECISION FUNCTION PROD(M,N)
C----- C
C     Function PROD(M,N) gives the value of FACT(M)/FACT(N).
C
      INTEGER M,N
      IF (M.GE.1 .AND. N.LT.M) THEN
          PROD = 1.
          DO 20 I = N+1,M
              PROD = PROD*DFLOAT(I)
20    CONTINUE
      ELSE
          PROD = 1.
      ENDIF
      RETURN
      END

C
C----- SUBROUTINE INTEGRAL
C----- C
C Subroutine subprogram that evaluates the integral that is involved in
C calculating QRTILDA(L,NA1,MA1),QJTLDA(L,NA1,MA1).
C Please note that the values of the the definite integral are exact.
C There is no approximation involved.
C
      IMPLICIT DOUBLE PRECISION (A-H,O-Z)
      IMPLICIT INTEGER*8 (I-N)
      COMMON/GAUQUA/ DRA(60),WE(60),IDRAMAX,YINT(11,11),ETA(60)
      COMMON/NS/ NVAR,NJ,LFREQ,NMAXP1,MMAXP1
C
      DOUBLE PRECISION D,XNUM,DIN,Y(11,11),SUM,A1
      DOUBLE PRECISION FACT,PROD
      DO 10 N1 = 1,NMAXP1
          DO 21 M1 = 1,MMAXP1
              SUM = 0

```

```

DO 30 K =0,M1-1
DO 40 L = 0,N1-1
  A1 = PROD(M1-1,M1-K-1)/FACT(K)
  XNUM = A1*(PROD(4*(N1-1)-2*L,2*(N1-1)-L)/FACT(2*(N1-1)-2*L))
  DIN = FACT(L)
  IA = 2**2*(N1-1)
  IB = N1-L+K
  IC = (-1)**(L+K)
  D = (IC*XNUM/IA)*1/(DIN*IB)
  SUM = SUM + D
40    CONTINUE
30    CONTINUE
YINT(N1,M1) = SUM
21    CONTINUE
10    CONTINUE
      RETURN
      END
C
C-----SUBROUTINE QTILDA
C-----C This subroutine calculates the value of Q(N,M) for different values of
C N and M.
C
IMPLICIT DOUBLE PRECISION (A-H,O-Z)
IMPLICIT INTEGER*8 (I-N)
COMMON/NS/ NVAR,NJ,LFREQ,NMAXP1,MMAXP1
COMMON/OP/CURFRTIL(60),CURFTIL(60),THPTR(11),
+ THPTJ(11),AMTR(11),AMTJ(11)
COMMON/QTIL/QRTILDA(11,11),QJTILDA(11,11)
COMMON/GAUQUA/ DRA(60),WE(60),IDRAMAX,YINT(11,11),ETA(60)
EXTERNAL XMPR
C
PI = 22.D0/7.D0
DO 10 N = 1,NMAXP1
  DO 20 M = 1,MMAXP1
    DUM = (4*N-3)*4*YINT(N,M)/(PI*XMPR(N))
    QRTILDA(N,M) = DUM*THPTR(M)
    QJTILDA(N,M) = DUM*THPTJ(M)
C
20    CONTINUE
C
10    CONTINUE

```

```

RETURN
END
C
C
C----- DOUBLE PRECISION FUNCTION XMPR(N)
C-----
C
C Subroutine subprogram that evaluates the value of M(2N)PRIME at 0.
C
IMPLICIT DOUBLE PRECISION (A-H,O-Z)
DOUBLE PRECISION FACT,PROD
PIINV = 7.D0/22.D0
XMPR = -2*(2**((2*(N-1)))*FACT(N-1)/PROD(2*(N-1),N-1))**2*PIINV
RETURN
END

C----- SUBROUTINE BTILDA
C-----
C
IMPLICIT DOUBLE PRECISION (A-H,O-Z)
IMPLICIT INTEGER*8 (I-N)
COMMON/QTIL/QRTILDA(11,11),QJTIlda(11,11)
COMMON/AA/XNU,DIF,FRK(90),BK,CK,MA1,CBULK(6),CONC(6,10001),
+      CONV(6,10001),AMTG,AMSS(11),THMPRSS(11),CINF,TRAN,
+      AAL,OM,NO,FA,QSS(11,11),R0,IZ,TEMP,XN,R,XKINF,WW(90),
+      CDDL
COMMON/OP/CURFRTIL(60),CURFJTL(60),THPTR(11),
+      THPTJ(11),AMTR(11),AMTJ(11)
COMMON/NS/NVAR,NJ,LFREQ,NMAXP1,MMAXP1
COMMON/BTIL/BRTILDA(11),BJTILDA(11),C1
COMMON/ETAS/ ALPHA,BETA,GAMMA,
+      XZ(60),YZ(60),VAR0(60),DNRZ(60),XI0,
+      ZETTILR(60),ZETTILJ(60),ETASTILR(60),
+      ETASTILJ(60),BZ(60),Y2
COMMON/CONC/ ETACTILR(60),ETACTILJ(60)
COMMON/GAUQUA/ DRA(60),WE(60),IDRAMAX,YINT(11,11),ETA(60)
COMMON/CUR/CURTILR(60),CURTILJ(60)
COMMON/CM/ CMTR(11),CMTJ(11)

```

```

C
EXTERNAL XMPR,XLEGP
C
XK1 = -C1*R0/XKINF
CALL INTEGRAL
DO 15 J=1,NMAXP1
    DUM1 = XK1*(4*J-3)/XMPR(J)
    DUMR = 0.
    DUMJ = 0.
    DO 25 I = 1,MMAXP1
        DUMR = DUMR+CMTR(I)*YINT(J,I)
        DUMJ = DUMJ+CMTJ(I)*YINT(J,I)
25    CONTINUE
C
BRTILDA(J) = DUM1*DUMR
BJTILDA(J) = DUM1*DUMJ
C
15    CONTINUE
C
RETURN
END
C -----
C----- SUBROUTINE PHITILDA
C -----
C
IMPLICIT DOUBLE PRECISION (A-H,O-Z)
IMPLICIT INTEGER*8 (I-N)
COMMON/PHI/PHITR(60),PHITJ(60)
COMMON/NS/NVAR,NJ,LFREQ,NMAXP1,MMAXP1
COMMON/BTIL/BRTILDA(11),BJTILDA(11),C1
COMMON/GAUQUA/ DRA(60),WE(60),IDRAMAX,YINT(11,11),ETA(60)
COMMON/AA/XNU,DIF,FRK(90),BK,CK,MA1,CBULK(6),CONC(6,10001),
+      CONV(6,10001),AMTG,AMSS(11),THMPRSS(11),CINF,TRAN,
+      AAL,OM,NO,FA,QSS(11,11),R0,IZ,TEMP,XN,R,XKINF,WW(90),
+      CDDL
COMMON/CONC/ ETACTILR(60),ETACTILJ(60)
COMMON/ETAS/ ALPHA,BETA,GAMMA,
+      XZ(60),YZ(60),VAR0(60),DNRZ(60),XI0,
+      ZETTILR(60),ZETTILJ(60),ETASTILR(60),
+      ETASTILJ(60),BZ(60),Y2
EXTERNAL XMPR,XLEGP

DO 10 I = 1, IDRAMAX

```

```

C
PHITR(I) = 0.
PHITJ(I) = 0.
C
DO 20 J = 1,NMAXP1
C
PHITR(I) = PHITR(I)+BRTILDA(J)*XLEGP(J-1,ETA(I))
PHITJ(I) = PHITJ(I)+BJTILDA(J)*XLEGP(J-1,ETA(I))
20  CONTINUE
C
PHITR(I) = PHITR(I)/C1
PHITJ(I) = PHITJ(I)/C1
C
10  CONTINUE
C
      RETURN
END
C
C
C-----
```

DOUBLE PRECISION FUNCTION XLEGP(N,XIN)

```

C-----
C
C This function calculates the legendre polynomial expansion for P(2*N,X)
C
INTEGER N,I,IA,IB,IC
DOUBLE PRECISION XIN,XNUM,DIN
DOUBLE PRECISION FACT,PROD,SUM
SUM = 0.
NP1=N+1
DO 10 K = 1,NP1
   I=K-1
   IA = 4*N-2*I
   IB = 2*N-I
   IC = 2*N-2*I
IF (N .EQ. 0) THEN
   XLEGP = 1
   RETURN
ENDIF
IF (XIN.EQ.0 .AND. IC.EQ.0) THEN
   XNUM = ((PROD(IA,IB)/FACT(IC))/FACT(I))
ELSE
   XNUM = ((PROD(IA,IB)/FACT(IC))/FACT(I))*XIN**IC
ENDIF
DIN = DFLOAT(2**((2*N)))
```

```

        SUM = SUM + (-1)**I*XNUM/DIN
10  CONTINUE
    XLEGP = SUM
    RETURN
    END
C
C -----
SUBROUTINE ETASTILDA
C -----
C
IMPLICIT DOUBLE PRECISION (A-H,O-Z)
IMPLICIT INTEGER*8 (I-N)
COMMON/NS/ NVAR,NJ,LFREQ,NMAXP1,MMAXP1
COMMON/SS/ ETASTSS(60),ZETASS(60),ETACSS(60),PHISS(60),
+          Q2SS(60),CSURSS(60),XIDENSS(60)
COMMON/BTIL/BRTILDA(11),BJTILDA(11),C1
COMMON/ETAS/ ALPHA,BETA,GAMMA,
+          XZ(60),YZ(60),VAR0(60),DNRZ(60),XI0,
+          ZETTILR(60),ZETTILJ(60),ETASTILR(60),
+          ETASTILJ(60),BZ(60),Y2
COMMON/OP/CURFRITL(60),CURFJITL(60),THPTR(11),
+          THPTJ(11),AMTR(11),AMTJ(11),CSURTILR(60),
+          CSURTILJ(60)
COMMON/GAUQUA/ DRA(60),WE(60),IDRAMAX,YINT(11,11),ETA(60)
COMMON/AA/ XNU,DIF,FRK(90),BK,CK,MA1,CBULK(6),CONC(6,10001),
+          CONV(6,10001),AMTG,AMSS(11),THMPRSS(11),CINF,TRAN,
+          AAL,OM,NO,FA,QSS(11,11),R0,IZ,TEMP,XN,R,XKINF,WW(90),
+          CDDL
DO 10 I = 1, IDRAMAX
    XNUMR = GAMMA*XIDENSS(I)*CSURTILR(I)/CSURSS(I)
    XNUMR = CURFRITL(I)-XNUMR
    XNUMJ = GAMMA*XIDENSS(I)*CSURTILJ(I)/CSURSS(I)
    XNUMJ = CURFJITL(I)-XNUMJ
    XDIN = XI0*((CSURSS(I)/CINF)**GAMMA)*XZ(I)
C
    ETASTILR(I)= XNUMR/XDIN
    ETASTILJ(I)= XNUMJ/XDIN
10  CONTINUE
    RETURN
    END
C
C -----
SUBROUTINE CONCTIL
C -----

```

```

C
IMPLICIT DOUBLE PRECISION (A-H,O-Z)
IMPLICIT INTEGER*8 (I-N)
COMMON/BTIL/BRTILDA(11),BJTILDA(11),C1
COMMON/SS/ ETASTSS(60),ZETASS(60),ETACSS(60),PHISS(60),
+ Q2SS(60),CSURSS(60),XIDENSS(60)
COMMON/AA/ XNU,DIF,FRK(90),BK,CK,MA1,CBULK(6),CONC(6,10001),
+ CONV(6,10001),AMTG,AMSS(11),THMPRSS(11),CINF,TRAN,
+ AAL,OM,NO,FA,QSS(11,11),R0,IZ,TEMP,XN,R,XKINF,WW(90),
+ CDDL
COMMON/CONC/ ETACTILR(60),ETACTILJ(60)
COMMON/NS/ NVAR,NJ,LFREQ,NMAXP1,MMAXP1
COMMON/OP/CURFRIL(60),CURFJIL(60),THPTR(11),
+ THPTJ(11),AMTR(11),AMTJ(11),CSURTILR(60),
+ CSURTILJ(60)
COMMON/GAUQUA/ DRA(60),WE(60),IDRAMAX,YINT(11,11),ETA(60)

C
DO I = 1, IDRAMAX
  CSURTILR(I)
+   = C1*ETACTILR(I)/((1/CSURSS(I))-(TRAN/CINF))
  CSURTILJ(I)
+   = C1*ETACTILJ(I)/((1/CSURSS(I))-(TRAN/CINF))
ENDDO

C
RETURN
END

C-----  

C
SUBROUTINE CALALTILDA
C-----  

C
C This subroutine calculates the AL coefficients using trapezoidal rule.
C
IMPLICIT DOUBLE PRECISION (A-H,O-Z)
IMPLICIT INTEGER*8 (I-N)
COMMON/NS/ NVAR,NJ,LFREQ,NMAXP1,MMAXP1
COMMON/GAUQUA/ DRA(60),WE(60),IDRAMAX,YINT(11,11),ETA(60)
COMMON/AL/ ALTR(11),ALTJ(11)
COMMON/OP/CURFRIL(60),CURFJIL(60),THPTR(11),
+ THPTJ(11),AMTR(11),AMTJ(11),CSURTILR(60),
+ CSURTILJ(60)
COMMON/AA/ XNU,DIF,FRK(90),BK,CK,MA1,CBULK(6),CONC(6,10001),
+ CONV(6,10001),AMTG,AMSS(11),THMPRSS(11),CINF,TRAN,
+ AAL,OM,NO,FA,QSS(11,11),R0,IZ,TEMP,XN,R,XKINF,WW(90),
+ CDDL

```

```

DOUBLE PRECISION XLEGP
C
XINVCINF=1.0/CINF
DO 10 I = 1,MMAXP1
SUMR = 0.
SUMJ = 0.
DO 20 J = 1,IDRAMAX
AR = (CSURTILR(J))*XINVCINF*XLEGP(I-1,DRA(J)))
SUMR = SUMR + AR*WE(J)
AJ = (CSURTILJ(J))*XINVCINF*XLEGP(I-1,DRA(J)))
SUMJ = SUMJ + AJ*WE(J)
20 CONTINUE
ALTR(I) = (4*I - 3)*SUMR
ALTJ(I) = (4*I - 3)*SUMJ
10 CONTINUE
RETURN
END
C
C-----SUBROUTINE CALAMTILDA
C-----C
C This subroutine calculates the AM coefficints using AL coefficints.
C
IMPLICIT DOUBLE PRECISION (A-H,O-Z)
IMPLICIT INTEGER*8 (I-N)
COMMON/NS/ NVAR,NJ,LFREQ,NMAXP1,MMAXP1
COMMON/AL/ ALTR(11),ALTJ(11)
COMMON/OP/CURFRTIL(60),CURFJTIL(60),THPTR(11),
+ THPTJ(11),AMTR(11),AMTJ(11),CSURTILR(60),
+ CSURTILJ(60)
EXTERNAL COEFF

DO 10 I = 1,MMAXP1
SUMR = 0.
SUMJ = 0.
DO 20 J = I,MMAXP1
PRINT *,I,J,COEFF(J-1,J-I),'COEFF'
SUMR = SUMR + ALTR(J)*COEFF(J-1,J-I)
SUMJ = SUMJ + ALTJ(J)*COEFF(J-1,J-I)
20 CONTINUE
AMTR(I) = SUMR
AMTJ(I) = SUMJ
10 CONTINUE
RETURN

```

```
      END
C
```

C-----

DOUBLE PRECISION FUNCTION COEFF(N,IR)

C-----

C

C This function subprogram calculates the coefficients in the legendre
C polynomial expansion.

C

INTEGER N,IR,IA,IB,IC

DOUBLE PRECISION FACT,PROD

DOUBLE PRECISION XNUM,DIN

IA = 4*N - 2*IR

IB = 2*N - IR

IC = 2*N - 2*IR

XNUM = (PROD(IA,IB)/FACT(IC))/FACT(IR)

DIN = 2**(2*N)

COEFF = ((-1)**IR)*XNUM/DIN

RETURN

END

C

C-----

SUBROUTINE RATCOMP(VR,VJ,CURR,CURJ,ZR,ZJ)

C-----

C

C This calculates the ratio between two complex numbers VR + j VJ and
C CURR + j CURJ

C

REAL*8 VR,VJ,CURR,CURJ,ZR,ZJ,DIN

C

DIN = CURR**2 + CURJ**2

C

ZR = (VR*CURR + VJ*CURJ)/DIN

ZJ = (VJ*CURR - VR*CURJ)/DIN

C

RETURN

END

C

C-----

SUBROUTINE CALCLTILDA

```

C-----
      IMPLICIT DOUBLE PRECISION (A-H,O-Z)
      IMPLICIT INTEGER*8 (I-N)
      COMMON/NS/ NVAR,NJ,LFREQ,NMAXP1,MMAXP1
      COMMON/CL/ CLTR(11),CLTJ(11)
      COMMON/CUR/CURTLR(60),CURTILJ(60)
      COMMON/GAUQUA/ DRA(60),WE(60),IDRAMAX,YINT(11,11),ETA(60)
      DOUBLE PRECISION XLEGP

C
      DO 10 I = 1,MMAXP1
         SUMR = 0.
         SUMJ = 0.
         DO 20 J = 1, IDRAMAX
            CR = (CURTILR(J))*XLEGP(I-1,DRA(J))
            SUMR = SUMR + CR*WE(J)
            CJ = (CURTILJ(J))*XLEGP(I-1,DRA(J))
            SUMJ = SUMJ + CJ*WE(J)
20      CONTINUE
            CLTR(I) = (4*I - 3)*SUMR
            CLTJ(I) = (4*I - 3)*SUMJ
10      CONTINUE
      RETURN
      END

```

```

C-----
      SUBROUTINE CALCMTILDA
C-----
C

```

C This subroutine calculates the AM coefficints using AL coefficints.

```

C
      IMPLICIT DOUBLE PRECISION (A-H,O-Z)
      IMPLICIT INTEGER*8 (I-N)
      COMMON/NS/ NVAR,NJ,LFREQ,NMAXP1,MMAXP1
      COMMON/CL/ CLTR(11),CLTJ(11)
      COMMON/CM/ CMTR(11),CMTJ(11)
      DOUBLE PRECISION COEFF

      DO 10 I = 1,MMAXP1
         SUMR = 0.
         SUMJ = 0.
         DO 20 J = 1, MMAXP1
            SUMR = SUMR + CLTR(J)*COEFF(J-1,J-I)
            SUMJ = SUMJ + CLTJ(J)*COEFF(J-1,J-I)
20      CONTINUE
            CMTR(I) = SUMR

```

10 CMTJ(I) = SUMJ
CONTINUE
RETURN
END
C

LIST OF REFERENCES

1. C. Gabrielli, *Identification of Electrochemical Processes by Frequency Response Analysis*, Solartron Instrumentation Group Monograph, The Solartron Electronic group Ltd., Farnborough, England, 1980.
2. C. Gabrielli, M. Keddam, and H. Takenouti, "New Trends in the Investigation of Electrochemical Systems by Impedance Techniques: Multi-Transfer Function Analysis," *Electrochim. Acta*, 35, 1553(1990).
3. C. Gabrielli and B. Tribollet, "A Transfer Function Approach for a Generalized Electrochemical Impedance Spectroscopy," *J. Electrochem. Soc.*, 141, 1147 (1994).
4. Paul T. Wojcik, *The Electrochemical Behavior of Copper and Copper Nickel Alloys in Synthetic Seawater*, Ph.D. Thesis, University of Florida, August, 1997.
5. B. Tribollet and J. Newman, "The Modulated Flow at a Rotating Disk Electrode," *J. Electrochem. Soc.*, 130, 2016(1983).
6. C. Deslouis and B. Tribollet, "Fundamental Aspects of Unsteady Mass Transfer by EHD and Diffusion Impedances," paper B2-9 presented at the 35th Meeting of the International Society of Electrochemistry, Berkeley, CA August 5-10, 1984.
7. P. Agarwal, M. E. Orazem, and L. H. García-Rubio, "Measurement Models for Electrochemical Impedance Spectroscopy," *J. Electrochem. Soc.*, 139, 1917 (1992).
8. M. E. Orazem, P. Agarwal, A. N. Jansen, P. T. Wojcik, and L. H. García-Rubio, "Development of Physico-Chemical Models for Electrochemical Impedance Spectroscopy," *Electrochimica Acta* 38, 1903 (1993).
9. P. Agarwal, O. D. Crisalle, M. E. Orazem, and L. H. García-Rubio, "Measurement Models for Electrochemical Impedance Spectroscopy: II. Determination of the Stochastic Contribution to the Error Structure," *J. Electrochem. Soc.*, 142, 4149 (1995).
10. M. E. Orazem, P. Agarwal, C. Deslouis, and B. Tribollet, "Application of Measurement Models to Electro-Hydrodynamic Impedance Spectroscopy," *J. Electrochem. Soc.*, 143, 948 (1996).

11. P. Agarwal, M. E. Orazem, and L. H. García-Rubio, *J. Electrochem. Soc.*, "Measurement Models for Electrochemical Impedance Spectroscopy: III. Evaluation of Consistency with the Kramers-Kronig Relations," 142, 4159 (1995).
12. H. W. Bode, *Network Analysis and Feedback Amplifier Design*, D. Van Nostrand Company, Inc., 1945.
13. M. Durbha, M. E. Orazem, and L. H. Garcia-Rubio, "Spectroscopy Applications of the Kramers-Kronig Transforms: Implications for the Error Structure Identification," *Journal of the Electrochemical Society*, 144, 48 (1997).
14. P. Agarwal, *Application of Measurement Models to Impedance Spectroscopy*, Ph.D. Thesis, University of Florida, 1994.
15. J. R. Macdonald and L. D. Potter, Jr., "A Flexible Procedure for analyzing Impedance Spectroscopy Results: Description and Illustrations," *J. Electrochem. Soc.*, 23, 61 (1987).
16. J. R. Macdonald, "Impedance Spectroscopy: Old Problems and New Developments," *Electrochim. Acta*, 35, 1483 (1990).
17. J. R. Macdonald and W. J. Thompson, "Strongly Heteroscedastic Nonlinear Regression," *Commun. Statist. Simula.*, 20, 843 (1991).
18. B. A. Boukamp, "A Nonlinear Least Squares Fit Procedure for Analysis of Immittance Data of Electrochemical Systems," *Solid State Ionics*, 20, 31 (1986).
19. M. E. Orazem, T. El Moustafid, C. Deslouis, and B. Tribollet, "The Error Structure of Impedance Spectra for Systems with a Large Ohmic Resistance with Respect to the Polarization Impedance," *J. Electrochem. Soc.*, 143, 3880 (1996).
20. J. Newman, *Electrochemical Systems*, 2nd ed., Prentice Hall Publications, Englewood Cliffs, NJ, 1991.
21. L. Nyikos and T. Pajkossy, "Fractal Dimension and Fractional Power Frequency-Dependent Impedance of Blocking Electrodes," *Electrochimica Acta*, 30, 1533 (1985).
22. W. H. Mulder and J. H. Sluyters, "An Explanation of Depressed Semi-circular Arcs in Impedance Plots for Irreversible Electrode Reactions," *Electrochimica Acta*, 33, 303 (1988).
23. B. Robertson, B. Tribollet, and C. Deslouis, "Measurement of Diffusion Coefficients by DC and EHD Electrochemical Methods," *J. Electrochem. Soc.*, 135, 2279 (1988).

24. P. Bernard and H. Takenouti, FRACOM: Logiciel MS-DOS d'acquisition et d'exploitation de fonction de transfert pour EI 1286 / FRA série 1250. (FRACOM: MS-DOS software for transfer function measurements and analyses for EI 1286 and FRA 1250 series), 5ème Forum sur les Impédances Electrochimiques, Monrouge, November 1991.
25. J. R. Macdonald, ed., *Impedance Spectroscopy: Emphasizing Solid Materials and Systems*, John Wiley & Sons, 1987.
26. R. de Levie, "Electrochemical Response of Porous and Rough Electrodes," in *Advances in Electrochemistry and Electrochemical Engineering*, 6, 329 (1967).
27. P. Delahay, *Double Layer and Electrode Kinetics*, Interscience Publishers, New York (1965).
28. H.H.Bauer, M.S.Spritzer, and P.J.Elving, "Double-Layer Capacity at a Pyrolytic Graphite Disk Electrode," *J. Electroanal. Chem.*, 17, 299 (1968).
29. M.Stieble and K.Jüttner, "Surface Blocking in the Redox System Pt / $[Fe(CN)_6]^{3-}$, $[Fe(CN)_6]^{4-}$: An AC Impedance Study," *J. Electroanal. Chem.*, 290, 163 (1990).
30. T. Gueshi, K. Tokuda and H. Matsuda, "Voltammetry at Partially Covered Electrodes: Part I. Chronopotentiometry and Chronoamperometry at Model Electrodes," *J. Electroanal. Chem.*, 89, 247 (1978).
31. T. Gueshi, K. Tokuda and H. Matsuda, *J. Electroanal. Chem.*, 101, 29 (1979).
32. K. Tokuda, T. Gueshi and H. Matsuda, "Voltammetry at Partially Covered Electrodes: Part III. Faradaic Impedance Measurements at Model Electrodes," *J. Electroanal. Chem.*, 102, 41 (1979).
33. J. O'M. Bockris and B. Yang, "A Thin-layer Flow Cell for In-situ Infrared Reflection-Adsorption Spectroscopic Measurements of the Electrode/Electrolyte Interphase," *J. Electroanal. Chem.*, 252, 209 (1988).
34. P. A. Christensen, A. Hamnett and P. R. Trevellick, "In-situ Infra-red Studies in Electrochemistry," *J. Electroanal. Chem.*, 242, 23 (1988).
35. H. Baltruschat, F. Lu, D. Song, S.K. Lewis, D.C.Zapien, D.G.Frank, G.N.Salaita and A.T.Hubbard, "Adsorption of Ferricyanide at Pt(111) as a Function of Electrode Potential Studied by Auger Spectroscopy," *J. Electroanal. Chem.*, 234, 229 (1987).
36. K. Winkler, "The Kinetics of Electron Transfer in $Fe(CN)_6^{4/3-}$ Redox System on Platinum Standard Size and Ultramicroelectrodes," *J. Electroanal. Chem.*, 388, 151 (1995).

37. W. Huang and R. McCreery, "Electron Transfer Kinetics of $\text{Fe}(\text{CN})_6^{3-/\text{4-}}$ on laser-activated and CN-modified Pt Electrodes," *J. Electroanal. Chem.*, 326, 1 (1992).
38. K. Kumimatsu, Y. Shigematsu, K. Uosaki and H. Kita, "Study of the $\text{Fe}(\text{CN})_6^{3-/\text{4-}}$ Redox System on Pt by EMIRS: Part I. Infrared Spectra of the Intermediates in the Charge Transfer," *J. Electroanal. Chem.*, 262, 195 (1989).
39. B. Levich, "The Theory of Concentration Polarization," *Acta Physicochimica, URSS*, 17, 257 (1942).
40. J. Newman, "Schmidt Number Correction for the Rotating Disk," *Journal of Physical Chemistry*, 70, 1327 (1966).
41. J. Newman, "Current Distribution on a Rotating Disk below the Limiting Current," *J. Electrochem. Soc.*, 113, 1235 (1966).
42. P. W. Appel, *Electrochemical Systems: Impedance of a Rotating Disk and Mass Transfer in Packed Beds*, Ph.D. dissertation, University of California, Berkeley, June, 1976.
43. Yu Filinovskii and V. A. Kir'yanov, *Dokl. Akad. Nauk. SSSR*, 156, 1412 (1964).
44. D. Schumann, "Électrochimie.- Sur l'Impédance de Diffusion en Basse Fréquence," *Compt. Rend. Acad. Scientifique Paris*, 262C, 624 (1966).
45. C. Deslouis, I. Epelboin, M. Keddam, and J. C. Lestrade, "Impedance de Diffusion d'un Disque Tournant en Régime Hydrodynamique Laminaire. Etude Expérimentale et Comparaison avec le Modèle de Nernst," *J. Electroanal. Chem. and Interfacial Electrochem.*, 28, 57 (1970).
46. E. Levart and D. Schuhmann, "Sur la Détermination Générale de l'Impédance de Concentration (Diffusion Convective et Réaction Chimique) pour une Électrode à Disque Tournant," *J. Electroanal. Chem. and Interfacial Electrochem.*, 53, 77 (1974).
47. V. Homsy and J. Newman, "An Asymptotic Solution for the Warburg Impedance of a Rotating Disk," *J. Electrochem. Soc.*, 121, 521 (1974).
48. E. Levart and D. Schuhmann, "Comparison of Some Solutions for the Warburg Impedance of a Rotating Disk," *J. Electrochem. Soc.*, 122, 1082 (1975).
49. D. A. Scherson and J. Newman, "The Warburg Impedance in the Presence of Convective Flow," *J. Electrochem. Soc.*, 127, 110 (1980).

50. E. Levart and D. Schuhmann, "Discussion on: The Warburg Impedance in the Presence of Convective Flow by D. A. Scherson and J. Newman," *J. Electrochem. Soc.*, 127, 2649 (1980).
51. B. Tribollet and J. Newman, "Analytic Expression for the Warburg Impedance for a Rotating Disk Electrode," *J. Electrochem. Soc.*, 130, 822 (1983).
52. C. Deslouis, C. Gabrielli, and B. Tribollet, "An Analytical Solution of the Nonsteady Convective Diffusion Equation for Rotating Electrodes," *J. Electrochem. Soc.*, 130, 2044 (1983).
53. B. Tribollet, J. Newman, and W. H. Smyrl, "Determination of the Diffusion Coefficient from Impedance Data in the Low Frequency Range," *J. Electrochem. Soc.*, 135, 134 (1988).
54. C. Delouis and B. Tribollet, "Flow Modulation Technique and EHD Impedance: A Tool for Electrode Processes and Hydrodynamic Studies," *Electrochimica Acta*, 35, 1637 (1990).
55. M. E. Orazem, C. Deslouis, and B. Tribollet, "Comparison of Impedance Models for Mass Transfer to a Disk Electrode," presented at the 191st Meeting of the Electrochemical Society, Montreal, Canada, May 4-9, 1997, paper in preparation.
56. Mr Cochran, "The Flow due to a Rotating Disc," *Proceedings of the Cambridge Philosophical Society*, 30, 365 (1935).
57. J. Newman, "Frequency Dispersion in Capacity Measurements at a Disk Electrode," *J. Electrochem. Soc.*, 117, 198 (1970).
58. K. Nisancioglu, "The Error in Polarization Resistance and Capacitance Measurements Resulting from Nonuniform Ohmic Potential Drop to Flush-Mounted Probes," *Corrosion*, 43, 258 (1987).
59. K. Nisancioglu, "Theoretical Problems Related to Ohmic Resistance Compensation," *The Measurement and Correction of Electrolyte Resistance in Electrochemical Tests*, ASTM STP 1056, American Society for Testing and Materials, Philadelphia, 61 (1990).
60. K. Nisancioglu and J. Newman, "The Short-Time Response of a Disk Electrode," *J. Electrochem. Soc.*, 121, 523 (1974).
61. P. W. Appel and J. Newman, "Radially Dependent Convective Warburg Problem for a Rotating Disk," *J. Electrochem. Soc.*, 124, 1864 (1977).
62. A. Frumkin, "Wasserstoffüberspannung und Struktur der Doppelschicht," *Zeitschrift für Physikalische Chemie*, 164, 121 (1933).

63. J. Newman, "The Polarized Diffuse Double Layer," *Transactions of the Faraday Society*, 61, 2229 (1965).
64. J. Newman, *Electrochemical Systems*, Second edition, Prentice Hall Publications, pp 250-252.
65. S. C. Chapra and R. P. Canale, *Numerical Methods for Engineers*, Second edition, McGraw-Hill Publishing company, pp 286-287.
66. D. Jahn and W. Vielstich, "Rates of Electrode Processes by the Rotating Disk Method," *J. Electrochem. Soc.*, 109, 849 (1962).
67. C. Deslouis and B. Tribollet, "Non stationary Mass Transfer in the Flow due to a Disk Rotating in an Ostwald Fluid: Application to the Measurement of the Molecular Diffusion Coefficient in a Polymer Solution," *Electrochimica Acta*, 23, 935 (1978).
68. J. R. Macdonald, ed., *Impedance Spectroscopy Emphasizing Solid materials and Analysis*, John Wiley and Sons, New York, 1987.
69. P. Agarwal, O. C. Moghissi, M. E. Orazem, and L. H. García-Rubio, "Application of Measurement Models for Analysis of Impedance Spectra," *Corrosion*, 49, 278 (1993).
70. P. Agarwal, M. E. Orazem, and A. Hiser, "Application of Electrochemical Impedance Spectroscopy to Metal Hydrides," *Hydrogen Storage Materials, Batteries, and Chemistry*, edited by D. A. Corrigan and S. Srinivasan, Electrochemical Society Proceedings Series, Pennington, N.J., 120 (1991).
71. P. Agarwal, M. E. Orazem, and L. H. García-Rubio, "Application of the Kramers-Kronig Relations in Electrochemical Impedance Spectroscopy," *Electrochemical Impedance: Analysis and Interpretation*, ASTM STP 1188, edited by J. Scully, D. Silverman, M. Kendig, American Society for Testing and Materials, Philadelphia, 115 (1993).
72. E. Levart and D. Schuhmann, *J. Electroanal. Chem.*, 28, 45 (1970).
73. C. Lanczos, *Applied Analysis*, Prentice-Hall, Inc., Engelwood Cliffs, NJ, 1956.
74. R. W. Hamming, *Numerical Methods for Scientists and Engineers*, McGraw-Hill Book Company, Inc., 1962.
75. D. Gottlieb and S. A. Orszag, *Numerical Analysis of Spectral Methods: Theory and Applications*, CBMS-NSF regional conference series in applied mathematics.

76. B. A. Finlayson and L. E. Scriven, "The Method of Weighted Residuals – A Review," *Appl. Mech. Rev.*, 19, 735 (1966).
77. C. W. Clenshaw, "The Numerical Solution of Linear Differential Equations in Chebyshev Series," *Proc. Cambridge Phil. Soc.*, 53, 134 (1957).
78. C. W. Clenshaw and H. J. Norton, "The Solution of Non-linear Ordinary Differential Equations in Chebyshev Series," *Comput. J.*, 6, 88 (1963).
79. E. L. Ince, *Ordinary Differential Equations*, London: Constable; New York: Dover.
80. D. Johnson, "Chebyshev Polynomials in the Spectral Tau Method and Application to Eigenvalue Problems", NASA Contract Report 198451.
81. G. E. P. Box and N. R. Draper, *Empirical Model-Building and Response Surfaces*, John Wiley & Sons, Inc., 1987.
82. H. W. Sorenson, *Parameter Estimation: Principles and Problems*, Marcel Dekker, Inc., 1980.
83. G. A. F. Seber, *Linear Regression Analysis*, John Wiley & Sons, New York, pp. 330–334 (1977).
84. P. Zoltowski, "The error function for fitting of models to immitance data," *J. Electroanal. Chem.*, 178, 11 (1984).
85. P. Zoltowski, "An Immitance Study of the Mechanism of Hydrogen Reactions on a Tungsten Carbide Electrode. Part I," *J. Electroanal. Chem.*, 260, 269 (1989).
86. P. Zoltowski, "An Immitance Study of the Mechanism of Hydrogen Reactions on a Tungsten Carbide Electrode. Part II," *J. Electroanal. Chem.*, 260, 287 (1989).
87. R. W. Christy, "Classical theory of optical dispersion," *American Journal of Physics*, 40, 1403 (1972).
88. A. Jutan and L. H. García-Rubio, "Spectroscopic data resolution using discriminant and eigenvalue analysis," *Process Control and Quality*, 4, 235 (1993).
89. L. K. DeNoyer and J. G. Good, *American Laboratory*, March, 1990. Software available from Spectrum Square Associates, Ithaca, NY, 114850.
90. A. N. Jansen, *Deep-Level Impedance Spectroscopy of Electronic Materials*, Ph.D. Dissertation, University of Florida, 1992.

91. C. Bacon, L. H. Garcia-Rubio, and M. E. Orazem, "Error Analysis for Spectroscopy Applications of the Kramers-Kronig Relations," *Journal of Physics D: Applied Physics*, submitted, 1996.
92. R. de L. Kronig, "On the theory of dispersion of x-rays," *J. Opt. Soc. Am. Rev. Sci. Instrum.*, 12, 547 (1926).
93. R. de L. Kronig, "Dispersionstheorie im rontgengebiet," *Physikal. Z.*, 30, 521 (1929).
94. H. A. Kramers, *Physikal. Z.*, 30, 522 (1929).
95. H.W. Bode, *Network Analysis and Feedback Amplifier Design*, D. Van Nostrand Company, Inc., 1945.
96. J. R. Macdonald, "Some New Directions in Impedance Spectroscopy Data Analysis," *Electrochimica Acta*, 38, 1883 (1993).
97. J. R. Macdonald, "Power-law Exponents and Hidden Bulk Relaxation in the Impedance Spectroscopy of Solids," *J. Electroanal. Chem.*, 378, 17 (1994).
98. B. A. Boukamp and J. R. Macdonald, "Alternatives to Kronig-Kramers Transformation and Testing, and Estimation of Distribtuiions," *Solid State Ionics*, 74, 85 (1994).
99. H. M. Nussenzveig, *Causality and Dispersion Relations*, Academic Press, New York, 1972.
100. J. Killingbeck and G. H. A. Cole, *Mathematical Techniques and Physical Applications*, Academic Press, New York, 1971, 227-230.
101. I. S. Gradshteyn and I. M. Ryzhik, *Table of Integrals, Series, and Products*, Academic Press, 1980, Eq. [3.241.3].
102. P. Agarwal, M. E. Orazem, and L. H. Garcia-Rubio, "The Influence of Error Structure on Interpretation of Impedance Spectra," *Electrochimica Acta*, 41, 1017 (1996).
103. J. R. Macdonald and V. I. Piterbarg, "On the transformation of colored random noise by the Kramers-Kronig Integral Transforms," *J. Electroanal. Chem.*, 428, 1 (1997).
104. M. E. Orazem, P. Agarwal, and L. H. Garcia-Rubio, "Critical Issues Associated with Interpretation of Impedance Spectra," *J. Electroanal. Chem. and Interfacial Chem.*, 378, 51 (1994).
105. M. Durbha, S. L. Carson, A. H. Kalajian, M. Lazzara, M. E. Orazem, and L. H. Garcia-Rubio, "Common Features of Electrochemical and Mechanical

Spectroscopy Measurements," AIChE Annual Meeting, Los Angeles, California, November 17, 1997

106. G. V. Vinogradov and A. Ya. Malkin, *Rheology of Polymers*, Mir Publishers, Moscow, 1980.
107. M. J. Lazzara, "Application of the Measurement Model to Acoustophoretic Measurements," Highest Honors Report, University of Florida, 1997.
108. S. L. Carson, "Application of Complex Spectroscopic Techniques to the Characterization of Particles in Suspension," Ph.D. dissertation in preparation, University of Florida, 1999.
109. Data provided by M. Carasso, Department of Materials Science and Engineering, University of Florida.
110. B. Davies, *Integral Transforms and Their Applications*, Applied Mathematical Series 2 nd Ed., Vol. 25, Springer-Verlag, New York, 1985.
111. B. Miller, M. I. Bellavance, and S. Bruckenstein, *J. Anal. Chem.*, 44, 1983 (1972).
112. S. Bruckenstein, M. I. Belleverance, and B. Miller, "The Electrochemical Response of a Disk Electrode to Angular Velocity Steps," *J. Electrochem. Soc.*, 120, 1351 (1973).
113. B. Miller and S. Bruckenstein, "Theoretical and Experimental Study of Electrohydrodynamically Modulated Current – Potential Curves at Rotating Disk Electrodes under Conditions of Mixed Electrode and Mass-Transfer Control," *J. Electrochem. Soc.*, 121, 1558 (1974).
114. C. Deslouis and B. Tribollet, in *Advances in Electrochemical Science and Engineering*, H. Gerischer and C. W. Tobias, Editors, VCH, New York, 205 (1991).
115. A. C. West, R. D. Grimm, D. Landolt, C. Deslouis, and B. Tribollet, "Electrohydrodynamic impedance study of anodically formed salt films on iron in chloride solutions," *J. Electroanal. Chem.*, 330, 693 (1992).
116. C. Deslouis, "Alternating-current and Electrohydrodynamic Impedances of Electrodes coated with Conductive or Redox Polymers," *Soviet Electrochem.*, 29, 24 (1993).
117. C. Deslouis and B. Tribollet, *J. Electrochem. Soc.*, 29, 75 (1993).
118. O. E. Barcia, O. R. Mattos, N. Pebere, and B. Tribollet, "Mass-Transport Study for the Electrodissolution of Copper in 1M Hydrochloric Acid Solution by Impedance," *J. Electrochem. Soc.*, 140, 2825 (1993).

119. R. C. Vidal and A. C. West, "Copper Electropolishing in Concentrated Phoshoric Acid : I. Experimental Findings," *J. Electrochem. Soc.*, 142, 2683 (1995).
120. R. C. Vidal and A. C. West, "Copper Electropolishing in Concentrated Phoshoric Acid : II. Theoretical Interpretation," *J. Electrochem. Soc.*, 142, 2689 (1995).
121. A. A Zaman and A. L. Fricke, "Viscoelastic Properties of High Solids Softwood Kraft Black Liquors," *I&EC Research*, 34, 382 (1995).
122. A. C. Merrington, *Viscometry*, Edward Arnold & Co., London, 1949.

BIOGRAPHICAL SKETCH

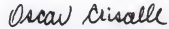
Madhav Durbha received a Bachelor of Technology in Chemical Engineering from the Indian Institute of Technology, Madras, in June 1993. He joined the Ph.D. program in the Department of Chemical Engineering at the University of Florida in August 1993. He conducted research at the CNRS, Paris, in the Spring/Summer of 1995 with financial support from the CNRS laboratories. He received the Ray W. Fahien Teaching award from the Department of Chemical Engineering at the University Florida for his outstanding contributions toward undergraduate education in the capacity of Teaching Assistant during the 1996/97 academic year. He also received Outstanding Academic Achievement award from the College of Engineering, University of Florida, in 1998. After receiving his Ph.D., Madhav Durbha will be joining i2 Technologies Inc., Irving, TX.

I certify that I have read this study and that in my opinion it conforms to acceptable standards of scholarly presentation and is fully adequate, in scope and quality, as a dissertation for the degree of Doctor of Philosophy.



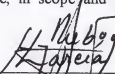
Mark E. Orazem, Chairman
Professor of Chemical Engineering

I certify that I have read this study and that in my opinion it conforms to acceptable standards of scholarly presentation and is fully adequate, in scope and quality, as a dissertation for the degree of Doctor of Philosophy.



Oscar D. Crisalle
Associate Professor of Chemical
Engineering

I certify that I have read this study and that in my opinion it conforms to acceptable standards of scholarly presentation and is fully adequate, in scope and quality, as a dissertation for the degree of Doctor of Philosophy.



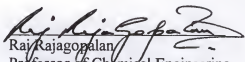
Luis H. Garcia-Rubio
Professor of Chemical Engineering
University of South Florida

I certify that I have read this study and that in my opinion it conforms to acceptable standards of scholarly presentation and is fully adequate, in scope and quality, as a dissertation for the degree of Doctor of Philosophy.



Chang W. Park
Associate Professor of Chemical
Engineering

I certify that I have read this study and that in my opinion it conforms to acceptable standards of scholarly presentation and is fully adequate, in scope and quality, as a dissertation for the degree of Doctor of Philosophy.


Raj Rajagopalan
Professor of Chemical Engineering

I certify that I have read this study and that in my opinion it conforms to acceptable standards of scholarly presentation and is fully adequate, in scope and quality, as a dissertation for the degree of Doctor of Philosophy.


Chen-Chi Hsu
Professor of Aerospace
Engineering, Mechanics and
Engineering Science

This dissertation was submitted to the Graduate Faculty of the College of Engineering and to the Graduate School and was accepted as partial fulfillment of the requirements for the degree of Doctor of Philosophy.

August 1998


Winfred M. Phillips
Dean, College of Engineering

Karen A. Holbrook
Dean, Graduate School

LD
1780
1998
•D953

